Fakulteta za
industrijski inženiring
Faculty of Industrial Engineering

Zbornik recenziranih prispevkov 9. mednarodne konference o razvoju industrijskega inženiringa: Priložnosti, potenciali in izzivi za zeleni prehod

Proceedings of Reviewed Papers of the 9th International Conference on the Development of Industrial Engineering: Opportunities, Potentials and Challenges for the Green Transition

Novo mesto, 21. november 2024

Sponzor konference | Sponsor of the conference:

Skupina HSE je največja proizvajalka električne energije iz obnovljivih virov v Sloveniji in nosilka zelenega prehoda. Sledi poglavitnim strateškim smernicam države in Evropske unije na področju trajnostnega razvoja ter temu nenehno prilagaja svojo dejavnost in storitve. Več kot polovica proizvedene električne energije iz skupine HSE že danes prihaja iz obnovljivih virov, končnim odjemalcem pa ponuja celovite in konkurenčne energetske rešitve na področju trajnostne energetske oskrbe in samooskrbe.

The HSE Group is the largest producer of electricity from renewable sources in Slovenia and a key player in the green transition. It adheres to the main strategic guidelines of the country and the European Union in the field of sustainable development, continuously adapting its activities and services accordingly. More than half of the electricity produced by the HSE Group already comes from renewable energy sources, and it offers end-users comprehensive and competitive energy solutions in the areas of sustainable energy supply and self-sufficiency.

Fakulteta za
industrijski inženiring
Faculty of Industrial Engineering

Zbornik recenziranih prispevkov 9. mednarodne konference o razvoju industrijskega inženiringa: Priložnosti, potenciali in izzivi za zeleni prehod

Proceedings of Reviewed Papers of the 9th International Conference on the Development of Industrial Engineering: Opportunities, Potentials and Challenges for the Green Transition

Novo mesto, 21. november 2024

Zbornik recenziranih prispevkov 9. mednarodne konference | Proceedings of Reviewed Papers of the 9th International Conference.

9. mednarodna konferenca o razvoju industrijskega inženiringa: Priložnosti, potenciali in izzivi za zeleni prehod. Novo mesto, 21. november 2024.

9th International Conference on the Development of Industrial Engineering: Opportunities, Potentials and Challenges for the Green Transition. Novo mesto, November 21, 2024.

Organizatorji konference | Conference Organizers:
Fakulteta za industrijski inženiring Novo mesto | Faculty of Industrial Engineering Novo mesto
Fakulteta za organizacijske študije Novo mesto | Faculty for organization studies Novo mesto
Rudolfovo – Znanstveno in tehnološko središče Novo mesto | Rudolfovo – Science and Technology Centre Novo mesto

Založnik zbornika | Publisher of Proceedings:
Fakulteta za industrijski inženiring Novo mesto | Faculty of industrial engineering Novo mesto
Kraj | Place: Šegova ulica 112, 8000 Novo mesto, Slovenija

Leto izida | Year: 2024

Uredniški odbor | Editorial Board:
mag. Iris Fink Grubačević
izr. prof. dr. Damir Vrančić
doc. dr. Boris Kraševec
doc. dr. Jelena Topić Božič
prof. dr. Simon Muhič

Programski odbor konference | Members of Programe Committee:
doc. dr. Tomaž Savšek, Fakulteta za industrijski inženiring Novo mesto, Slovenija (predsednik)
zasl. prof. dr. Dorian Marjanović, University of Zagreb, Faculty of Mechanical Engineering, Hrvaška
zasl. prof. dr. Rudolf Pušenjak, Fakulteta za industrijski inženiring Novo mesto, Slovenija
prof. dr. Simon Muhič, Fakulteta za industrijski inženiring Novo mesto, Slovenija
prof. dr. Janez Povh, Rudolfovo – Znanstveno in tehnološko središče Novo mesto, Slovenija
prof. dr. Boris Bukovec, Fakulteta za organizacijske študije v novem mestu, Slovenija
prof. dr. Matej Makarovič, Fakulteta za informacijske študije v Novem mestu, Slovenija
prof. dr. Julius Kaplunov, Keele University, UK
prof. dr. Matej Daniel, Faculty of Mechanical Engineering, Czech Technical University in Prague, Czech Republic
izr. prof. dr. Lea Colarič Jakše, Visoka šola za upravljanje podeželja Grm Novo mesto, Slovenija
izr. prof. dr. Damir Vrančić, Institut Jožef Stefan, Slovenija
izr. prof. dr. Dolores Modic, Inovation and Management at Nord University Business School, Nord University, Norway
dr. Georgios Kordogiannis, Institut Jožef Stefan, Slovenija
dr. Barbara Zupančič, Kemijski inštitut, Slovenija
mag. Iris Fink Grubačević, Fakulteta za industrijski inženiring Novo mesto, Slovenija

Recenzenti | Reviewers:
dr. Mladen Bošnjaković
dr. Ante Čikić
dr. Nikola Jakšić
dr. Urban Močnik
dr. Dolores Modic
dr. Simon Muhič
dr. Milica M. Perić
dr. Matej Pleterski
dr. Marica Prijanovič Tonkovič
dr. Rudolf Pušenjak
dr. Jelena Topić Božič
dr. Damir Vrančić

Tehnični urednik | Technical Editor: Matic Medvešek, dipl. inž. str.

Tisk na zahtevo.

Fakulteta za industrijski inženiring Novo mesto je izključni imetnik vseh materialnih avtorskih pravic v tej publikaciji. Avtorji so odgovorni za vsebinsko ustreznost prispevkov v publikaciji.

The Faculty of Industrial Engineering Novo mesto is the exclusive holder of all material copyrights for this publication. The authors are responsible for the content of the contributions in the publication.

CIP - Kataložni zapis o publikaciji
Narodna in univerzitetna knjižnica, Ljubljana

62-027.31:502.131.1(082)

MEDNARODNA konferenca o razvoju industrijskega inženiringa (9 ; 2024 ; Novo mesto)
Priložnosti, potenciali in izzivi za zeleni prehod = Opportunities, potentials and challenges for the green transition : zbornik recenziranih prispevkov 9. mednarodne konference o razvoju industrijskega inženiringa = proceedings of reviewed papers of the 9th International Conference on the Development of Industrial Engineering : Novo mesto, 21. november 2024 / [organizatorji konference Fakulteta za industrijski inženiring Novo mesto [in] Fakulteta za organizacijske študije Novo mesto [in] Rudolfovo - Znanstveno in tehnološko središče Novo mesto ; uredniški odbor Iris Fink Grubačević ... et al.]. - Novo mesto : Fakulteta za industrijski inženiring = Faculty of Industrial Engineering, 2024

ISBN 978-961-7097-14-6
COBISS.SI-ID 215372035

KAZALO | TABLE OF CONTENTS

Standardisation of Measurement and Assessment of Circular Economy: the Introduction of ISO 59000 Standards

Urška Fric[1,2], Jelena Topić Božič[2,3], Simon Muhič[2,3,4]

[1]Faculty of Information Studies in Novo mesto, Ljubljanska cesta 31a, 8000 Novo Mesto, Slovenia
E-mail: urska.fric@fis.unm.si

[2]Rudolfovo – Science and Technology Center Novo mesto, Podbreznik 15, 8000 Novo mesto, Slovenia
E-mail: jelena.topic.bozic@rudolfovo.eu

[3]Faculty of Industrial Engineering Novo mesto, Šegova ulica 112, 8000 Novo mesto, Slovenia
E-mail: simon.muhic@fini-unm.si

[4]INOVEKS, Cesta 2. grupe odredov 17, 1295 Ivančna Gorica
E-mail: simon.muhic@inoveks.si

***Abstract**: Circular economy (CE) is a broad concept with three main principles. The first is the preservation and enhancement of natural capital by controlling finite stocks and balancing the flows of renewable resources. The second is optimising the productive use of resources by circulating products, components, and materials at the highest level of utility. The third principle is stimulating the system's effectiveness by revealing and excluding negative externalities from the beginning. Several institutions monitor the state of CE with different indicators. Indicators proposed by the European Commission can be direct or indirect. Some direct CE indicators include waste generation, recycling rate, recycling/reuse of specific waste streams, and reuse rate. Indirect indicators refer to green public procurement, trading in recyclable secondary raw materials, investments, growth, and workforce within a CE. Standardisation in correlation with key performance indicators (KPIs) is necessary to remove bias from evaluation, especially when a hierarchy is employed in the KPIs for quantification and decision-making. Several standards have been proposed in recent years to reduce the uncertainty and lack of precision about the CE paradigm and associated concepts. The new ISO 59000 standards published in May 2024, which set a common language and conceptual framework to narrow the terms, measures, and indicators, are still unknown, especially among enterprises in Slovenia. The paper presents the CE indicators for Slovenia and the ISO 59004 framework for measuring and assessing the effectiveness of circularity.*

***Keywords:** circular economy, standardisation, ISO 59000, monitoring CE framework, Slovenia*

***Classification:** Scientific paper*

1 INTRODUCTION

Over the last forty years, various environmental legislation has been adopted. Today, the European Union (EU) environmental law, or the environmental acquis, consists of more than 500 directives, regulations, and decisions. The pursuit of EU environmental policies has contributed to achieving resource efficiency through applying the circular economy concept, which has become a growing market trend over the last decade. To achieve the goal of all three pillars of sustainable development (economic development, social development, and environmental protection), the circular economy, as stated by the Ellen MacArthur Foundation in 2016, represents a response to the pressures of a growing economy, consumption of finite resources, and the carrying capacity of the environment [1].

The EU is still too slow or not far enough advanced to move from a linear to a circular economy. Some Member States have progressed, some have stagnated, and some have regressed. According to 2023 data, Slovenia has made progress, ranking 11th out of all Member States in terms of overall circularity [2].

Although monitoring progress from a linear to a circular economy is methodologically and institutionally supported at the EU level and monitored by several indicators, standardisation should ensure impartiality in monitoring/assessment. A robust framework is needed to transition from a linear to a circular economy comprehensively, and standardisation should be its boundary. The monitoring process is a difficult task, mainly because there is no single generally acceptable set of indicators or one such indicator, or there is a great variety of indicators, which may result from a different understanding of the CE concept by individual stakeholders [3].

A successful transition to CE must have rigorous technical underpinnings and require global participation. In addition to solid technical foundations, a consensus between stakeholders will add legitimacy to new business practices. Standards created by voluntary consensus bodies are uniquely positioned to serve such purposes as they are developed by systematically determining the scope of the work, agreeing on terminology, and building on that foundation to create detailed specifications [4]. Given that the International Organization for Standardisation (ISO) has only recently launched a set of international standards for 2024, many questions arise about the role of standardisation in the transition from a linear to a circular economy. However, lack of knowledge of the standards remains a key challenge.

The present paper sheds light on the purpose and objectives of standardisation, which is seen as the creation of frameworks, requirements, guidelines, and tools to monitor the transition from a linear to a circular economy, measured through indicators. ISO 59000 is crucial to integrate into business strategy, as it contributes to profitability, environmental preservation, and organisational social responsibility.

2 METHODOLOGY

The paper relies on secondary sources. The standardisation presentation is based on a systematic literature review (SLR) to identify, evaluate, and interpret all available research to address research questions in a specific field. The digital collections, scientific journals, and conference papers have been searched using keywords. The authors have used at least three different terms for the search area and combined keywords using Boolean operators, quotation marks, order, and search strings in various combinations. The authors have searched digital repositories multiple times to find as many relevant secondary sources as possible. The secondary sources (articles, studies, reports) are evaluated using the Currency, Relevance, Authority, Accuracy, and Purpose (CRAAP) method. The presentation of indicators is based on using a statistical database, namely EUROSTAT.

3 RESULTS AND DISCUSSION

CE approach promotes the responsible and cyclical use of resources. Years ago, CE was endorsed as a policy to minimise environmental burdens and stimulate the economy [5]. CE is an umbrella concept that includes lowering material input and minimising waste generation to decouple economic growth from natural resource use [5, 6]. The transition towards CE hinges on the effective measurement of CE practices through indexes and frameworks, which are not just facilitators but are integral to the realisation and optimisation of a CE [7–9]. In this context, indicators and frameworks are vital for setting and achieving specific, quantifiable targets [7].

In 2018, the European Commission assessed elements to reach a theoretical consensus on the CE concept. This resulted in a monitoring framework with indicators obtained with already available data linked to different phases of CE [10, 11]. The EU monitoring framework for the CE, released in 2018, included ten key indicators covering every phase of the product life cycle and the significant aspects of competitiveness [12]. In 2023, the revised CE Monitoring Framework came forth, which includes a new dimension on global sustainability and resilience, adding to the existing four dimensions of the previous monitoring framework: production and consumption, waste management, secondary raw materials, secondary raw materials, competitiveness and innovation. The new monitoring framework, shown in Figure 2, includes new indicators: material footprint, resource productivity, consumption footprint, greenhouse gas emissions from production activities and material dependency [13]. The indicator change has led to a redefinition of how CE should be measured in the EU. The EU sought to homogenise the indicator framework proposed in 2018, possibly because the framework developed in 2018 did not approach the analysis from a holistic perspective [14].

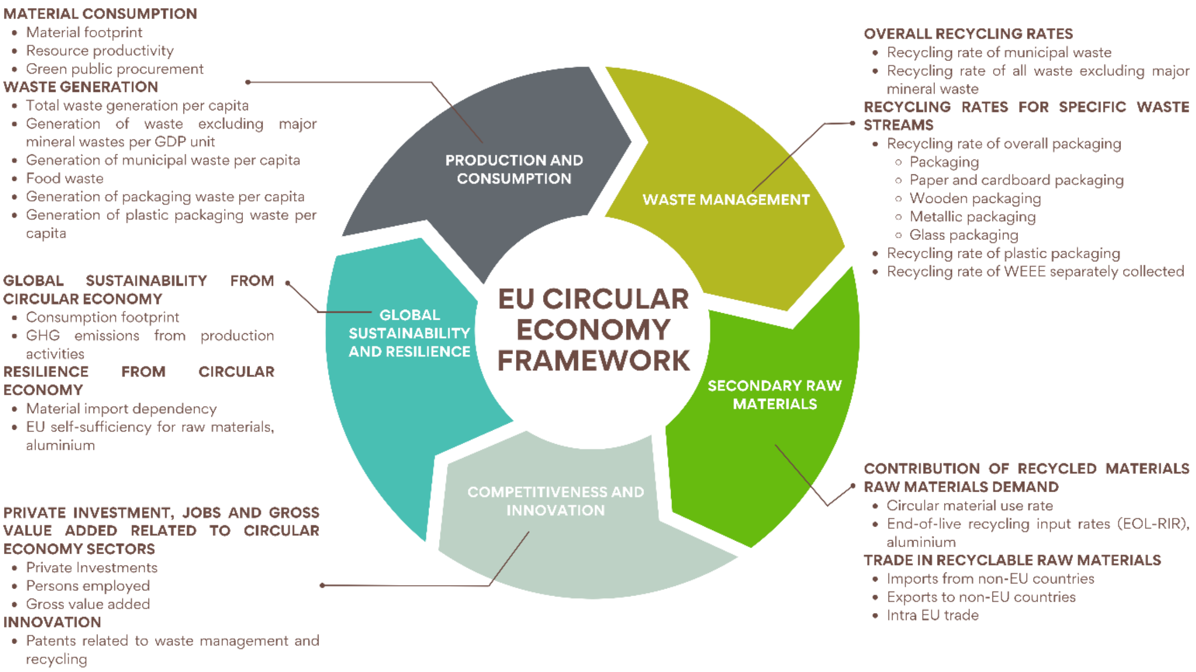

Figure 1: Revised CE framework

Table 1 and Figure 2 show data and trends on the Global sustainability and resilience dimension. The consumption footprint in Slovenia decreased until 2022 when an increase was observed. Nevertheless, the trend is better when compared to the EU, where an increase has been observed over the years, as until 2019, the consumption footprint showed a continuously increasing trend. In 2020, the COVID-19 pandemic occurred, leading to a general decrease in consumption footprint [15]. Since 2021, a rising trend has been observed, and the latest available data shows that it exceeded pre-COVID-19 values.

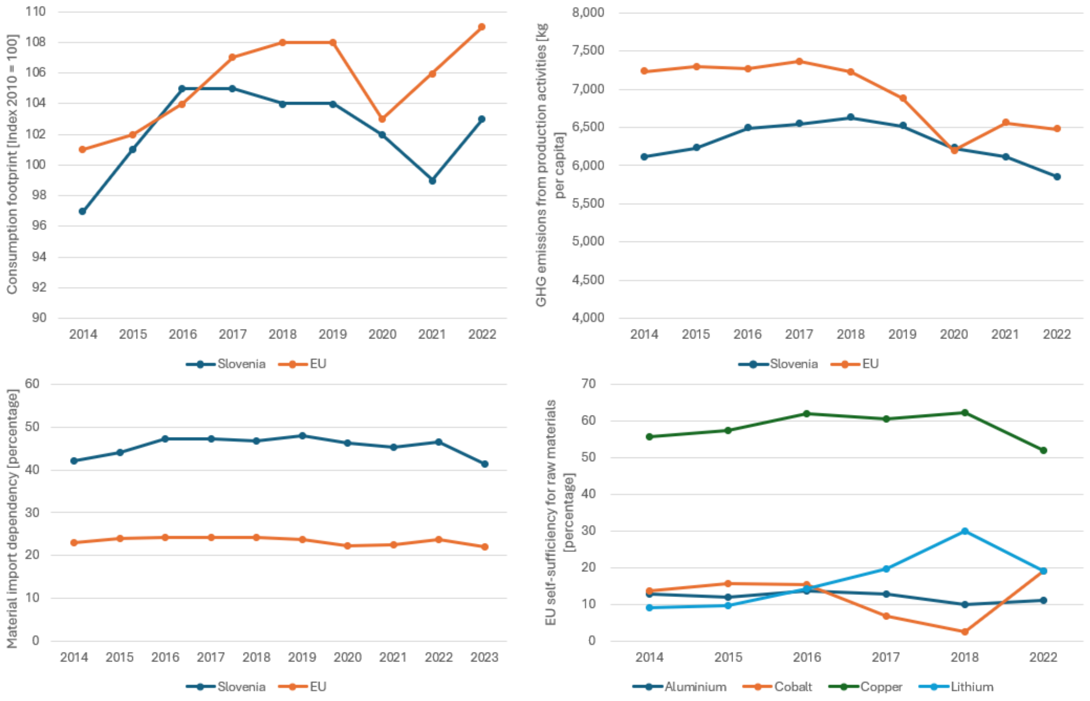

Figure 2: Trends for global sustainability and resilience from the circular economy dimension (2014 – 2022/23)

GHG emission data in the EU showed a decreasing trend at the lowest value reported in 2020, as the shrinking of production and demand temporarily impacted GHG emission reductions [16]. Data on material import dependency shows that Slovenia. However, a decreasing trend has been observed since 2019 and still relies heavily on imports as material import dependency exceeds 40 %, almost twice as high as in the EU (22 %). Regarding self-sufficiency of raw materials, the EU exceeds 50 % self-sufficiency for copper and limestone; however, the latest data on aluminium, cobalt, and lithium shows that the percentage is below 20 %.

Table 1:Values for global sustainability and resilience from the circular economy dimension.

Monitoring Framework CE Indicators	SI (EU Average)	Year	Rank of Slovenia in the EU	Indicator Explanation
GLOBAL SUSTAINABILITY AND RESILIENCE				
Global sustainability from the circular economy				
Consumption footprint (Index 2010=100)	103 (109)	2022	6/27	The indicator estimates the environmental impacts of EU and Member States' consumption by combining data on consumption intensity and environmental impacts of representative products covering five consumption areas: food, mobility, housing, appliances, and household goods.
*GHG emissions from production activities (kg per capita***)**	5858 (6476)	2022	12/27	This indicator presents GHG emissions of all production activities undertaken in the EU economy. It includes emissions from international air transport undertaken by EU-resident airlines and excludes emissions from private households.
Resilience from the circular economy				
Material import dependency (percentage)	41.5 (22)	2023	20/27	The indicator provides the ratio of imports over direct material inputs, showing how much an economy relies upon imports to meet its material needs.
EU self-sufficiency for raw materials, aluminium (percentage)	/ (11)	2022		The indicator measures how much the EU is independent from the rest of the world for several raw materials. The graph shows the trends for aluminium, cobalt, copper, and lithium.

An indicator within the Monitoring CE Framework is the circular material use rate. The circularity rate has been compiled since 2019 and calculated retrospectively to 2004 [2]. The circular material use rate in the years 2014–2022 in Slovenia and the EU is presented in Figure 3. The circularity use in Europe has not exceeded 12 %. The circularity rate in Slovenia is below the EU, and on average, the value in the 2014–2022 period was 9.5 %; the circularity rate in 2022 ranked Slovenia in 18th place. The two highest-ranked countries were Belgium and the Netherlands, with 22.2 % and 27.5 % circularity rates, respectively [13].

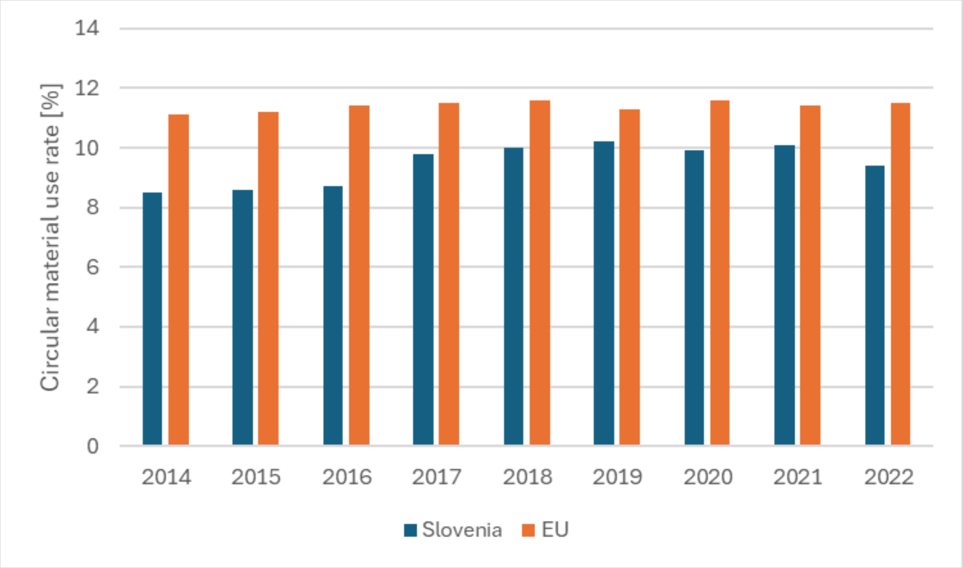

Figure 3: The circular material use rate in 2014–2022 (data source: Eurostat)

According to the European Court of Auditors, an audit report on circular economy in member states, the EC Framework for monitoring the EU's transition to a circular economy did not fully capture all the essential aspects, lacking specific indicators relating to the circular design of products [2]. Developing CE indicators metrics comes with a set of challenges. One of the main objectives is the vital use of key performance indicators (KPIs) and targets, confirming the notion that “what you cannot measure, you *cannot manage*” [17].

Several standards regarding the CE have been proposed in recent years to reduce the uncertainty and lack of precision about the CE paradigm and associated concepts [18]. In recent years, two standards have been published in the CE by the British Standards Institution and French Standardization Association (AFNOR), BS 8001:2017 and XP X30-901:2018, respectively [6, 18]. BS 8001:2017 standard sets a general framework; however, the guidance for monitoring the CE strategy requires applying CE principles in organisations. However, the guidance for monitoring the CE strategy remains vague [6]. On the other hand, XP X30-901:2018 aims to set a holistic view of the CE and provides a general approach for implementing CE projects [18]. The two standards differ in the aim, application, phases, and main fundamentals. The objective of the BS 8001:2017 standard is framework and guidance, which can be applied to any organisation and has eight defined phases. It is not intended nor suitable for certification purposes.

On the other hand, XP X30-901 sets requirements and guidelines, and its application is an organisation's CE project management system. It has defined five phases and seven areas of action. AFNOR offers certification. Both standards cover all three dimensions: economic, social and environmental [19]. Due to the need for standardisation and harmonisation of CE in 2018, the ISO/TC 323 “CE” technical committee was established [15], and the first ISO standards on CE were published in May 2024. A set of standards on CE is designed to harmonise the understanding of CE. It aims to develop frameworks, guidance, support tools and requirements for implementing activities of all involved organisations and to maximise the contribution to sustainable development [20].

The CE ISO 59000 family includes several ISO standards and two technical reports which have been recently published or are currently under development, with a more detailed overview shown in Figure 4 [21–27]:

- ISO 59004 Circular economy – Vocabulary, principles and guidance for implementation (published in May 2024).
- ISO 59010 Circular economy – Guidance on transitioning business models and value networks (published in May 2024).
- ISO 59020 Circular economy – Measuring and assessing circularity performance (published in May 2024).
- ISO 59014 Environmental management – Guidelines on secondary materials (status in September 2024: under publication, final production steps (up to seven weeks).
- ISO 59040 Product Circularity Data Sheet (status in September 2024: under development; in the inquiry phase with ISO members.
- ISO/TR 59032:2024 Circular economy – Review of existing value networks (published in May 2024).
- ISO/CD TR 59031 Circular economy – Performance-based approach – Analysis of case studies (status in September 2024: under development; the committee is reviewing a draft).

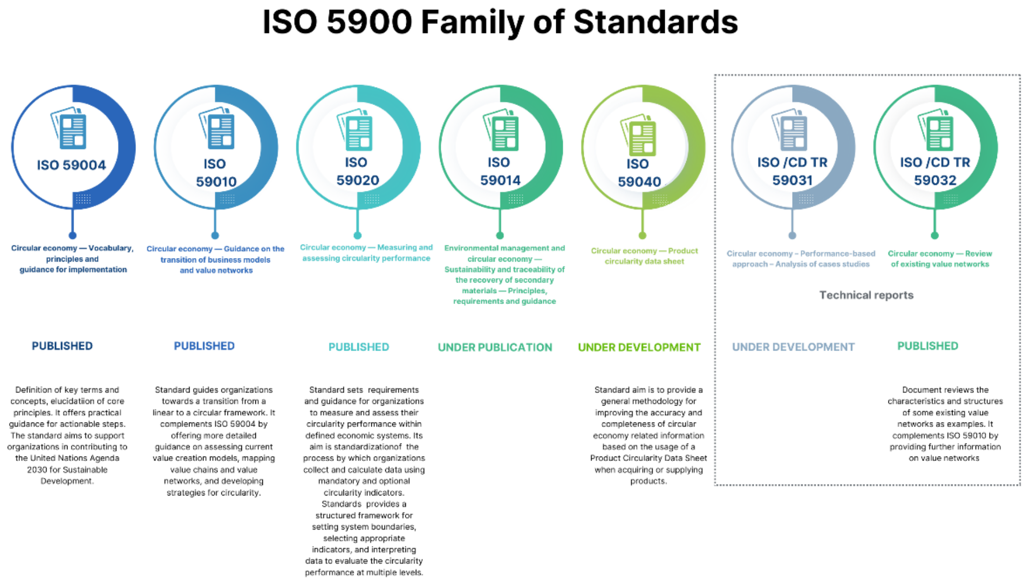

Definition of key terms and concepts, elucidatiion of core principles. It offers practical guidance for actionable steps. The standard aims to support organizations in contributing to the United Nations Agenda 2030 for Sustainable Development.

Standard guides organizations towards a transition from a linear to a circular framework. It complements ISO 59004 by offering more detailed guidance on assessing current value creation models, mapping value chains and value networks, and developing strategies for circularity.

Standard sets requirements and guidance for organizations to measure and assess their circularity performance within defined economic systems. Its aim is standardizationof the process by which organizations collect and calculate data using mandatory and optional circularity indicators. Standards provides a structured framework for setting system boundaries, selecting appropriate indicators, and interpreting data to evaluate the circularity performance at multiple levels.

Standard aim is to provide a general methodology for improving the accuracy and completeness of circular economy related information based on the usage of a Product Circularity Data Sheet when acquiring or supplying products.

Document reviews the characteristics and structures of some existing value networks as examples. It complements ISO 59010 by providing further information on value networks

Figure 4: ISO 5900 family of standards (source: own elaboration based on data from [21–27]

ISO 59020 standard circularity indicators, which serve as quantitative or qualitative measures of various circularity aspects, have been established with the introduction. These indicators can be utilised at any stage of the life cycle of a circular action, including concept testing during simulation, design phases, regular planning, and operational monitoring. The indicators to measure circularity aim to calculate the circularity performance and are divided into core and additional circularity indicators [28].

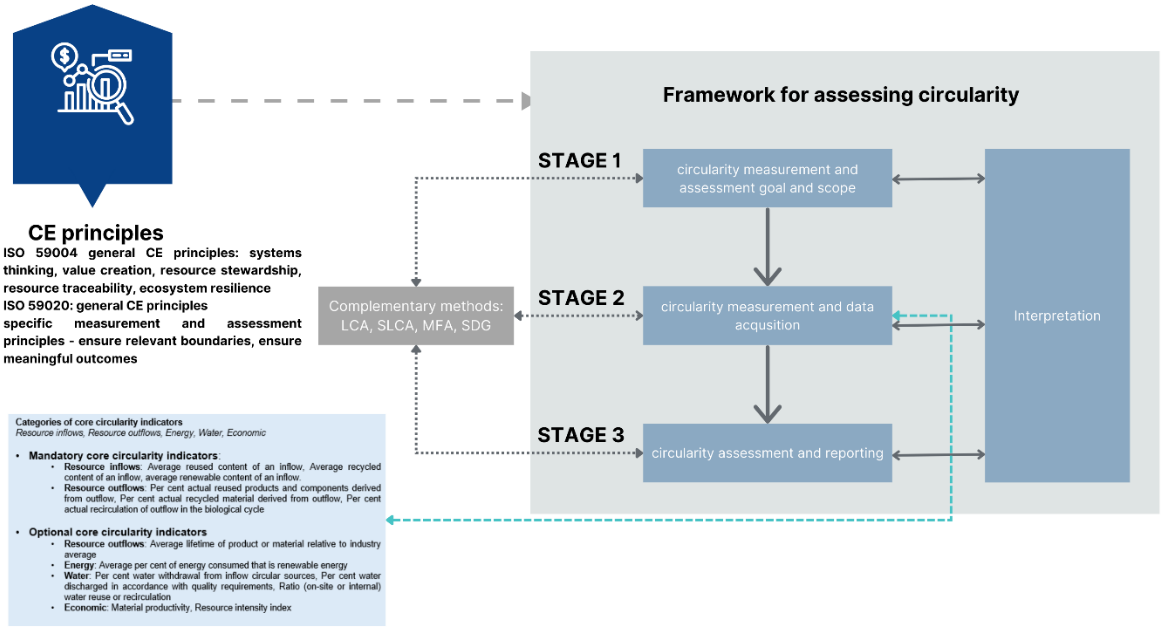

ISO 59004 general CE principles: systems thinking, value creation, resource stewardship, resource traceability, ecosystem resilience
ISO 59020: general CE principles
specific measurement and assessment principles - ensure relevant boundaries, ensure meaningful outcomes

Categories of core circularity indicators
Resource inflows, Resource outflows, Energy, Water, Economic

- **Mandatory core circularity indicators**:
  - **Resource inflows**: Average reused content of an inflow, Average recycled content of an inflow, average renewable content of an inflow.
  - **Resource outflows**: Per cent actual reused products and components derived from outflow, Per cent actual recycled material derived from outflow, Per cent actual recirculation of outflow in the biological cycle
- **Optional core circularity indicators**
  - **Resource outflows**: Average lifetime of product or material relative to industry average
  - **Energy**: Average per cent of energy consumed that is renewable energy
  - **Water**: Per cent water withdrawal from inflow circular sources, Per cent water discharged in accordance with quality requirements, Ratio (on-site or internal) water reuse or recirculation
  - **Economic**: Material productivity, Resource intensity index

Figure 5: ISO 59020 circularity assessment framework (source: own based on [24])

ISO 59000 standard provides a framework to guide users within organisations of all types and sizes through the measurement and assessment process, which includes system boundary setting and choice of indicators, and to process and interpret data consistently and reproducibly [24]. The framework is elaborated in Figure 5, and it consists of three main stages:

- definition of goal and scope and setting system boundaries;
- data acquisition;
- circularity assessment and reporting.

A set of core indicators belonging to resource inflows, resource outflows, energy, water, and economics has been specified for circularity assessment. With the introduction of standards, consolidation in the application of indicators is expected to ensure unified use, which presents a way to compare different organisations and systems.

4 CONCLUSION

Circular Economy (CE) is increasingly recognised as a key issue on the EU political agenda, particularly in addressing environmental challenges. However, there is significant variation in performance across different sectors. Monitoring progress is complicated by the lack of universally accepted indicators stemming from various stakeholders' diverse interpretations of the CE concept. To enhance CE initiatives, there is a need for greater standardisation, which would provide frameworks, guidance, tools, and requirements for organisations involved in CE activities. This would enable them to maximise their contributions to Sustainable Development and the transition to a CE.

The paper on ISO standards on CE marks an essential step toward establishing more consistent definitions and monitoring processes for CE implementation.

For standards and practices derived from these standards to be practical, they must be meaningfully integrated into organisations' business strategies. This integration can significantly enhance business performance and uphold social responsibility.

Businesses, governments, and organisations can effectively monitor, control, and audit operations with clear and validated definitions. This allows for comparing practices to ensure the successful implementation of CE initiatives and helps prevent greenwashing. Furthermore, these proposed standards could be expanded to include applications that monitor how CE approaches generate long-term circular advantages and evaluate the practical adoption of CE principles.

Funding

This research was funded by the Slovenian Research and Innovation Agency Research Program, Public call ARRS-RPROJ/2023/Appl. 375.

REFERENCES

[1] ELLEN MACARTHUR FOUNDATION. Circular economy introduction [online]. 2016 [vid. 2024-09-08]. Available at: https://www.ellenmacarthurfoundation.org/topics/circular-economy-introduction/overview

[2] EUROPEAN COURT OF AUDITORS. Special report: Circular economy Slow transition by member states despite EU action [online]. 2023. Available at: https://www.eca.europa.eu/ECAPublications/SR-2023-17/SR-2023-17_EN.pdf

[3] MAZUR-WIERZBICKA, Ewa. Circular economy: advancement of European Union countries. Environmental Sciences Europe [online]. 2021, **33**(1), 111. ISSN 2190-4715. Available at: doi:10.1186/s12302-021-00549-0

[4] MORRIS, K.c., Vincenzo FERRERO, Buddhika HAPUWATTE, Noah LAST a Nehika MATHUR. Standards as Enablers for a Circular Economy. In: Technology Innovation for the Circular Economy [online]. B.m.: John Wiley & Sons, Ltd, 2024 [vid. 2024-09-08], s. 1–16. ISBN 978-1-394-21429-7. Available at: doi:10.1002/9781394214297.ch1

[5] MORAGA, Gustavo, Sophie HUYSVELD, Fabrice MATHIEUX, Gian Andrea BLENGINI, Luc ALAERTS, Karel VAN ACKER, Steven DE MEESTER a Jo DEWULF. Circular economy indicators: What do they measure? Resources, Conservation, and Recycling [online]. 2019, **146**, 452–461. ISSN 0921-3449. Available at: doi:10.1016/j.resconrec.2019.03.045

[6] PAULIUK, Stefan. Critical appraisal of the circular economy standard BS 8001:2017 and a dashboard of quantitative system indicators for its implementation in organizations. Resources, Conservation and Recycling [online]. 2018, **129**, 81–92. ISSN 0921-3449. Available at: doi:10.1016/j.resconrec.2017.10.019

[7] MARTINHO, Vítor João Pereira Domingues. Insights into circular economy indicators: Emphasizing dimensions of sustainability. Environmental and Sustainability Indicators [online]. 2021, **10**, 100119. ISSN 2665-9727. Available at: doi:10.1016/j.indic.2021.100119

[8] MUÑOZ, Santiago, M. Reza HOSSEINI a Robert H. CRAWFORD. Towards a holistic assessment of circular economy strategies: The 9R circularity index. Sustainable Production and Consumption [online]. 2024, **47**, 400–412. ISSN 2352-5509. Available at: doi:10.1016/j.spc.2024.04.015

[9] SAIDANI, Michael, Bernard YANNOU, Yann LEROY, François CLUZEL a Alissa KENDALL. A taxonomy of circular economy indicators. Journal of Cleaner Production [online]. 2019, **207**, 542–559. ISSN 0959-6526. Available at: doi:10.1016/j.jclepro.2018.10.014

[10] EC, European Commission. Measuring Progress towards Circular Economy in the European Union–Key Indicators for a Revised Monitoring Framework. B.m.: European Commission Brussels, Belgium. 2023

[11] RINCÓN-MORENO, J., M. ORMAZÁBAL, M. J. ÁLVAREZ a C. JACA. Advancing circular economy performance indicators and their application in Spanish companies. Journal of Cleaner Production [online]. 2021, **279**, 123605. ISSN 0959-6526. Available at: doi:10.1016/j.jclepro.2020.123605

[12] PACURARIU, Roxana Lavinia, Sorin Daniel VATCA, Elena Simina LAKATOS, Laura BACALI a Mircea VLAD. A Critical Review of EU Key Indicators for the Transition to the Circular Economy. International Journal of Environmental Research and Public Health [online]. 2021, **18**(16), 8840. ISSN 1660-4601. Available at: doi:10.3390/ijerph18168840

[13] EUROSTAT. Improved circular economy monitoring framework now live [online]. 2023 [vid. 2024-09-02]. Available at: https://ec.europa.eu/eurostat/web/products-eurostat-news/w/wdn-20230515-1

[14] CASTILLO-DÍAZ, Francisco José, Luis J. BELMONTE-UREÑA, Fernando DIÁNEZ-MARTÍNEZ a Francisco CAMACHO-FERRE. Challenges and perspectives of the circular economy in the European Union: A comparative analysis of the member states. Ecological Economics [online]. 2024, **224**, 108294. ISSN 0921-8009. Available at: doi:10.1016/j.ecolecon.2024.108294

[15] SALA, Serenella a MENGUAL Esther SANYE. Consumption Footprint: assessing the environmental impacts of EU consumption. JRC Publications Repository [online]. 19. leden 2022 [vid. 2024-09-03]. Available at: https://publications.jrc.ec.europa.eu/repository/handle/JRC126257

[16] EEA. ETC CE Report 2024/7 Nowcasting and outlooks of EEA circular economy indicators. Eionet Portal [online]. 2024 [vid. 2024-09-03]. Available at: https://www.eionet.europa.eu/etcs/etc-ce/products/etc-ce-report-2024-7-nowcasting-and-outlooks-of-eea-circular-economy-indicators

[17] VOUKKALI, Irene, Iliana PAPAMICHAEL, Pantelitsa LOIZIA, Demetris F LEKKAS, Teresa RODRÍGUEZ-ESPINOSA, Jose NAVARRO-PEDREÑO a Antonis A ZORPAS. Waste metrics in the framework of circular economy. Waste Management & Research [online]. 2023, **41**(12), 1741–1753. ISSN 0734-242X. Available at: doi:10.1177/0734242X231190794

[18] HERAS-SAIZARBITORIA, Iñaki, Olivier BOIRAL a Francesco TESTA. ISO 59000 Standards for the Circular Economy: a Call for Accuracy. Circular Economy and Sustainability [online]. 2024 [vid. 2024-09-02]. ISSN 2730-5988. Available at: doi:10.1007/s43615-024-00370-w

[19] ARANA-LANDIN, German, Waleska SIGÜENZA, Beñat LANDETA-MANZANO a Iker LASKURAIN-ITURBE. Circular economy: On the road to ISO 59000 family of standards. Corporate Social Responsibility and Environmental Management [online]. 2024, **31**(3), 1977–2009. ISSN 1535-3966. Available

at: doi:10.1002/csr.2665
[20] ISO. ISO/TC 323 – Circular economy. ISO [online]. 2024 [vid. 2024-09-06]. Available at: https://www.iso.org/committee/7203984.html
[21] ISO. ISO 59014. ISO [online]. 2024 [vid. 2024-09-03]. Available at: https://www.iso.org/standard/80694.html
[22] ISO. ISO 59004:2024. ISO [online]. 2024 [vid. 2024-09-03]. Available at: https://www.iso.org/standard/80648.html
[23] ISO. ISO 59010:2024. ISO [online]. 2024 [vid. 2024-09-03]. Available at: https://www.iso.org/standard/80649.html
[24] ISO. ISO 59020:2024. ISO [online]. 2024 [vid. 2024-09-03]. Available at: https://www.iso.org/standard/80650.html
[25] ISO. ISO/DIS 59040. ISO [online]. 2024 [vid. 2024-09-03]. Available at: https://www.iso.org/standard/82339.html
[26] ISO. ISO/TR 59032:2024. ISO [online]. 2024 [vid. 2024-09-03]. Available at: https://www.iso.org/standard/83044.html
[27] ISO. ISO/CD TR 59031. ISO [online]. 2024 [vid. 2024-09-03]. Available at: https://www.iso.org/standard/81183.html
[28] ZORPAS, Antonis A. The hidden concept and the beauty of multiple “R” in the framework of waste strategies development reflecting to circular economy principles. Science of The Total Environment [online]. 2024, **952**, 175508. ISSN 0048-9697. Available at: doi:10.1016/j.scitotenv.2024.175508

Utilization of Waste Heat from Industrial Air-Cooled Compressors

Dušan Gordić[1], Vladimir Vukašinović[1], Mladen Josijević[1], Jelena Nikolić[1], Aleksandar D. Aleksić[1]

[1]Faculty of Engineering, University of Kragujevac, Serbia
E-mails: gordic@kg.ac.rs, vladimir.vukasinovic@kg.ac.rs, mladen.josijevic@fink.rs, jelena.nikolic@fink.rs, aleksandar.d.aleksić@fink.rs

Abstract: *Industrial compressed air systems are generally considered inefficient, with end users consuming only 10% to 30% of primary energy. Therefore, the inefficiencies of these systems must be minimized. By improving compressed air components and systems and using them correctly, you can save 20% to 50% on electricity, reduce costs, reduce downtime and increase productivity. A relatively large number of measures and activities can be implemented to reduce energy consumption in compressed air systems. The purpose of the work is to present the process of analyzing the use of waste heat from an air-cooled compressor for space heating in an industrial company. The method is applied to a case study of an industrial company in the food industry. The utilized waste heat presents 36.6% of the total electricity consumed by compressors in the facility. This energy efficiency measure saves more than 3% of the total heat consumed in the company while the payback period is less than 7 months.*

Keywords: *compressed air, industrial compressors, heat recovery, energy efficiency, energy savings*

Article Classification: *Scientific paper*

1 INTRODUCTION

Compressed air has a very wide application in industry. Many production plants, from small craft workshops to large industrial plants, use compressed air in two ways: as an energy transfer medium and as a part of the process when the air comes into contact with the product. Compressed air is widely used in industries such as general manufacturing, automotive, food and beverage, plastics, chemicals, pharmaceuticals, semiconductors and electronics, agriculture and farming, and construction [1].

Compressor operation requires a substantial quantity of electrical energy, and compressed air energy expenses account for a significant portion of total energy costs in the majority of industrial companies [2]. Industrial compressed air systems are generally considered inefficient, with end users consuming only 10% to 30% of primary energy [3]. Therefore, the inefficiencies of these systems must be minimized. By improving compressed air components and systems and using them correctly, one can save 20% to 50% on electricity, reduce costs, reduce downtime, and increase productivity [4]. A relatively large number of measures and activities can be implemented to reduce electricity consumption in compressed air systems [2, 5, 6, 7].

Besides, additional savings in heat energy consumption in industrial facilities can be achieved by using the waste heat generated in the compressor cooling process. Using cooling fluids (water [8] or air [9]) in a well-designed and constructed heat regeneration system, an industrial facility can utilize up to 50% to 90% of this waste heat for various purposes [10]. It is estimated that about 15 kW of thermal energy is available for every 500 l/s of compressor capacity (at full load) [11]. The most cost-effective technique to recover the heat is to use it for space heating. It requires an air-cooled compressor through which the cooling air is introduced and heated. This heat recovery method is cost-effective since it recovers all heat, including radiated heat in the compressor. The heated cooling air must be routed through a duct system to the consuming area. In most factory environments, the noise produced by compressors and any reduction in the freshness of the recovered air typically go unnoticed. However, in more sensitive working areas, such as IT assembly zones, it may be necessary to consider sound attenuation and air filtering measures [12]. This type of heat recovery can only be employed during the heating season. In the non-heating season, the waste heat is discharged to the outside environment. In general, the payback periods of using waste heat recovery for space heating in various industrial companies are usually very short (often less than one year [13]).

Considering the above, this paper considers the utilization of waste heat from air-cooled compressors for heating purposes in an industrial plant in Kragujevac, Serbia.

2 METHOD

The method applied in the paper is presented in Figure 1.

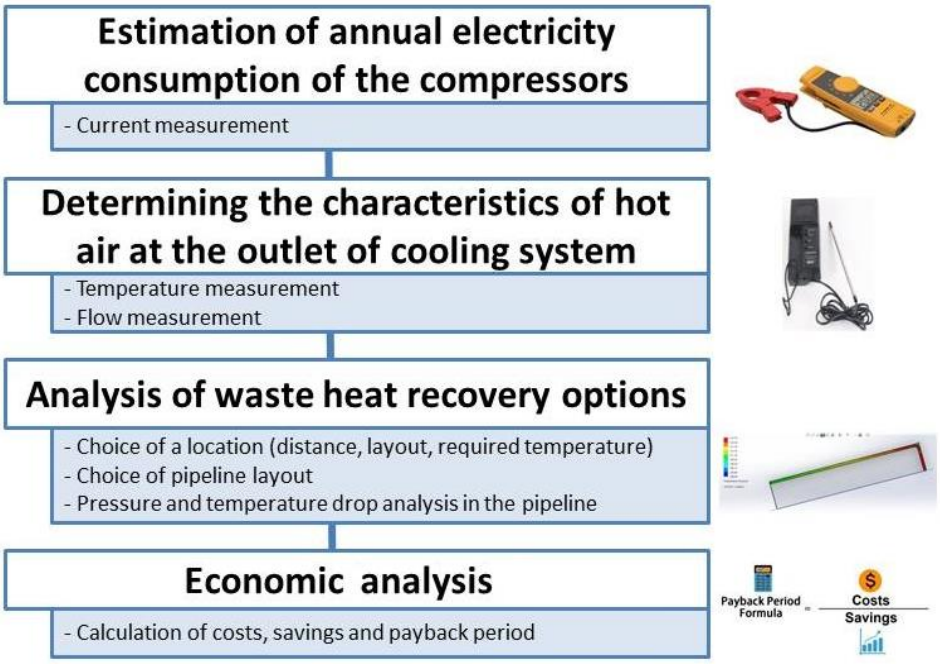

Figure 1: The method for estimating the potential of waste heat utilization from industrial air-cooled compressors

The first step considers estimating annual electricity consumption E [kWh] of a compressor using the following equation:

$$E = \sum_{i=1}^{n} I_i \cdot U \cdot \sqrt{3} \cdot \cos \varphi_i \cdot \tau_i \cdot 10^{-3} \tag{1}$$

Where:

n [-]	- number of working regimes of a compressor,
I_i [A]	- air compressor motor current (average measured value for all three phases) in the *i*-th operating mode of the compressor,
U [V]	- three-phase voltage (400 V adopted value),
$\cos \varphi_i$ [-]	- power factor at the *i*-th operating mode of a compressor,
τ_i [h]	- estimated annual engagement of a compressor in the *i*-th operating mode.

Detachable Jaw True RMS AC/DC Clamp Meter Fluke 365 was used to measure the current (Figure 2). The Fluke 365 is a robust handheld meter with detachable clamps, intended for measurements in facilities with difficult access. Current (AC and DC), voltage (AC and DC) and resistance can be measured with this device.

<u>Technical specification (current):</u>

Range AC - DC	200 A
Resolution AC - DC	0,1 A
Accuracy	±2 %

Figure 2: Clamp Meter Fluke 365

The nominal value of the power factor is adopted based on the manufacturer's data shown on the nameplate of the electric motor of the compressor. If the compressor load significantly deviates from the rated, the power factor change is determined using the diagram typical for 3-phase induction motor shown in Figure 3.

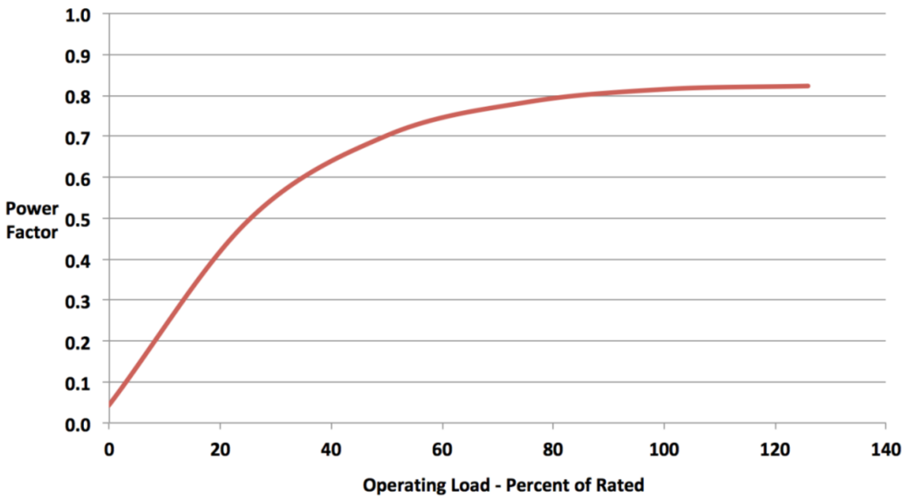

Figure 3: Variation of electric motor power factor with load change

The second step is to determine the thermodynamic properties of hot air at the outlet of the cooling system, which involves measuring the air temperature and flow rate. The measurements were performed using an ALNOR CompuFlow 8525 thermal anemometer, Figure 4. ALNOR CompuFlow 8525, enables the measurement of air speed and temperature at several points in the ducts. Using measured air speed data in several points of the cross section of the outlet cooling channel and knowing the geometry of the canal, the volumetric flow rate is calculated.

Technical specification:

Temperature range	0-70 °C
Resolution	0,1 °C
Accuracy	±0,3 °C
Air speed range	0,1-10 m/s
Resolution	0,05 m/s
Accuracy	±2,5%

Figure 4: ALNOR CompuFlow 8525 Thermal Anemometer

The analysis of waste heat recovery options first assumes the identification of a location where waste heat can be utilized. The required temperature and heating period are specified for the location. The distance from the outlet to the recovery location and the layout constraints are also determined. These parameters are necessary for designing the duct layout considering the shortest and most efficient path. Finally, the SOLIDWORKS Flow Simulation, a computational fluid dynamics (CFD) solution built into the SOLIDWORKS 3D CAD, is used to analyze the pressure and temperature drop in the duct line. A temperature analysis is necessary to determine the temperature of the air available at the location, while a pressure analysis should determine the necessity of installing an additional fan in the system.

The total amount of available waste heat WH [kWh] can be calculated from:

$$WH = \sum_{i=1}^{n} q_i \cdot \rho \cdot C_p \cdot (t_i - t_s) \cdot \tau_i \cdot \%\tau_i \cdot 10^{-5} \qquad (2)$$

Where:
ρ [kg/m^3] - air density (adopted value 1,1 kg/m^3 for the temperature range 20-50 °C),
q_i [m^3/s] - volumetric flow of cooling the air in the *i*-th operating mode of a compressor,
C_p[J/kgK] - isobaric specific heat of air (adopted value 1000 J/kgK for the temperature range 20-50 °C),
t_i [°C] - air temperature at the duct outlet (heated room inlet) at the *i*-th operating mode of the compressor,
t_s [°C] - heated room temperature,
τ_i [h] - estimated annual engagement of a compressor in the *i*-th operating mode,
$\%\tau_i$ [%] - percentage of compressor working time when a heat recovery system can be used.

The final step is economic analysis, which includes calculating investment costs, estimating energy savings, and calculating a simple payback period.

3 RESULTS WITH DISCUSION

The proposed methodology was applied in a margarine processing company located in Kragujevac, Serbia. Compressed air is used in the company as an energy transfer medium for various pneumatic actuators, as well as to package the finished product. Two oil-injected Atlas Copco GA11 d1 rotary screw compressors are used. Both compressors operate in the load-unload mode. The waste heat generated during cooling is not utilized within the facility but instead is released outside through an opening in the outer wall of the compressor station (Figure 5).

Figure 5: The compressors at the production facility

To estimate the amount of electricity required for compressor operation, data on their annual time of engagement in full load and unloaded modes were taken from the control unit of the compressors. The currents were measured on several occasions and then the measured values were averaged. Using equation (1), the estimated annual electricity consumption of compressors is about 61.8 MWh (Table 1).

Table 1: Estimated annual electricity consumption of compressors

Compressor	1	2
Annual engagement - loaded [h]	1588	1518
Annual engagement - unloaded [h]	1121	1440
Total annual engagement [h]	2709	2958
Measured current - loaded [A]	22	
Measured current - unloaded [A]	15	
Nominal power factor (cosθ) [-]	0.85	
Power factor - loaded [-]	0.85	
Power factor - unloaded [-]	0.81	
Annual electricity consumption - loaded [kWh]	20,574	19,667
Annual electricity consumption - unloaded [kWh]	9,436	12,121
Total electricity consumption [MWh]	30.010	31.788
Total electricity consumption for both compressors [MWh]	**61.798**	

The cooling system of the compressors includes an axial fan. The average measured speed at the outlet cross section (0,6 m x 0,3 m) of the cooling system was 1,8 m/s regardless of the operation mode of compressors. Therefore, the volumetric flow of hot air was 0.324 m^3/s in both of the regimes. The cooling air temperature depended on the compressor operation mode. When the compressors were unloaded, it was 45 ˚C, but when they were loaded, it was 50 ˚C. Considering the air temperature in the compressor room (22 °C on average), the compressors consume about 85% of energy for cooling, which can be considered inefficient.

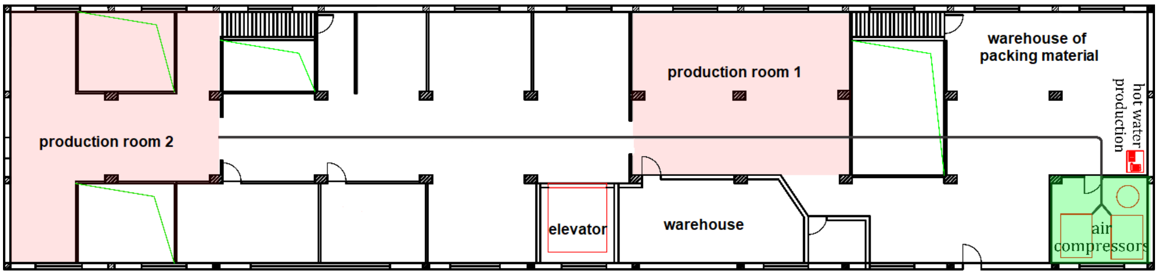

Figure 6: The position of the compressor room and possible locations of waste heat use

Two possible alternatives were analyzed for the selection of a location where waste heat can be utilized, production rooms 1 and 2 from Figure 6. The length of the duct is 15 m for room 1, i.e., 40 m for room 2. The ducts should be routed throughout the building, with the inside temperature of passing rooms estimated to be 18 °C. The results of pressure and temperature drop analyses in both cases performed in SOLIDWORKS Flow Simulation (Figure 7) were presented in Table 2. Although the ducts in both solutions were not routed outside the building, the performed simulation indicated an air temperature drop, especially in the case of room 2. The pressure drop analysis indicated that, in both scenarios, the total pressure drop—including the 5 Pa local pressure drop caused by the fully open damper—is below the maximum allowable pressure drop for the cooling air ducts (30 Pa [14]). Therefore, there is no need to include a fan at the outlet of the cooling air ducts in both cases.

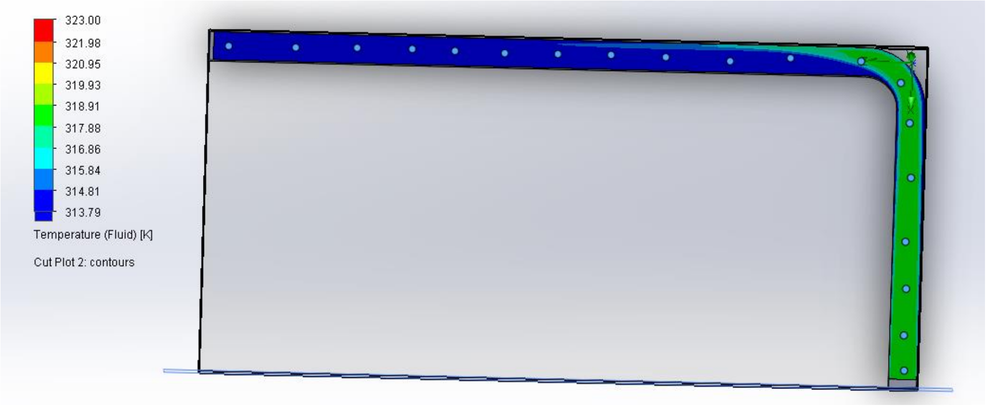

Figure 7: Temperature distribution in waste heat distribution duct (unloaded mode, 15 m duct)

Table 2: The results of pressure and temperature drop analysis

Production room	1		2	
Duct length [m]	15 m		40 m	
Compressors’ working mode	Load	Unloaded	Load	Unloaded
Air temperature at duct outlet [°C]	44	39.8	35.9	33.5
Pressure drop in the duct [Pa]	2.2	2.2	4.2	4.2

Taking into account that both rooms should be heated to 20 °C and using equation 2, the total estimated annual waste heat potential for heating the room 1 is 47.1 MWh, and for heating the room 2 is 31,6 MWh. In the case of room 1, it presents about 76% of consumed electricity for compressing air, while for room 2, it is about 51%. Nevertheless, the heat recovery system can be used only during the heating season. Therefore, it was estimated that only at 48% of compressors’ working time the heat recovery system can be used. This gives 22.6 MWh for the final total estimated annual waste heat potential for room 1 and 15.2 MWh for room 2. The three-year average total annual heat energy consumption for process and space heating in the factory is 725 MWh. The total savings of heat energy using waste heat from the compressors is 3.1% for heating the production room 1 and 2% in case of heating the production room 2.

With a heat (natural gas) price of 4,200 RSD/MWh and an exchange rate of 117 RSD/EUR, the total saving of 811 € will be in case of heating the production room 1, i.e., 544 € in case of heating the production room 2.

The estimated costs were 20 €/m for duct construction and 70 € for a gravity-operated damper, so in case 1, the total costs came to 440 €, or 940 € in case 2. There are no additional costs for adjustments or modifications of the factory heating system. This finally gives the payback period of 0.54 years (6.5 months) for the shorter duct and 1.73 years (20.7 months) for the longer duct.

4 CONCLUSION

The solution for using the waste heat from air-cooled compressors for space heating is relatively simple. The only needed modification in the system is the addition of ducting and associated dampers. The solution has a significant potential for increasing energy efficiency in the industry, even though it is used for a limited period of heating season.

The prerequisite for efficient application is the proximity of the space that is heated and the compressor. Increasing the duct length has a negative influence both on pressure and temperature drops of hot air. The case study reveals that in the case of a 15 m long duct line, which can be considered moderately long, the utilized waste heat accounts for 36.6% of the total electricity consumed by compressors. This energy efficiency measure saves more than 3% of the total heat consumed in the company, while the payback period of the energy efficiency measure is less than 7 months.

It should also be mentioned that a common issue with this heat recovery system is the absence of a clear indicator showing that heat is being recovered. Often, it remains in its winter setting throughout the year, leading to overheating during the summer. Similarly, it frequently releases heat when set to summer mode during the winter months. To prevent these problems, installing a clear indicator on the compressor control panel that displays the temperature of the recovered heat would be beneficial.

LITERATURE

[1] GIAMPAOLO, Tony. *Compressor Handbook: Principles and Practice*. Second Edition. Gistrup: River Publishers, 2023. ISBN 978-8770227377.
[2] SAIDUR, R., N.A RAHIM in M. A HASANUZZAMAN, A review on compressed-air energy use and energy savings. *Renewable and Sustainable Energy Reviews,* 2010, vol. 14, issue. 4, 1135-1153. DOI: https://doi.org/10.1016/j.rser.2009.11.013
[3] YEAPLE, Franklin D. *Fluid power design handbook*. 3rd Edition. New York: Marcel Dekker, Inc, 1996. ISBN 978-0824795627.
[4] GORDIĆ, Dušan et al. Ušteda energije u industrijskim sistemima komprimovanog vazduha kroz saniranje curenja. *Energija, ekonomija, ekologija*. 2008, vol. 10, issue. 1-2, 174-177.
[5] MOUSAVI, Smaeil, Sami KARA in Bernard KORNFELD. Energy Efficiency of Compressed Air Systems. In: *Procedia CIRP* [online]. 2014, vol. 15, 313-318. DOI: https://doi.org/10.1016/j.procir.2014.06.026
[6] RADGEN, Peter in Edgar BLAUSTEIN. *Compressed Air Systems in the European Union Energy, Emissions, Savings Potential and Policy Actions.* Stuttgart: LOG_X Verlag GmbH, 2001. ISBN 3-932298-16-0
[7] ŠEŠLIJA, Dragan, Ivana IGNJATOVIĆ in Slobodan DUDIC. Increasing the Energy Efficiency in Compressed Air Systems [online]. IntechOpen, 2012. Available at: https://www.intechopen.com/chapters/40201
[8] BRONISZEWSKI, Mariusz in Sebastian WERLE, The study on the heat recovery from air compressors, E3S Web of Conferences 70, 03001 (2018) Available at: https://doi.org/10.1051/e3sconf/20187003001
[9] HERNÁNDEZ, Herrera et al. Energy savings in compressed air systems a case of study. V: *IOP Conference Series: Materials Science and Engineering* [online]. 2021, roč. 1154, č. 1, 012009. DOI: https://doi.org/10.1088/1757-899x/1154/1/012009
[10] BEALS, Chris et al. Improving Compressed Air System Performance – A Sourcebook for Industry U.S. Department of Energy, Washington D.C., 2004. [13.09.2024]. Available at: https://www.energy.gov/eere/amo/articles/improving-compressed-air-system-performance-sourcebook-industry
[11] GORDIĆ, Dušan. Energy and Environmental Management in the Furniture Industry. Kragujevac: Faculty of Engineering, University of Kragujevac, 2011. ISBN 978-86-86663-77-1
[12] THUMANN, Albert in Scott DUNNING. *Plant Engineers and Managers Guide to Energy Conservation.* 10th Edition. Lilburn: Fairmont Press, 2011. ISBN 978-1-4398-5606-2
[13] Good Practice Guide 238: Heat recovery from air compressors [15.09.2024]. Available at: https://controlgear.net/documents/good_practice_guide_238_heat_recovery_from_air_compressors_1396339838.pdf
[14] Atlas Copco Oil-injected rotary screw compressors GA 11+, GA 15+, GA 18+, GA 22+, GA 26+, GA 30 Instruction book [13.09.2024]. Available at: https://www.aircompressorsdirect.com/manuals/atlasga30manual_2.pdf

9th International Conference on the Development of Industrial Engineering
21. November 2024
Novo mesto, Slovenia

Sound radiation into space through laminate structures using hybrid materials with contrast properties

Danilo Jereb[1], Mihael Ramšak[2], Anatolij Nikonov[3]

[1]Faculty of industrial engineering Novo mesto, Šegova ulica 112, 8000 Novo mesto, Slovenia
E-mail: avtokleparstvo.jereb@gmail.com

[2]Slovenian National Building and Civil Engineering Institute, Dimičeva ulica 12, 1000 Ljubljana, Slovenia

[3]Univeristy of Ljubljana, Faculty of Mechanical Engineering, Aškerčeva cesta 6,1000 Ljubljana, Slovenia
E-mail: anatolij.nikonov@fs.uni-lj.si

***Abstract**: In recent years, the problem of sound transmission through various materials has increasingly focused on the shape and position of the materials through which sound is transmitted. One of the technical solutions for directing sound radiation through hybrid materials of laminate structures is the production of hybrid panels, which consist of metallic and non-metallic materials. The research deals with the transmission of sound through a hybrid panel consisting of an aluminum base to which a bitumen panel is glued. From the results of the experimental analysis it was found that the effect of the bitumen layer has a dual role. On the one hand, the sound insulation of the hybrid two-layer board increases, and on the other hand, the radiation coefficient increases as well. Based on the results of this research, we can conclude that materials that exhibit a certain level of viscous damping, which usually increases the reduction of the amplitude of vibration of structures, can potentially be used to improve the acoustic sound-insulating properties in practical applications.*

***Keywords:** damping, hybrid materials, sound radiation, sound insulation*

***Article Classification:** Scientific Paper*

1 INTRODUCTION

In many industrial applications, materials with damping properties are often used to reduce sound radiation and/or control vibrations. Thin rectangular plates are widely used in engineering. They are used as structural elements in mechanical engineering, construction, shipping, bridge building and also as structural elements in the aerospace industry, etc.

Sound cannot radiate from room to room, but is transmitted between rooms by exciting the separating structures in one room (with sound), which then radiate into the adjacent room due to the excited vibrations (waves) of the sound. The radiation of sound from room to room is reflected in various physical quantities that are strongly influenced by the material through which the sound is radiated. With a technology that combines the use of several types of material, or what we call ''multi material design'', we can significantly influence the desired radiation results.

In recent decades, extensive studies have been carried out in the field of the acoustic behaviour of thin panels. One of the best known monographs is the book by F. Fahy “Sound and Structural Vibrations - Radiation, Transmission and Response” [1]. This book contains a unified quantitative account of the physical mechanisms and properties of the linear interaction between sound frequency vibrations in compressible fluids and the structures with which they are in contact. The book by C. Hopkins “Sound Insulation” [2] is a comprehensive guide to the theory of sound and vibration and its application to the measurement and prediction of sound insulation in buildings. The monograph enables the reader to deal with a wide range of issues related to sound insulation during the design and construction phases of a building and to solve problems in existing buildings. At the same time, the monograph by L.E. Kinsler et. al “Fundamentals of Acoustics” [3] introduces the physical and mathematical concepts associated with the generation, transmission and reception of sound waves and covers the basic physics and engineering aspects of the discipline.

Panels, especially hybrid panels composed of materials with contrasting mechanical properties, are often used to create complex structures. In order to control sound radiation, the source of which is structural panel elements, it is necessary to comprehensively study the sound radiation of such structures. Normally, studies on sound radiation from structures are limited to the physical properties of the acoustic signals. In fact, radiation analysis helps to evaluate the influence of physical parameters and geometry in terms of subjective criteria, thus providing the right answers to the technical problem of noise.

The influence of boundary conditions on the sound radiation properties of rectangular panels was investigated in [4]. The transverse displacement response of vibrating rectangular plates was presented using an analytical method. Some numerical experiments were also carried out. Five different types of boundary conditions were exemplarily analysed and calculated to compare the influence of the different boundary conditions. Rectangular plates with different point forces and different thicknesses were also investigated to further verify the influence of boundary conditions. To systematically investigate the influence of boundary conditions on sound radiation for frequencies below the critical frequency of the vibrating plate, the authors in [5] calculated the average radiation efficiency and radiation power for a rectangular plate in an infinite barrier using the modal method. It can be seen that the freely clamped plate has the lowest radiation efficiency, while the clamped plate has the highest for most frequencies between the natural fundamental frequency of the plate and the critical frequency.

Much research has been done on the study of plate radiation. For example, in [6], a method was developed to increase the radiation efficiency of rectangular plates with unobstructed edges below the critical frequency of the plate. The efficiency of unobstructed plate radiation is estimated by comparing with experimental data on sound radiation from sphere-plate impacts. It is found that the expression is more accurate than the model of a simply supported plate and more versatile than the model of sound radiated from the free edge of the plate with a plane. It appears that the sound radiated from the vibrations of the plate, which does not propagate near the spherical plate joints, plays a minor role. The improvements in accuracy compared to the simply supported model with plane obstacles are typically in the range of 4 to 12 dB, with the largest improvements occurring at low frequencies. A statistical method for limiting the radiated sound power with a certain confidence level is also being developed and tested against measured data.

Much of the research in recent years has been devoted to multilayer structures. In the paper [7], an accurate and simple method for the free vibration of a laminated rectangular composite plate with mixed layers is proposed. A plate with mixed layers is defined as a laminated plate. It is found that the introduction of mixed layers is a very effective approach for the design of the dynamic properties of laminated composite plates.

Sound insulation is an important aspect of the effectiveness of materials and constructions used to reduce noise in rooms. In [8], the sound insulation values of single- and double-skin walls predicted by analytical models were compared with experimental results. In the laboratory experiments, test specimens were set up in a standard measuring room. From the results, it can be concluded that the experimental results at low frequencies are significantly influenced by resonance effects related to the generation of standing waves in acoustic chambers and vibration modes introduced into the dynamic system by restricting the movement of the panel along its boundary. In [9] the sound transmission losses for a finite plate with a bounded viscoelastic layer are investigated. The influence of the plate parameters on the sound transmission of panels in the low frequency range is discussed, and the methods can be used to optimize damped sandwich panels.

One of the technical solutions to control sound transmission through hybrid materials of laminate structures is the production of hybrid panels consisting of metallic and non-metallic materials. The combination of different materials is often used in various technical applications, with which we achieve different effects on physical phenomena. The research deals with sound radiation through a hybrid panel consisting of an aluminum base to which a bitumen sheet is glued. At the same time, the sound insulation of the hybrid panels under consideration was investigated.

The aim of the research is an experimental analysis of the acoustic behaviour of a panel made of hybrid materials, with which we want to determine whether the introduction of this type of methodology for the development of structural elements can reduce the sound-induced vibrations of a panel made of hybrid materials and, consequently, reduce the sound radiation caused by the vibrations of the panel in this way.

2 MATERIALS AND MESUREMENT METHOD

2.1 Laboratory specimens preparation

The research deals with a laminate panel that consists of two completely different thin layers of material that have completely different mechanical properties and structures, namely an aluminum panel and a bitumen layer that has significantly lower stiffness and greater damping properties compared to the aluminum layer.

In this study, methods for joining completely different materials were investigated and finally a joining method based on the principle of bonding was chosen. This proved to be the optimal method when selecting such materials, as bitumen, being a viscous and fusible material, offers this possibility. The preparation of the surfaces for bonding is also very important, with degreasing and cleaning the materials of impurities being the most important.

A schematic representation of a two-layer laminate panel is shown in Figure 1.

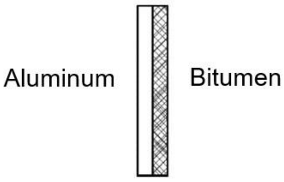

Figure 1: Schematic representation of a cross-section of a two-layer laminated panel.

The width of the mounted panel is 97 cm and the height 151 cm. The relatively light metal panel is made of standardized cold-rolled aluminum and the aluminum alloy ENAW5754 and is 1.5 mm thick. The bitumen layer is 4.5 mm thick and is firmly bonded to the aluminum layer. Under the influence of high temperatures, bitumen turns into a viscous, molten substance, which in itself has an adhesive effect on another material. To increase the adhesive effect, a bitumen substance melted in an organic solvent is used, which in our case is applied to the metal surface.

2.2 Preparation of measuring equipment and installation of samples

The acoustic laboratory consists of two hermetically sealed rooms separated by an opening in which a rectangular sample in the form of a laminated two-layer panel is placed. The panel was firmly fixed in the opening by gluing and sealing with bitumen tape. The sound is transmitted from one room to another through this panel. During the transmission of sound, there must be no loss of sound through gaps or openings at the edges of the panel.

Both rooms have similar dimensions, the same heights and a similar volume. We have labelled them ROOM 1 and ROOM 2. The volume of Room 1 is 52.0 m^3, while the volume of Room 2 is slightly smaller due to the geometry of the architecture and is 49.2 m^3. In both rooms, soft polyurethane foam panels are glued in certain places in mirror image, cut out on one side in the shape of small pyramids, which increases the absorption surface of the panels and acts as a sound absorber, as such a material is an excellent sound absorber. Curved plastic panels are suspended from the ceiling, which ensure that the sound is distributed throughout the room. As already mentioned, the two rooms are separated by a wall in which there is an opening the size of a large window measuring 97 cm x 151 cm. We installed the panel in the opening so that there is a bitumen layer in room 1 and an aluminum part of the laminated panel in room 2 (Figure 2). The joint between the panel and the wall was sealed with a permanently elastic butyl-based sealant for sealing various joints, also known as bitumen tape. We equipped the rooms with loudspeakers and microphones and determined the exact positions where the audio-acoustic equipment was to be placed.

2.3 Sound insulation and sound radiation measurement procedure

Two types of measurements were carried out, namely measurements of the sound insulation of a laminated two-layer panel and measurements of panel vibrations or accelerations on the panel surface to determine the radiation coefficient. The sound insulation measurements were carried out in accordance with the ISO 10140-2 standard [10].

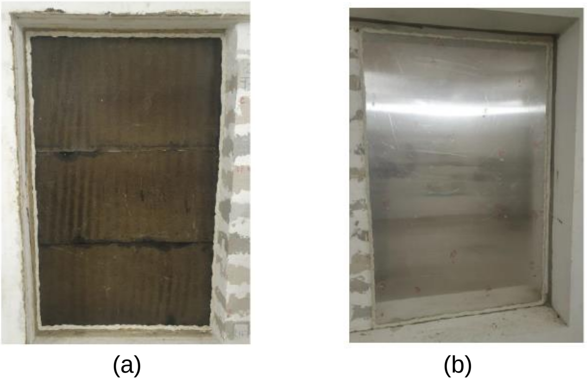
(a) (b)

Figure 2: Placement of the sample in the opening of the acoustic laboratory: (a) bitumen layer of the double-layer laminate panel in room 1, (b) aluminum layer of the double-layer laminate panel in room 2

Sound insulation expresses how well a structural element (sample or product) prevents the propagation of sound through this object. It is determined by the ratio between the sound power impinging on the element and the sound power emitted by the element. Laboratory measurements of airborne sound insulation are mainly used to compare the sound insulation of different test elements and to calculate the sound insulation on site or in the field. The purpose of field measurements is usually to verify that a certain level of sound insulation or acoustic performance has been achieved.

Figure 3 shows the arrangement of the audio-acoustic devices in rooms 1 and 2. In room 1, i.e. on the bitumen layer side of the hybrid panel, we install a reverberant loudspeaker and a receiving microphone, which is also mounted on a swivel stand. All audio-sound devices are then connected with cables to the control panels in the room for carrying out the measurements, from where they are further connected to the measuring devices. In room 2, i.e. on the side of the aluminum part of the panel, we install a transmission loudspeaker fed with pink noise. In the same room we install a transmitter microphone mounted on a swivel stand.

Figure 3: Positioning of the audio-acoustic equipment in Room 1 (left) and Room 2 (right).

When measuring sound insulation, the sound pressure level was measured first to determine how much the sound energy is reduced as it passes through the sample. Then the reverberation time was measured, and finally the background noise, also known as background noise, was measured.

Sound radiation is about the coupling of structurally excited waves with sound waves in the environment. The main interest in studying the phenomenon of radiation lies in the bending waves of the plate that radiate into the surrounding air. The radiation is normally described by the radiation coefficient σ. This is defined as the ratio of the power radiated to the power emitted by a large moving piston, with $ka \gg 1$, where a is the radius of the piston and k is the wavelength with a uniform mean square velocity of motion equal to the mean square velocity of motion of the plate particles in space and time. In other words, the radiation efficiency describes the ratio between the radiation of a specimen vibrating like a large excited piston and the power actually radiated from the specimen into the receiving space. If the radiation coefficient is 1, the plate radiates the same power as a moving piston with the same area and the square of the mean velocity. It can be argued that the plates are much less or much more efficient at radiating sound than a piston.

The measurement of the radiation coefficient was carried out in room 2, i.e. on the aluminum side of the hybrid laminate panel. To mount the accelerometer, we used natural beeswax (see Figure 4), which forms an impermeable barrier between the aluminum and the accelerometer on the smooth aluminum plate, creating an adhesive effect between the two objects. When mounting the sensor on the control point, it was also necessary to fix the connection cable so that it did not hang freely on the sample plate, as it could cause unwanted interference during the measurements. We did this with adhesive tape, which made installation quick and easy. We determined that we would record a 30-second measurement interval for each measurement point.

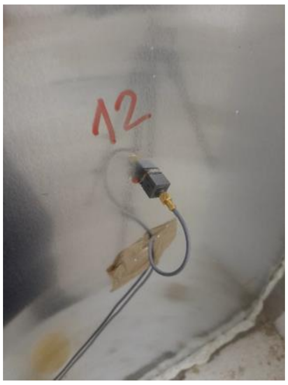

Figure 4: Mounting the accelerometer on the aluminum layer.

The vibration measurements of the laminate panel were carried out by first determining the measurement points on the sample. Then pink noise was emitted in the opposite room (room 1) using a loudspeaker, and in room 2 an accelerometer was attached to the previously determined and marked points and measurements were taken for each position of the accelerometer on the panel. 17 measurement points were selected on the sample.

3 EXPERIMENTAL RESULTS

Measurements of sound insulation were performed using two methods: (1) the so-called measurement on the "quiet side," where the microphone for measuring sound pressure was placed in three positions within the room opposite the room containing the speaker, and (2) the measurement on the "loud side," where the microphone was positioned in three locations within the same room as the speaker (see Figure 5). In both cases, the microphone was set at a height of approximately 1.2 m and at a distance of about 1 m from the panels. The excitation of the tested panel was carried out using sound pressure at five predefined frequencies: 100 Hz, 250 Hz, 500 Hz, 1000 Hz, and 2000 Hz, during which the first three resonant frequencies of the panel were recorded.

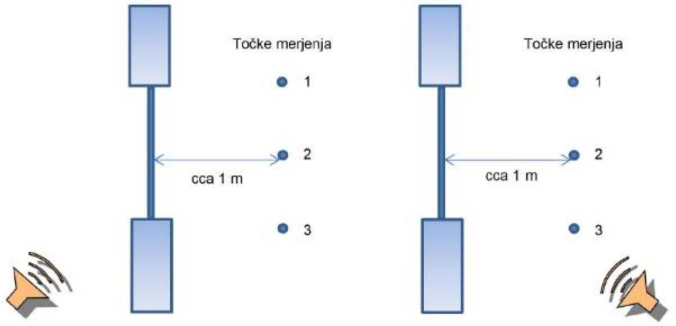

Figure 5: Placement of the sample, speaker and microphone in the case of measurements on the "quiet side" (left) and on the "loud side" (right).

The measurements of the sound pressure levels were carried out separately for the aluminum layer and for the two-layer laminated panel made of aluminum and bitumen, for the first three resonance frequencies of the sample.

Based on the data on the sound pressure levels at different excitation frequencies of the samples, a comparative analysis of the effects of the damping layer on the measured sound pressure level was carried out. The results of the comparison of the sound pressure levels between a single-layer aluminum panel and a two-layer laminated panel consisting of an aluminum layer and a bitumen layer are shown in Figure 6a for the example of measurements on the “loud side” and in Figure 6b for the example of measurements on the “quiet side”. The diagrams for the single-layer aluminum sheet are shown with a dashed line and the diagrams for the two-layer sheet are shown with a solid line.

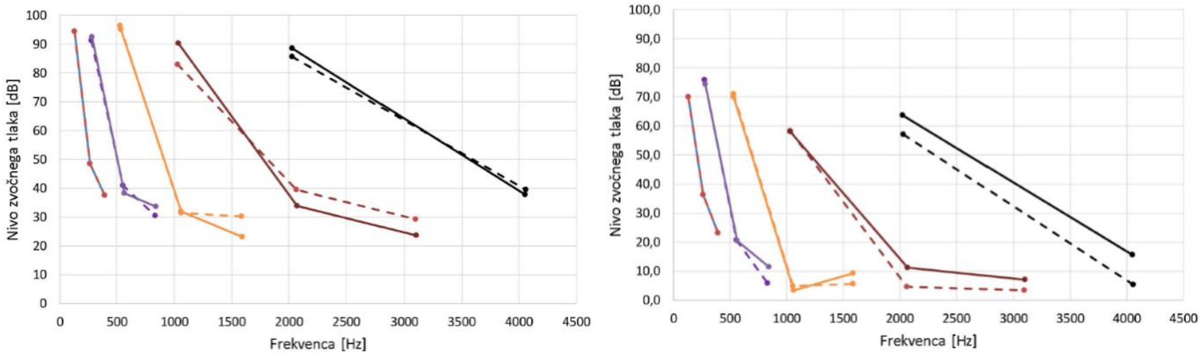

(a) (b)

Figure 6: Sound pressure levels as a function of frequency for nominal excitations with five different frequencies (a) on the “loud side” and (b) on the “quiet side”.

The diagrams in Figure 6 show that the influence of the damping layer, i.e. the bitumen layer, manifests itself in the higher frequency range, namely above 1000 Hz. At the same time, we can see that there is a difference between the sound pressure levels measured on the “loud” and the “quiet side”. In fact, the sound pressure levels on the “loud” side are 20 – 25 dB higher than the sound pressure levels on the “quiet side”.

3.1 Sound insulation measurement results

The next step was to analyse the insulation performance of the panels. Figures 7a and 7b show the sound insulation curves for a single-layer aluminum panel and a double-layer panel consisting of an aluminum and a bitumen layer.

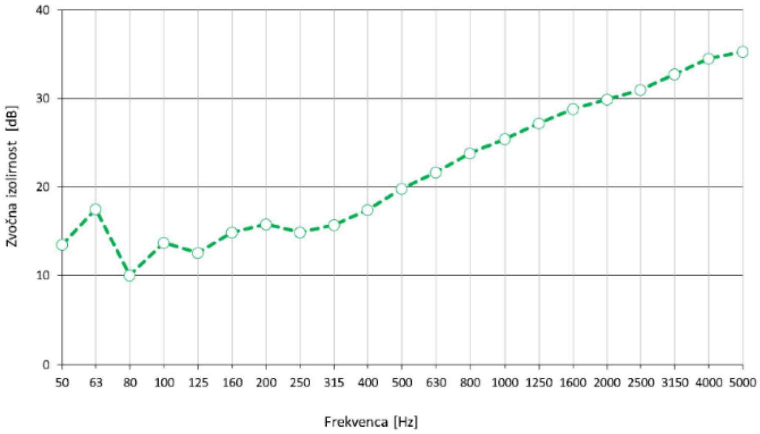

(a)

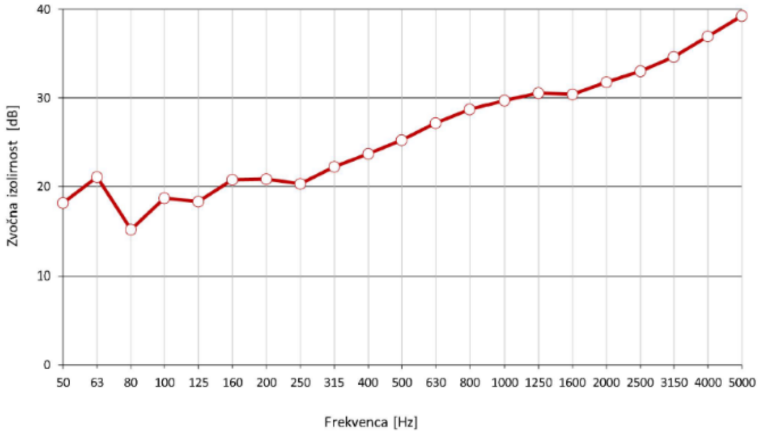

(b)

Figure 7: Sound insulation by one-third octave bands for (a) a single-layer aluminum layer and (b) a double-layer panel consisting of an aluminum and bitumen layer.

The sound insulation values were determined on the basis of experimental data on sound pressure levels and reverberation times in third-order bands in the audible frequency range from 50 Hz to 5000 Hz. The measurements were carried out three times; the diagrams show the average sound insulation values.

From the sound insulation diagrams shown, we can conclude that the effect of the damping properties of the bitumen layer is reflected in the acoustic properties of the flat component in such a way that the sound insulation of the two-layer panel increases by around 5 - 6 dB in the measurement frequency range from 100 Hz to 1000 Hz and by 2 - 4 dB in the frequency range from 1000 Hz to 5000 Hz.

A comparison of the two sound insulation curves shown in Figures 7a and 7b shows that the sound insulation of an aluminum panel in the frequency range between about 500 Hz and about 1250 Hz increases with frequency by about 6 dB/octave. The situation is similar for an aluminum panel with a bitumen layer, where the sound insulation in this frequency range is naturally higher due to the additional bitumen, namely by around 5 to 6 dB. The difference is smaller than one would expect given the different masses of the aluminum panel alone and the aluminum panel with an additional bitumen layer.

It follows that materials that exhibit some degree of viscous damping, which usually also increases the reduction in the level of vibration amplitudes of structures, can potentially be used to improve acoustic sound insulation in practical applications.

3.2 Radiation coefficient measurement results

This section presents the results of measurements of the radiation coefficient of a single-layer aluminum panel and a double-layer panel, consisting of an aluminum layer and a bitumen layer, placed between two rooms, namely room 1 and room 2 (Figure 8). The values for the radiation coefficient were determined on the basis of experimental data on the sound power and particle velocity on the surface of the panel in third-order bands in the audible frequency range from 50 Hz to 5000 Hz. The measurements were carried out three times; the average sound insulation values are given in the diagrams.

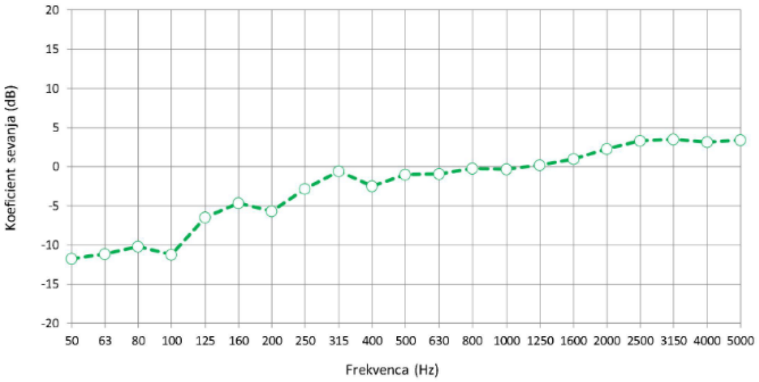

(a)

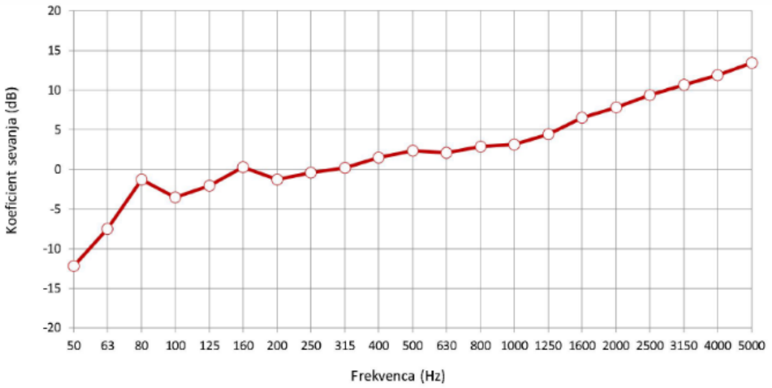

(b)

Figure 8: Radiation coefficient by one-third octave bands for (a) a single-layer aluminum layer and (b) a two-layer panel consisting of an aluminum and bitumen layer.

From the radiation coefficient diagrams shown, we can conclude that the effect of the damping properties of the bitumen layer is reflected in the dynamic properties of the flat structural element in such a way that the radiation coefficient of the two-layer plate increases by around 2 - 4 dB in the measurement frequency range from 100 Hz to 1000 Hz and by 5 - 10 dB in the frequency range from 1000 Hz to 5000 Hz.

4 CONCLUSION

The aim of the research was to develop and test technical solutions for the production of hybrid panels that are used in construction and other technical industries as structural elements for noise reduction. To this end, a hybrid panel was produced consisting of two layers, namely a thin aluminum plate bonded to a layer of bitumen. This pattern was installed in an opening that separates two hermetically sealed spaces. In the production of the hybrid panel pattern, an effective bond was ensured between materials that are very different in structure and have significantly different mechanical properties.

From the results of the experimental analysis obtained during the implementation of the master's thesis on a hybrid panel consisting of two layers with different mechanical and acoustic properties, which included the performance of dynamic and acoustic measurements, we can primarily conclude that the effect of the bitumen layer bonded to the aluminum layer plays a dual role. On the one hand, the sound insulation of the hybrid two-layer panel increases, on the other hand, the radiation coefficient increases slightly due to the addition of a bitumen layer.

From the diagrams shown, we can conclude that the influence of the damping layer, i.e. the bitumen layer, manifests itself in the higher frequency range, namely above 1000 Hz. At the same time, we can see that there is a difference between the values of the sound pressure levels measured on the "loud side" and on the "quiet side".

From the results of this investigation, we can conclude that materials that exhibit a certain degree of viscous damping, which usually also increases the reduction of vibration amplitudes of structures, can potentially be used to improve acoustic sound insulation in practical applications.

LITERATURE

[1] Fahy, F. *Sound and structural vibrations-radiation, transmission and response*. London: Academic Press Limited, 1994.
[2] Hopkins, C. *Sound Insulation*. Burlington, Oxford: Butterworth-Heinemann, 2007.
[3] Kinsler, L.E. et al. *Fundamentals of Acoustics*. New York, Chichester,Weinheim, Brisbane, Singapore, Toronto, ed. 4: John Wiley & Sons, 2000.
[4] Qiao, Y.F., Q.B. Huang, and L.L. Li. Influence of boundary conditions on sound radiation characteristic from rectangular plates. *Journal of Low Frequency Noise Vibration and Active Control*. 2007, vol. 26(2), 115–133.
[5] Tadeu, A., J. Antonio and D. Mateus. Sound insulation provided by single and double panel walls - a comparison of analytical solutions versus experimental results. *Applied Acoustics*. 2004, vol. 65(1), 15–29.
[6] Oppenheimer, C.H. and S. Dubowsky. A radiation efficiency for unbaffled plates with experimental validation. *Journal of Sound and Vibration*. 1997, vol. 199(3), 473–489.
[7] Feng, L. and S.K. Ramanathan. On application of radiation loss factor in the prediction of sound transmission loss of a honeycomb panel. *International Journal of Acoustics and Vibrations*, 2012, vol. 17(1), 47-51.
[8] Dijckmans, A., G. Vermeir and W. Lauriks. Sound transmission through finite lightweight multilayered structures with thin air layers. *The Journal of the Acoustical Society of America*. 2010, vol. 128(6), 3513–3524.
[9] Du, S., F. An and B. Liu. On the sound transmission loss of finite plates with constrained viscoelastic layer. *Applied Acoustics*. 2019, vol. 149, 32–38.
[10] “Acoustics — laboratory measurement of sound insulation of building elements—part 2: Measurement of airborne sound insulation,” International Standard ISO, 10140–2, 2021.

9th International Conference on the Development of Industrial Engineering
21. November 2024
Novo mesto, Slovenia

Advanced Energy Consumption Prediction with LSTMs and Hybrid Models

Jelena Joksimović[1], Jure Kos[1], Krištof Debeljak[1], Janez Povh[1]

[1]Rudolfovo – Science and Technology Centre Novo mesto, Podbreznik 15, 8000 Novo mesto, Slovenia
E-mails: jelena.joksimovic@rudolfovo.eu, jure.kos@rudolfovo.eu, kristof.debeljak@rudolfovo.eu,
janez.povh@rudolfovo.eu

Abstract: *In the context of hybrid energy systems that integrate multiple energy sources, including solar power, supercapacitors, UPS batteries, generators, hydrogen cells, and the grid, accurate energy consumption prediction is essential for efficient energy management. This work presents the application of Long Short-Term Memory (LSTM) neural networks and hybrid models, developed at our Laboratory for Energy Management ({LabE). Instead of increasing the prediction step for LSTMs to 96 for day-ahead predictions, we adopted an interval-based approach, where 96 one-step LSTM predictions were made, each corresponding to 15-minute intervals. These predictions were then combined and weighted against the centroid of the behavioral cluster to which the day belonged, producing an accurate one-day energy forecast. Our experimental results demonstrate that this hybrid method, by leveraging both temporal predictions and daily behavioral patterns, effectively balances computational load and prediction accuracy, making it well-suited for short-term energy forecasting in hybrid energy systems.*

Keywords. *energy consumption, energy management, LSTMs, k-Means, deep learning*

Article Classification: *Scientific paper*

1 INTRODUCTION

Energy management (EM) has become a crucial part of business strategies, particularly in industrial sectors where companies aim to optimize energy use for cost savings, de-carbonization, and improved resilience [4]. Businesses are increasingly investing in technologies that integrate renewable energy resources, such as solar power, and energy storage solutions. These advancements have increased the complexity of Energy Management Systems (EMS) and the data they generate, creating new opportunities for applying Machine Learning (ML) and Artificial Intelligence (AI) to enhance energy efficiency and reduce operational costs. ML algorithms are valuable for analyzing vast datasets derived from smart meters and various energy sources, enabling organizations to predict future energy supply and demand and identify inefficiencies. Deep Learning (DL) models, such as neural networks, excel at capturing complex relationships between multiple variables, allowing for precise predictive modeling of energy consumption using historical data and weather factors [7, 8]. Recent advancements in Recurrent Neural Networks (RNNs), particularly Long Short-Term Memory (LSTM) networks, have shown great promise in electric load forecasting [10]. These models are designed to capture sequential data patterns, making them well-suited for day-ahead energy consumption forecasting. However, predicting for a full 24-hour period, with 96 prediction steps (15-minute intervals), presents challenges, such as longer training times and reduced reliability due to fluctuations in energy demand. To address these challenges, we adopted a hybrid approach by clustering daily consumption patterns and weighting LSTM predictions based on the cluster's centroid. This method, inspired by the temporal-behavior coalescing forecast model [9], merges behavioral insights with LSTM predictions, improving the accuracy and robustness of day-ahead forecasts.

2 METHODS

2.1 Long Short-term Memory (LSTM) for temporal forecasting

LSTM is one of the very successful variants of state-of-art RNN and is widely used in the context of time series data. Even though RNNs provide good accuracy, they have been found to underperform in long-term memory as RNNs are unable to use information from the distant past. Also, LSTM can learn patterns with long dependencies. A memory cell, which is the main reason LSTM is superior in these tasks, is composed of four units: an input gate, an output gate, a forget gate, and a self-recurrent neuron. The gates control the interactions between neighboring memory cells and the memory cell itself, as illustrated in Figure 1. Whether the input signal can alter the state of the memory cell is controlled by the input gate.

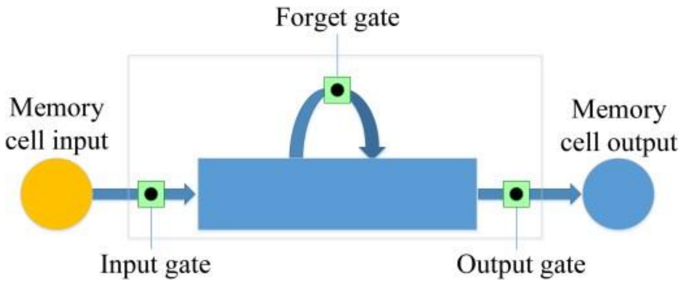

Figure 1: LSTM memory cell [3]

On the other hand, the output gate can control the state of the memory cell on whether it can alter the state of the other memory cell. In addition, the forget gate can choose to remember or forget its previous state [6, 2].

2.2 k-Means clustering for daily behavior analysis

In addition to using LSTM models for regression tasks in predicting energy consumption, we incorporate an unsupervised learning technique k-Means clustering [1], to further enhance our model's accuracy. k-Means is a well-known clustering algorithm that groups similar data points based on a predefined number of clusters, denoted as *k*. For this study, we set *k = 10*, meaning that we cluster daily energy consumption behaviors into 10 distinct groups. The distance metric we use to assign daily patterns into clusters is Euclidean distance:

$$d(X,Y) = \sqrt{\sum_{i=1}^{n}(x_i - y_i)^2} \tag{1}$$

a metric that calculates the straight-line distance between two points in a multi-dimensional space.

2.3 Hybrid prediction method: LSTMs + k-Means clustering

Our initial model was designed to compute a single LSTM prediction for 96 steps ahead, where each step represents a 15-minute interval, allowing us to forecast the entire day from 00:00 to 23:59. The LSTM model is trained using sequences of length 672, corresponding to the past 7 days (15-minute intervals) to capture long-term dependencies in energy consumption patterns. While this method effectively generated a full-day forecast in a single pass, it encountered challenges due to accumulated error over such long sequences, which led to under-satisfying results in prediction accuracy. Given the suboptimal performance of the full-day prediction approach, we shifted to an alternative method to improve accuracy:

Interval-based hybrid predictions. Instead of single long-sequence LSTM prediction, we apply an interval-based approach that breaks down the day-ahead prediction into smaller, more manageable parts. Specifically, we calculate 96 separate one-step predictions, where each prediction targets a single 15-minute interval. For each of these intervals (e.g., 00:00-00:15, 00:15-00:30, etc.), we use a time series of length 390 (roughly 4 days of historical data) to predict the next 15-minute energy consumption. After generating these 96 one-step predictions, we concatenated them to form a full-day forecast. This approach mitigated the errors associated with long-sequence predictions, focusing on more manageable, accurate one-step forecasts.

2.4 Evaluation metrics

For model performance comparison, we use mean absolute error (MAE) and root mean square error (RMSE). These indicators are defined as:

$$MAE = \frac{1}{n}\sum_{i=1}^{n}|y_i - \hat{y}_i| \tag{2}$$

$$RMSE = \sqrt{\frac{1}{n}\sum_{i=1}^{n}(y_i - \hat{y}_i)^2} \tag{3}$$

where $\hat{y}_i$ is the predicted value of energy consumption, y_i is the actual value of energy consumption and *n* is the number of samples.

3 DATA

The data used in this work is past energy consumption data (in Watts) of the Labtop, the technical laboratory in Rudolfovo, from January 4, 2024 (2024-01-04 00:00:15) until September 8, 2024 (2024-09-08 00:00:00). Day here starts from 15 minutes after midnight and ends at midnight, so we have 15 minutes granularity. In Table 3, we can see descriptive statistics of the dataset.

Table 1: Summary statistics for Energy consumption (W) in Labtop from January 4 to September 8, 2024

count	**mean**	**std**	**min**	**Q1**	**Q2**	**Q3**	**max** 23458	805.2	594.5
	0	463	636	859	6988				

We have 23458 data points, making it 244 days. Average 15 minutes energy consumption is 805W, minimal and maximal are respectively 0 and 6988 W, while Q1, Q2 and Q2 represent quartiles of energy consumption.

From this raw data, we extracted several important features for the model feeding, and our results are presented in the next section:

- **season** (from 0 to 3),
- **energy consumption lags**[1] (from 1 to 30),
- **month** (from 1 to 12),
- **day of the week** (from 1 to 7),
- **is weekend?** (0 or 1).

4 RESULTS

The LSTM model was structured with two LSTM layers, each containing 150 units. The ReLU activation function was used to introduce non-linearity, and the Adam optimizer [5] with a learning rate of 0.001 was employed for training. The model was compiled with the ’mean_squared_error’ loss function. Training was conducted over 20 epochs with a batch size of 32, ensuring efficient convergence by incorporating early stopping to prevent over-fitting. The sequence length was set to 10, after several experiments, and the prediction time step was 1 for each of the 96 prediction models, as described in the Methods section. We employed k-Means clustering with 10 clusters to identify days with similar energy usage profiles. The data was standardized using StandardScaler. These clusters were then utilized to enhance the predictive model by integrating behavioral patterns into the temporal predictions. In Figure 2, the 10 daily load profiles for Labtop are illustrated. We observe that Clusters 2, 5, 6, and 9 represent days that are calm during the night and very active during the day, with Cluster 6 showing significantly higher consumption during the evening hours. The x-axis ranges from 0 to 96, representing a full day with 15-minute granularity. Additionally, Clusters 4 and 7 exhibit the opposite behavior. The remaining clusters are almost singletons, representing days with distinct patterns that differ from the rest.

After calculating all 96 LSTM interval predictions and concatenating them into a single day data vector, this vector was then processed through the cluster prediction algorithm, where the centroid of the corresponding cluster was identified. The centroid vector and the LSTM prediction vector were then averaged to generate the final hybrid predictions, which are depicted in blue in Figure 3. The error metrics, MAE and RMSE, in Watts, are presented in Table 2. The MAE indicates that, on average, the predictions are approximately 160 Watts off, while the RMSE reveals that some errors are larger, as evidenced by the higher value of 261.8 Watts.

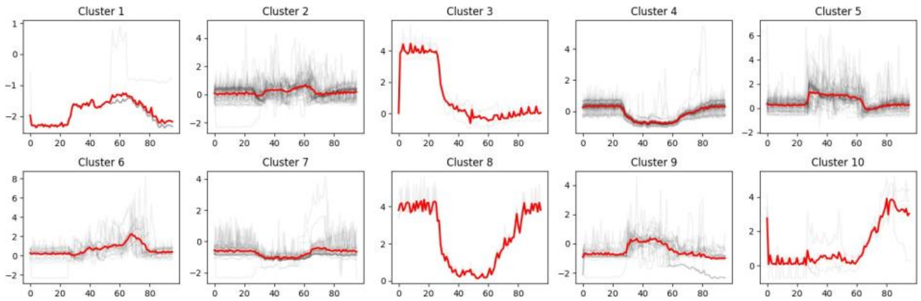

Figure 2: 10 clusters of daily energy load profiles in Labtop. Centroids are represented by red color, while all the actual time series are in grey

---

[1] *For lag = 1 energy consumption is the consumption of the previous day at the same time; for lag = 2, it is the consumption from two days ago, etc. So here we track one month of previous consumptions as the most important features for prediction for one day ahead.*

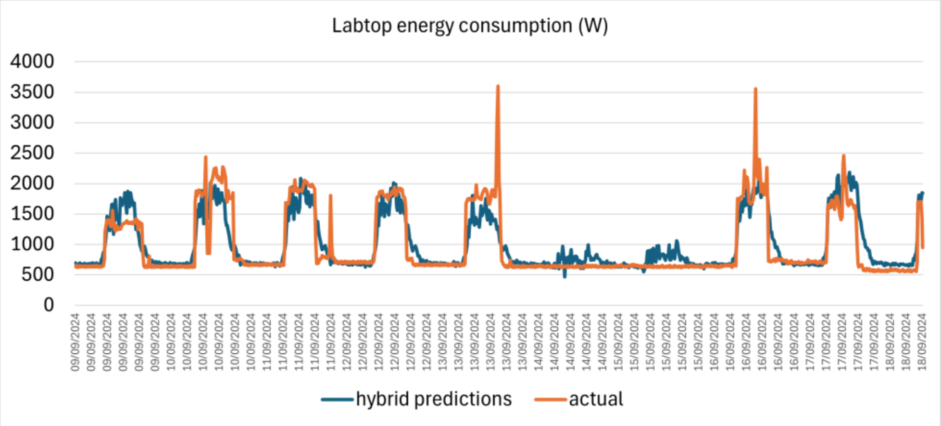

Figure 3: Predictions on the serving dataset (unseen data from 9th of September to 18th of September)

Table 2: Evaluation metrics of a hybrid model (W)

	MAE	RMSE
Hybrid model	159.98	261.8

5 DISCUSSION AND FUTURE WORK

Day-ahead forecasting, especially when predicting energy consumption over a full 24-hour period, presents a challenge for LSTM models due to the need for 96 consecutive prediction steps (each representing 15-minute intervals). The longer the sequence length, the more difficult it becomes to maintain accuracy and reliability. Energy demand in a single building, such as our laboratory, is inherently volatile and more susceptible to fluctuations than forecasting for a large industrial enterprise, town, or country. This granularity of consumption makes the task more complex and prone to error, amplifying the need for robust models. To overcome this, we incorporated a hybrid approach by clustering daily consumption patterns and weighting LSTM predictions based on the centroid of the cluster to which the predicted pattern belongs. This hybrid methodology demonstrated outstanding performance when tested on unseen data from the Labtop environment. Our results show that our approach effectively captures and predicts energy consumption patterns with high accuracy. However, our current work does not yet account for additional external factors like holidays or weather, which could further refine these predictions, particularly for components like lighting or HVAC systems that are weather-sensitive. Incorporating these elements into future models, along with data on solar irradiance, temperature, and holiday schedules, would enhance the forecast's adaptability to real-world conditions. The next step in this research is also to integrate these consumption predictions with solar energy production forecasts, which have already been developed for a 5-day horizon using *Bidirectional LSTM Neural Networks*. By combining these two models, we aim to shift toward task scheduling and energy source optimization research, specifically investigating how to allocate and manage different energy sources (e.g., solar, grid, UPS batteries) based on predicted loads and demand over the next 3-5 days. This will provide a robust framework for enhancing energy efficiency and sustainability in buildings by leveraging precise forecasting and intelligent resource allocation.

REFERENCES

[1] Aghabozorgi, S., Seyed Shirkhorshidi, A., Ying Wah, T.: Time-series clustering â a decade review. Information Systems **53**, 16–38 (2015). Available at: https://doi.org/https://doi.org/10.1016/j.is.2015.04.007, https://www. sciencedirect.com/science/article/pii/S0306437915000733

[2] Almalaq, A., Zhang, J.J.: Evolutionary deep learning-based energy consumption prediction for buildings. IEEE Access **7**, 1520–1531 (2019). Available at: https://doi.org/10.1109/ACCESS.2018.2887023

[3] Bao, W., Yue, J., Rao, Y.: A deep learning framework for financial time series using stacked autoencoders and long-short term memory. PLoS ONE **12** (07 2017). Available at: https://doi.org/10.1371/journal.pone.0180944

[4] Deloitte: Smart energy management for industrials (2021), Available at: https://www2. deloitte.com/us/en/insights/industry/power-and-utilities/smart-energy-management.html, accessed: 2024-03-25

[5] Dubey, S.R., Singh, S.K., Chaudhuri, B.B.: Activation functions in deep learning: A comprehensive survey and benchmark. Neurocomputing **503**, 92– 108 (2022). Available at: https://doi.org/https://doi.org/10.1016/j.neucom.2022.06.111, https://www.sciencedirect.com/science/article/pii/S0925231222008426

[6] Hochreiter, S., Schmidhuber, J.: Long Short-Term Memory. Neural Computation **9**(8), 1735–1780 (11 1997). Available at: https://doi.org/10.1162/neco.1997.9.8.1735, https:// doi.org/10.1162/neco.1997.9.8.1735

[7] Jeong, H.: Predicting the output of solar photovoltaic panels in the absence of weather data using only the power output of the neighboring sites. Sen- sors **23**(7) (2023). Available at: https://doi.org/10.3390/s23073399, https://www.mdpi.com/ 1424-8220/23/7/3399

[8] Jha, A.V., Appasani, B., Gupta, D.K., Ramavath, S., Khan, M.S.: Machine Learning and Deep Learning Approaches for Energy Management in Smart Grid 3.0 pp. 121– 151 (2023), Available at: https://link.springer.com/10.1007/978-3-031-38506-3_6, series Title: Power Systems

[9] Liu, C., Li, F., Zhang, C., Sun, B., Zhang, G.: A day-ahead prediction method for high-resolution electricity consumption in residential units. Energy **265**, 125999 (2023). Available at: https://doi.org/https://doi.org/10.1016/j.energy.2022.125999, https://www.sciencedirect.com/science/article/pii/S0360544222028857

[10] Vidyakant, J., Appasani, B., Gupta, D., Ramavath, S., Khan, M.S.: Machine learning and deep learning approaches for energy management in smart grid 3.0 pp. 121–151 (09 2023)

Sustainable Product Development: Research and Implications

Dorian Marjanović[1,2]

[1]University of Zagreb, Faculty of Mechanical Engineering and Naval Architecture, Ivana Lučića 5, 10002 Zagreb, Croatia
E-mail: dorian.marjanovic@fsb.unizg.hr

[2]Faculty of Industrial Engineering Novo Mesto, Šegova ulica 112, 8000 Novo mesto, Slovenia

Abstract: *The evolution of engineering design processes has undergone significant transformations over time, driven by a convergence of factors that have bolstered their effectiveness and relevance. This progression is intricately intertwined with technological advancements and the dynamic shifts in societal needs and values.*

In the contemporary landscape, the ecological challenges we face transcend geopolitical boundaries, posing a critical threat to the well-being and harmonious coexistence of both current and future generations on a global scale. As a result, manufacturing companies hold a pivotal role in shaping the future of the environment and society.

To adhere the sustainability criteria, products must be intricately designed with their entire life cycle in mind, enabling them to be manufactured, transported, maintained, utilized, recycled, or disposed of with minimal environmental impact. Companies face mounting pressure to comply with legislation, as well as the escalating demands from customers and investors for tangible evidence of the sustainability of their offerings.

Incorporating sustainability into the operational culture of manufacturing companies poses a formidable challenge across all organizational levels, spanning from overarching company philosophies to day-to-day activities. To effectively implement sustainable product development practices, companies must comprehend and embrace the ecological challenges of our era, alongside key sustainability frameworks and principles of sustainable engineering.

Keywords: *sustainability, product development, eco-design*

Article Classification: *Scientific paper*

1 INTRODUCTION

Design is a fundamental force [1] that shapes the world around us. As articulated by Simon, design is an activity that aims to create better environments and experiences. Historically, the evolution of design processes, tools, practices, and outcomes has primarily centered on the tangible products themselves. However, the emerging paradigm of design for sustainability extends this focus, emphasizing the integration of people and technology to enhance quality of life with minimum impact to environment.

Sustainable product development has become a pressing priority for companies worldwide, particularly in manufacturing sectors, where products significantly impact environmental, social, and economic systems. Sustainable engineering, defined as the optimal balancing of economic, environmental, and social criteria throughout a product's lifecycle, is increasingly shaping how research and development (R&D) departments approach design and production. As ecological pressures mount so does the need for products designed with sustainability in mind—from conception to end-of-life.

This article discusses the critical components of sustainable product development and emphasizes the necessity for R&D teams to be aware of current environmental challenges, technological advances, and sociopolitical shifts. We will also examine the sustainability frameworks guiding development and the levers that can drive sustainable engineering.

2 ENVIRONMENTAL CHALLENGES AND THEIR IMPACT ON R&D

By 2023, six of nine planetary boundaries—limits proposed by Stockholm Resilience Centre, within which humanity can safely operate—had been crossed, primarily due to human activity [1]. These include climate change, biodiversity loss, land-system change, and disruptions to global nutrient cycles. Manufacturing industries contribute to these pressures through resource extraction, emissions, and waste production.

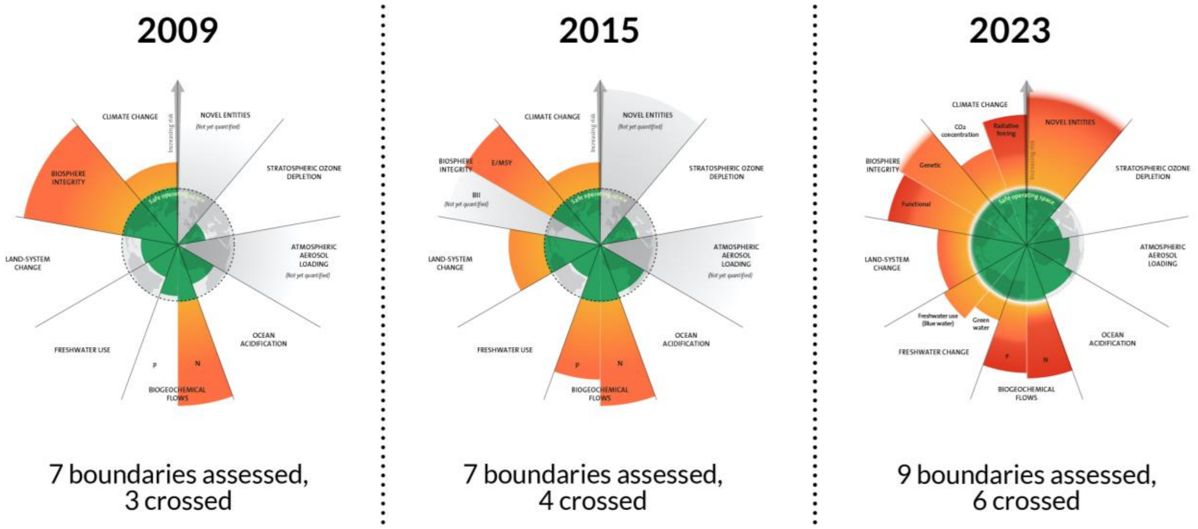

Figure 1. Planetary boundaries (Azote for Stockholm Resilience Centre, based on analysis in Richardson et al. [2]

For R&D teams, this environmental context necessitates a shift in priorities. Developing sustainable products means integrating lifecycle thinking from the earliest design stages. Materials, energy consumption, and waste disposal must be considered holistically to reduce a product’s total environmental footprint. As ecological boundaries close in, manufacturers are under pressure to design products that are durable, repairable, and recyclable, ensuring minimal waste.

2.1 The Role of Technology in Sustainable Product Development

Technological innovation is a key enabler of sustainability in product development, and Industry 5.0 has significant influences on product development through achievements in three aspects:

1. **Digitalization and Virtualization**: Tools such as computer-aided design (CAD), digital twins, and simulation software allow developers to model and refine products digitally, reducing the need for physical prototypes. This lowers material consumption and accelerates design iteration while also providing insights into the long-term performance of sustainable designs.

2. **Internet of Things (IoT)**: IoT systems enable real-time monitoring of production processes and product use, providing data that can inform decisions on energy use, efficiency, and environmental impact. These insights help optimize resource management across a product's lifecycle.

3. **AI and Data Analytics**: AI-driven analytics enable companies to identify inefficiencies and opportunities for improvement in product development. For instance, AI can help streamline production by optimizing material selection, reducing waste, and forecasting environmental impacts through lifecycle assessments.

Technological developments have empowered R&D teams to innovate more efficiently, but this progress is coupled with the need to consider the sociopolitical context in which these innovations are deployed [3].

2.2 Sociopolitical Shifts and Regulatory Pressure

Alongside technological advancements, sociopolitical changes are shaping the landscape of sustainable product development. Here we will consider shifts in Environmental Awareness, Legislation and Compliance, and Adoption of Autonomous Systems.

Increased Environmental Awareness resulted is increasing pressure for companies to demonstrate environmental responsibility [2]. Consumers now expect transparency on the environmental and social impacts of the products they buy. Companies that fail to meet these expectations face reputational risks and loss of market share.

Legislation and Compliance: New regulations, such as the **Ecodesign for Sustainable Products Regulation (ESPR)** in the European Union (see illustrative excerpt in table 1. mandate that products meet sustainability criteria such as energy efficiency, durability, and recyclability. These laws are designed to ensure that products are sustainable across their entire lifecycle. Non-compliance not only risks legal penalties but can also result in exclusion from key markets.

Table 1. Timeline of Regulations regarding sustainability in the EU and Germany (illustrative excerpt)

Regulation	**Year**
Paris Agreement	**2015**
Social Development Goals (UN)	**2016**
European Green Deal	**2019**
EU Circular Economy Plan	**2020**
Ecodesign for Sustainable Products Regulation (ESPR) Digital Product Passport (DPP)	**2022**
EU Batteries Regulation Environmental Social Governance Rating Act (ESG) Supply Chain Act Carbon Border Adjustment Mechanism (CABM)	**2023**
Corporate Sustainability Reporting Directive (CSRD) in force	**2024**
ESPR in force including Prototype Carbon Fund (PCF) for batteries	**2025**
CABM definitive regime	**2026**
DPP for Batteries in force	**2027**
DPP in definitive regime	**2030**
Minimal recycling quotas for battery materials	**2036**

Adoption of Autonomous Systems: The increasing use of AI and automation in R&D, exemplified by tools like **ChatGPT** for data analysis and workflow optimization, allows teams to streamline complex tasks and accelerate sustainable innovation. These systems also support the development of autonomous production lines that can minimize energy use and material waste.

These shifts reinforce the need for companies to adapt not just technologically but also strategically. Regulatory pressure, combined with evolving consumer expectations, requires that sustainability be a core business objective rather than a peripheral concern.

2.3 Sustainability Models and Strategies

The importance of structured approach to sustainability. Business motivation is probably best argumentation to promote sustainability challenges within the companies through radical innovative products and services and related new business models” [4]. Sustainability models offer structured approaches for integrating environmental, social, and economic considerations into product development. Proposed sustainable business models are based on concept of extended customer value which is based on the following values: (1) Creating value for individual customers and the company; (2) Creating value for the public and the company; (3) Creating value for the public and individual customers. Such approaches recognize a domain at the intersection of the above; (4) Creating value for the public, individual customers, and the company [5].

Companies that want to transform traditional linear production to sustainable business models need to translate sustainability strategies into business activities, create competitive advantage, and generate extended customer value, which includes benefits for the company, customers, and society [4]. Although such strategies are very case dependent within the circular economy framework, key sustainability strategies incorporate:

- **Efficiency**: Minimizing resource use and waste production during manufacturing.
- **Consistency**: Ensuring that products use renewable or recyclable materials, aligning with natural ecological systems.
- **Sufficiency**: Avoiding overproduction and overconsumption by developing products that meet essential needs without excess.

3 IMPLEMENTATION ISSUES

By adopting coherent sustainability model, companies and R&D departments can align product design with both ecological limits and consumer expectations, setting the foundation for a more responsible production paradigm. Effective implementation of sustainable development within engineering requires a comprehensive framework that encompasses normative, strategic, and operational levels [6], [7], [13]. Each level plays a crucial role in embedding sustainability into the core functions of engineering organizations, ensuring that the ethos of sustainability is not merely an ancillary consideration but a fundamental aspect of operational effectiveness.

3.1 Normative level: Embedding Sustainability into organizational culture

The first step in integrating sustainable development is to align the organization’s philosophy and values with sustainability principles. This alignment requires organizations to clearly state their commitment to sustainability as a fundamental value influencing all decisions. This leads to a cultural shift; successful integration must foster a culture of sustainability. When sustainability is woven into the organizational culture, it cultivates a shared sense of responsibility among employees. Studies show that organizations that prioritize sustainability often experience higher employee engagement and productivity [6].

A culture that values sustainability empowers engineers to prioritize ecological and social factors in their work. This means training employees, aligning company values with environmental goals, and ensuring that every decision—from top management to daily operations—reflects a commitment to sustainability. Workshops and seminars can educate employees on sustainability's relevance, fostering a values-driven workforce. Designating sustainability champions within teams can further enhance this cultural commitment.

3.2 Strategic Level: Developing sustainable methods and processes

At the strategic level, organizations must create methods and processes that operationalize sustainable engineering practices. Incorporating sustainability into engineering processes not only addresses environmental concerns but can also provide a competitive advantage. Companies adopting sustainable practices often report cost savings, enhanced brand reputation, and increased customer loyalty [7]. Aligning sustainability with business objectives can lead to innovative design and optimized processes.

Organizations should foster sustainability assessment tools, such as Product Carbon Footprint (PCF) or Life Cycle Assessments (LCA) and sustainability metrics, to evaluate the impacts of engineering decisions [8], [13]. This involves developing frameworks and tools that guide engineers in making informed decisions with long-term sustainability in mind. Strategic partnerships with academic institutions can facilitate research and development of innovative sustainable technologies, ensuring that engineering practices evolve in line with sustainability goals.

3.3 Operational level: Effective planning and execution

The operational level focuses on the planning, execution, control, and monitoring of engineering activities. Successful operationalization of sustainable practices requires clear guidelines to ensure sustainability is considered at every project stage. Implementing sustainability in engineering activities leads to better project outcomes by systematically addressing environmental and social impacts. Research indicates that projects with solid sustainability frameworks experience fewer delays and cost overruns due to proactive risk management [8].

To achieve effective operational planning, organizations should integrate sustainability criteria into project management methodologies. This includes establishing performance indicators that reflect sustainability goals, conducting regular sustainability audits, and engaging stakeholders throughout the project lifecycle. Furthermore, organizations should adopt agile methodologies that allow for iterative assessment and adaptation of practices based on sustainability outcomes.

In today’s market, consumers and investors are increasingly demanding evidence of sustainable design. Recent research shows that only 15% of American and European consumers are not interested in buying and/or paying for sustainable products and that majority of 78% of consumers have sustainability as a top 5 value driver in at least one product category during purchase [8]. Rapid adoption of green products at the market has been seen in the emerging sustainability megatrend. Companies that demonstrate transparency and commitment to sustainability through certifications, reporting, and lifecycle assessments can strengthen their market position and build trust with stakeholders.

4 IMPORTANCE OF EARLY STAGES IN SUSTAINABLE PRODUCT DEVELOPMENT

The early stages of product development are where the most impactful sustainability decisions are made. Development strategy, material selection and manufacturing processes, procurement and production, use and maintenance, disassembly and product features determined in the design phase directly influence a product’s environmental and social footprint. Potentials to influence environmental impact is the highest at the early product development and design phases [5]. For example, using recycled or renewable materials from the outset reduces the demand for virgin resources and lowers carbon emissions during production. To unlock potentials design team should expand the boundaries through collaboration of all involved parties.

Lifecycle assessments should inform these decisions, enabling designers to foresee how a product will perform environmentally throughout its lifecycle. Early adoption of sustainability criteria ensures that products are easier to maintain, repair, and recycle, thus reducing long-term waste and resource use. Conversely, neglecting sustainability in the design phase often locks companies into environmentally harmful practices that are difficult and costly to reverse.

5 TRANSFORMATIONS IN ENGINEERING DESIGN PROCESSES

The technological evolution from mechatronic systems in the 1960s to the current era of smart products or product service systems highlights significant advancements. In the context of the fourth and fifth industrial revolutions, challenges include managing large data volumes, ensuring cybersecurity, and meeting customer demands for personalization and sustainability. However, these challenges also present opportunities for creating smarter products, reducing costs, and improving operational efficiency through IoT and data analytics [9].

Effective collaboration among stakeholders throughout the product lifecycle is crucial for leveraging digital data and making informed decisions. Technological tools like Augmented and Virtual Reality (AR/VR) are instrumental in Smart Product Development (SPD). The shift from Lean Product Development (LPD) to SPD emphasizes waste reduction and the integration of Industry 4.0 technologies for value-added processes. Industry 5.0 builds on these foundations, prioritizing resilience, environmental sustainability, and human-centered design.

Integrating sustainability into early-stage design and innovation processes often involves tough decisions that place sustainability aspects in conflict with business imperatives [10]. It is a common design situation when there are no solutions that can satisfy multiple objectives at once. In such situations compromises are necessary and trade-offs between design properties are traditional engineering activities. Trade-offs are specially challenging in the context of early design for sustainability in manufacturing companies [11].

Navigating trade-offs in the uncertain and dynamic nature of early design activities presents additional challenges to an already complex task [12]. In the early stages, designers often face rapidly changing requirements and shifting stakeholder priorities, which can complicate decision-making. The need to balance product properties competing interests, such as cost, functionality, and aesthetic appeal, adds to this complexity. Moreover, decisions concerning sustainability introduce another layer of difficulty when managing these trade-offs. As environmental considerations become increasingly critical, designers must weigh the long-term impacts of their choices against immediate project demands without clear understanding and framework to evaluate sustainability in absolute scale.

While trade-offs are a common practice in product development, their execution is not straightforward, particularly when it comes to evaluating sustainability during the early phases of product development. Many existing sustainability evaluation methods offer tools for the relative comparison of various product variants being developed. However, establishing a framework with sustainability indicators that enables absolute metrics remains an area for further research. Such a framework should address the current challenges outlined in Figure 2.

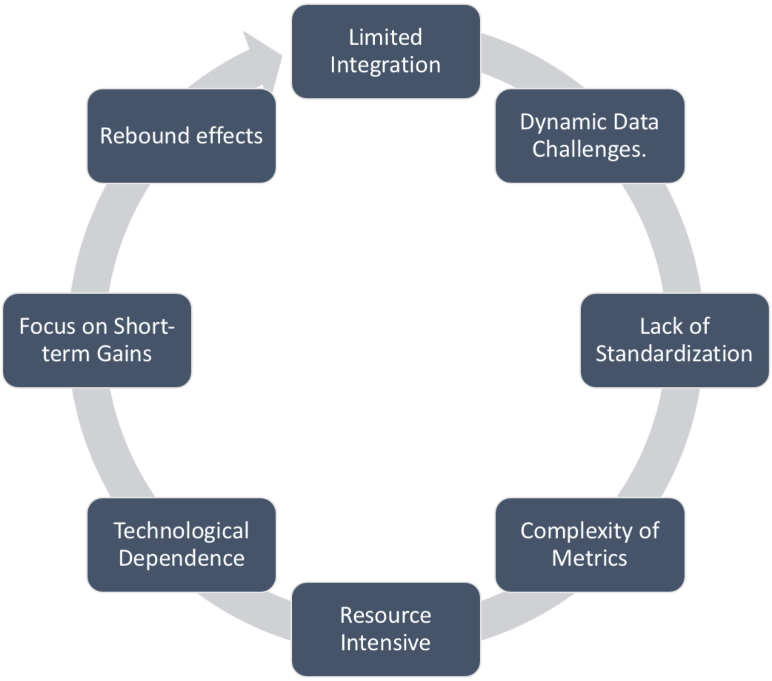

Figure 2. Sustainability evaluation problem groups

Limited Integration: Many sustainability indicators are often assessed in isolation rather than holistically, which can lead to an incomplete understanding of a product's sustainability. This fragmentation makes it difficult to grasp the overall environmental and social impacts.

Dynamic Data Challenges: Collecting and analysing data throughout the product lifecycle can be static or dynamic, complicating the evaluation process. Early design phases often lack real-time data, which is crucial for informed decision-making.

Lack of Standardization: There is no universally accepted framework or standard for sustainability indicators, leading to inconsistencies in measurement and reporting. This can result in confusion among stakeholders and hinder comparability across products or industries.

Complexity of Metrics: Sustainability encompasses various dimensions—economic, environmental, and social. Balancing these often-conflicting aspects can be challenging, particularly when trying to prioritize one over the others during the design process. While we have developed methods for relative assessments, i.e., the comparison of different products we do not have absolute sustainability metric on a product level.

Resource Intensive: Implementing comprehensive sustainability assessments can be resource-intensive, requiring significant time, expertise, and technology. This can be a barrier for companies, especially smaller ones, in adopting sustainable practices.

Technological Dependence: While technologies like Big Data and AI are useful, their effectiveness relies on the quality of data and integration across systems. If these technologies are not adequately implemented, they may not yield meaningful insights.

Focus on Short-term Gains: Early design decisions often prioritize immediate market needs or cost-saving measures over long-term sustainability goals, leading to choices that may undermine overall sustainability.

Rebound effects: Limited understanding of how the new product will influence the user behaviour [1]. Designers have limited understanding of behavioural mechanisms and we have no tools to simulate such a sociotechnical phenomenon.

Addressing these challenges is essential for effectively integrating sustainability into product design and ensuring that the evolution of engineering design processes reflects the growing importance of sustainability. Traditional design approaches, which prioritized technical performance and cost-effectiveness, have given way to more integrated methods that also consider environmental and social factors. Based on literature review this process is demanding and every company seeks its own path. A systematic analysis of 33 research articles on sustainable product design [10a] *„encompasses the holistic incorporation of sustainability principles from the onset of design, ensuring that sustainability impacts are considered throughout a product's lifecycle “.* Almost half of analyses papers are predominantly focused on strategic sustainability by converting normative principles into actionable, operational measures.

This convergence of factors has redefined engineering design, making sustainability an essential element of modern product development. This requires a deep understanding of sustainable materials, lifecycle assessments, and regulatory requirements, which can be overwhelming in the face of other pressing design challenges. Ultimately, the interplay between these various factors not only heightens the difficulty of the design process but also underscores the importance of integrating sustainability into early design thinking. By addressing these challenges proactively, designers can create solutions that are not only innovative but also responsible and forward-thinking.

6 CONCLUSION

Sustainable product development is no longer an option - it is a necessity. The environmental challenges of our time, coupled with technological advancements and shifting sociopolitical pressures, demand a fundamental shift in how products are designed, manufactured, and consumed.

For R&D departments, this means adopting a lifecycle approach that integrates sustainability into every phase of product development. By leveraging technological tools like AI, IoT, and digitalization, and aligning with sustainability models such as the circular economy, companies can design products that meet the expectations of regulators, consumers, and investors.

While incorporating sustainability into manufacturing operations presents challenges, the long-term benefits—both for the environment and the business—are clear. Companies that take a proactive approach to sustainable engineering will not only contribute to solving global environmental crises but also position themselves for long-term success in an increasingly eco-conscious world.

However, a key problem in the early design phases is the limited integration of sustainability indicators across different lifecycle stages, which often leads to assessments that focus on either single indicators or narrow aspects of sustainability. Although some research efforts have developed models and tools for monitoring sustainability, the challenge remains in creating comprehensive frameworks that effectively integrate multiple indicators and lifecycle stages. Additionally, while technological advancements facilitate data collection and analysis, there is a need for more cohesive approaches that can encompass economic, environmental, and social dimensions of sustainability in product design. Overall, the literature underscores the importance of developing robust sustainability indicators and integrating Industry 4.0 technologies to assess and enhance sustainability throughout the entire product lifecycle.

Sustainable design and product development prioritizes not only user values but also seeks to minimize environmental impact, reflecting a holistic understanding of sustainability. By fostering collaboration between designers, technologists, and stakeholders, we can develop solutions that not only meet immediate user needs but also contribute to a sustainable future. As we advance, it is crucial to redefine our design objectives to encompass broader societal and ecological considerations, ensuring that our innovations resonate with the pressing challenges of our time.

REFERENCES

[1] Pigosso, D.C.A., *Towards the Prevention of Rebound Effects by Design*, Keynote lecture at DESIGN 2024, 18th International Design conference, Cavtat May, 2024. Available at: https://www.youtube.com/live/rZKtFEbb9cs
[2] Richardson, J., Steffen W., Lucht, W., Bendtsen, J., Cornell, S.E., et.al. 2023. *Earth beyond six of nine Planetary Boundaries*, Science Advances, 9, 37.
[3] Marjanović, D., Štorga, M., Škec, S., (eds.) *Design Research: The Sociotechnical Aspects of Quality, Creativity, and Innovation*. Springer, 2023. Available at: https://doi.org/10.1007/978-3-031-50488-4
[4] Tukker, A., Emmert, S., Charter, M., Vezzoli, C., Sto, E., Andersen, M., Geerken, T., Tischner, U. & Lahlou, S. *Fostering change to sustainable consumption and production: an evidence based view*. Journal of Cleaner Production, 16(11), 1218–1225. 2008.
[5] Lüdeke-Freund, F., *Towards A Conceptual Framework of Business Models for Sustainability*, Knowledge Collaboration & Learning for Sustainable Innovation ERSCP-EMSU conference, Delft, 2010
[6] Seegrün, A,, Hardinghaus, L., Riedelsheimer, T., Lindow, K., *Incorporating sustainability into product lifecycle management: a systematic literature review*, Proceedings of the Design Society , Volume 4: DESIGN 2024 , May 2024 , pp. 1437 – 1446. Available at: https://doi.org/10.1017/pds.2024.146
[7] Robertson-Smith, G., Markwick, C., *Employee Engagement A review of current thinking*, Institute for Employment Studies, Brighton, UK, 2009.
[8] Gathen von der, A., Broby, Eckert, N., Kastbjerg, C., *The Demand Revolution*, MIT Press, 2024
[9] Marconnet, B., Gaha, R., Assuad, C., Martinsen, K., Eynard, B., *Selecting sustainability indicators for smart product design based on industry 4.0/5.0 technologies: analysis and proposal of a methodological framework*, Proceedings of the Design Society , Volume 4: DESIGN 2024 , May 2024 , pp. 1369 – 1378, Cambridge University Press. Available at: https://doi.org/10.1017/pds.2024.139m
[10] Parolin, G., McAloone, T.C. and Pigosso, D.C.A. (2023), The Effects of Scenarios on Decision- Making Quality in Early Design – An Empirical Study, Proceedings of the Design Society, Cambridge University Press, Vol. 3, pp. 3375–3384. Available at: https://dx.doi.org/10.1017/pds.2023.338.
[11] Pigosso, D.C.A., Mcaloone, T.C. and Rozenfeld, H. (2014), “*Systematization of best practices for ecodesign implementation”,* in Marjanovic., D. et all., eds, Proceedings of International Design Conference, DESIGN 2014, Dubrovnik, pp. 1651–1662.
[12] Parolin, G., McAloone C. T., Pigosso, D.C.A., What's the catch? *Trade-off challenges in early design for sustainability*, D2024 Proceedings of the Design Society , Volume 4: DESIGN 2024 , May 2024 , pp. 1399 – 1408, DOI: https://doi.org/10.1017/pds.2024.142
[13] Riedelsheimer, T*., Digital Twins for real-time Life Cycle Assessment of Products*, Presentatation at ECO Design 2023, Fraunhofer IPK Webinar, 2024

Use of computational fluid dynamics to evaluate the performance of rudder with leading-edge tubercles

Matic Medvešek[1,2], Simon Muhič[1,2]

[1]*Faculty of Industrial Engineering Novo mesto, Šegova ulica 112, 8000 Novo mesto, Slovenia*
E-mail: matic.medvesek@fini-unm.si

[2]*Rudolfovo – Science and Technology Centre Novo mesto, Podbreznik 15, 8000 Novo mesto, Slovenia*
E-mail: simon.muhic@fini-unm.si

Abstract: *Biomimetics imitates natural, highly specialized shapes, thereby presenting potential for optimizing products and processes. This paper presents a study on the use of biomimetics to improve the performance of a vessel's rudder by integrating tubercles on the leading edge, similar to the pectoral fins of a humpback whale. The purpose of implementing tubercles on the rudder is to increase the lift-to-drag ratio, thereby improving the vessel's manoeuvrability, particularly in the range of higher angles of attack. Using TCAE software for numerical fluid dynamics simulation, we conducted a three-dimensional analysis of the steady-state flow of a viscous fluid for both a conventional rudder and a rudder with added tubercles on the leading edge. The* $k-\omega\ SST$ *turbulence model was used for turbulence modeling. Simulations for both rudders were performed at angles of attack ranging from 7° to 22°. The comparison of results shows a disadvantage of rudder with tubercles in region of 7° to 11° angles of attack. At an angle of attack of 11° an advantage of it starts to show, continuing up to 22°. The highest advantage is achieved at an angle of attack of 14°, where a 6.2 % increase in drag results in a 27.6 % increase in dynamic lift.*

Keywords: *biomimetics, dynamic lift, tubercles, rudder, computational fluid dynamics*

Article Classification: *Scientific paper*

1 INTRODUCTION

Whales use their fins for swimming, they have two pectoral fins and one tail fin. The latter is used for locomotion, similar to how a vessel uses a propeller. The pectoral fins are mostly used for performing manoeuvres, similar to how a rudder functions on a vessel. Humpback whales have special tubercles on the leading edge of their pectoral fins, a feature not found on other cetaceans [1].

Early research by Fish et al. [2] revealed how tubercles enhance the humpback whale's agility by reducing drag and increasing lift, allowing efficient manoeuvrability. Miklosovic et al. [3] later applied this concept to airfoils, showing that tubercles reduce drag and delay stall at high angles of attack (AOA), improving aerodynamic efficiency. Johari et al. [4] observed that tubercles generate counter-rotating vortex-pairs which help regulate fluid flow, effectively reducing pressure drag. Custodio [5] further explained that these vortices increase the effective surface area, enhancing stability in turbulent flow. In aerospace, Stanway [6] demonstrated improvements in lift-to-drag ratios and noise reduction, particularly for helicopter rotors. Similarly, Pedro et al. [7] showed that propellers with tubercles reduce cavitation and increase thrust efficiency in marine applications. However, as Hansen [8] noted, tubercle geometry (wavelength and amplitude) must be optimized for specific flow conditions, adding complexity to the design process.

The rudder's function is to generate a torque force around the vessel's center of gravity, causing it to rotate around its vertical axis, thereby changing its direction. The rudder's characteristics is determined by the size of the drag force and dynamic lift force. The drag force slows the vessel down, making it undesirable, so we aim for the lowest possible value. The dynamic lift force generates torque on the vessel, which is the primary reason for using the rudder. Therefore, we aim to increase the dynamic lift force, reduce drag force and improve their ratio. Using biomimetic principles in the form of tubercles on the leading edge of the rudder allow for the improvement of these characteristics.

The article provides an example of applying biomimetic principles to enhance rudder performance. The research aims to investigate the optimization potential of rudder design. A case study is presented featuring a rudder developed for use on a human-powered vessel. Impact of using tubercles on leading edge of rudder are investigated using Computational Fluid Dynamics.

2 METHODS

2.1 Numerical model

Law of conservation of mass defines that the element always consists of the same number of molecules, meaning its mass must remain constant. Fluid is a continuum, meaning that the mass entering the control volume must also simultaneously exit. At every moment, the entire control volume must be filled with fluid. External forces that act on the control volume are equal to the time rate of change of momentum within the control volume and the net inflow of momentum across the control surface [9].

Law of conservation of mass and momentum are the governing equations describing fluid motion. The following equation shows the basic equations which determines the conservation [10]:

$$\frac{\partial(\phi\rho)}{\partial t} = -\left(\frac{\partial(\phi\rho v_x)}{\partial x} + \frac{\partial(\phi\rho v_y)}{\partial y} + \frac{\partial(\phi\rho v_z)}{\partial z}\right) + \gamma \tag{1}$$

Computational Fluid Dynamic simulations are based on Navier-Stokes equations. These are used to calculate the relations between cells, providing total motion description of uncompressible Newtonian fluid. They account the influence of external and internal or viscous forces on fluid motion. They form the basis of numerical analysis in fluid dynamics. Equation in vector shape is shown [10]:

$$\frac{D\vec{v}}{Dt} = \vec{f}m - \frac{1}{\rho_0}\vec{\nabla}p + \mathcal{V}_0\Delta\vec{v} \tag{2}$$

Navier-Stokes equations are due to their complexity analytically unsolvable for real spatial flows. The only way to calculate them is by using numerical techniques. Various methods and models are used, by which the computation becomes solvable. Their main differences are the purpose of what we want to simulate and how accurately or within what time frame.

The starting point for conducting fluid dynamics simulations is defining a 3D model on which the simulations are performed. First a 3D model of a conventional rudder was created. The shape of the conventional rudder was designed with the goal of creating a test model of simple shape that would combine simulation simplicity and possibility for tubercle implementation. This would ensure a reference comparison with the rudder featuring tubercles. Dimensions such as cord, span and surface area were derived from rudders used on similar vessels [11]. Aspect ratio was based on measurements of the humpback whale’s pectoral fin [12]. NACA 0012 profile was chosen due to its popularity in nautical applications [11]. Planform of humpback whale’s pectoral fins is elliptical and tapered, with a smooth narrowing towards the tip [1]. To simplify the design, we used a tapered shape that ends with a flat edge. Rudder has a maximum cord length of 77 mm which is on the top 100 mm of span. Lower section starts to taper and reaches 47 mm at full span of 285 mm (Figure 1). Rudder tip is rounded to prevent excessive induced drag while still maintaining a relatively simple shape.

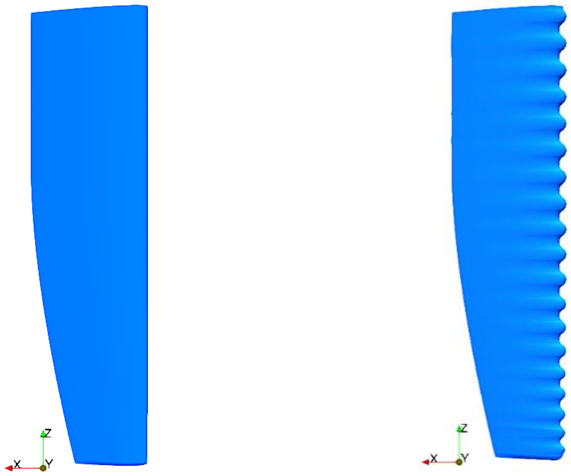

Figure 1: 3D model of conventional rudder (left) and of a rudder with added tubercles (right)

The conventional rudder served as the basis for modeling the rudder with added tubercles. The only difference between them is the presence of tubercles, ensuring that these would be the sole factor causing differences in the simulation results. Shape of these is based on the ratio of amplitude/cord length A/c and wavelength/cord length λ/c. These ratios were determined based on the results of physical experiments conducted in a wind tunnel [8]. Tubercles were added to the rudder with the aim of improving the vessel's manoeuvrability. For this purpose, a tubercle configuration with the highest dynamic lift within the entire AOA range was selected. The rudder profile depth varies throughout the span, so the tubercle dimensions are adjusted accordingly. Figure 1 shows a 3D model of conventional rudder and rudder with added tubercles.

The identification of differences in performance of a rudder with tubercles, is conducted using two numerical experiments simulating fluid flow. One is with a conventional rudder and the other with added tubercles. The potential improvement in performance using tubercles was thus assessed based on the differences between the two simulations. The TCAE software was used for the fluid dynamics simulation with Reynolds Averaged Navier-Stokes (RANS) approach.

The turbulence model was selected based on the key focus of the observation. From the past research into the impact of tubercles on flow conditions, the most important part is to determine the laminar-turbulent transition process [13]. For this reason, the $k - \omega\ SST$ turbulence model was chosen, as it allows a good description of flow behavior in such regime [13]. The rudder of a vessel, with an average speed of $2.22\ \mathrm{m/s}$, was analysed. Fluid properties was used for seawater at 20°C. Dynamic viscosity was $\mu = 0{,}0010016\ \mathrm{Pas}$ and density $\rho = 998{,}2\ \mathrm{kg/m^3}$.

The main goal of the simulation was to analyse the dynamic lift force in the range of higher AOA. We wanted to simulate also the circumstances in low AOA, for evaluation, so the rudder was analysed at AOA between 7° and 22°, with the step of 3°. Each simulation was performed with the rudder model placed at a different AOA relative to the x-axis, ensuring that the velocity field always flowed in the direction of the x-axis.

2.2 Grid independency test

The validation of simulation results was done by comparing simulation results with different mesh cell quantity, with the goal of proving that the computational mesh was independent of the results [13]. Mesh setup is fundamental for a quality simulation. Several factors affect mesh quality. It is essential to refine the mesh in areas where there are large velocity and pressure gradients. Shape and orientation of the cells should not affect the fluid flow or the final results [14]. Each mesh is evaluated by comparing results to other simulations with varying mesh quantities.

Rudder with added tubercles in 16° AOA was used for the grid independency test. Accuracy of the simulation results was verified by validating the results of multiple simulations with different mesh densities (Table 1). Each subsequent simulation had a mesh 30 % denser than the previous one. The drag force on the rudder F_x represents the force parallel to the fluid flow. The dynamic lift force F_y represents the force perpendicular to the fluid flow. Force F represents the resultant force.

Table 1: Grid independency test results

Case	Background mesh size [mm]	Force designation	Force [N]	Difference [N]	Rel. difference [%]
1.	65	F_x	9.583		
		F_y	30.602		
		F	32.076		
2.	50	F_x	10.227	0.64	6.72
		F_y	34.290	3.69	12.05
		F	35.792	3.72	11.58
3.	35	F_x	9.763	0.46	4.54
		F_y	34.153	0.14	0.40
		F	35.530	0.26	0.73

Table 1 shows grid independency test results between three meshes. Sufficient accuracy of maximum relative force difference of 5 % for each sequential simulation was set. Results between case 2 and case 3 were satisfactory, therefore case 2 was chosen for further simulations.

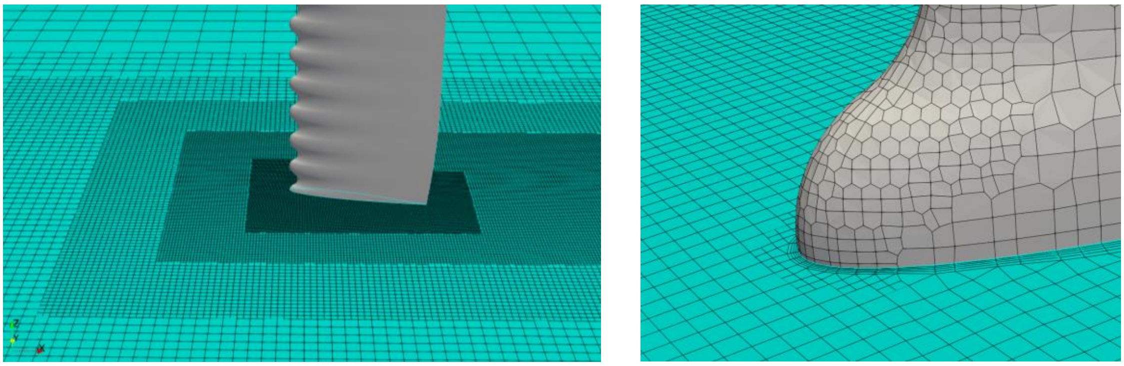

Figure 2: Mesh generation on cross section of domain (left) and with mesh on surface of the rudder (right)

Figure 2 presents a mesh from chosen case 2 (Table 1). Figure 2 (left) shows a cross section of simulated domain, denser mesh around rudder is generated with the aim of capturing complex flow behaviour. Figure 2 (right) shows a detailed view of one tubercle with visible mesh. Mesh in form of layers for capturing boundary layer is also visible on the cross section.

3 RESULTS AND DISCUSSION

Figure 3 represents the results of forces obtained through fluid dynamics simulations. Several simulations were conducted with rudder at different AOA.

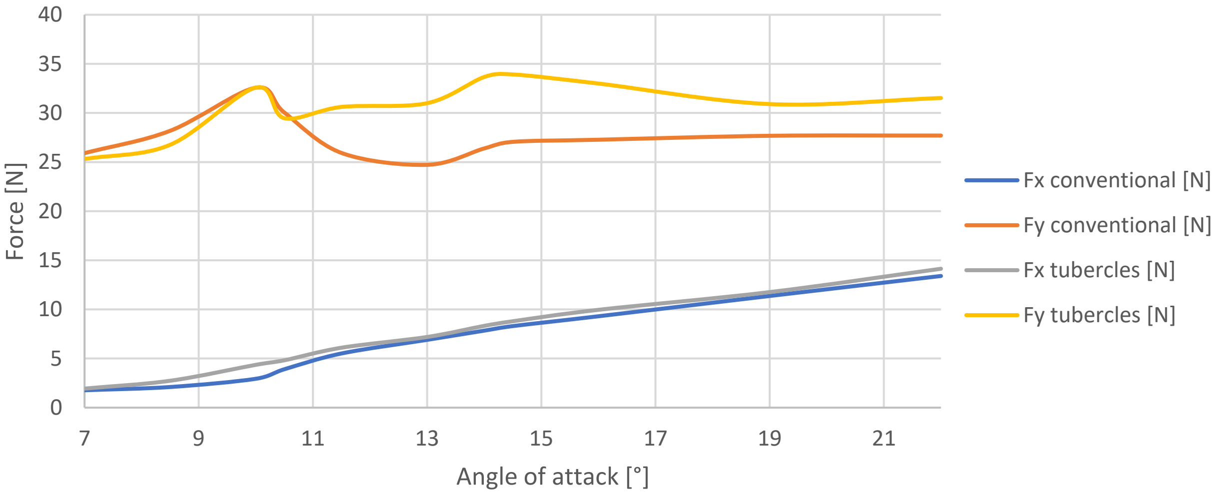

Figure 3: Force comparisons between the two rudders in the AOA span (7° - 22°)

In the region of 7° to 10° the conventional rudder has almost linear propagation of value. Rudder with added tubercles has a bit lower value in between but reaches approximately the same value at 10° (Figure 3). Because of higher average dynamic lift and lower drag the conventional ruder is preferred in that region. Beyond 10° AOA a drastic difference in the behaviour of the rudders is noticeable. Dynamic lift decreases on both rudders. At 10,5° large differences between the rudders can be observed. Conventional rudders dynamic lift is decreasing far lower as of rudders with tubercles. Similar behaviour in dynamic lift values was also observed by Stanway [6], who found that the reason for the difference is duo to formation of streamwise counter-rotating vortex-pairs behind the tubercles, which help delay flow separation.

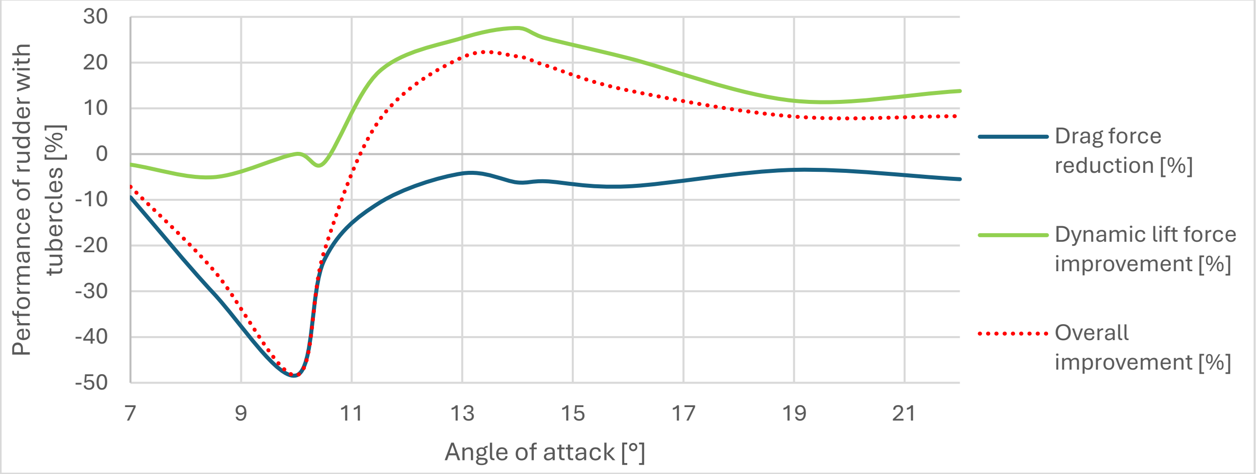

Figure 4: Advantage of rudder with added tubercles in different AOA

Figure 4 illustrates the performance improvement of a rudder with tubercles compared to a conventional rudder, based on relative differences in drag and lift forces. The overall improvement is calculated as the mean value of drag reduction and lift force improvement, with positive values indicating better performance. For optimal performance, both drag reduction and lift force improvement should be positive. The drag force reduction values are negative, indicating that the rudder with tubercles experiences higher drag across the entire range AOA. From 7° to 11° AOA, the overall performance of the rudder with tubercles is negative, indicating reduced performance. However, between 11° and 22° AOA, the rudder with tubercles shows improved performance, as seen in the positive values of the overall improvement curve. Maximum improvement occurs at 14° AOA, where the rudder with tubercles achieves a 27.6% increase in dynamic lift force.

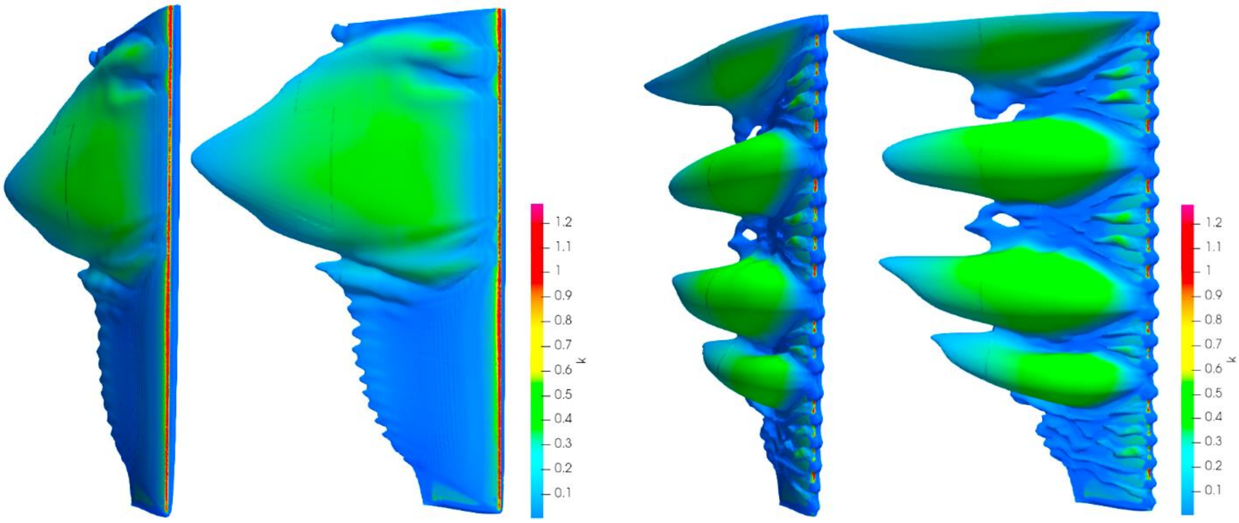

Figure 5: Constant velocity magnitude contour on conventional rudder (left) and on rudder with tubercles (right)

Figure 5 illustrates a constant velocity contour comparison on conventional rudder and on rudder with tubercles. Simulations shown here were performed at 13° AOA. Contour is set to velocity magnitude of $1.2\ \mathrm{m/s}$. Free flow velocity of the fluid is $2.2\ \mathrm{m/s}$. Contour therefore illustrates the region with a slowed down flow affected by the rudder interaction. Colouring of the contour is determined by the turbulent kinetic energy k magnitude.

In the 13° AOA total boundary separation with loss of dynamic lift is expected for conventional rudder [15]. The conventional rudder is experiencing a single large region of slower flow, visible on the left side of Figure 5. Rudder with added tubercles is generating a pattern of smaller regions, correlation with tubercle position can be observed (Figure 5 - right). These regions are always positioned between two tubercles. A size of two different scales of regions can be observed. Mostly there are small regions, but there are also four very large ones. Figure 5 (right) shows that turbulent kinetic energy magnitude and large regions are also corelated. Behind the tubercles where areas of high turbulent kinetic energy is observed, small regions emerge. On the contrary low turbulent kinetic energy enables formation of larger contours.

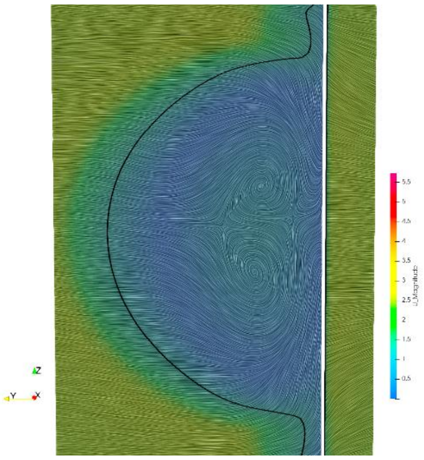

Figure 6: Visualization of counter-rotating vortex-pair

Figure 6 illustrates the cross section of contour presented on Figure 5. Flow trajectory paths present the conditions in action. Counter-rotating vortex-pair formation can clearly be seen, aligning with the findings of Stanway [6].

Size of low velocity regions generated by the rudders shown in Figure 5 is observed also in profile view (perpendicular to the z-axis). Figure 7 is presenting flow separation comparison between the two rudders. Observed profile is set 48 mm below the top of the rudder, between the third and fourth tubercle. The conventional rudder is experiencing a large separation spanning from the leading to the trailing edge on the low-pressure side. Rudder with added tubercles has a much smaller separation region. Flow separation starts behind the leading edge, but it reattaches back to the rudder.

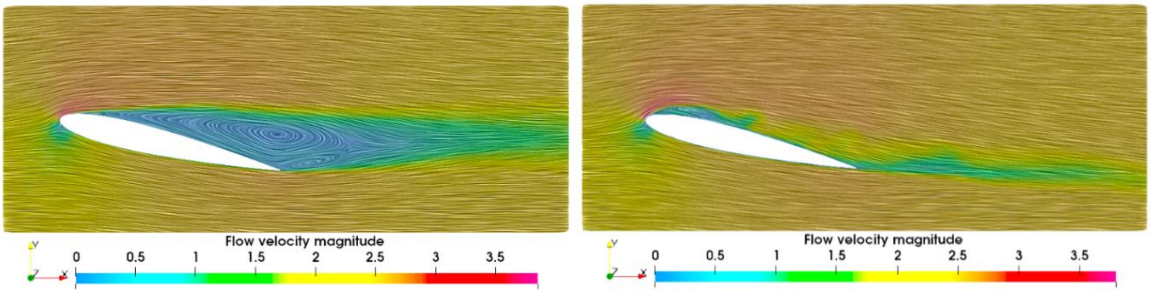

Figure 7: Fluid flow trajectory around conventional rudder (left) and rudder with tubercles (right)

Figure 7 shows large differences in profile surface area of the separation regions. Dynamic lift force enhancement on the rudder with tubercles can be seen by the flow path trajectory on the low-pressure side. Flow changes direction and is almost parallel to the rudder profile. Meanwhile flow next to the conventional rudder is almost undisturbed on the low-pressure side.

4 CONCLUSION

Comparison of performance between conventional rudder and rudder with added tubercles on leading edge was performed. Computational fluid dynamic simulations were performed with computational fluid dynamics software TCAE. RANS method and $k-\omega\ SST$ turbulence model was used. Simulations were performed in the region of 7° to 22° AOA.

Rudder with added tubercles on the leading edge provides a performance improvement in the region of 11° to 22° AOA. The best performance improvement is observed at 14° where rudder with tubercles experiences 27,6 % increase in dynamic lift and an 6,2 % increase in drag. Because the dynamic lift increase is much higher than drag it is presumed to provide better performance.

The analysed tubercle pattern and shape demonstrated improved performance in certain regions, it is estimated that further optimization could enhance boundary layer adhesion to the rudder. That could contribute to lower added drag and improved dynamic lift. The simulation results show good agreement with previous research on similar phenomena, further supporting the reliability of the observed outcomes. To fully evaluate and verify the accuracy of the calculated results, force values should also be measured through physical experiments under real-world conditions.

REFERENCES

[1] E. FISH, Frank et al. The Tubercles on Humpback Whales' Flippers: Application of Bio-Inspired Technology. V: *Applying Mechanical Design to Experimental Biology*. Salt Lake City: Oxford University Press, 2011, pp. 203–213.

[2] E. FISH, Frank and Juliann M. BATTLE. Hydrodynamic Design of the Humpback Whale Flipper. *Journal of Morphology*. 1995, pp. 51–60.

[3] MIKLOSOVIC, D. S. et al. Leading-edge tubercles delay stall on humpback whale (Megaptera novaeangliae) flippers. *Physics of Fluids*. 2004, 16(5). ISSN 10706631

[4] JOHARI, H. et al. Effects of Leading-Edge Protuberances on Airfoil Performance. *AIAA JOURNAL*. 2007, 45(11), pp. 2634–2642.

[5] CUSTODIO, D. The Effect of Humpback Whale-Like Protuberances on Hydrofoil Performance. 2007.

[6] STANWAY, Michael. *Hydrodynamic effects of leading-edge tubercles on control surfaces and in flapping foil propulsion*. 2008.

[7] PEDRO, Hugo T.C. and Marcelo H. KOBAYASHI. Numerical study of stall delay on humpback whale Flippers. *46th AIAA Aerospace Sciences Meeting and Exhibit*. 2008.

[8] LEE HANSEN, Kristy. *Effect of Leading Edge Tubercles on Airfoil Performance*. Adelaide, 2012. Research Thesis. The University of Adelaide.

[9] ŠKERGET, Leopold. *Mehanika tekočin*. University of Maribor, Faculty of Mechanical Engineering, Ljubljana: University of Ljubljana, Faculty of mechanical engineering, 1994.

[10] GREENSHIELDS, Christopher J. and Henry G. WELLER. Notes on computational fluid dynamics: general principles [online]. 2022, 291 [viewed 20. 09. 2024]. Available at: https://doc.cfd.direct/notes/cfd-general-principles/index/

[11] LARSSON, Lars, Rolf E. ALIASSON and Michal ORYCH. *Principles of Yacht Design*. 4. edition. London: Adlard Coles Nautical, 2014.

[12] E. FISH, Frank, Laurens E. HOWLE and Mark M. MURRAY. Hydrodynamic flow control in marine mammals. V: *Going with the Flow: Ecomorphological Variation across Aquatic Flow Regimes*. San Antonio: Oxford University Press, 2008, pp. 788–800.

[13] SATHYABHAMA, A and B K SREEJITH. Numerical Investigation on the Effect of Leading-Edge Tubercles on the Laminar Separation Bubble. *Journal of Applied Fluid Mechanics*. 2022, 15(3), pp. 767–780. ISSN 1735-3645

[14] SADREHAGHIGHI, Ideen. *Mesh Generation in CFD*. 2020.

[15] NATIONAL ADVISORY COMMITTEE FOR AERONAUTICS. *Airfoil tools* [online]. 15. July 2023 [viewed 18. 08. 2023]. Available at: http://airfoiltools.com/airfoil/details?airfoil=n0012-il

Numerical and experimental analysis of single-phase fluid flow in a plate heat exchanger with a dimple heat plate structure

Urban Močnik[1,2], Bogdan Blagojevič[1,3], Simon Muhič[1,4]

[1]Faculty of Industrial Engineering Novo mesto, Šegova ulica 112, 8000 Novo mesto, Slovenia
E-mail: urban.mocnik@fini-unm.si

[2]Danfoss Trata d.o.o., Ulica Jožeta Jame 16, 1210 Ljubljana, Slovenia
E-mail: urban.mocnik@danfoss.com

[3]Plinovodi d.o.o., Cesta Ljubljanske brigade 11b, 1000 Ljubljana, Slovenia
E-mail: bogdan.blagojevic@siol.net

[4]INOVEKS, d.o.o., Cesta 2. grupe odredov 17, 1295 Ivančna Gorica, Slovenia
E-mail: simon.muhic@inoveks.si

Abstract: *A device that enables heat transfer between liquids of different temperatures without mixing the liquids is called a heat exchanger. In a plate heat exchanger, the two fluids are separated by corrugated walls made of thin steel sheet-heat plates. A plate heat exchanger with a dimpled structure of the heating plate is characterized by a number of dimples, the shape of which determines the properties of the heat exchanger. Despite the increasing recognition of the favorable characteristics of these heat exchanges, the understanding of the fluid flow characteristics within such channels remains relatively unexplored. A thorough knowledge of the flow conditions in these channels is essential for the successful and efficient development of new products. This paper presents an investigation of single-phase water flow in a plate heat exchanger with a dimple structure using computational fluid dynamics (CFD) and experimentally. The numerical analysis was performed using two turbulence models: the Realizable* $k-\varepsilon$ *model with an Enhanced wall treatment and the* $k-\omega\ SST$ *model. The results of the Realizable* $k-\varepsilon$ *model matched the experimental results relatively well, and the* $k-\omega\ SST$ *model predicted a higher pressure drop compared to the experimental results. These investigations showed that despite the relatively low velocity of the liquid in the channel, due to its shape, turbulent flow occurs. Two different flow regimes in the channel of the considered heat exchanger were also identified: the live regime, which dominates the heat transfer, and the dead regime, where a recirculation zone is formed behind the brazing point, which reduces the effective area for heat transfer. The size of this dead regime does not change significantly with velocity in the turbulent state of the flow.*

Keywords*: plate heat exchanger, dimple pattern, experimental testing, computational fluid dynamics, pressure drop*

Article Classification: *Scientific paper*

1 INTRODUCTION

A heat exchanger is a device that facilitates the transfer of heat between two or more liquids of different temperatures. These devices are essential in various industrial systems and are also prevalent in district heating systems.

A plate heat exchanger is a specific type where hot and cold fluids are separated by thin, corrugated walls known as heat plates. These plates, made of stainless steel, are arranged in such a way that they form multiple channels for water flow, with half connected to the primary side and the other half to the secondary side. Copper, used as a bonding material, seeps into the edges and junctions of the plates due to the capillary effect, creating seals and brazing points in a vacuum furnace.

The design of these heat plates significantly influences the heat exchanger's performance. The most common design globally is the fishbone or chevron pattern, characterized by the angle and depth of distinctive straight corrugations as presented in Fig 1B. Heat exchangers with this design are known as brazed plate heat exchangers (BPHE) and have been in use since the 1970s [1].

Recently, a new design featuring a dimple pattern has been developed, which enhances the heat exchanger's efficiency. Unlike the traditional straight corrugations, this design incorporates numerous dimples, as illustrated in Fig. 1A, defining the characteristics of this advanced type of heat exchanger.

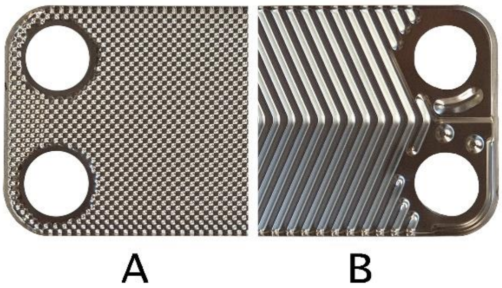

Figure 1: A - The dimple pattern, and B – the fishbone pattern heat plate

Although there is extensive literature on fluid flow through channels in the context of BPHE, there is a lack of available research on dimple pattern heat exchangers. Observing liquid flow at a micro-level within these heat exchangers is challenging due to the small channels and complex structure [2].

Some researchers, such as Focke and Knibbe [3], have made partial progress in this area. However, the advent of computational fluid dynamics (CFD) has provided a powerful tool for investigating fluid flow conditions within plate heat exchangers. Initially, studies focused on two-dimensional flows, as seen in the work of Metwally and Manglik [4], who examined flow and temperature distribution, friction factors, and the Nusselt number in the sinusoidal sections of heat exchanger channels. Kanaris et al. [5] expanded on this by incorporating more complex geometries and observed similar phenomena. With advancements in computing power, researchers began to study entire BPHE channels. Han et al. [6] analyzed several consecutive channels, observing flow distribution and heat transfer. Their numerical results deviated from experimental data by up to 35 %, with some discrepancies attributed to the experimental setup itself. Gherasim et al. [7] used a computer model of two BPHE plates, excluding the distribution channel geometry and assuming uniform fluid flow velocity at the inlet and outlet. They tested various turbulence models at different flow velocities, finding that the Realizable $k-\varepsilon$ turbulence model with Non-equilibrium wall functions and an average dimensionless wall distance y^+ between 2.8 (for Re = 400) and 11.25 (for Re = 3000) produced results closest to experimental data, with numerical results differing by 10 % to 16 %.

Gullapalli and Sundén [8] conducted simulations of fluid flow through the channels of a plate heat exchanger with various corrugation angles. They included inlet and outlet connections to replicate laboratory conditions. Using the LRR-IP (Reynolds Stress) turbulence model, they performed multiple calculations with different boundary conditions on the plate walls, such as constant heat flux and constant wall temperature. Their heat transfer results were 20 % to 30 % lower, and pressure differences were 10 % to 35 % lower than laboratory values. Despite these discrepancies, they found CFD to be a valuable tool for comparing different heat plate shapes, identifying potential geometric flaws in corrugations, and determining velocity profiles within the channels.

Tiwari et al. [9] used CFD tools to analyze a case involving two channels where a nanofluid flowed counter-currently. They employed a $k-\varepsilon$ turbulence model and conducted a laboratory experiment with the same plate heat exchanger configuration as in their numerical calculations. The numerical results differed from the experimental results by a maximum of 3.75 %.

Lee and Lee [10] performed non-stationary CFD analyses using the large eddy simulation (LES) approach on a small section of a fishbone heat plate heat exchanger. They observed oscillations in the turbulent flow regime, which increased both heat transfer and pressure drop.

Sarraf et al. [11] conducted both laboratory and CFD analyses on a two-channel sample. They compared numerical results with thermal camera recordings of the plate pack's exterior during laboratory experiments. The temperature distribution difference between CFD and experimental results was within 10 %. They used a $k-\varepsilon$ turbulence model and the $k-\omega$ model but faced convergence issues with the $k-\omega$ turbulence model. They identified two types of fluid flow in the fishbone patterned heat plates: "helical" flow, which moves from inlet to outlet along the grooves, and "cross" flow, which moves across the grooves. The dominant flow type depends on the mass flow rate and the angle between the grooves on the heat plate.

Piper et al. [12] conducted a numerical study on a pillow plate heat exchanger featuring a periodic pillow-like pattern. They identified two distinct flow areas within the channel: the meander core, essential for heat transfer, and the recirculation zone behind the welded joint, which reduces efficiency. They proposed several solutions to enhance efficiency, potentially increasing it by up to 37 %. Their numerical analysis used a domain derived from a transformation simulation, representing a small, periodically repeating part of the entire channel. They simplified calculations using all possible symmetries and employed the $k-\varepsilon$ turbulence model with constant heat flux as a boundary condition on the domain wall.

Yogesh et al. [13] investigated the influence of pipe geometry in a tubular heat exchanger with cooling fins. They used the $k-\omega$ turbulence model instead of the commonly used $k-\varepsilon$ model to achieve results more consistent with their reference. The $k-\omega$ model results were 5.2 % and 6.6 % lower than the reference values, while the $k-\varepsilon$ model results differed by 26.9 % and 44.8 %.

Al Zahrani et al. [14] performed a numerical analysis of a plate heat exchanger with five plates, two channels on the hot side, and two on the cold side, using the $k-\varepsilon$ turbulence model. They compared their numerical results with experimental data obtained by Muley and Manglik [15], finding deviations of ≤10 %.

As previously noted, while extensive research exists on chevron plate heat exchangers, there is a lack of literature on dimple pattern heat exchangers. In the presented study, the fluid flow in a channel formed by dimple pattern heat plates was numerically analyzed. Numerical results were validated our with laboratory experiments using a newly developed measurement method that allows for direct comparison.

2 NUMERICAL ANALYSIS OF FLUID FLOW

2.1 Channel Geometry Modeling

The heat plate's three-dimensional (3D) model was generated by scanning the real plate using a 3D scanner. The dimple's smallest possible representative part, presented in Fig. 2C in orange, was extracted from the scanned model. Using a CT scan, the appropriate shape of the brazing point was determined and incorporated into the 3D model. The complete cell model was created by mirroring across the relevant edges. This symmetric cell was then duplicated by additional mirroring to generate the full numerical domain as presented in Fig. 2A.

A cell constructed in this way is therefore symmetrical in all three planes. A real sheet metal cell is not symmetrical due to various technological and material inequalities. This is shown in Fig. 2B, where the STL (3D surface image) and the modeled (symmetric) surface are superimposed. These inequalities had to be taken into account when modeling the geometry. Inequalities were resolved by placing the true cell geometry midway between the most open and most closed geometry. Fig. 2C shows: blue - the most closed geometry, red - the most open geometry, and green - the middle geometry.

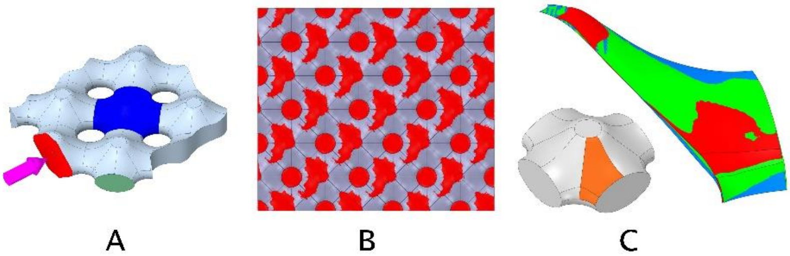

Figure 2: A - part of the channel with cell model (blue); arrow (pink) indicates flow direction, domain inlet (red), cell inlet/outlet (green); B – superimposed 3D model and 3D scan; C - Comparison of different cell geometries

During the research, it was discovered that due to the uniform velocity distribution on the inlet surfaces, the fluid flow in the first few cells had not yet developed to the extent that it could be considered representative. The situation appears in the last few cells. For the aforementioned reasons, rather than longitudinal periodic boundary conditions, we decided to extend the domain to the smallest possible number of consecutive cells, where useful results could still be obtained for the $k-\omega$ turbulence model, i.e. 14 consecutive cells. At the end of the geometric model, there is an extension to prevent backflow on the outlet surface. On this geometry, a study of the independence of the mesh density from the pressure difference calculation result was conducted.

Fig. 3 shows the geometry that was made from the base cell. This served as a basis for modeling narrower or wider domains. In the basic geometry, the number of cells is 28, but when referring to e.g. 14×2 cells means 14 consecutive cells in the y direction and 2 parallel cells in the x direction.

A study of the independence of the result from the geometry width was performed on domains that also have a length of 14 cells, and the widths are presented in Fig. 3 above. Domains that have more parallel cells (2, 3, and 6) have the same number of inlet and outlet surfaces. Each outlet surface also has its extension. Green lines indicate the application of symmetry boundary conditions.

In this article, when refered to the water velocity, it is ment the average velocity of fluid through the largest cross-section of the cell indicated in Fig 2 in red.

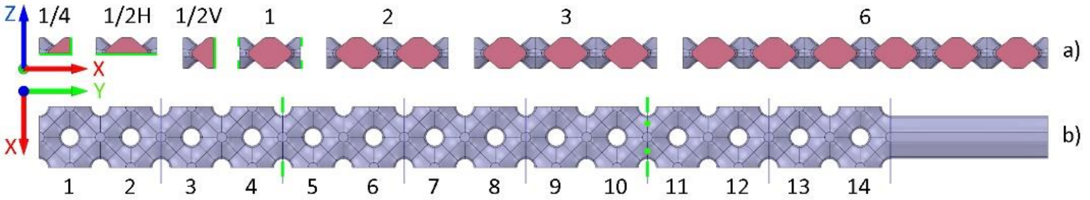

Figure 3: The basic geometry with numbering of: a) narrower or wider geometry, and b) successive cells

2.2 CFD Simulation

The calculations were carried out using Ansys Fluent 2021 software, which works on the finite volume method. The turbulent flow was simulated with the averaged Navier-Stokes equations (RANS). The Reylnods stresses were calculated with the turbulence models Realizable $k-\varepsilon$ with the Enhanced wall treatment (EWT) wall function (henceforth $k-\varepsilon$) and $k-\omega\ SST$ (henceforth $k-\omega$) [16]. The velocity-pressure coupling was performed with the coupled scheme.

The coupling between velocity and pressure was performed using a coupled scheme. Change in significant quantitives such as: residuals, area average velocity through the area between the 12th and 13th cell (Fig. 3b), area average pressure between the 2nd and 3rd cell (Fig. 3b), the maximal y^{+}on the wall and velocities in left and right points, (Fig. 3b, green points between 10th and 11th cell) were monitored. Motion of incompressible fluid is represented by these two euations [16]:

$$\frac{\partial\rho}{\partial t} + \nabla\cdot(\rho\vec{u}) = S_m \tag{1}$$

$$\frac{\partial}{\partial t}(\rho\vec{u}) + \nabla\cdot(\rho\vec{u}\vec{u}) = -\vec{\nabla}p + \nabla\cdot(\bar{\bar{\tau}}) + \rho\vec{g} + \vec{F} \tag{2}$$

The dimensionless distance between the wall and the mesh node closest to the wall is given by the equation [16]:

$$y^{+} = \frac{\rho\Delta y u_{\tau}}{\mu} \tag{3}$$

where

$$u_{\tau} = \left(\frac{\tau_{\omega}}{\rho}\right)^{\frac{1}{2}} \tag{4}$$

The geometry was divided into seven elements, where the boundary between the elements presents the plane on which the results were monitored, as shown in Fig. 3. The vertical lines represent the planes on which the area average pressure was obtained. The pressure difference on one element (two consecutive cells), was calculated by subtracting the pressure at the beginning from the pressure at the end of the element. Thus, a pressure drop on all individual elements along the model was obtained. These results were compared with those obtained through laboratory experiments.

2.3 Mesh Generation

Ansys Fluent (with Fluent meshing) software environment was also used to create the mesh. Since the flow conditions in the presented geometry is challenging, a polyhedros were used to construct the mesh. Past test showed that using such mesh up to four times fewer volume elements approximately half the computational memory and down to one-fifth of the computational time is needed compared to tetrahedral meshes, but still achieve the same accuracy [17].

A mesh density independence study was conducted with ten different mesh densities. They are presented in Table 1 (number of finite volumes is for basic geometry presented on Fig. 3b). Data for maximal y^{+} for each mesh density at different velocities are also presented in the Table 1.

Table 1: Mesh properties for basic geometry

Mesh	No. of finite volumes x1000	Maximal y^+ at different velocities		
		0.7 [m/s]	0.45 [m/s]	0.2 [m/s]
Mesh1	107	3.4	2.3	1.3
Mesh2	144	3.4	2.5	1.4
Mesh3	184	3.3	2.4	1.3
Mesh4	271	2.6	1.9	1.0
Mesh5	534	1.3	1.0	0.5
Mesh6	744	1.2	0.9	0.6
Mesh7	1159	1.1	0.8	0.5
Mesh8	1465	1.2	0.9	0.6
Mesh9	2409	1.1	0.8	0.5
Mesh10	5372	1.0	0.7	0.5

The average y^+ for Mesh4 using the $k-\varepsilon$ turbulence model is 1.01 at a velocity of 0.7 m/s. With the $k-\omega$ turbulence model, the y^+ remains at a similar level. The ratio of maximum to average y^+ is approximately 2.6 and remains consistent in all cases.

2.4 Boundary Conditions

In all calculations, it was assumed that the fluid flow is three-dimensional, turbulent, stationary, single-phase, and incompressible. Since there is no energy equation, the effects of natural convection and heat radiation are also neglected. Water was used as a working fluid with constant physical properties (temperature of 15.2 °C).

When the considered item is placed in a water loop, the water velocity in the channel is between 0.2 m/s and 0.7 m/s [18]. Thus, all calculations were made in seven discrete points with inlet boundary conditions with water velocity of 0.2 m/s to 0.7 m/s.

Symmetry boundary conditions (as presented in Fig. 3a in green) were applied for the 14×1/4, 14×1/2H, 14×1/2V, and 14×1 geometries. The 14×2, 14×3, and 14×6 geometries do not have symmetry boundary conditions determined.

3 EXPERIMENTAL ANALYSIS OF FLUID FLOW

The essence of the device for measuring the pressure difference on one channel of a plate heat exchanger, presented in Figure 4, is a set of two big containers of the same size, with one container facing the other, and a measuring sample clamped between them.

The test sample is made of two stainless heat plates brazed with copper, in the same way as conventional heat exchangers are made. Thus, the internal channel geometry is ensured to be the same as that of a conventional heat exchanger. The channel is processed in such a way that it can be clamped between large containers. Measurements were performed on three samples, with the width of the sample always being 19 cells and the length being 31, 24, and 16 consecutive cells.

Since the diameter of the large container is significantly larger than the diameter of the pipe through which the water enters it, the flow of water in big containers is extremely slow. Therefore, we can assume that the pressure field in the vessel is homogeneous. This means that the pressure and thus the velocity conditions are the same on all inlet surfaces, which enables a direct comparison with the results from the CFD simulation. A flow diverter is also installed at the water inlet, which directs the water toward the walls of the container and prevents part of the flow from entering the sample directly. The water is also mixed, which ensures a uniform water temperature.The pressure sensor is installed on the wall of the container, where no swirling of the flow is expected, and this also ensures a stable pressure measurement.

The water through the described assembly and pipe system is driven by a frequency-controlled pump. The water tank and expansion tank ensure constant pressure in the system. A constant temperature is maintained via a cooling heat exchanger. The temperature of the water is measured in the center of the container before the water enters the sample with an RTD temperature sensor. The flow is measured with a magnetic flow meter.

Stationary conditions were achieved during the measurement, with the recording of the measurement lasting no less than 30 s. All measured parameters were recorded simultaneously with a frequency of 5 Hz. The result is the average of all measured quantities. Measurements were taken at discrete points with water velocities of 0.2, 0.3, 0.4, 0.45, 0.5, 0.6, and 0.7 m/s through the inlet surfaces. Measurements of the pressure drop at a different water temperatures were also carried out to determine influence of temperature on pressure drop. Temeperatures were 15.2 °C, 16 °C, 18 °C, 20 °C and 25 °C with the maximum standard deviation of 0.19 °C.

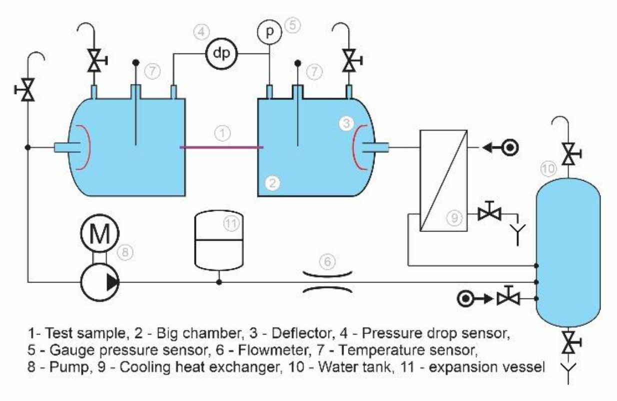

Figure 4: Test bench scheme

Measurement uncertainty is presented in Table 2.

Table 2: Uncertainties of the used measuring equipment

Parameter	Measurement method	Uncertainty range
Temperature	RTD	± 0.5 K
Flowrate	Magnetic flowmeter	± 1 % of reading
Pressure drop	Diaphragm compact dp sensor	± 1 % of reading

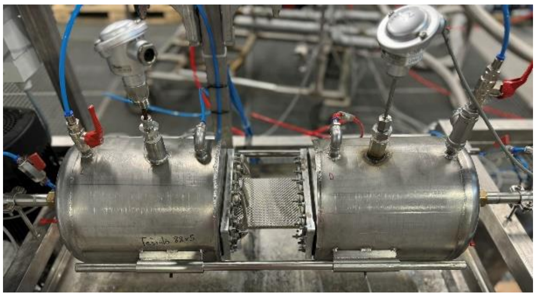

Figure 5: Photo of the big chamber assembly with the test sample clamped in between

4 RESULTS AND DISCUSSION

As presented, a mesh density independence study was conducted with ten different meshes, three boundary conditions and two turbulence models ($k-\varepsilon$ and $k-\omega$). The dependence of the results obtained by simulations on mesh density for the pressure drop between 9th and 10th cell marked on Fig. 3b is shown in Fig. 6. As a reference mesh number 4 (Mesh4) with 271000 finite volumes, which means approximately 10000 finite volumes per dimple cell, was used in this graph. This mesh was chosen to be used in all further calculations due to manageable number of mesh elements and the result difference from the grid-independent solution is a rational 3 % to 4 % for $k-\varepsilon$ and $k-\omega$ turbulence models and for all used velocities in the considered channel except the $k-\omega$ solution at water velocity 0.7 m/s, which no longer follows other solutions as presented in Fig 6. The considered XB12L heat plate contains approximately 1500 dimple cells, making it essential to carefully select the mesh density for calculations. This will ensure that the solutions can accurately represent conditions throughout the entire channel, or even across multiple channels, of the heat exchanger in the future analyses and computing resources will remain within reasonable boundaries.

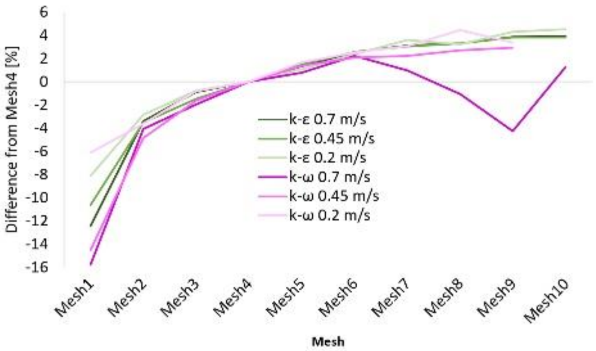

Figure 6: Dependence of numerical results on mesh density

The calculation result dependence of the width of the domain on the results of pressure drop is shown in Fig. 7. 14×3 geometry is used as a reference for the $k-\varepsilon$ turbulence model, and 14×1 geometry is used as a reference for the $k-\omega$ turbulence model.

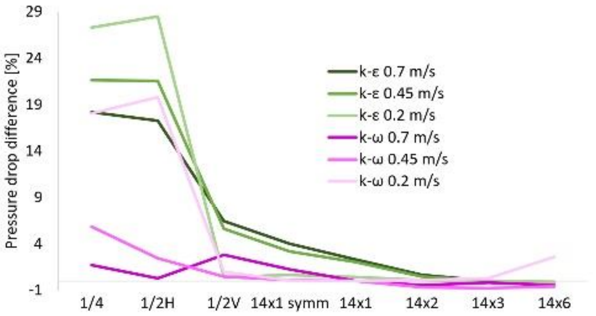

Figure 7: Dependence of numerical result on geometry width

To obtain results that are independent of domain geometry the minimum required length is 14 consecutive cells. The minimum required width is 1 cell for $k-\omega$ turbulence model (Fig. 3a, no. 1), and 3 parallel cells (Fig. 3a, no. 3) for $k-\varepsilon$ turbulence model. For the domains 1/4 and 1/2H (the cells are cut horizontally) the prediction of pressure drop is significantly higher than the pressure drop prediction on the rest of the calculations. For vertically sectioned cells, the 1/2V domain, the results are still high for $k-\varepsilon$ and closer to the measurement results for $k-\omega$ turbulence model. Geometries "14×1" in "14×1 symm" are the same in the "14×1 symm" had symmetry boundary conditions applied on the side wall. The "14×1" geometry had wall definition on all external surfaces and thus boundary mesh was also applied on side of the geometry. The results with symmetry boundary conditions are worse than those without. From the results, it can be seen that with the $k-\varepsilon$ turbulence model result stabilizes with an increasing number of parallel cells. With the use of $k-\omega$ turbulence model, the result does not change with an increasing number of parallel cells. The "14×3" domain was chosen as the most appropriate for $k-\varepsilon$ turbulence model and "14×1" domain was chosen as the most appropriate for $k-\omega$ turbulence model. The dependence of the pressure drop result on the distance (number of cells) from the inlet is presented in Fig. 8. The result on cells 9 and 10 is used as a reference in this graph.

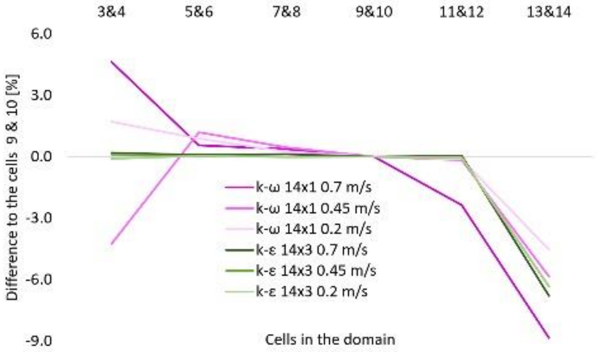

Figure 8: Dependence of the result of the pressure drop on the domain length

The pressure drop along the domain varies due to the inlet and outlet conditions. As shown in Fig. 8 it stabilizes on cells from 7 to 10. The pressure drop on cells 9 and 10 was chosen for validation with results from laboratory measurements.

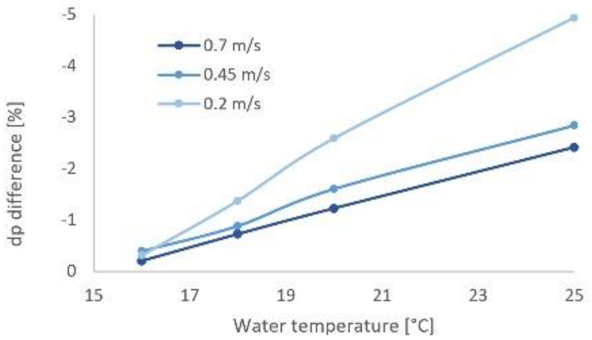

Figure 9: Impact of water temperature on pressure drop

The pressure drop is also influenced by water temperature, so laboratory measurements and analysis were conducted to determine how the fluctuating temperature impacts to pressure drop result.

The dependence of the result of pressure drop on the water temperature is shown in Fig. 9. Measurement result with water temperature of 15.2 °C is used as a reference.

From the graph, it is evident that the relationship in this range is linear, while the deviation increases nonlinearly as water flow decreases. The uncertainty in the measured pressure drop due to temperature fluctuations during the measurement is well below 0.5 %.

In Fig. 10 the laboratory measurement results on a sample of 31×19 cells are shown in the black curve. To compare measurement results and CFD results directly, the pressure drop measurement result should be divided by 31 and multiplied by 2 to obtain the pressure drop along the two cells – the same length as used in the CFD result (9th and 10th cells). In Fig. 10a there are also results from CFD simulations obtained by using $k-\varepsilon$ (green) and $k-\omega$ (pink) turbulence model. All the curves are associated with power-law functions. The aforementioned chart shows that prediction from $k-\omega$ turbulence model is high above while prediction from $k-\varepsilon$ turbulence model is relatively close to the measurement result.

The chart in Fig. 10B presents the relative difference between numerical calculations and laboratory results, where results on abscissa contain the results of laboratory measurements.

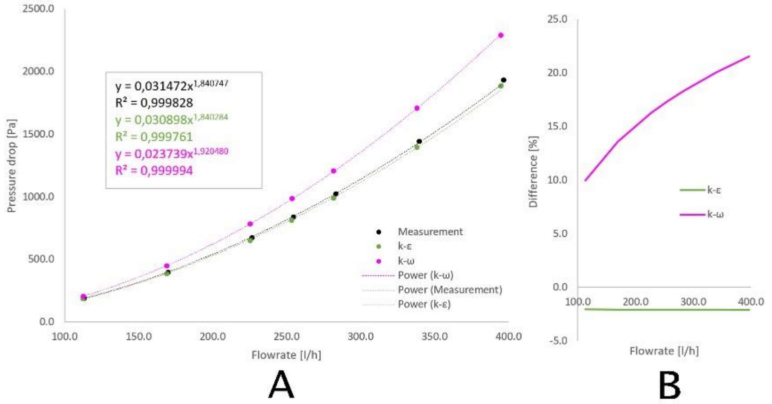

Figure 10: A - CFD and measurement results with associated power-law functions; B - relative difference between laboratory measurements and numerical solutions $k-\varepsilon$ and $k-\omega$ turbulence models

Fig. 11 illustrates the relative difference between the values calculated from the regression equations and the results from laboratory measurements or CFD simulations.

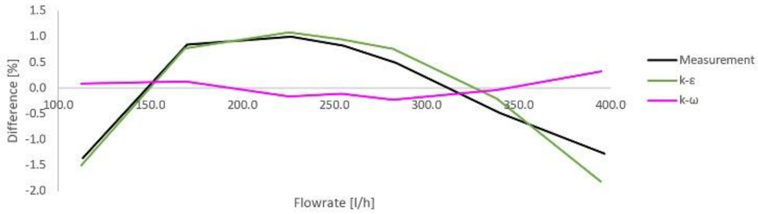

Figure 11: Relative difference between calculated values from regression equations and laboratory measurements and CFD simulations

Results obtained on samples with lengths of 24 and 16 cells are not presented in this paper. The pressure drop results for the sample with 24 cells are, on average, approximately 1 % higher, and for the sample with 16 cells, about 2 % higher compared to the longest sample. Given the intentional design for mounting the sample in the test bench, it can be assumed that the pressure conditions at each individual inlet or outlet surface are consistent.

As a result, the water velocities are uniform throughout the sample. The effect of the wall on the pressure drop is negligible due to the relatively large width of the test sample. Additionally, any impact from potential temperature inhomogeneity within the water is negligible.

The influence of sample length, however, is not negligible. We can assume that fluid flow in a big container is fully laminar, including just before it enters the sample. As the flow enters the cells, it doesn't immediately transition to a fully developed turbulent flow; several cells are required for this transition. Although the exact length of this inlet region is unknown, it is the same across all samples. It can also be noted that the pressure drop in this region is higher than in the fully developed turbulent flow within the sample. As a result, the impact of the inlet region on the pressure drop per cell is greater in shorter samples than in longer ones. This explains why the pressure drop per cell increases as the sample length decreases. Thus, the results from the longest sample were chosen as the most suitable.

The graph in Fig. 10A displays smooth curves that align well with the corresponding power-law functions, confirming that both the laboratory measurements and numerical calculations were performed correctly. The fit between the power-law functions and the measured data or CFD calculations is illustrated in the graph in Fig. 11. It can be concluded that all values fall within a ±1.8 % range.

The graph in Fig. 10A shows that the $k-\varepsilon$ model predicts an average pressure drop 2,1 % lower than the measured values. This difference is relatively consistent across the entire range, as clearly shown in Figs. 10B and 11. In contrast, numerical calculations using the $k-\omega$ turbulence model predict an average pressure drop difference of 16.7 % compared to the laboratory measurements, but this discrepancy varies with water velocity, as depicted in Fig. 10B. The agreement with the power-law curve is similar to the measurements, but with slightly inverse trend, as seen in Fig. 11.

Fig. 12 illustrates the volume of the domain where the water velocity is positive in the y-direction (from inlet to outlet). Fig. 12B shows the predicted volume from the $k-\varepsilon$ model, while Fig. 12A represents the prediction from the $k-\omega$ turbulence model. The region where the velocity in the y-direction is positive is referred to as the "live zone," while the region with negative y-direction velocity is termed the "dead zone." The shape of the "live zone" is visible in Fig. 12.

Fig. 10 shows that the $k-\omega$ turbulence model predicts, on average, a 18.8 % higher pressure drop compared to the $k-\varepsilon$ model. This may be due to the $k-\omega$ model predicting a significantly different "dead zone" behind the brazing point, as seen in Fig. 12. The "dead zone" predicted by the $k-\varepsilon$ model not only differs in shape but is also considerably smaller. With the $k-\varepsilon$ model, the dead zone comprises 22.3 % of the total volume, while with the $k-\omega$ model, it makes up 31.6 %. The size of the "dead zone" remains nearly constant across the analyzed velocity range.

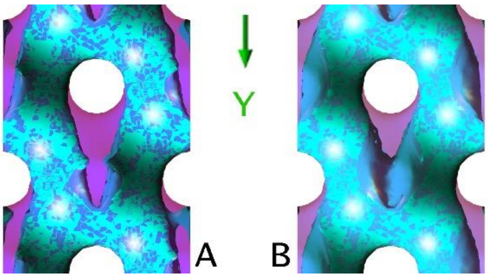

Figure 12: The volume of the water in which the velocity of water in the y-direction is positive: A - $k-\omega$ and B - $k-\varepsilon$

In this research, the use of the $k-\varepsilon$ turbulence model (for steady-state simulations) proved to be a robust and reliable method for predicting the pressure drop in the analyzed geometry. There was no significant convergence issues encountered, regardless of the mesh density used in the calculations. This is further supported by a study where the dependency of the results on mesh density was assessed, showing that the results gradually converged to the true value (Fig. 6). Additionally, the results remained stable throughout the domain (Fig. 8), allowing for a shorter domain, which in turn reduced computation time or allowed for a higher mesh density, resulting in improved accuracy. The behavior of the results across different velocities closely matched the measurement data (Figs. 10 and 11), providing reliable results comparable to laboratory measurements.

When using the $k-\omega$ turbulence model, it was not possible to obtain reliable solutions for longer samples. As the mesh density increased, the results became unpredictable, with unusual behavior along the domain and discrepancies in the results at different velocities compared to the measurements (Figs. 10 and 11). This suggests that the $k - \omega$ turbulence model produced fairly unreliable results. However, it is important to note that the flow in the channel is indeed turbulent at the given velocities. This is evident from the non-linear relationship between pressure drop and flow rate, which would otherwise indicate laminar flow.

As the mesh density increases, the solution approaches the true value due to the higher resolution in solving the equations. However, convergence issues become more frequent, indicating a highly turbulent flow. In the densest mesh, the turbulence becomes too intense, causing the time-independent solution to eventually fail.

It can be concluded that steady-state simulations using the $k - \omega$ turbulence model are not suitable for predicting the pressure drop in the analyzed heat exchanger. On the other hand, the $k - \varepsilon$ turbulence model proves to be a reliable choice for predicting pressure drop in channels formed by the dimple pattern heat plate.

5 CONCLUSION

In this article, a comprehensive analysis of the flow state in a plate heat exchanger featuring a dimple-pattern heat plate structure is presented. The research was conducted in two interconnected areas: laboratory experimentation and numerical simulation. Several laboratory measurements were performed on the channel of the XB12L heat exchanger and developed a novel methodology for conducting these measurements using big chambers. This new approach produced reliable results. It was confirmed that fluid flow in the channel is turbulent at all examined velocities.

On the numerical side, the optimal mesh density was identified, offering a favorable balance between result accuracy and computational resource usage. Additionally, the best numerical domain size for different turbulence models was determined. It was found that in steady-state simulations, the use of the $k - \varepsilon$ realizable turbulence model with Enhanced Wall Treatment is more suitable than the $k - \omega$ turbulence model.

Future research will focus on measuring the entire channel, including the velocity distribution in the area around the heat exchanger's porthole, and conducting simulations for the complete channel.

NOMENCLATURE

F	External body forces [N]
g	Gravitational acceleration [m/s^2]
p	Pressure, [Pa]
u	Velocity, [m/s]
S_m	Mass added to the continuous phase [kg]
u_τ	Velocity at a distance Δy, [m/s]
Δy	Distance from the wall, [m]
y^+	Dimensionless distance from the wall, [-]
μ	Dynamic viscosity, [kg/(ms)]
ρ	Density, [kg/m^3]
τ_ω	Wall shear stress, [Pa]
$\bar{\bar{\tau}}$	Stress tensor [-]

REFERENCES

[1] FERNANDES et al., C., “New Plates for Different Types of Plate Heat Exchangers,” *Recent Patents Mech. Eng.*, vol. 1, no. 3, pp. 198–205, 2012, doi: 10.2174/2212797610801030198.

[2] S. G. Kandlikar and W. J. Grande, “Evolution of Microchannel Flow Passages,” *Heat Transf. Eng.*, vol. 24, no. 1, pp. 3–17, 2003, doi: 10.1080/01457630390116077.

[3] W. W. Focke and P. G. Knibbe, “Flow visualization in parallel-plate ducts with corrugated walls,” *J. Fluid Mech.*, vol. 165, pp. 73–77, 1986, doi: 10.1017/S0022112086003002.

[4] H. M. Metwally and R. M. Manglik, “Enhanced heat transfer due to curvature-induced lateral vortices in laminar flows in sinusoidal corrugated-plate channels,” *Int. J. Heat Mass Transf.*, 2004, doi: 10.1016/j.ijheatmasstransfer.2003.11.019.

[5] A. G. Kanaris, A. A. Mouza, and S. V. Paras, “Flow and heat transfer in narrow channels with corrugated walls a CFD code application,” *Chem. Eng. Res. Des.*, vol. 83, no. 5 A, pp. 460–468, 2005, doi: 10.1205/cherd.04162.

[6] et al. Han, X. H., “A numerical and experimental study of chevron, corrugated-plate heat exchangers,” *Int. Commun. Heat Mass Transf.*, 2010, doi: 10.1016/j.icheatmasstransfer.2010.06.026.

[7] I. Gherasim, N. Galanis, and C. T. Nguyen, “Heat transfer and fluid flow in a plate heat exchanger. Part II: Assessment of laminar and two-equation turbulent models,” *Int. J. Therm. Sci.*, vol. 50, no. 8, pp. 1499–

1511, 2011, doi: 10.1016/j.ijthermalsci.2011.03.017.
[8] V. S. Gullapalli and B. Sundén, “Cfd simulation of heat transfer and pressure drop in compact brazed plate heat exchangers,” *Heat Transf. Eng.*, 2014, doi: 10.1080/01457632.2013.828557.
[9] A. K. Tiwari, P. Ghosh, J. Sarkar, H. Dahiya, and J. Parekh, “Numerical investigation of heat transfer and fluid flow in plate heat exchanger using nanofluids,” *Int. J. Therm. Sci.*, vol. 85, pp. 93–103, 2014, doi: 10.1016/j.ijthermalsci.2014.06.015.
[10] J. Lee and K. S. Lee, “Flow characteristics and thermal performance in chevron type plate heat exchangers,” *Int. J. Heat Mass Transf.*, 2014, doi: 10.1016/j.ijheatmasstransfer.2014.07.033.
[11] K. Sarraf, S. Launay, and L. Tadrist, “Complex 3D-flow analysis and corrugation angle effect in plate heat exchangers,” *Int. J. Therm. Sci.*, 2015, doi: 10.1016/j.ijthermalsci.2015.03.002.
[12] M. Piper, A. Zibart, J. M. Tran, and E. Y. Kenig, “Numerical investigation of turbulent forced convection heat transfer in pillow plates,” *Int. J. Heat Mass Transf.*, vol. 94, pp. 516–527, 2016, doi: 10.1016/j.ijheatmasstransfer.2015.11.014.
[13] S. S. Yogesh, A. S. Selvaraj, D. K. Ravi, and T. K. R. Rajagopal, “Heat transfer and pressure drop characteristics of inclined elliptical fin tube heat exchanger of varying ellipticity ratio using CFD code,” *Int. J. Heat Mass Transf.*, vol. 119, pp. 26–39, 2018, doi: 10.1016/j.ijheatmasstransfer.2017.11.094.
[14] et al. Al zahranI, S., “A thermo-hydraulic characteristics investigation in corrugated plate heat exchanger,” *Energy Procedia*, vol. 160, pp. 597–605, 2019, doi: 10.1016/j.egypro.2019.02.211.
[15] R. M. M. A. Muley, “Experimental Study of Turbulent Flow Heat Transfer and Pressure Drop in a Plate Heat Exchanger With Chevron Plates,” *J. Heat Transfer*, Feb. 1999, doi: 10.1115/1.2825923.
[16] ANSYS Inc, *ANSYS Fluent Theory Guide*, Release 19. Canonsburg, 2018.
[17] M. Peric and S. Ferguson, “The Advantage of polyhedral meshes,” *Dynamics - Issue 24, The customer magazine of the CD-adapco Group*, pp. 4–5, 2005.
[18] “Internal sources Danfoss Trata d.o.o.,” Ljubljana, 2022.

Environmental priorities in the circular economy: examples from iron-based technologies

Andreea Oarga-Mulec[1], Uroš Luin[1,2], Keith Skene[3,4], Matjaž Valant[1,2]

[1] University of Nova Gorica, Materials Research Laboratory, Vipavska 11c, Ajdovscina, 5270, Slovenia
E-mail: andreea.oarga@ung.si

[2]Green Technology Center, Erjavčeva ulica 2, Nova Gorica, 5000, Slovenia
E-mails: uros.luin@ung.si; matjaz.valant@ung.si

[3]Biosphere Research Institute, 5A The Den, Letham, Angus, DD8 2PY United Kingdom
E-mail: krskene@gmail.com

[4]The Living Laboratory, University of Dundee, Riverside Drive, Dundee, DD2 1QH, United Kingdom
E-mail: krskene@gmail.com

Abstract: *The circular economy (CE) framework is crucial for promoting resource efficiency and minimizing waste, but it cannot achieve its sustainability goals alone. To achieve a truly sustainable future, broader social, environmental and economic aspects need to be taken into account. Rather than separating biological and technological cycles, as the CE principles are depicted in the Ellen MacArthur Foundation's butterfly diagram (EMF, 2017), we propose an integrated approach that prioritises environmental aspects and includes a conceptual framework, socio-economic changes and implementation processes. It is crucial to re-evaluate the environmental aspects and strengthen their importance within the CE framework. Within this concept we present the case of iron, the most widely used metal, widely available compared to others and has been an essential part of societal development for more than 5,000 years. With its abundance, safety and electrochemical properties, iron is an ideal material for low-carbon energy technologies. We discuss how advanced iron-based technologies have a high potential to be successfully integrated into the CE, we evaluate different electrochemical energy storage systems and present advances in thermochemical Fe-Cl cycles for hydrogen production. An innovative thermal system for hydrogen production based on the thermochemical Fe-Cl cycle was evaluated in a life cycle assessment (LCA) study and shows the importance of choosing sustainable energy sources to minimise environmental impact. Sustainable production methods for iron are also analysed to demonstrate their potential to reduce the carbon footprint of the iron and steel industry. Finally, efforts should focus on minimising environmental impact and optimising resource recovery.*

Keywords: *circular economy, resource efficiency, sustainability, iron, hydrogen*

Article Classification: *Scientific paper*

1 INTRODUCTION

Material consumption is a major driver of environmental degradation, with humanity consuming around 20 billion tonnes of engineered materials per year, or 2.7 tonnes per person [1]. This consumption, driven by global development and economic growth, contributes to biodiversity loss, carbon emissions and resource depletion, particularly by extractive industries. Material consumption has been a key driver of industrial development, leading to a close relationship between resource exploitation and economic progress. From the early use of natural materials such as stone and bone to advanced materials such as steel, silicon and polymers, humanity's dependence on finite resources has shaped societal growth. However, this dependence poses a pressing problem: the need for sustainable practices to ensure that current and future generations can continue to thrive. CE proposes an alternative by redirecting material flows into loops through repair, reuse and recycling. However, the CE faces challenges, such as the high energy requirements of resource recovery and the ongoing need to extract new materials [2]. In addition, traditional CE models, such as the butterfly diagram [3], oversimplify real-world material use by separating biological and technical cycles, when in reality they are often intertwined. Recycling processes, which are crucial for extending product life, face obstacles such as energy consumption, material degradation and limited recycling pathways. As materials degrade over time, even recycled materials cannot fully replace virgin resources. In addition, the complexity of mixed-material products complicates recycling efforts.

Extractive industries, which are often excluded from CE models, play an important role in resource flows but contribute significantly to environmental pollution through waste and energy consumption. To achieve true sustainability, these industries need to be integrated into CE frameworks while recognizing the limits of recycling and material recovery. Modern CE initiatives aim to optimize the use of materials, and here we discuss iron, a metal that is widely available compared to others and has been an integral part of societal development for over 5,000 years. This paper reviews the challenges of CE and presents iron as a pertinent example of how sustainability issues can be addressed through smarter resource utilization.

2 MATERIALS AND METHODS

The analysis presented draws on current discussions and critically reviews on the CE framework and its application to iron-based technologies [4, 5]. Preliminary data from a Life Cycle Assessment (LCA) of a thermal hydrogen production prototype based on a thermochemical Fe-Cl cycle is included to provide complementary information to enhance the environmental perspective on the materials use and future scale-up. The innovative thermochemical cycle consists of the reaction between cost-effective materials such as iron and hydrochloric acid for the generation of hydrogen. Details of the chemistry of the thermochemical cycle for hydrogen production system are given in detail in [6] and other necessary data were provided by the stakeholder. This preliminary LCA refers to the construction phase of the system, including the manufacture of materials, building components and devices. The construction of the building has not been considered as it is assumed that the system will either be integrated into an existing industrial facility or built as a stand-alone unit. While this study focuses on the construction phase, the LCA analysis will be later extended to the use phase, taking into account electricity consumption, emissions from thermal processes during system operation. For the LCA analysis, we used SimaPro 9 (PRé Sustainability,The Netherlands) in accordance with ISO 14040, ISO 14044 and EN 15804 and the Ecoinvent v3.9 database to model data representing all possible inputs.

3 RESULTS AND DISCUSSION

3.1 Circular economy and environmental prioritization

The critical review emphasized that an effective framework for the CE must prioritize environmental sustainability by focusing on the conservation of natural resources and the protection of ecosystem health (Table 1). Rather than viewing the environment as a sink for waste and recycled materials, the CE should focus on minimizing damage and promoting regeneration. An important aspect of this is nutrient management, as the uncontrolled release of recycled biological materials into ecosystems can cause significant disruption and impact the ecosystem services. These nutrient flows, if poorly managed, can trigger nonlinear ecological responses, such as tipping points. Therefore, strategies to effectively manage nutrient cycling are critical to maintaining ecological balance within the CE framework. In addition to environmental aspects, the CE must also include socio-economic dimensions. This requires policy reforms, changes in consumer behavior and greater transparency within supply chains. While resource efficiency is important, it is equally important to consider the cultural, social and economic factors that influence sustainability. Transparent supply chain networks combined with changing consumer behavior are essential for effective implementation of CE. The role of consumers, market dynamics and corporate accountability are central to driving the necessary changes, supported by policies that promote circular consumption patterns.

The CE also needs to move beyond a narrow focus on material flows to a systems-level approach that recognizes the interconnectedness of economic, social and environmental systems. Relying solely on recycling and resource efficiency is not enough to achieve true sustainability. Instead, a broader framework is needed that incorporates environmental responsibility, societal values and coherent policies. In addition, this broader approach must include the raw materials industry and develop strategies for resource recovery and circular product design to ensure that sustainability principles are applied throughout the life cycle of materials.

Table 1: Comparison of current circular economy framework and proposed integrated approach

Objective	**Current CE framework**	**Proposed integrated approach**
Environmental consideration	Assumes unlimited capacity for biological materials absorption in ecosystems	Considers biophysical constraints
Separation of cycles	Divides biological and technical cycles	Integrates cycles, with focus on their interdependence
Socio-economic aspects	Limited integration	Incorporates conceptual framework for socio-economic changes and implementation processes
Approach to restoration	Focuses on circular use of materials	Includes appropriate restoration to natural reserves, aligning with ecological balance
Visual representation	Butterfly diagram separating cycles	New model emphasizing fluid flow across the biophysical environment

3.2 Iron in emerging energy technologies

Iron is an example of the complexity of CE. Its abundant availability and established recycling processes make it a promising material for circular initiatives. Table 2 summarizes the electrochemical properties of iron compared to other elements for low-carbon energy technologies. For example, iron outperforms zinc and nickel in terms of specific capacity, with a range between 960 and 1439 mA h g^{-1} depending on its oxidation state (Fe^{2+} or Fe^{3+}). However, it underperforms in comparison with aluminum and lithium which exhibit specific capacities of 2980 mA h g^{-1} and 3,861 mA h g^{-1}, respectively. Despite these capacity limitations, iron has other notable properties that increase its suitability for large-scale energy storage applications. Its low cost ($0.12/kg), high end-of-life (E-o-L) recycling rate of 62% and low toxicity contribute to its sustainability, especially when compared to lithium, which has moderate toxicity and a much lower recycling rate of less than 5%, it faces significant challenges regarding environmental impact and has significant resource depletion concerns. While aluminum is also a competitive material due to its higher specific capacity and wide availability (8.2% in the Earth's crust), its recycling processes are energy-intensive, which poses a challenge for large-scale circular applications. From a technical point of view, iron can be electro-reduced by cold electrolysis, whereas aluminum cannot be electroplated from aqueous solutions. These properties make iron a promising material for large-scale energy storage, even if its use in aqueous rechargeable batteries is still limited by passivation, hydrogen evolution and low efficiency [5].

Table 2: Comparative properties of iron and selected elements used in low-carbon energy technologies [5, 7].

Element (electrons transferred)	Price ($ per kg)	Abundance (%)	Specific capacity (mA h g^{-1})	Volumetric capacity (mA h cm^{-3})	Redox potential (V)	E-o-L recycling rate (%)	Toxicity
Fe (2)	0.12	5.300	960	7557	-0.45	62	Low
Fe (3)			1439	11 328			
Al (3)	2.73	8.200	2980	8046	-1.66	51	Low
Li (1)	14.56	0.002	3861	2062	-3.04	<5	Moderate
Zn (2)	3.12	0.004	820	5845	-0.76	45	Medium
Mg (2)	19.56	2.000	2205	3833	-2.37	13	Very low
Cu (2)	10.71	0.007	843	7558	+0.34	55	High
Ni (2)	20.56	0.009	913	8136	-0.26	16	High

The iron and steel industry, which is responsible for a third of global CO_2 emissions, faces challenges in the transition to low-carbon processes [8]. While this transition is complex and slow, driven by innovation and climate action, it is essential to reduce future emissions. Sustainable production methods such as hydrogen-based iron reduction and electrolysis deserve more attention as we move towards a decarbonized energy future, with a focus on reuse, remanufacturing and regenerative materials. For example, processes such as direct iron reduction (DRI) using hydrogen (H_2DRI), methane (CH_4DRI) or DRI electric arc furnace (DRI-EAF) show potential to reduce CO_2 emissions by 6%, 97% and 50% respectively compared to conventional blast furnace technologies [9, 10]. Iron extraction processes such as molten oxide electrolysis and electrowinning have shown a CO_2 reduction potential of up to 96% and 95% respectively [11, 12]. Advances in energy storage and battery technology are rapidly increasing and the versatility of iron has led to its application in new energy technologies that are scalable, environmentally friendly and have a high energy density. Examples of iron-based chemical cycles in energy storage and recent developments in this field show that iron redox flow batteries can reach a maximum energy efficiency of 87%, iron-air batteries of 94% or emerging iron batteries such as battolyser of 90% [13].

However, modern iron-based technologies still have environmental impacts (e.g. high-water demand, energy consumption, carbon emissions during transport), especially in their production processes. These technologies fulfil several sustainability criteria, but their own environmental impacts need to be further assessed.

3.3 LCA in development of sustainable innovations

LCA is an effective tool that guides sustainable technology innovation on three levels: (1) it identifies environmental impacts at early stages; (2) it supports optimization as technologies evolve by addressing key issues; and (3) once optimization is complete, LCA validates the environmental benefits achieved and ensures that final products meet sustainability targets [14]. The preliminary results of the LCA analysis of the thermal hydrogen production prototype show the environmental impacts of materials, particularly the use of steel in the thermal decomposition and regeneration module, due to the use of corrosive substances (HCl), but also due to the use of aluminum and Refractory Ceramic Fiber (RCF) insulation, which drives high contributions to climate change and metal depletion. On the other hand, there are minimal impacts for marine eutrophication, natural land transformation, and ozone depletion and a net positive impact on water resources, as evidenced by the negative water depletion values (-0.0002 m^3 for the hydrogen production module and -0.012 m^3 for the thermal decomposition module). The next steps in this research will focus on scaling up the prototype which offers the potential to improve material efficiency, reduce environmental impacts per unit of hydrogen, and optimize production processes [15]. LCA becomes even more critical at scale, as it helps identify key areas where resource use can be reduced and recycled, ensuring that sustainable materials and designs are integrated early in the innovation process. Scaling also allows for cost reduction and enhanced sustainability, particularly through material substitution and improved recycling technologies, that fit into the circular economy goals.

4 CONCLUSION

This study discusses the importance of integrating CE principles to drive sustainable innovations, particularly in material use. There is a critical need to prioritize environmental sustainability considering the resource conservation, ecological protection, and promoting regenerative practices, while also integrating socio-economic factors such as policy reforms and consumer behavior. The electrochemical properties, recyclability and low environmental impact of iron gives it significant potential for use in low-carbon energy technologies, as in the example of thermal hydrogen production prototype. However, the hydrogen production system revealed high environmental impacts, especially from the steel use. Scaling up this system offers opportunities to improve material efficiency, reduce environmental burdens, and improve resource management, proving that research on specific technologies combining sustainability aspects with particular technical issues is greatly needed.

REFERENCES

[1] ASHBY, M. F. *Materials and the environment eco-informed material choice. 3rd Edition*. Butterworth-Heinemann, Elsevier, 2021.

[2] YANG, M., CHEN, L., WANG, J., MSIGWA, G., OSMAN, A.I., FAWZY, S., ROONEY, D.W. and YAP, P.S. Circular economy strategies for combating climate change and other environmental issues. *Environmental Chemistry Letters*. 2023, **21**(1), 55-80.

[3] EMF. What is the Circular Economy? 2017, https://www.ellenmacarthurfoundation.org/circular-economy/what-is-the-circular-economy, accessed 24 September 2024.

[4] SKENE, K.R., and OARGA-MULEC, A. The circular economy: the butterfly diagram, systems theory and the economic pluriverse. *Circular economy: an applied scholarly journal on circular economy*. 2024, **2**(3), 1-25.

[5] OARGA-MULEC, A., LUIN, U. and VALANT, M. Back to the future with emerging iron technologies. *RSC advances*. 2024, **14**(29), 20765-20779.

[6] VALANT, M. and LUIN, U. Chemistry of the iron-chlorine thermochemical cycle for hydrogen production utilizing industrial waste heat. *Journal of Cleaner Production*. 2024, **438**, p.140681.

[7] NUSS, P., POHJALAINEN, E., BACHER, J., MANOOCHEHRI, S., d'ELIA, E., MANFREDI, S. and JENSEN, P. Towards more sustainable management of material resources in Europe, Publications Office of the European Union. 2022, *JRC technical report*, https://doi.org/10.2760/57936.

[8] CHANG, Y., WAN, F., YAO, X., WANG, J., HAN, Y. and LI, H. Influence of hydrogen production on the CO2 emissions reduction of hydrogen metallurgy transformation in iron and steel industry. 2023, *Energy Reports*, **9**, 3057-3071.

[9] LING, J., YANG, H., TIAN, G., CHENG, J., WANG, X. and Yu, X. Direct reduction of iron to facilitate net zero emissions in the steel industry: A review of research progress at different scales. 2024, *Journal of Cleaner Production*, p.140933.

[10] HORNBY, S. and BROOKS, G. Impact of Hydrogen DRI on EAF Steelmaking, https://www.midrex.com/tech-article/impact-of-hydrogen-dri-on-eaf-steelmaking/, accessed September 12, 2024.

[11] DRAXLER M., SORMANN, A., KEMPKEN, T., HAUCK, T., PIERRET, J.C., BORLEE, J., Di DONATO, A., De SANTIS, M., WANG, C. *Green steel for Europe - technology assessment and roadmapping*. Green Steel for Europe Consortium, Mach, 2021.

[12] WANG, X., YANG, H., YU, X., HU, J., CHENG, J. and JING, H. Research progress in the preparation of iron by electrochemical reduction route without CO_2 emissions. 2023, *Journal of Applied Electrochemistry*, **53**(8), 1521-1536.

[13] NAMBAFU, G.S., HOLLAS, A.M., ZHANGS, S., RICE, P.S., BOGLAIENKO, D., FULTON, J.L., LI, M., HUNAG, Q., ZHU, Y., REED, D.M. LIU, X., LI, T., YUANG, Z. and LI, X. Low-cost all-iron flow battery with high performance towards long-duration energy storage. 2022, *Journal of Energy Chemistry*, **73**, 445-451.

[14] van der GIESEN, C., CUCURACHI, S., GUINÉE, J., KRAMER, G.J. and TUKKER, A. A critical view on the current application of LCA for new technologies and recommendations for improved practice. 2020, *Journal of Cleaner Production*, **259**, p. 120904.

[15] ROHILLA, T. and KUMAR, M. Challenges with sustainable green hydrogen production: role of materials, design, multi-scale modeling, and up-scaling. In: P. SINGH, A.K. AGARWAL, A. THAKUR, R.K. SINHA, ed. *Energy, Environment, and Sustainability*. Singapore, Springer, 2024, https://doi.org/10.1007/978-981-97-1339-4_19

Implementation of a computerised system in a pharmaceutical laboratory

Kristian Peklaj[1], Mitja Cerovšek[1]

[1]*Faculty of Industrial Engineering Novo mesto, Šegova ulica 112, 8000 Novo mesto, Slovenia*
E-mails: mitja.cerovsek@fini-unm.si, kristian.peklaj@gmail.si

Abstract: *In this paper, we focused on the process of setting up a computerised system in pharmaceutical laboratory. The challenge presented by the topic is not in the technical solution, but in compliance with the regulatory requirements that computerised system in the pharmaceutical environment must achieve. The purpose of this work is to present the process of introducing a computerised system into a highly regulated pharmaceutical environment. The process includes a validation approach for which we have prepared the necessary steps, taking into account the latest GAMP 5 good practice guidelines for automated computerised systems. The integrity of the data generated by the computerised system is crucial and in our case, it is controlled by following the ALCOA++ guidelines. By examining the relevant European legislation, we extracted what the computerised system must achieve and in what way it must be implemented in a regulated laboratory environment. We presented the necessary steps and documents that must be prepared or delegated to the supplier when implementing the system. Carrying out all the steps in the sequence presented is mandatory for releasing such a system into regular use. We limited the practical part of the task to a system that fits to the laboratory environment and will be implemented according to the approach dictated by the GAMP 5 guidelines.*

Keywords: *ALCOA++, good practice, pharmacy, data integrity**,** GAMP 5, computerized system, validation*

Article Classification: *Scientific paper*

1 INTRODUCTION

The pharmaceutical industry is a highly regulated environment where the implementation of a computerized system is a rather complex process. Any possible error that occurs in the process of drug manufacturing or drug testing can have a negative impact on patients who consume pharmaceutical products. Inadequate operation of a computerized system in the pharmaceutical industry can lead to serious consequences. Therefore, it must be ensured that such a system is properly tested and fully validated before it is released to production. Computerized systems are considered complex equipment for a reason, as systems have become really powerful in recent years and offer endless possibilities for use, analysis, data collection, and reporting of results. These endless possibilities of use also mean endless possibilities for errors to occur. Due to the difficulty and complexity of today's computerized systems, their validation is a tough challenge. Therefore, validation must be approached very strategically, with a clear goal of what is expected from the system. An important role in the validation process is played by the personnel responsible for system validation. Validation of the computerized system is usually carried out by experienced expert teams who have been working in a regulated pharmaceutical environment for a long time. It is specific knowledge that is difficult to acquire in formal education.

The research question of this study is: How can the integration of European and U.S. regulatory frameworks, including GAMP 5 and ALCOA++ guidelines, improve the validation process of computerized systems in the pharmaceutical industry, ensuring compliance with Good Manufacturing Practices (GMP), Good Laboratory Practices (GLP), and data integrity (DI) standards?

This question emerges from the detailed exploration of various regulations and guidelines (EudraLex, European Pharmacopoeia, U.S. Pharmacopeia, GAMP 5, ALCOA++, etc.), their role in ensuring compliance, and their application in the validation, documentation, and operation of computerized systems in the pharmaceutical sector. It focuses on understanding how these guidelines and regulations contribute to achieving regulatory compliance, improving DI, and ensuring the proper functioning of systems impacting the quality of results and documentation.

The purpose of this research is to present the validation documentation required for establishing a new computerized system in accordance with the GAMP 5 guidelines. The research focuses on the leveraging method, which allows utilizing existing, verified data (e.g., supplier documentation, system specifications) to streamline the validation process, especially for components that have been previously qualified. The study emphasizes the importance of supplier assessment to ensure that the supplier meets the necessary requirements for DI and quality management. It also explores various documents necessary for validation, such as User Requirements Specifications (URS), risk assessments, system specifications, and QP. Additionally, the research highlights the significance of structured, traceable documentation, such as the Traceability Matrix (TM), to ensure proper alignment of requirements, specifications, and testing. Overall, the goal is to provide a clear framework for the validation of computerized systems, ensuring compliance with regulatory standards and maintaining system integrity throughout its lifecycle.

1.1 Description of the methodology

The introduction of the computerized system must be carried out in accordance with the legislation and pharmacopoeias that must be followed in order to produce pharmaceutical products. Using the compilation method, the literature on the requirements of European legislation, the European and American Pharmacopoeia, and relevant guidelines was reviewed. From the obtained information, it was determined whether adherence to the guidelines meets the regulatory requirements. At the same time, innovative approaches in the guidelines were explored that could optimize the complex validation of computerized systems.

The text analyses several regulatory requirements and guidelines relevant to the implementation, validation, and documentation of computerized systems in the pharmaceutical industry, primarily within the European Union and the United States. The key points are:

- European Legislation,
- European Pharmacopoeia (Ph. Eur.),
- U.S. Pharmacopeia (USP) and CFR,
- GAMP 5 Guidelines,
- ALCOA++ Principles,
- FDA Warning Letters,
- Comparison of other studies.

The analysis emphasizes the importance of adhering to regulatory frameworks and guidelines to ensure the proper validation, documentation, and management of computerized systems in pharmaceutical manufacturing and laboratory environments.

1.2 Hypotheses

During the review of the available literature and work in the company’s laboratory environment, the following hypotheses were developed:

- Hypothesis 1: At implementation of the new system the validation approach for laboratory system is the same as the production system.
- Hypothesis 2: At implementation of the new laboratory system there are possible process improvements and simplifications of the validation approach.

2 LITERATURE REVIEW

The most important requirements that are mandated by the regulation and must be considered in every project involving the implementation of a new computerized system have been extracted. Taking into account good practices from the GAMP 5 and ALCOA++ guidelines, possible simplifications and improvements of the validation process were presented to the reader.

2.1 Overview of European legislation

For pharmaceutical companies operating in the territory of the European Union, it is first and foremost important that they comply with European legislation. In the chapters below, the content of the directives that directly or indirectly refer to the computerized system discussed in this work is described.

Directive 2001/83/EC establishes the Community code for medicinal products for human use. It mandates that all processes in the pharmaceutical industry be validated and that equipment used in manufacturing be detailed and validated. Equipment must also be accessible for inspection by authorized personnel. Manufacturers holding a license to produce drug products must adhere to GMP guidelines [1].

The GMP requires compliance with Commission Delegated Regulation (EU) No 1252/2014, which supplements Directive 2001/83/EC for active substances in medicinal products. Manufacturers must adhere to GMP principles, maintain Good Documentation Practice (GDP), and implement a quality risk management system. All production activities must be documented in real-time according to GDP, with proper batch records kept. Additionally, equipment must be properly designed and its use carefully planned [2].

Commission Directive (EU) 2017/1572 updates Directive 2001/83/EC on Good Manufacturing Practice (GMP) for medicinal products for human use, replacing the outdated Directive 2003/94/EC. It applies to licensed manufacturers and importers, requiring member states to conduct regular inspections to ensure GMP compliance. The directive mandates proper planning and validation of premises and equipment to ensure product quality and minimize errors. A robust documentation system must be in place to guarantee DI, with data processing systems validated for proper storage and accessibility. Electronic data must be protected from unauthorized access, loss, or damage, with backup copies and an audit trail. Deviations from procedures and product issues must be documented and investigated.

Additionally, any significant changes or new processes affecting production must be validated [3].

Directive 2004/9/EC requires EU member states to inspect laboratories for compliance with GLP as outlined in Directive 2004/10/EC. The goal of GLP is to ensure consistency across member states, allowing test results from one lab to be accepted by others. Inspections focus on ensuring proper record-keeping for equipment maintenance, calibration, and validation. Raw data from automated systems must be properly documented and archived, with any changes justified and signed by authorized personnel. Computer systems must be secure, accurate, and protected against unauthorized changes. Malfunctions must be investigated and documented. Study results should be complete and consistent with raw data. Access to archived data is restricted to authorized personnel, and all access is logged. Additionally, equipment must be properly calibrated, maintained, and serviced during inspections [4].

Directive 2004/10/EC aims to harmonize regulations related to GLP for non-clinical safety testing of various products. It emphasizes the use of validated computerized systems for data acquisition, storage, and environmental control, requiring these systems to be properly designed, maintained, and calibrated. All data must be accurately recorded, signed, and dated by the responsible person. Proper documentation of equipment maintenance, calibration, and system validation is also required to ensure compliance with GLP standards [5].

In order to meet the requirements of the directives examined in the previous chapters, the European Commission prepared a collection of rules and regulations governing drug products in the European Union called EudraLex. EudraLex consists of ten parts, with Volume 4 being relevant to this case, as it contains the GMP Guidelines for medicinal products for human and veterinary use. Volume 4 includes several chapters that were studied in more detail:

- Chapter 3 – Premise and Equipment,
- Chapter 4 – Documentation,
- Annex 11 – Computerised Systems,
- Annex 15 – Qualification and validation [6].

2.2 Overview of the European Pharmacopoeia

The Ph. Eur. is a comprehensive document available online with the appropriate license. While reviewing the introductory pages, it was noted that the general working principles are described in individual regulatory guidelines, which are freely available on the European Directorate for the Quality of Medicines & HealthCare (EDQM) website [7]. Therefore, during further research between the chapters in the Ph. Eur., no concrete regulations on computerized systems, the validation of computerized systems, or the qualification of laboratory equipment were detected. The research was then continued within the EDQM regulatory guidelines. The first relevant document discovered was entitled "Qualification of equipment - basic document." This document aims to harmonize the requirements of the ISO/IEC 17025 standard for testing and calibration laboratories within the network of official medicine control laboratories (OMCL). It consists of four brief chapters:

- Selection of instruments and suppliers,
- Installation and release for use,
- Periodic and motivated instrument checks,
- In-use instrument checks [7].

The validation of computerized systems is essential to ensure DI and the proper functioning of systems impacting the quality of results, document control, and data storage. The validation guidelines categorize systems into exempted, simple, and complex systems, with different validation requirements for each. For all systems, manufacturers must maintain an inventory including system identification, purpose, validation status, storage location, and responsible person. Systems must be validated before use to ensure they meet the user’s requirements. The scope of validation depends on system complexity, with more complex systems requiring extensive testing. If a supplier is part of a verified program, OMCL may rely on their tests, reducing the validation scope to Performance Qualification (PQ). A Qualification Plan (QP) outlines the validation activities, including review of URS, test strategy, and performance criteria. The plan must be approved by relevant stakeholders before execution. If additional testing or revisions are required, the plan can be updated. The validation process includes several stages, such as Installation Qualification (IQ), Operational Qualification (OQ), and PQ for complex systems, and culminates in a Qualification Report (QR) that confirms the system's suitability for use. Deviations during validation must be documented and assessed for their impact. Validated systems require periodic inspections to maintain their validated state. They must be protected against intrusions and physical damage (e.g., fire, power outages) and accessible only to authorized personnel with personalized login credentials. Audit Trails (AT) must record system events, such as user logins, data changes, and system activities, and cannot be disabled by users. For systems supporting electronic signatures, a declaration must confirm their equivalence to manual signatures. DI must be ensured, including regular backups, secure storage, and a clear recovery policy in case of system failure. Software versions should be archived, and change control procedures must be documented for system updates or modifications. Major changes, such as replacing hardware, require full re-validation. Finally, user training is mandatory, both for initial system use and for updates or changes, ensuring users are informed about relevant system changes and procedures. [8].

2.3 Review of U.S. Pharmacopeia

The American non-profit organization U.S. Pharmacopeia (USP) prescribes the use of the Code of Federal Regulations (CFR). The CFR is publicly available online, where the contents of all 50 titles covered by the Code can be accessed. Title 21, which pertains to the field of food and medicine, is relevant to their study. Title 21 includes over 1,400 parts of the code that prescribe requirements to be observed in the field of food and drugs. Several chapters are therefore relevant to their study. Related to GMP, the following addresses can be found:

- Part 210 - Current good manufacturing practice in manufacturing, processing, packing, or holding of drugs,
- Part 211 - Current good manufacturing practice for finished pharmaceuticals,
- Part 58 - Good laboratory practice for nonclinical laboratory studies,
- Part 11 - Electronic records; electronic signatures [9].

The review of Part 58 and Part 11 regulations focuses on adherence to GLP, excluding clinical laboratory studies. The regulations require that equipment be clean, calibrated, validated, and well-maintained. There must be proper procedures for equipment use, and personnel must be trained. Test data must be properly stored, with access limited to authorized personnel. Additionally, equipment used for data generation or environmental control must be appropriately designed and have sufficient capacity to function properly [10]. Part 11 regulates computerized systems, focusing on electronic records and electronic signatures. It is required by the FDA for all regulated products. The regulations are divided into sections that cover:

Subpart B – Electronic records:

- 11.10 Controls for closed systems (13 requirements),
- 11.30 Controls for open systems (1 requirement),
- 11.50 Signature manifestations (5 requirements),
- 11.70 Signature/record linking (1 requirements) [11].

Subpart C – Electronics signatures:

- 11.100 General requirements (5 requirements),
- 11.200 Electronic signature components and controls (7 requirements),
- 11.300 Controls for identification codes/passwords (5 requirements) [12].

It is necessary to include these requirements in the URS document and thus require supplier to comply with 21 CFR Part 11.

2.4 Review of guidelines

In order to optimally integrate the findings from the previous chapter into consideration, the guidelines were also examined. The findings of the study should ensure compliance with regulatory requirements. Several different guidelines were studied. The focus of the study is on the GAMP 5 guidelines, which ensure the regulatory compliance of computerized systems, and the ALCOA++ guidelines, which ensure the achievement of the appropriate level of DI and GDP,

2.4.1 GAMP 5

GAMP 5 guidelines provide best practices for managing computerized systems throughout their lifecycle, which is divided into four phases: concept, project, operation, and retirement. In the concept phase, companies evaluate automation opportunities, assess benefits and drawbacks, and decide whether to proceed with purchasing the system. A Initial Risk Assessment (IRA) is required before moving to the project phase, which includes planning, preparing technical specifications, configuring the system, and creating test documentation. After successful validation, the system is confirmed for regular use. The guidelines emphasize risk reduction, and traceability of activities, particularly for more complex systems. Roles and responsibilities of both the buyer and supplier are also clearly defined throughout the lifecycle [13].

GAMP 5 categorizes computerised systems into 4 categories that differ from each other in configurability and customization (the higher the category, the higher level of configurability and customization the computerised system achieves). GAMP 5 thus describes 4 different categories of computerised systems:

- Category 1 - Infrastructure Software,
- Category 3 – Standard system components,
- Category 4 – Configurable components,
- Category 5 – Applications and components that are custom made [13].

Individual systems can consist of one or more GAMP 5 categories. Companies usually categorize the system according to the component that achieves the highest level [13]. Figure 1 shows an example of a computerised system that contains all 4 categories and would thus be categorized as GAMP category 5.

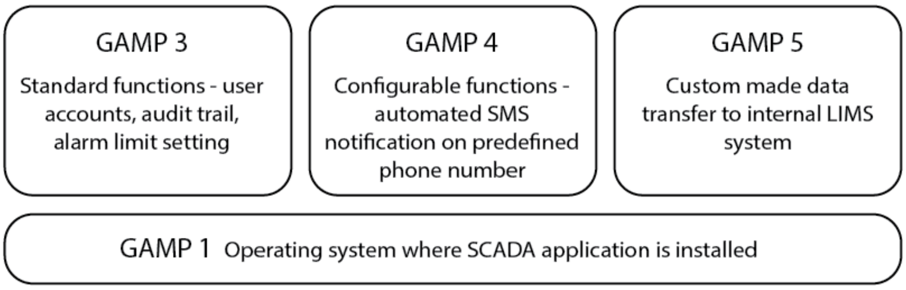

Figure 1: Example of a computerised system categorization into category 5 [13]

Before using computerized equipment, appropriate verification must be carried out depending on the category. For categories 4 and 5 components, it is crucial to thoroughly evaluate the supplier. Due to the complexity of these systems, the leveraging method is applied, using the supplier's technical specifications and test documentation.

The V-model (see figure 2) outlines the steps and validation results required for a successful validation strategy. It defines the necessary specifications and tests for each phase, ensuring the creation of appropriate documentation. The model also allows for the involvement of both the supplier and the customer throughout the process [14].

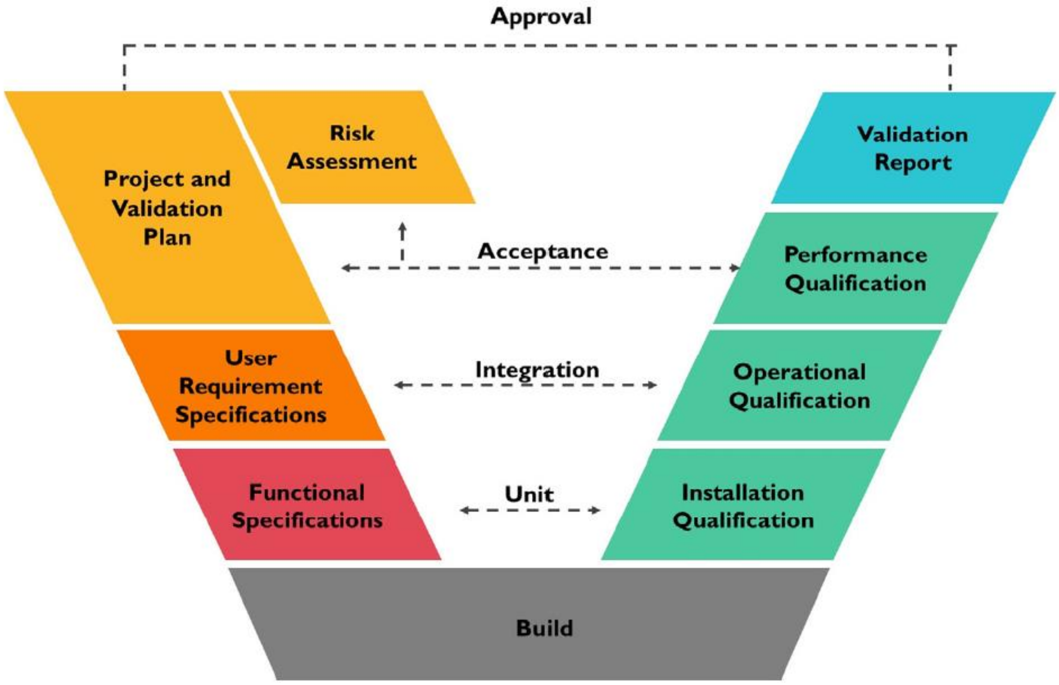

Figure 2: GAMP 5 V-model [14]

One of the first authors to mention the validation of computer systems as early as 1979 is Boehm R., who is the author of the work "Guidelines for Verifying and Validating Software Requirements and Design Specifications." In the aforementioned work, he presents the so-called V-model, which can be found in the GAMP 5 guidelines as a basis today [15].

The release of the system into use is approved by the regulated company when the adequacy of the system is confirmed by the successfully implemented and completed planned testing phases. Before handing over the system to the user, the project team must prepare instructions for working with the system, instructions for maintenance and the process of maintaining the validated state of the system. The guidelines also describe in detail the phase of operation and retirement, which are not yet relevant to their topic. A special chapter of the GAMP 5 guidelines is dedicated to suppliers and developers of computerised systems, with useful guidelines and instructions on what expectations regulated companies have of them.

2.4.2 ALCOA++

High level of DI is the basis for manufacturing pharmaceutical companies, as in this way to guarantee the veracity of data, identity, product safety, efficiency and a high level of quality [16]. The acronym ALCOA was first introduced by the FDA in the 1990s with the aim of directing regulated industries to achieve compliance with the FDA's DI requirements. ALCOA's guidelines cover electronic, written and hybrid data and are critical to the provision of GDP [17]. The acronym consists of the initials of the principles:

- **A**ttributable,

- **L**egible,
- **C**ontemporaneous,
- **O**riginal,
- **A**ccurate [18].

In 2010, 4 more principles called CCEA were added to the ALCOA guidelines. This is how the abbreviation ALCOA-CCEA was born, which was later renamed to ALCOA+. The abbreviation CCEA is a composite of the initials of principles [17]:

- **C**omplete,
- **C**onsistent,
- **E**nduring,
- **A**vailable when needed [18].

Not long ago, on September 10, 2023, the European Medicines Agency (EMA) added a tenth principle to the ALCOA+ abbreviation in its guidelines for computerized systems and electronic data in clinical studies. This principle was denoted by an additional '+' in the abbreviation, resulting in ALCOA++ [18]. The tenth principle of the guidelines stands for:

- Traceable.

Data must be traceable throughout the data lifecycle. All changes to data, metadata must be traceable, must not obscure the original information and must be explained if necessary. Changes should be documented as part of metadata (e.g. audit trail) [18]. The regulation does not mention compliance with the ALCOA++ principles, but the requirements according to individual principles are still found. Table 1 shows where in the European regulation the requirements to achieve the first five principles of ALCOA++ can be found and was prepared by the organization ECA Academy.

Table 1: First five principles of ALCOA++ in European Regulation [19]

	EudraLex Volume 4, 1.del **4. Documentation** **6. Quality control**	**EudraLex Volume 4, 2. del** **5. Process equipment** **6. Documentation and records**	**EudraLex Volume 4, Annex 11**
A	[4.20, c & f], [4.21, c in I], [4.29, e]	[6.14], [6.18], [6.52]	[2], [12.4], [15]
L	[4.1], [4.2], [4.7], [4.8], [4.9], [4.10]	[5.43] [6.11], [6.14], [6.15], [6.50]	[7.1], [9], [10], [17]
C	[4.8]	[6.14]	[12.4], [14]
O	[4.9], [4.27], [4. Paragraph "Record"]	[6.14], [6.15], [6.16]	[8.2], [9]
A	[4.1], [6.17]	[5.40], [5.45], [6.6]	[Paragraph "Principles"], [5], [6], [10], [11]

An analysis of warning letters was conducted by the FDA, in which it was found that the most frequent violations are directly related to poor documentation practices. Among the most common problems is the falsification of data in order to achieve the desired specification. Therefore, regulatory authorities have increased their attention in the area of providing DI. Data is a key part of the records managed by the computerised system. DI is one of the foundations for ensuring pharmaceutical quality. By implementing the ALCOA++ approach, the potential risks can be detected and prevented [14]. According to a review of FDA warning letters, the main reasons for not achieving a sufficient level of DI are in the way of management, organizational and individual behaviour, poor quality culture, in company processes and technology [20].

3 RESULTS AND DISCUSSION

The results of this study highlight the validation documentation necessary for the establishment of a new computerized system in the pharmaceutical industry. Through an analysis of the GAMP 5 guidelines, the study identified the frequent use of the leveraging method, which allows the reuse of already verified information or systems to streamline the validation process. For instance, if an identical system, such as a balance, has already been qualified, the results from the previous system can be applied to the new installation, reducing the need for additional testing. In cases where the leveraging method is used, certain tests, like OQ, can be skipped, and only IQ and PQ tests may be necessary.

The study found the leveraging method particularly useful when relying on test documentation provided by system suppliers. By leveraging the manufacturer's test documentation, system specifications, and configuration specifications, the validation process is more efficient. However, all supplier documentation must be pre-approved by the customer. One critical component of this documentation is the TM, which clearly links the URS to the test specifications. It is recommended that the TM is prepared by the author of the test documentation to ensure accuracy and clarity.

Furthermore, the study emphasizes that validation documentation must be structured and logically connected. The validation process for computerized systems requires a variety of documents—such as the IRA, Functional Risk Assessment (FRA), URS, QP, IQ, OQ, PQ, and QR — which must be interrelated throughout the project. Consistent document structure and thoughtful naming conventions are essential for traceability and efficient management of changes or updates. This organizational approach helps ensure proper oversight and facilitates faster access to necessary documentation.

The study also elaborates on several key documents involved in computerized system validation:

1. User Requirements Specification: URS document outlines the requirements set by the user for the equipment, covering general, functional, and regulatory requirements. These requirements must be clear, testable, and relevant to ensuring the system's functionality and compliance with regulatory standards [13].
2. Supplier Assessment: Prior to purchasing equipment, the supplier's ability to meet the specified requirements is evaluated. Different levels of supplier assessments are performed based on the criticality of the system, ranging from baseline assessments to audits at the supplier’s location [13].
3. Initial Risk Assessment: The IRA is conducted before qualification activities to assess the risks associated with the system, including its impact on patient health, product quality, and DI. The IRA helps determine the appropriate GAMP 5 category and the necessary qualification approach.
4. System Specifications: Once a system is selected, the manufacturer provides detailed system specifications, including Configuration Specification (CS), Functional Specification (FS), Hardware Design Specification (HDS), and Software Design Specification (SDS). These documents ensure that the system meets the URS and is fit for purpose.
5. Functional Risk Assessment: If the IRA does not fully assess certain risks, a more detailed FRA is performed. This assessment focuses on critical requirements related to DI and patient health, using methods like Failure Modes and Effects Analysis (FMEA) to mitigate potential risks [13].

Qualification Plan: The QP outlines the strategic plan for validating the system, including the necessary activities for each phase of the implementation process. It provides a roadmap for ensuring that all validation steps are completed in accordance with regulatory guidelines. In Figure 3, shows the architecture of the documentation for the project phase leading up to the start of using the computerized system. The QP document can be prepared by either the supplier or the customer.

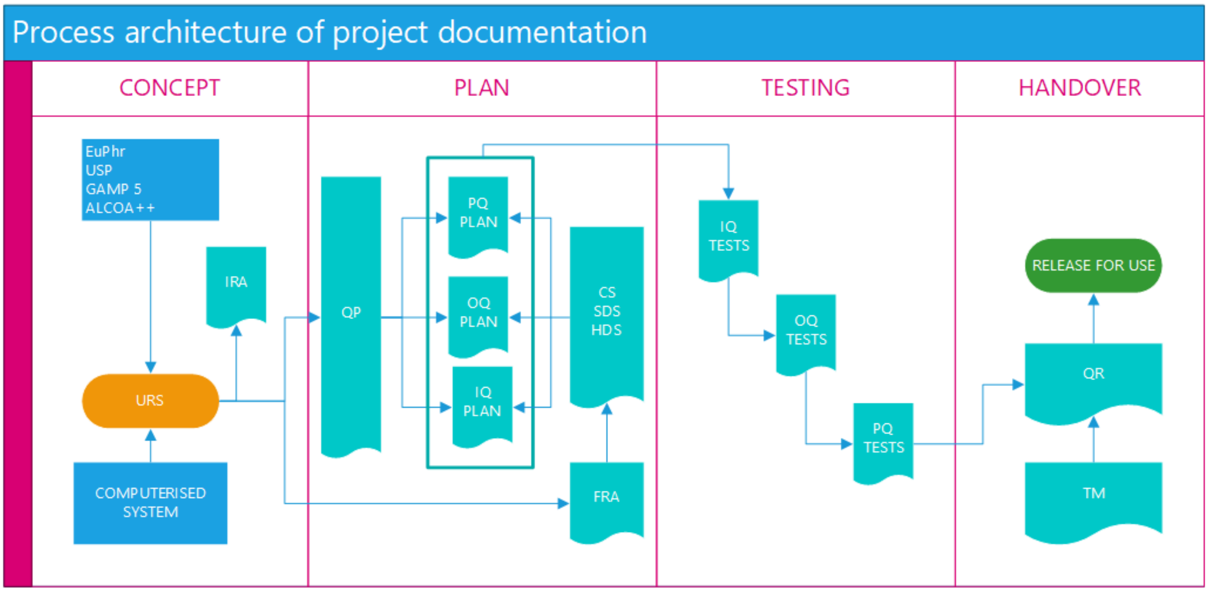

Figure 3: Process architecture of project documentation

6. Installation Qualification: IQ tests verify that the system is installed and functioning correctly. This includes testing system components, access rights, and integration with other systems [21]. Automated testing methods can be used as long as they ensure DI [13].
7. Operational Qualification: OQ tests ensure that the system’s key functions are operating as expected. Calibration tests and operation functionalities tests are performed to confirm the system's readiness for operational use [8].
8. Performance Qualification: PQ confirms that the system meets the user’s requirements in its intended environment. It involves testing the system under real-life conditions, and any deviations must be documented and addressed [21].
9. Traceability Matrix: The TM ensures the traceability of all requirements through the validation process. It links each requirement in the URS to the corresponding system specification and test phase, providing a

comprehensive overview of coverage [13].

10. Qualification Report: The QR summarizes the results of the validation process, including any deviations found during testing. Once all issues are resolved, the system is deemed qualified and ready for use [21].

In conclusion, the study provides a comprehensive overview of the essential documentation and processes required for the successful validation of computerized systems in the pharmaceutical industry. It underscores the importance of structured documentation, clear communication between stakeholders, and adherence to regulatory guidelines to ensure the system's functionality, compliance, and DI.

3.1 Discussion

Through the review of legislation, pharmacopoeias and relevant guidelines, we extracted the necessary steps and documents of the process of introducing a computerised system into the pharmaceutical laboratory. Mainly by following the GAMP 5 guidelines, we tried to find possible simplifications of the validation process. During the research work and the preparation of the entire set of necessary documentation and strategic planning, in the following chapters we answered the 2 set hypotheses.

Hypothesis 1: At implementation of the new system the validation approach for laboratory system is the same as the production system

In the second hypothesis, researched whether there is a difference between the qualification approach for the laboratory system and the qualification approach for the production system. When reviewing legislation, regulatory requirements and guidelines, we found that European legislation separates GLP and GMP. When we examine both directives, we find that every computerised system, for use in GLP and GMP, must be properly validated before use in a regulated environment. In the EudraLex collection of European regulatory requirements, we need to achieve compliance with Annex 11, while the US regulatory requirements dictate compliance with 21 CFR Part 11. Neither regulatory requirement differs in requirements nor divides the production and laboratory systems in such a way that either system could be validated on a smaller scale. We came to the same conclusion after reviewing the GAMP 5 guidelines, which do not divide the mentioned systems and dictate the direction for the validation of computerised systems in the good ''x'' practice (GxP) pharmaceutical environment. A possible difference in the qualification approaches between GLP and GMP is identified in defining the criticality of URS requirements and, consequently, in the FRA. When creating the URS requirements for the system in the GLP environment, we do not have a requirement that would have a potential impact on the patient's health. In the case of GMP system, however, the probability of a direct impact on the patient is possible. Because of the higher level of criticality, we believe that testing a production computerised system is more extensive than a laboratory system. We also expect a difference in the FRA, where we expect that, despite the introduction of validation mitigating measures, we still do not reach a low level of criticality for systems that are in direct contact with the product. That's why we have to procedurally ensure the appropriate level of system security through adjustments in the production process.

Based on the findings, hypothesis 2 is confirmed.

Hypothesis 2: AT implementation of the new laboratory system there are possible Process improvements and simplifications of the validation approach.

Regulatory requirements set a direction, a qualification approach that leads us to a validated computerised system. The regulatory validation process is quite complex and time-consuming. Therefore, we can profitably use the previous experience of good practices, which are combined in guidelines such as, for example, the GAMP 5 guidelines, which we studied as part of this work. The lengthy process can be simplified by using artificial intelligence, by combining test phases such as IQ and OQ into one IOQ test phase and avoiding interphase confirmation and signing of documentation. The guidelines discuss the topic of random testing, which could be used to achieve a higher coverage of the system's testability. When repeating the qualification of equipment that we have already validated in the past, we can use the leveraging method to assess which tests should be repeated and which should no. The OQ phase can be omitted in the replicated system.

Process improvements are possible, so hypothesis 2 is confirmed.

3.2 Comparison of other studies

The study titled *Ensuring Regulatory Compliance of Computer Systems in the Pharmaceutical Industry* [22], was compared to the current study, and the following findings were made:

Both studies focus on regulatory compliance and validation of computer systems in the pharmaceutical environment, though they employ different approaches. The Zupin's study addresses 21 CFR Part 11 (FDA) and Annex 11 (EMA) regulations, analysing common issues based on FDA warning letters. In contrast, this document also follows 21 CFR Part 11, Annex 11, including USP, Ph. Eur. ,GAMP 5 guidelines and ALCOA++ principles, taking into account the impact of European legislation, such as EudraLex. The Zupin's study covers the entire validation lifecycle, while this paper focuses on the initial stages of system implementation.

Both studies describe the importance of maintaining compliance throughout the system's lifecycle. The Zupin's study outlines the key steps and resources needed to manage compliance, while this study provides a detailed approach to implementing a structured validation documentation framework and a systematic approach of computer system release to production. Both studies agree that the critical aspects of compliance in the pharmaceutical industry align with global guidelines and that documentation must be thorough, traceable, and prepared for review by regulatory authorities.

4 CONCLUSION

This study explores the essential documentation and processes for validating computerized systems in the pharmaceutical industry. It highlights the importance of structured documentation, adherence to regulatory guidelines, and clear communication to ensure system functionality, compliance, and DI. The analysis of GAMP 5 guidelines reveals the use of the leveraging method, which allows previously validated system data to be reused, reducing testing requirements and streamlining the validation process.

The study emphasizes the need for well-organized validation documentation, such as the TM and QP, to maintain traceability and efficiently manage changes. It also underscores the importance of risk assessments like the IRA and FRA in guiding the validation process based on system criticality.

In conclusion, the study confirms that while the validation process is complex, strategies such as leveraging and process simplifications can improve efficiency. Both hypotheses are confirmed: the validation approach for laboratory and production systems is similar, and process improvements are possible.

The vast majority of the validation documentation of pharmaceutical companies is confidential, which was identified during the study as one of the greatest obstacles or limitations of the research.

4.1 Suggestions for improvements

The GAMP 5 guidelines have recently been revised because of the emergence of new technologies, such as Artificial Intelligence (AI), Machine Learning (ML), chaining of data blocks (Blockchain), open source software, cloud computing [13]. The latter clearly indicates an increase in the use of the aforementioned technologies and their inclusion in the concept of Pharma 4.0. The purpose of Pharma 4.0, like Industry 4.0, is to improve efficiency and ensure a higher level of quality through the use of digital technologies and automation.

Digital maturity and DI design enable an effective digitization strategy and are supported by well-managed automated and information systems. GAMP 5 guidelines aim to ensure that GxP computerised systems are fit for their intended use and that GxP electronic records and data are properly managed throughout the data lifecycle to ensure DI [13]. In the future the use of blockchain technology could improve efficiency, transparency and data security in the pharmaceutical industry [23].

With the help of AI and ML, the processes currently carried out by operators in the laboratory could be simplified and even improved [24]. By using modern technologies, we would thus increase the detectability, the prediction of a possible malfunction, or a trend out of limit even before it happens. The main difference is that, for example, an operator performs a certain operation once per month, but thanks to powerful computerised systems and algorithms, AI could perform operations all the time and compare it throughout the entire period of operation. A big contribution would be the operator's time saved, which would not be needed for operator operations. In addition to the complexity of the algorithm that we would have to develop, an even greater challenge would be the validation of such a system function. When we validate the system, we must ensure that it remains the same throughout the whole lifetime of the system. The purpose of validation is to validate the state as we will use it. So AI and ML cause us a problem, because as the system learns and evolves, it changes the state of the system that we validated at the initial validation. The regulation strictly requires that changes to the system must be managed through a protocol for controlled changes, which includes a revalidation of the system as part of the implementation of the change. These problems were not foreseen by the guidelines. Giving free hands to AI and ML would not be compliant with legislation and regulatory requirements. One possible solution would be to allow the computerised system to learn, but not implement the acquired knowledge into the system automatically, but have the system administrator implement it through a change protocol. After the implementation, we could perform a partial validation of the system, namely only the module that was upgraded. Eventually, after a few updates, the system would evolve to the point where what he gained would be useful to the process. However, we must take into account that every such update requires a team that implements and validates the change.

The new version of GAMP 5 describes and recommends the use of random testing as a new testing technique, which should lead to a higher level of testing scope, greater detection of possible malfunctions and, consequently, a higher level of system reliability. From a practical point of view, with laboratory computerised systems, all processes are very clearly defined in the instructions for the use of computerised system, which the company prescribes and which, as a regulatory requirement, must be adhered to without deviations. If the operator does not act in accordance with the work instructions, he breaks the rules and thus performs the analysis inconsistently with the procedure, which means that the result of analysis is not adequate. We describe this because the scenario of using the instrument is already very clear and defined in advance. Moreover, the analysis flow process is validated and should not be performed differently than defined in the work instructions. This process is fully tested as part of the PQ phase, so the usefulness of random testing is questionable. We also consider whether the time we will spend on random testing is justified, given that the entire analysis process is very rigid and regulated. We can see the sense in using automated random testing. However, when we automate something, it becomes prescribed and is no longer random. Random testing is thus only applicable in combination with AI and ML, which could lead to truly random situations.

The GAMP 5 guidelines often direct the simplification of processes using the leveraging method. Of course, when using this approach, the risks to which the pharmaceutical company could be exposed must be assessed. Through the study, the usefulness of the tactic is recognized, especially in transferring the responsibility of creating project documents and test specifications, which can be transferred to the supplier, instead of writing them internally. Combining IQ and OQ documents into IOQ is part of the leveraging method [13]. In practice, we already use the leveraging method when validating identical systems or identical families of systems. Thus, upon implementation, full validation is performed only for the first system (e.g. IQ, OQ, PQ), and for all subsequent ones, only IQ and a small part of PQ are performed. The method of leveraging can go even further. We could also use a supplier evaluation that was already made by another company, if of course that company was willing to share this information with us and we have a similar approach for evaluating suppliers. When using the leveraging method, we are concerned about the confidentiality of the information of the pharmaceutical industry. It is this secrecy that largely prevents cooperation between these companies and the sharing of good practices. In the case of Slovenian pharmaceutical companies, from the point of view of the method of leveraging, the cooperation of Novartis and Sandoz could be very welcome, because until recently, these two companies had the same quality assurance system. At the same time, the companies are not competitive in terms of the portfolio of products they produce [25].

4.2 Opportunities for future research

Possible improvements from chapter 4.1, highlights several emerging opportunities for future research in the pharmaceutical industry related to the validation of computerized systems, particularly in light of new technologies like Artificial Intelligence (AI), Machine Learning (ML), Blockchain, and digital automation under the concept of Pharma 4.0:

- how to validate AI and ML supported systems while ensuring compliance with regulatory requirements,
- blockchain technology could improve data security and transparency in the pharmaceutical industry. Research could explore its practical applications for enhancing validation and traceability in regulated environments,
- the introduction of random testing techniques in qualification process could benefit from AI and ML to make testing more effective, especially in automated and highly regulated systems where randomness is traditionally hard to achieve,
- leveraging previously validated systems and supplier evaluations can streamline the validation process. Research could explore how companies can collaborate more effectively while ensuring confidentiality and competitiveness,
- further research could focus on automating tasks like combining IQ and OQ phases to reduce time and workload while ensuring compliance and reliability,
- with the rise of digital technologies under Pharma 4.0, future studies could explore how digital maturity can enhance the validation process and improve overall system reliability in pharmaceutical environments.

These areas offer promising directions for optimizing and advancing the validation of computerized systems in the pharmaceutical industry.

REFERENCES

[1] European Parliament, “Directive 2001/83/EC of the European Parliament and of the Council of 6 November 2001 on the Community code relating to medicinal products for human use,” *Official Journoal,* vol. 027, no. 01/01/2022, pp. 0067-0128, 2001.

[2] European commission, “Commission Delegated Regulation (EU) No 1252/2014 of 28 May 2014 supplementing Directive 2001/83/EC of the European Parliament and of the Council with regard to principles and guidelines of good manufacturing practice for active substances for med. prod.,” *Official Journoal,* p. 337/1 do 337/7, 2014.

[3] European Commission, “Commission Directive (EU) 2017/1572 of 15 September 2017 supplementing Directive 2001/83/EC of the European Parliament and of the Council as regards the principles and guidelines of good manufacturing practice for medicinal products for human use,” *Official Journoal,* p. 238/44 do 238/50, 2017.

[4] European Parliament, “Directive 2004/9/EC of the European Parliament and of the Council of 11 February 2004 on the inspection and verification of good laboratory practice (GLP),” *Official Journal,* vol. L 050, p. 0028 do 0043, 2004.

[5] European Parliament, “Directive 2004/10/EC of the European Parliament and of the Council of 11 February 2004 on the harmonisation of laws, regulations and administrative provisions relating to the application of the principles of good laboratory practice and the verification o,” *Official Journoal,* vol. L50/44, pp. 82 - 98, 2004.

[6] European Commission, “Volume 4 - Good Manufacturing Practice (GMP) guidelines,” *EudraLex,* 2024.

[7] EDQM - European Directorate for the Quality of Medicines & HealthCare, QUALIFICATION OF EQUIPMENT, Strasbourg: Council of Europe, 2023.

[8] EDQM - European Directorate for the Quality of Medicines & HealthCare, VALIDATION OF COMPUTERISED SYSTEMS, Strasbourg: Council of Europe, 2018.

[9] National Archives and records administration, “Title 21,” Code of federal regulations, 12 February 2024. [Online]. Available: https://www.ecfr.gov/current/title-21. [Accessed 22 February 2024].

[10] FDA - Food and Drug Administration, Department of Health and Human Services, 21 CFR Part 58, Rockville: Federal Register, 2011.

[11] FDA - Food and Drug Administration, Department of Health and Human Services, 21 CFR Part 11 Subpart B, Rockville: Federal register, 2003.

[12] FDA - Food and Drug Administration, Department of Health and Human Services, 21 CFR Part 11 Subpart C, Rockville: Federal register, 2003.

[13] ISPE, GAMP 5: A Risk-Based Approach to Compliant GxP Computerized Systems (Second Edition), Florida: ISPE, 2022.

[14] F. V. F. M.-M. Francisca Pedro, “Impact of GAMP 5, data integrity and QbD on quality assurance in the pharmaceutical industry: How obvious is it?,” *Drug Discovery Today,* vol. 28, no. 11, 2023.

[15] J. K.-S. M. P. V. S.-V. C. K. Andreas Hoffmann, “Computer system validation: An overview of official requirements and standards,” *Pharmaceutica Acta Helvetiae,* vol. 72, no. 6, pp. 317-325, 1998.

[16] J. Wechsler, “Data Integrity Key to GMP Compliance,” *Pharmaceutical Technology,* vol. 38, no. 8, p. 2, 2014.

[17] M. Durivage, Data Integrity for the FDA Regulated Industry, Lambertville: Quality Systems Compliance LLC, 2019.

[18] European Medicines Agency, Guideline on computerised systems and electronic data in clinical trials, Amsterdam: European Medicines Agency, 2023, pp. 12-13.

[19] ECA Academy, The GMP Questions & Answers Guide, GMP advisor, Heidelberg: ECA Academy, 2020.

[20] M. A. K. Z. R. Naseem A. Charoo, “Data integrity issues in pharmaceutical industry: Common observations, challenges and mitigations strategies,” *International Journal of Pharmaceutics,* vol. 631, 2023.

[21] EDQM - European Directorate for the Quality of Medicines & HealthCare, VALIDATION OF COMPUTERISED SYSTEMS, ANNEX 2 – VALIDATION OF COMPLEX COMPUTERISED SYSTEMS, Strasbourg: Svet evrope, 2018.

[22] Z. Gašper, Zagotavljanje regulatorne skladnosti računalniških sistemov v farmacevtski industriji, Kranj: University of Maribor, 2016.

[23] Y. L. Xuanping Wu, “Blockchain recall management in pharmaceutical industry,” *Procedia CIRP,* vol. 83, pp. 590-595, 2019.

[24] S. B. K. V. L. G. Ruchika S. Patil, “Artificial intelligence in pharmaceutical regulatory affairs,” *Drug Discovery Today,* vol. 28, no. 9, 2023.

[25] MMC RTV Slovenija, “Sandoz (in z njim Lek) se bo ločil od Novartisa,” MMC RTV Slovenija - gospodarstvo, 25 Avgust 2022. [Online]. Available: https://www.rtvslo.si/gospodarstvo/sandoz-in-z-njim-lek-se-bo-locil-od-novartisa/638265. [Accessed 31.12.2022 December 2022].

Sustainable use of salt and clay in 3D printing: experimental analysis and potential for construction materials

Vesna Pungerčar[1]

[1]Rudolfovo - Science and Technology Centre Novo mesto, Podbreznik 15, 8000 Novo mesto, Slovenia
E-mail: vesna.pungercar@rudolfovo.eu

***Abstract**: Using salt and clay as sustainable materials for additive manufacturing, particularly 3D printing, is an innovative solution to reduce environmental problems related to salt waste. The main challenge arises from the increasing quantities of salt waste produced by desalination and industrial potassium extraction. Most of the salt waste causes environmental pollution because high salt levels alter the salinity of soil and water. Animals and vegetation cannot adapt to such drastic changes in a short time, leading to a reduction in biodiversity. Despite its negative effects on building structures due to crystallization, salt, especially sodium chloride, offers promising properties such as heat and moisture storage, antibacterial effects, and potential health benefits. This research includes an experimental analysis of mixtures of salt, clay, and additives such as straw and starch to produce 3D-printed cylinders. An experimental analysis of mixtures of salt, clay, and additives, such as straw and starch, used to produce 3D-printed cylinders. Four material groups were tested: clay (C), salt-clay (CS), salt-clay-straw (CSS), and salt-starch-clay (SSC). The 3D cylinders were printed using a 3D printer with material extrusion and then evaluated with visual assessments and optical 3D scanning. The 3D scanning enabled comparison with a reference model and identification of deformations and deviations. The results indicate that salt and clay mixtures are suitable for 3D printing, although some mixtures encountered issues with shape and stability. The best printing performance was achieved with formulations where salt was properly combined with other materials. The addition of straw and starch improved certain properties, but deformations during the drying process were still present. The study concludes that salt as a waste material holds potential for use in sustainable construction materials, though further recipe optimization and testing in larger projects are necessary.*

***Keywords:** sustainable material, 3D printing, 3D scanning, salt, industrial waste*

***Article Classification:** Scientific paper*

1 INTRODUCTION

In recent decades, research has shown that salt holds potential as a material for new technologies, including 3D printing [1]. As a porous material offers salt promising possibilities for additive manufacturing. There are different approaches in additive manufacturing [1]. The most common methods in the field of building materials are 3D printing with melting, binder jetting [2–5], and material extrusion. Binder jetting is a known method that has been used for the last 30 years [2] and creates a 3D object by applying a binder onto thin layers of powder. Sometimes, heat is also used for the post-treatment of surfaces and better connections between powder particles [6]. 3D printing with material extrusion is a method where pre-mixed printing paste is pushed through a moving nozzle to create a three-dimensional object by layering material in height.

The primary materials used in 3D printing include polymers, metals, concrete, and ceramics [7]. Currently, researchers are exploring various sustainable and waste materials due to the increasing environmental concern. Emerging Objects conducts innovative research using traditional materials like clay, water, and wheat straw to explore the potential of traditional clay craftsmanship [2]. They developed a portable robotic system for 3D printing large-scale structures on sites [2]. Their findings revealed that the wall thickness achieved through 3D printing was significantly thinner than that of conventional adobe walls [2]. In another project, the team employed a cryogenic process to convert used tires into powder suitable for 3D printing applications [2]. Pringle et al. focused on advancing research in 3D printing with wood particles. In the U.S. furniture industry, approximately 150 tons of wood-based waste is generated daily [8]. The research group aimed to incorporate wood waste into composite polymers, targeting wood content levels of up to 90% in 3D printing applications. Another potential material to be 3D printed is also sand, which can be printed using a layer-by-layer process. Sand particles are bonded with a binding adhesive and can be designed into complex 3D shape [9].

Different research groups have already developed various 3D printing pastes with salt (salt with starch, salt with cement) for construction purposes [4, 5, 10]. The first 3D-printed salt objects were made of salt, maltodextrin, and water. They were very small and were created at the Solheim Additive Manufacturing Laboratory at the University of Washington [4]. The printing paste was further improved by researchers from Emerging Objects and those at TU Delft. The former succeeded for the first time in printing larger salt pieces, which were connected with secondary construction to create the first 3D-printed salt pavilion [2]. The latter group focused more on the mechanical properties of the salt and starch mixture [4]. Japanese researchers also explored how to make salt molds using 3D printing, which can be easily dissolved later [11].

These research projects on 3D printing with salt have primarily focused on prototyping, with almost no emphasis on assessing salt's impact on print quality. While the literature details methods for evaluating 3D print quality, few address salt-based projects specifically. A common method for evaluating 3D printing quality is dimensional accuracy testing, where the printed object's dimensions are compared against the original digital model by using 3d scanning [12]. Other methods include surface roughness measurement [13], mechanical property testing [14] and porosity analysis [15].

Salt as a new building material has attracted attention over the past two decades due to the growing global population [16]. It has increasingly appeared as a waste product of desalination and potash extraction processes (Figure 1). 15,906 desalination plants worldwide produce 141.5 million m³ of brine each day [17]. Intensive agricultural practices need fertilizers like potash, which produce between 52,000 and 437,000 m³ of salt waste per day [18]. The quantity of sodium chloride (NaCl) in the desalination and potash extraction processes is the highest, ranging between 60% and 95% [17, 18]. Most of the salt waste causes environmental pollution because high salt levels alter the salinity of soil and water [19–21]. Animals and vegetation cannot adapt to such drastic changes in a short time, leading to a reduction in biodiversity [19, 21–23].

Figure 1: Discharge of salt into the natural environment (Monte Kali, Germany) [24]

Salt has primarily been used in cooking and food preservation, later becoming a traded commodity. Today, it is used in approximately 14,000 different products, mainly in the chemical and food industries [25, 26]. Salt is a naturally abundant material [25, 27] that retains moisture and heat [24, 25, 28–30], dissolves at 75.3% relative humidity at 20°C [25], and has a specific heat capacity of 0.853 J/(g·K) [25]. It is also antibacterial [27] and used therapeutically for respiratory diseases, skin issues, and even lung cancer [31–35].

Due to issues related to salt in walls, its high value, and historical scarcity, salt has been challenging to fully embrace as a new raw material in other industrial sectors [30]. Some historical examples of salt building material were found in hot, dry climates. They are usually located near salt flats or salt lakes, where other building materials are not available. The most common method for obtaining salt as a building material was by cutting small salt blocks from salt flats and using them in masonry construction [36–38]. Composite salt materials combine salt with cement, clay, volcanic ash, or starch [38, 39]. Historic examples include Egypt's karshif, salt stones bound with salt-clay mortar [38] and Roman marine concrete made from volcanic ash, lime, and seawater for seawalls [40]. Modern uses include salt concrete with 50% salt waste for nuclear waste protection [41–43].

Karshif is known as one of the oldest salt-based construction materials, containing up to 95% salt [44]. It was primarily used in arid climatic regions with extremely high temperatures. With climate change, the number of dry regions worldwide is increasing. These areas are facing a growing demand for fresh water. This has led to a greater production of salt waste, as many water extraction solutions are linked to processes that generate salt as a byproduct. At the same time, these regions are struggling with construction challenges, as the cost of building materials has surged significantly over the past decade. Additionally, many commonly-used materials such as cement are environmentally harmful due to emissions during their production [45]. Therefore, it is crucial to seek innovative construction solutions that efficiently utilize local raw materials and contribute to reducing carbon emissions and environmental pollution. Additive technologies, such as 3D printing, offer potential solutions that can simplify construction processes, even in extremely demanding climates.

The aim of this study was to investigate a new building material for arid areas using 3D printing. The first objective of the research project was to utilize locally available materials and improve the resource efficiency of building materials. The second objective was to reduce environmental pollution by using salt waste. The 3D printing of new salt-clay materials was evaluated using 3D scanning and visual criteria.

2 MATERIALS AND METHODS

The experiments discussed here were part of a broader investigation previously detailed by Pungercar et al. [1], which evaluated various material mixtures in 3D printing with salt. This review focuses specifically on the salt-clay mixtures. As outlined in the earlier publication [1], four material groups were systematically tested: C (clay), CS (salt-clay), CSS (salt-clay-straw), and SSC (salt-starch-clay). The experiments highlighted that salt, due to its inherent porosity, necessitated the inclusion of a binder to cohesively hold the salt crystals during the material extrusion process. However, each group consisted of six variations of material mixtures, labeled A through F. Mixture A served as the initial formulation, which was refined through iterative modifications in mixtures B to F. Adjustments were made to the water content in Mixture B if the printed paste in Mixture A was found to be either too liquid or too dry. Once Mixture B achieved the required printing quality, the salt concentration was increased in Mixture C to enhance resource efficiency, with further adjustments to the water content made as necessary. However, managing the properties of the printing mortar through salt and water adjustments proved complex, as the salt-to-water ratio did not exhibit linear behaviour. In phases with salt-clay mixtures, water content was modulated to a maximum of 13% (by mass) with straw and minimized to 8% with starch (see Table 1). The materials employed included salt from Diacleanshop, clay from Sibelco, maltodextrin starch from Myprotein, straw, and distilled water (Table 1).

Table 1: Material groups CS: clay, salt; CSS: clay, salt, straw; and SSC: clay, salt, starch, with six sequential material mixtures (A-F) [1]

Group	Mixture	Ratio salt : clay	Salt (g)	Clay (g)	Destilled water (g)	Alcohol (g)	Straw (g)	Starch (g)
CS	A	60:40	900	600	140	-	-	-
	B	60:40	900	600	190	-	-	-
	C	60:40	900	600	190	-	-	-
	D	70:30	1050	450	200	-	-	-
	E	80:20	1200	300	250	-	-	-
	F	80:20	1200	300	210	-	-	-
CSS	A	60:40	720	480	180	-	-	-
	B	60:40	720	480	180	-	30	-
	C	64:36	840	480	180	-	10	-
	D	70:30	840	360	180	-	10	-
	E	70:30	840	360	162	-	10	-
	F	70:30	840	360	160	-	10	-
SSC	A	60:40	720	480	150	15	-	180
	B	70:30	560	240	80	8	-	100
	C	80:20	800	200	100	10	-	125
	D	78:22	900	225	140	10	-	140
	E	75:25	750	250	100	10	-	125
	F	80:20	800	200	100	10	-	150

All test cylinders, measuring 10 x 10 x 10 cm, were produced using a material extrusion method. The Potterbot Micro 10 3D printer was specifically selected for this purpose due to its specialization in ceramic printing. This printer features a suitable printing volume for cylindrical shapes, with a maximum diameter and height of 254 mm, as well as an adjustable layer thickness, with a maximum of 12.7 mm. Prior to the 3D printing process, the optimal speed and pressure settings for the newly developed materials had not been established, necessitating preliminary adjustments to the printer's parameters. The printer offered a broad range of speeds, from 30 to 130 mm/s, along with pressure settings adjustable between 5 and 25 psi. Generally, the printer is capable of achieving a dimensional accuracy of approximately ±0.5 mm. However, in this study, accuracy was influenced by variations in calibration and the material behavior of the newly formulated salt mixtures.

To evaluate the quality of the 3D prints, both visual assessments and optical 3D scanning techniques were employed. The optical scanning was conducted using the Keyence VL device, which utilizes laser triangulation technology to obtain 3D coordinate measurements with an impressive accuracy of 2 micrometers (μm) and a scanning speed of up to 2,000 points per second. The evaluation process involved a systematic comparison of the printed models against a digital reference model, which facilitated the identification of deformations, inaccuracies, and deviations. This digital comparison yielded valuable insights into the printing quality, significantly contributing to the overall findings of the original study.

As previously published in Pungercar et al. [1] this study was conducted in 4 phases (Figure 2). The four phases of this research provided critical insights into the mixing, printing, and evaluation processes for salt-clay mixtures in 3D printing with material extrusion. By systematically investigating each aspect, the study contributed valuable knowledge to the field of additive manufacturing, particularly in the utilization of unconventional materials. In the phase 1: Mixing materials, salt waste was mixed with clay to achieve a homogeneous consistency. Various additives were incorporated to enhance surface quality, to modify viscosity (using maltodextrin), and to improve structural stability (with straw). The viscosity of the salt-clay mixture was optimized by adding starch (maltodextrin) and alcohol. The inclusion of alcohol reduced the solubility of starch and prevented the formation of non-

Newtonian fluids [46] that would occur with starch and water alone. Additionally, straw was tested for its structural stability benefits, given its availability and its potential to improve the insulation properties of the material.

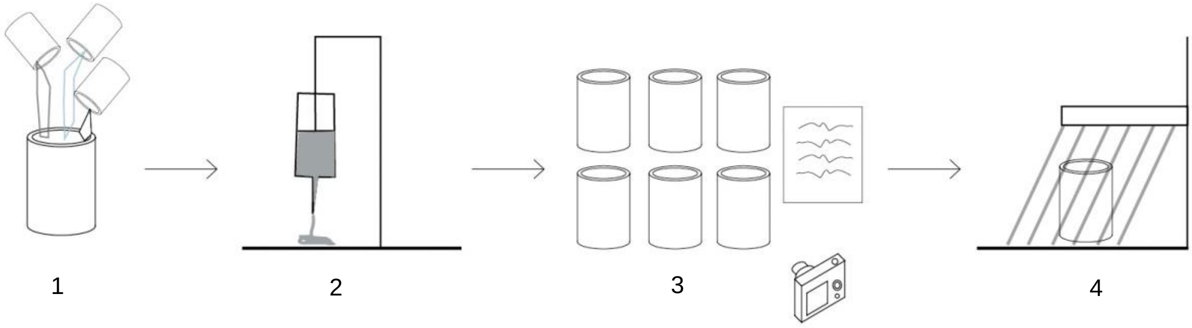

Figure 2: Research procedure: (1) - Phase 1: Mixing of materials, (2) - Phase 2: 3D printing, (3) - Phase 3: Drying of materials at room temperature and visual evaluation, (4) - Phase 4: 3D scanning and comparison with reference model [1].

All test cylinders were printed during Phase 2 using a 3D extrusion printer with a nozzle diameter of 6 mm, at a printing speed ranging from 40 to 60 mm/s (Figure 3). The 3D model of each cylinder was sliced into 66 layers, each with a height of 1.5 mm. Initially, the clay cylinder (group C) took 8 minutes to print at 60 mm/s. However, the other material groups required a maximum of 20 minutes at a printing speed of 40 mm/s. As the properties of the materials changed, the printer settings also had to be adjusted. This process of mixing and adjusting the printing parameters was carried out continuously to ensure optimal 3D printing quality. Ultimately, a consistent speed of 40 mm/s was selected for easier comparison across the samples.

Figure 3: 3D printing with salt-clay mixture.

In Phase 3, all 19 test cylinders were printed using the same settings. However, during the printing process, the design and surface properties of the cylinders varied visually. Cylinders with the least visible deformations were selected from each material group (C, CS, CSS, SSC) and compared with the reference cylinder C. Cylinder C was printed from pure clay and served as a benchmark for assessing deformations in the other material groups. Visual criteria were employed to evaluate the materials: the ability to extrude the printed material through the nozzles, retention of the 3D-printed shape, bonding time between layers, feasibility of adding additional layers, and surface quality. These criteria were summarized from the literature [47, 48]. In Phase 4, the cylinders were dried for 28 days at room temperature (21 °C). Subsequently, they were 3D scanned (Figure 4). 3D scanner enabled the digital comparison of the 3D cylinders with the desired geometry (3D model), facilitating the identification of minor deviations, inaccuracies, or inconsistencies.

3 RESULTS AND DISCUSSION

This review summarizes the key findings from previously published research concerning the utilization of 3d printing with material extrusion and salt-clay mixtures for 3D printing [1]. The material extrusion demonstrated significant potential for 3D printing with clay-based materials. However, the results indicated limitations when working with salt-clay mixtures (see Figure 5). The relationships between printer settings, material properties, and print quality were critical in achieving satisfactory outcomes. This process often required a considerable amount of time and a trial-and-error approach. The optimal 3D printing speed for consistent results was 40 mm/s. It was found that faster speeds could lead to inaccuracies, especially if the mixture was too dry or too porous due to insufficient water. A 6 mm nozzle proved most effective for salt-clay mixtures. With a smaller nozzle frequent clogging was noticed. A layer height of 1.5 mm was determined to be suitable. Thinner layers caused material overlapping, while thicker layers resulted in poor adhesion. Replacing the printing material necessitated disassembling the printer components, which could disrupt the continuity 3D prints due to the printer's limited material capacity. This required careful manual adjustments to maintain the overall finish and integrity of the prints.

Figure 4: 3D printed Cylinder. From left to right: Material mixture with insufficient water content, material mixture with excessive water content, material mixture with optimal proportions of components (Photo: EBB TUM).

The evaluation of four material groups underscores the complexities of 3D printing with novel materials. In general, while the C group laid the foundation for effective printing processes, the CS and CSS groups highlighted the need for optimal water content and material stability. The SSC group demonstrated the advantages of viscosity control, collectively illustrating that tailored approaches are crucial for achieving desired outcomes in 3D printing. All investigated material groups were categorized during visual evaluation into three quality categories based on the 3D printing process: poor (3), average (2), and good (1). A rating of 1 indicated the best 3D printing quality, while a rating of 3 denoted the lowest quality with printing issues (see Table 2).

Table 2: Evaluation of 3D Printing for 4 material groups C: clay; CS: clay, salt; CSS: clay, salt, straw; and SSC: clay, salt, starch with 6 sequential combinations (mixtures A-F) [1].

Group	Mixture	Pushing the printed paste	Retention of printed shape	Bonding time between layers	Feasibility of Adding Additional Layers	Surface Quality	Photo
C	A	1	1	1	1	1	
CS	A	3	-	-	-	3	
	B	2	2	-	-	-	
	C	1	1	-	1	1	
	D	1	1	-	1	1	
	E	3	-	-	-	-	
	F	3	-	-	-	-	
CSS	A	2	2	3	3	1	
	B	2	2	3	3	3	
	C	1	1	3	1	2	
	D	2	2	3	3	3	
	E	3	3	3	3	3	
	F	3	3	3	3	3	
SSC	A	1	1	1	1	1	
	B	1	1	1	1	1	
	C	-	-	-	-	-	
	D	3	2	3	3	1	
	E	1	2	2	1	1	
	F	1	3	2	2	1	

The C group achieved smooth 3D printing of clay, primarily due to thorough preparation. A 10 kg block of clay was divided into smaller pieces, and 350 ml of distilled water was added, allowing the mixture to soak for two to three days. This preparation was essential; without it, the 3D printing process became significantly challenging. In contrast, the CS group encountered difficulties with its five mixtures. Mixtures A-C lacked sufficient water, causing clogs, while E and F contained excessive water. Mixture D emerged as the most effective, resulting in a uniform surface and well-bonded layers. In the CSS group, mixtures A and B showed partial printing capabilities but faced stability issues. Mixtures D and F had too much water, making full-sized prints impossible. Mixture C stood out with a favourable 64:36 salt-to-clay ratio, enabling even layer deposition and stability. Although the shape was satisfactory, the surface was rough and porous due to straw inclusion, and the drying time was notably extended. In the SSC group, mixture A exhibited high viscosity, facilitating easy injection and resulting in a homogeneous print without cracks or deformations. The layers bonded effectively, and the surface displayed minimal crystallization. However, mixtures B through F demonstrated lower performance due to high viscosity, which led to shape deformation at the bottom of the cylinder.

3D scanning enabled accurate and rapid 3D scanning of the cylinders. We could accurately measure how much the printed objects changed from their original shape (Figure 5 and Table 3). The deformation of the cylinders was represented using a color scale, making it easy to see the differences among the four material groups (C, CS, CSS, SSC) compared to the intended design (3D model) (see Table 3). The color scale indicates the amount of deformation: dark blue represents a negative change of -10 mm, while red shows a maximum increase of +10 mm. Light green indicates no change (±0), and a neutral color means the change is greater than 10 mm. After using optical 3D scanning on the cylinders, we created profiles with horizontal and vertical cross-sections to measure the differences. Table 3 provides details on the horizontal and vertical cross-sections. The horizontal cross-section shows the layer widths at half the height of the print (50%) and highlights the maximum difference in the outer surface. The vertical cross-section shows how the material changes and deforms in height.

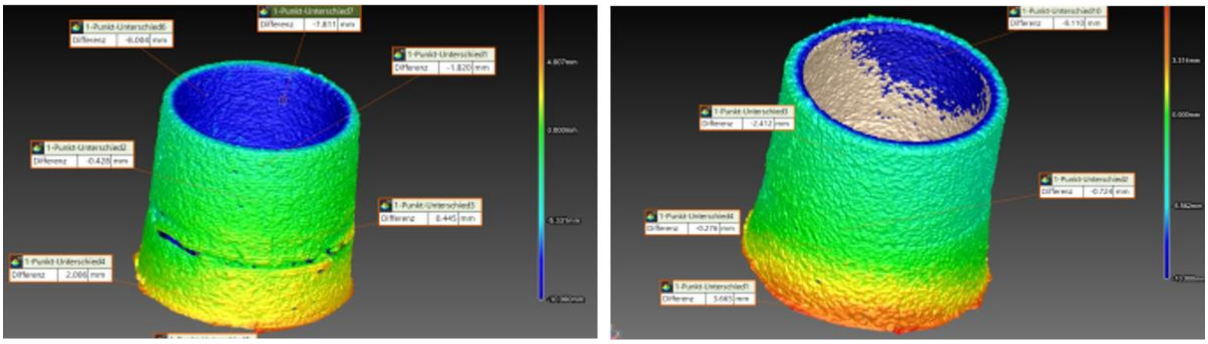

Figure 5: Examples of deviations from the desired 3D model for the C group (left) and the CS group (right).

Table 3: maximal differences among the four cylinders (C, CS, CSS, SSC) compared to the intended geometry (3D model) (dark blue = negative deviation of -10 mm, red = maximum elongation of +10 mm, light green = smallest deviation (±0), neutral color = base geometry exceeds a deviation of 10 mm) [1].

	C	CS	CSS	SSC
	Clay	Clay, salt	Clay, salt, straw	Clay, salt, starch
Horizontal cross-section:				
Width bottom left (mm)	5.340	7.103	5.997	6.163
Width bottom right (mm)	5.436	6.848	6.256	7.865
Width top left (mm)	5.261	6.684	6.772	6.963
Width top right (mm)	5.021	6.703	4.919	7.017
Vertical cross-section:				
Reduced height (mm)	1,458	2,402	3,121	3,300

The comparison of the four material groups reveals significant differences in 3D printing performance. The C group (clay) had a homogeneous and fine-grained structure. This made it the most suitable material for 3D printing. The printed cylinder showed minimal deviations from the base model. Layer widths varied from 5.021 mm to 5.340 mm. Deviations were caused by trapped air and unbinding of the clay. Lower layers also deformed unevenly due to weight above. A vertical cross-section recorded deviations of 1.458 mm from the original model. In contrast, the CS group combined salt and clay. This mixture was non-homogeneous, leading to greater deformations in comparison with C group. The printed cylinder displayed deviations ranging from 6.703 mm to 7.103 mm. The maximum height reduction was 2.402 mm. The CSS group contained clay, salt, and straw. This mixture formed the third more deformations. The printed cylinder exhibited deviations of 6.163 mm to 7.103 mm in layer width. It was also 3.121 mm to 3.751 mm shorter than the original geometry. The drying and shrinkage rates were slower. However, visible straw and larger salt crystals were noticed. The SSC group used a mixture of clay, salt, and starch. This group showed the greatest deformations due high viscosity of the material. Deviations ranged from 6.703 mm to 7.865 mm at horizontal cross-section and. up to 3.300 mm in vertical cross-section.

None of the printed cylinders achieved the expected dimensions, indicating the presence of deviations and deformations during the printing process. Damage (cracks) were not visible despite the deformations. Increased material heterogeneity and reduced water content significantly degraded print quality. A higher water content improved material printability, but also weakened the structural integrity of the paste, leading to larger deviations and deformations during drying. All scanned cylinders were found to be shorter than the 3D model, as the weight of the upper layers flattened and expanded the lower layers.

4 CONCLUSION

This review summarizes key findings from earlier research on 3D printing with material extrusion and salt-clay mixtures. The material extrusion demonstrated significant potential for printing with clay-based materials, but limitations were noted with salt-clay mixtures. The interplay between printer settings, material properties, and print quality was crucial, often requiring time-consuming trial-and-error adjustments. The optimal 3D printing speed was 40 mm/s, and a 6 mm nozzle was most effective for avoiding clogging.

The study evaluated four material groups, revealing complexities in 3D printing with novel materials. The C group (clay) performed well due to thorough preparation, while the CS and CSS groups highlighted the need for optimal water content. The CSS group showed promise with a favourable salt-to-clay ratio, despite rough surfaces due to straw inclusion.

Using salt as a construction material in additive manufacturing shows potential. Recognized as an environmentally problematic waste material from desalination and potassium industries, salt also offers beneficial properties to be used 3d printing. The research indicated that up to 70% salt could be incorporated into 3D printing mixtures, though further optimization is needed to enhance strength and reduce cracking.

Future steps should include exploring different to improve stability and reduce deformations. Testing salt in larger projects and real construction sites would also be beneficial. Despite technical challenges, the study concludes that salt has significant potential in additive manufacturing, especially in high-temperature and low-humidity environments where its properties can be effectively utilized.

REFERENCES

[1] V. Pungercar, M. Hutz, and F. Musso, “3D Print with Salt,” *3D Printing for Construction with Alternative Materials, Digital Innovations in Architecture, Engineering and Construction*, pp. 91–125, 2023, doi: 10.1007/978-3-031-09319-75.
[2] M. Ganter, *Salty parts - 3DP in Salt.* [Online]. Available: http://depts.washington.edu/open3dp/2011/03/salty-parts-3dp-in-salt/ (accessed: May 11 2020).
[3] E. Geboers, “The Salt Project,” Master thesis, Architecture and The Built Environment, TU Delft, 2015. Accessed: Nov. 20 2019. [Online]. Available: https://repository.tudelft.nl/islandora/object/uuid:528c3ddc-8a7e-4b95-89a3-60185109e674?collection=education#
[4] R. Rael and V. San Fratello, *Printing architecture: Innovative Recipes for 3D Printing*. New York: Princeton Architectural Press, 2018.
[5] L. Yuan, S. Ding, and C. Wen, “Additive manufacturing technology for porous metal implant applications and triple minimal surface structures: A review,” *Bioactive materials*, vol. 4, no. 1, pp. 56–70, 2019, doi: 10.1016/j.bioactmat.2018.12.003.
[6] J. A. Gonzalez, J. Mireles, Y. Lin, and R. B. Wicker, “Characterization of ceramic components fabricated using binder jetting additive manufacturing technology,” *Ceramics International*, vol. 42, no. 9, pp. 10559–10564, 2016, doi: 10.1016/j.ceramint.2016.03.079.
[7] S. Lodha *et al.,* “Sustainable 3D printing with recycled materials: a review,” (in En;en), *J Mech Sci Technol*, vol. 37, no. 11, pp. 5481–5507, 2023, doi: 10.1007/s12206-023-1001-9.
[8] A. M. Pringle, M. Rudnicki, and J. M. Pearce, “Wood Furniture Waste–Based Recycled 3-D Printing Filament,” *Forest Products Journal*, vol. 68, no. 1, pp. 86–95, 2018, doi: 10.13073/FPJ-D-17-00042.
[9] H. Qiang, Z. Shan, H. Yang, W. Song, Y. Sun, and L. Liu, “High-Performance 3D Sand Printing Process Using Interlayer Heating,” *Additive Manufacturing Frontiers*, vol. 3, no. 3, p. 200154, 2024, doi: 10.1016/j.amf.2024.200154.
[10] J. Li, C. Wu, P. K. Chu, and M. Gelinsky, “3D printing of hydrogels: Rational design strategies and emerging biomedical applications,” *Materials Science and Engineering: R: Reports*, vol. 140, p. 100543, Apr. 2020, doi: 10.1016/j.mser.2020.100543.
[11] Y. Marutani and T. Kamitani, “Manufacturing sacrificial patterns for casting by salt powder lamination,” *Rapid Prototyping Journal*, vol. 10, no. 5, pp. 281–287, 2004, doi: 10.1108/13552540410562313.
[12] K. Wi, V. Suresh, K. Wang, B. Li, and H. Qin, “Quantifying quality of 3D printed clay objects using a 3D structured light scanning system,” *Additive Manufacturing*, vol. 32, p. 100987, 2020, doi: 10.1016/j.addma.2019.100987.
[13] N. A. Sukindar *et al.,* “Evaluation of the surface roughness and dimensional accuracy of low-cost 3D-printed parts made of PLA-aluminum,” *Heliyon*, vol. 10, no. 4, e25508, 2024, doi: 10.1016/j.heliyon.2024.e25508.
[14] H. Shiratori, A. Todoroki, M. Ueda, R. Matsuzaki, and Y. Hirano, “Testing method for evaluating mechanical properties of 3D printed CFRP with curved fibers by four-point bending test of L-shaped specimen,” *Composites Part C: Open Access*, vol. 6, p. 100187, 2021, doi: 10.1016/j.jcomc.2021.100187.
[15] M. Naftaly *et al.,* “Non-Destructive Porosity Measurements of 3D Printed Polymer by Terahertz Time-Domain Spectroscopy,” *Applied Sciences*, vol. 12, no. 2, p. 927, 2022, doi: 10.3390/app12020927.
[16] United Nations Secretariat, “Expert Group Meeting on Completing the Fertility Transition,” *Population Newsletter*, vol. 73, 2002. [Online]. Available: https://www.un.org/en/development/desa/population/publications/pdf/newsletter/News73.pdf

[17] E. Jones, M. Qadir, M. T. van Vliet, V. Smakhtin, and S.-M. Kang, “The state of desalination and brine production: A global outlook,” *Science of the Total Environment*, vol. 657, pp. 1343–1356, 2018. [Online]. Available: http://collections.unu.edu/view/UNU:6695

[18] H. Rauche, Ed., *Die Kaliindustrie im 21. Jahrhundert*. Berlin, Heidelberg: Springer Berlin Heidelberg, 2015.

[19] T. Hoepner and S. Lattemann, “Chemical impacts from seawater desalination plants — a case study of the northern Red Sea,” *Desalination*, vol. 152, 1-3, pp. 133–140, 2003, doi: 10.1016/S0011-9164(02)01056-1.

[20] A. Musfique and A. Rifat, “An Assessment of the Environmental Impact of Brine Disposal in Marine Environment,” *International Journal of Modern Engineering Research (IJMER)*, vol. 2, no. 4, pp. 2756–2761, 2012. [Online]. Available: http://citeseerx.ist.psu.edu/viewdoc/summary?doi=10.1.1.417.1405

[21] P. Palomar and I. J. Losada, “Impacts of Brine Discharge on the Marine Environment: Modelling as a Predictive Tool,” *Desalination, Trends and Technologies*, 279-310, 2011, doi: 10.5772/14880.

[22] U. Braukmann and D. Böhme, “Salt pollution of the middle and lower sections of the river Werra (Germany) and its impact on benthic macroinvertebrates,” *Limnologica*, vol. 41, no. 2, pp. 113–124, 2011, doi: 10.1016/j.limno.2010.09.003.

[23] G. Reta *et al.,* “Environmental impact of phosphate mining and beneficiation: review,” *IJH*, vol. 2, no. 4, 2018, doi: 10.15406/ijh.2018.02.00106.

[24] V. Pungercar and F. Musso, “Hygrothermal Performance of Salt (NaCl) for Internal Surface Applications in the Building Envelope,” *Materials*, vol. 15, no. 9, p. 3266, 2022, doi: 10.3390/ma15093266.

[25] S. R. Feldman, “Sodium Chloride,” in *Encyclopedia of chemical technology*, R. E. Kirk and D. F. Othmer, Eds., New York, NY: Wiley, 2003.

[26] R. M. Geertman, “SODIUM CHLORIDE: CRYSTALLIZATION,” in *Encyclopedia of separation science*, I. D. Wilson, Ed., San Diego, Calif., London: Academic, 2000, pp. 4127–4134. [Online]. Available: http://www.sciencedirect.com/science/article/pii/B0122267702060610

[27] S. B. Jeong, K. J. Heo, and B. U. Lee, “Antimicrobial Air Filters Using Natural Sea Salt Particles for Deactivating Airborne Bacterial Particles,” *International journal of environmental research and public health*, vol. 17, no. 1, 2019, doi: 10.3390/ijerph17010190.

[28] J. L. Aragones, E. Sanz, and C. Vega, “Solubility of NaCl in water by molecular simulation revisited,” *The Journal of chemical physics*, vol. 136, no. 24, 244506-1, 2012, doi: 10.1063/1.4728163.

[29] N. N. Makhlouf, D. Maskell, A. Marsh, S. Natarajan, M. Dabaieh, and M. M. Afify, “Hygrothermal performance of vernacular stone in a desert climate,” *Construction and Building Materials*, vol. 216, pp. 687–696, 2019, doi: 10.1016/j.conbuildmat.2019.04.244.

[30] V. Pungercar and F. Musso, “Salt as a Building Material: Current Status and Future Opportunities,” *TPJ*, vol. 6, no. 2, 2021, doi: 10.15274/tpj.2021.06.02.4.

[31] A. V. Chervinskaya and N. A. Zilber, “Halotherapy for treatment of respiratory diseases,” *Journal of aerosol medicine : the official journal of the International Society for Aerosols in Medicine*, vol. 8, no. 3, pp. 221–232, 1995, doi: 10.1089/jam.1995.8.221.

[32] J. Hedman, T. Hugg, J. Sandell, and T. Haahtela, “The effect of salt chamber treatment on bronchial hyperresponsiveness in asthmatics,” *Allergy*, vol. 61, no. 5, pp. 605–610, 2006, doi: 10.1111/j.1398-9995.2006.01073.x.

[33] S. Horowitz, “Salt Cave Therapy: Rediscovering the Benefits of an Old Preservative,” *Alternative and Complementary Therapies*, vol. 16, no. 3, pp. 158–162, 2010, doi: 10.1089/act.2010.16302.

[34] T. Horvath, “Speleotherapy: a special kind of climatotherapy, its role in respiratory rehabilitation,” *International rehabilitation medicine*, vol. 8, no. 2, pp. 90–92, 1986, doi: 10.3109/03790798609166185.

[35] R. Rashleigh, S. M. S. Smith, and N. J. Roberts, “A review of halotherapy for chronic obstructive pulmonary disease,” *International Journal of Chronic Obstructive Pulmonary Disease*, vol. 9, pp. 239–246, 2014, doi: 10.2147/COPD.S57511.

[36] J. COUCH, Ed., *Pliny’s Natural history: In thirty-seven books*. A translation on the basis of that by Dr. Philemon Holland, ed.1601. Leicester Square: George BakclAY, 1847-48. Accessed: Mar. 4 2020. [Online]. Available: https://archive.org/stream/plinysnaturalhis00plinrich/plinysnaturalhis00plinrich_djvu.txt

[37] H. Gibb and C. F. Beckingham, *The Travels of Ibn Battuta: AD 1325-1354*: Taylor & Francis, 2017. [Online]. Available: https://books.google.de/books?id=8gckDwAAQBAJ

[38] A. Petruccioli and C. Montalbano, *Oasi di Siwa: Azioni per lo sviluppo sostenibile = Siwa Oasis actions for a sustainable development*. Bari: DICAR, 2011.

[39] A. Farouk Mohamed, “Comparative study of traditional and modern building techniques in Siwa Oasis, Egypt: Case study: Affordable residential building using appropriate building technique,” *Case Studies in Construction Materials*, vol. 12, e00311, 2020, doi: 10.1016/j.cscm.2019.e00311.

[40] E. Gotti, J. P. Oleson, L. Bottalico, R. Cucitore, C. Brandon, and R. L. Hohlfelder, “A comparison of the chemical and engineering characteristics of Ancient Roman hydraulic concrete with a modern reproduction of Vitruvian hydraulic concrete,” *Archaeometry*, vol. 50, no. 4, pp. 576–590, 2008, doi: 10.1111/j.1475-4754.2007.00371.x.

[41] D. F. Griffin and R. L. Henry, *The effect of salt in concrete on compressive strength, water vapor transmission, and corrosion of reinforcing steel: Y-R007-05-012*. Port Hueneme, California: U.S. Naval Civil Engineering Laboratory.

[42] T. U. Mohammed, H. Hamada, and T. Yamaji, “Performance of seawater-mixed concrete in the tidal environment,” *200528-004900*, vol. 34, no. 4, pp. 593–601, 2004, doi: 10.1016/j.cemconres.2003.09.020.

[43] J. Xiao, C. Qiang, A. Nanni, and K. Zhang, “Use of sea-sand and seawater in concrete construction: Current status and future opportunities,” *Construction and Building Materials*, vol. 155, pp. 1101–1111, 2017, doi: 10.1016/j.conbuildmat.2017.08.130.

[44] L. Rovero, U. Tonietti, F. Fratini, and S. Rescic, “The salt architecture in Siwa oasis – Egypt (XII–XX centuries),” *Construction and Building Materials*, vol. 23, no. 7, pp. 2492–2503, 2009, doi: 10.1016/j.conbuildmat.2009.02.003.

[45] L. Shen *et al.,* “Factory-level measurements on CO2 emission factors of cement production in China,” *Renewable and Sustainable Energy Reviews*, vol. 34, pp. 337–349, 2014, doi: 10.1016/j.rser.2014.03.025.

[46] M. Kurakake, M. Noguchi, K. Fujioka, and T. Komaki, “Effects on Maize Starch Properties of Heat-treatment with Water–ethanol Mixtures,” *Journal of Cereal Science*, vol. 25, no. 3, pp. 253–260, 1997, doi: 10.1006/jcrs.1996.0097.

[47] X. Mu *et al.,* “Porous polymeric materials by 3D printing of photocurable resin,” *Mater. Horiz.*, vol. 4, no. 3, pp. 442–449, 2017, doi: 10.1039/C7MH00084G.

[48] K. Wi, V. Suresh, K. Wang, B. Li, and H. Qin, “Quantifying quality of 3D printed clay objects using a 3D structured light scanning system,” *Additive Manufacturing*, vol. 32, p. 100987, 2020, doi: 10.1016/j.addma.2019.100987.

Dispersive waves in elastic plates with the application of the symbolic programming

Rudolf Pušenjak[1]

[1]*Faculty of Industrial Engineering Novo mesto, Šegova ulica 112, 8000 Novo mesto, Slovenia*
E-mail: rudolf.pusenjak@fini-unm.si

***Abstract**: The article presents a computer approach for the unified derivation of dispersion relations in elastic plates by using symbolic programming. By means of the developed computer program, dispersion relations of various types of propagation of waves in isotropic elastic plates are obtained. The focus is intended to the treatment of the Rayleigh-Lamb waves due to the great importance in the non-destructive testing of large structures. The construction of dispersion curves for Rayleigh-Lamb waves requires the numerical calculation of roots of transcendental dispersion relations, which is achieved by using Newton-Raphson method and arc-length continuation of branches of dispersion curves.*

***Keywords:** dispersive waves, elastic plates, Rayleigh-Lamb waves, Newton-Raphson method*

***Article Classification:** Scientific paper*

1 INTRODUCTION

Propagation of guided, especially Rayleigh-Lamb waves, is widely applied in non-destructive testing of geometrically large structures such as metal plates, sheets and composites [1,2]. Guided waves in such structures are dispersive and are described by means of dispersion relations. In this paper, the unified methodology of derivation of various types of dispersion relations is presented using the symbolic programming in Mathematica®. Derived dispersion relations are posed in the form of homogeneous transcendental equations, which in particular types of dispersion relations can be resolved analytically, but in the case of Rayleigh-Lamb dispersion relations, which for practice are the most important ones, the numerical solving of dispersion equations is inevitable. On the basis of the previous research [3], the Newton-Raphson iterative method is proposed for numerical computation of roots of Rayleigh-Lamb dispersion equations. The reason for such a choice lies in fact, that Newton-Raphson method enables the calculation of real, imaginary and complex wavenumbers in a completely natural way. However, due to the multi-valued solutions, the original Newton-Raphson method must be supplemented with the ability to follow individual branches in a multitude of dispersion curves. This goal was successfully reached by the application of the arc-length continuation method [3].

2 WAVE EQUATIONS OF HOMOGENEOUS ISOTROPIC ELASTIC PLATES

Wave equations of homogeneous isotropic elastic plates are derived from governing equations of the general 3D problem of isotropic elastic solid in terms of components of stress and strain tensor. Governing equations consist of equation of motion, of Hooke's law, which relates the components of stress tensor to the components of strain tensor and of Cauchy relation between components of strain tensor and partial derivatives of displacements [4]:

$$\begin{aligned} &\sigma_{ij,j} + \rho f_i = \rho \ddot{u}_i, \qquad (i,j=1,2,3) \\ &\sigma_{ij} = \lambda \varepsilon_{kk} \delta_{ij} + 2\mu \varepsilon_{ij}, \\ &\varepsilon_{ij} = \frac{1}{2}\left(u_{i,j} + u_{j,i}\right). \end{aligned} \tag{1.a,b,c}$$

In equations (1.a,b,c), u_i denote the components of the displacement vector and $\ddot{u}_i$ denote partial derivatives of second order of displacement components over the time (or the components of generalized accelerations). Through σ_{ij} the components of the stress tensor are denoted, while ε_{ij} represent the components of the strain tensor. Through f_i the components of the body forces on the unit of the mass if present may be specified, ρ denotes the mass density on the unit of volume, λ and μ are Lame's constants and δ_{ij} represents Kronecker symbol. The Einstein's convention of summation for indexes *i,j* or *k*, when repeated, is used.

In this paper, we shall treat dispersion relations of plates under assumption that external forces do not act on the body and will set f_i=0. We shall consider the geometric properties of plates such as shown in Fig. 1, where it is assumed that the wave propagates in the direction of the x_1-coordinate, in which the plate is unbounded in both the positive and negative directions. The half width of the plate is denoted by *h*. It is further assumed that stress state remains unchanged in the direction of the x_3-coordinate, as a result of which the original 3D problem can be reduced to a planar problem in the x_1-x_2 plane.

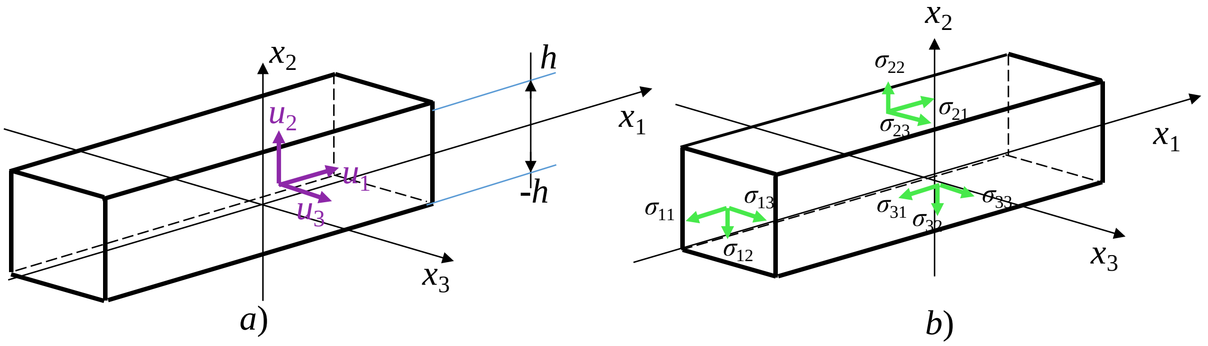

Figure 1: Geometric properties of homogeneous isotropic elastic plate
a) components of the displacement vector, b) components of the stress tensor

By introducing Caichy relation between strains and displacements into Hooke's law and after that by putting the obtained result into equation of motion, we derive the Navier's equation

$$(\lambda+\mu)u_{j,ji}+\mu u_{i,jj}=\rho\ddot{u}_i, \tag{2}$$

Instead of the Navier's equation in the component form it is advantageous to apply the equation in the compact vector form:

$$(\lambda+\mu)\nabla\nabla\mathbf{u}+\mu\nabla^2\mathbf{u}=\rho\ddot{\mathbf{u}}, \qquad \mathbf{u}=(u_1,u_2,u_3), \tag{3}$$

where ∇^2 denotes the Laplace operator. The system of equations (3) is coupled, but can be decoupled by using Helmholtz decomposition. To achieve this, the displacement vector $\mathbf{u}$=(u_1,u_2,u_3) is formed by the sum of the gradient of the scalar potential φ and the rotor of the vector potential $\mathbf{\Psi}=\left(\Psi_{x_1},\Psi_{x_2},\Psi_{x_3}\right)$. The rotor operation is not unique, so we additionally require that divergence of the vector potential is equal zero. Therefore, the Helmholtz decomposition is performed by applying the pair of equations

$$\mathbf{u}=\nabla\varphi+\nabla\times\mathbf{\Psi}, \qquad \nabla\mathbf{\Psi}=0. \tag{4.a,b}$$

By putting Eq. (4.a) into Eq. (3) and by following the rules $\nabla\cdot\nabla\varphi=\nabla^2\varphi,\ \nabla\cdot(\nabla\times\mathbf{\Psi})=0$, the Navier's equation is transformed to the decomposed form

$$\nabla\left[(\lambda+2\mu)\nabla^2\varphi-\rho\ddot{\varphi}\right]+\nabla\times\left[\mu\nabla^2\mathbf{\Psi}-\rho\ddot{\mathbf{\Psi}}\right]=\mathbf{0}, \tag{5}$$

which reveals that the displacement vector (4.a) is a solution to the Navier's equation (3) if it satisfies the following wave equations

$$\begin{aligned}&\nabla^2\varphi-\frac{\rho}{(\lambda+2\mu)}\ddot{\varphi}=0, && c_L=\sqrt{\frac{\lambda+2\mu}{\rho}},\\ &\nabla^2\mathbf{\Psi}-\frac{\rho}{\mu}\ddot{\mathbf{\Psi}}=0, && c_T=\sqrt{\frac{\mu}{\rho}},\end{aligned} \tag{6.a,b}$$

where c_L denotes the longitudinal and c_T the transversal wave velocity, respectively. Therefore, two kinds of wave motion propagate in elastic solid, where the first one is the pressure wave of the scalar potential and the second is the shear wave of the vector potential. From both Eqs. (6.a,b) it also follows that pressure wave at positive values of Lame's constants propagates faster than the shear wave.

2.1 Dispersion relations of wave propagation in homogeneous isotropic elastic plates

We can now derive dispersion relations of wave propagation in homogeneous isotropic elastic plates, but the aim of this paper is to derive the relations in the form of more general characteristic equation. For example, the celebrated Rayleigh-Lamb dispersion relations of guided waves in elastic plate, which are so important in non-destructive testing of materials, will be obtained by properly choosing the constants of the characteristic equation. According to the Fig. 1, the wave equations (6.a,b) are considered in the Cartesian coordinate system, whereby all potential variations in the direction of the x_3-coordinate are excluded by $\partial/\partial x_3=0$. To reach the aforementioned goal we must assume that all three components of the vector potential are nonzero, because of which the components of the displacement vector in Eq. (4.a) have the following form

$$u_1=\frac{\partial\varphi}{\partial x_1}+\frac{\partial\Psi_{x_3}}{\partial x_2},\quad u_2=\frac{\partial\varphi}{\partial x_2}-\frac{\partial\Psi_{x_3}}{\partial x_1},\quad u_3=\frac{\partial\Psi_{x_2}}{\partial x_1}-\frac{\partial\Psi_{x_1}}{\partial x_2}. \tag{7}$$

The outer surfaces of the plate located at heights $x_2=\pm h$ are traction-free, which requires the fulfilment of 6 boundary conditions

$$\sigma_{21}(x_1,\pm h,t)=\sigma_{22}(x_1,\pm h,t)=\sigma_{23}(x_1,\pm h,t)=0. \tag{8}$$

The components of the stress tensor occurring in these boundary conditions are depicted in Fig. 1.b and can be expressed by putting Eq. (7) into Eq. (1.b):

$$\begin{aligned}
\sigma_{21}&=\mu\left(u_{1,2}+u_{2,1}\right)=\mu\left(2\frac{\partial^2\varphi}{\partial x_1\partial x_2}+\frac{\partial^2\Psi_{x_3}}{\partial x_2^2}-\frac{\partial^2\Psi_{x_3}}{\partial x_1^2}\right),\\
\sigma_{22}&=(\lambda+2\mu)u_{2,2}+\lambda u_{1,1}=\lambda\left(\frac{\partial^2\varphi}{\partial x_1^2}+\frac{\partial^2\varphi}{\partial x_2^2}\right)+2\mu\left(\frac{\partial^2\varphi}{\partial x_2^2}-\frac{\partial^2\Psi_{x_3}}{\partial x_1\partial x_2}\right),\\
\sigma_{23}&=\mu u_{3,2}=\mu\left(\frac{\partial^2\Psi_{x_2}}{\partial x_1\partial x_2}-\frac{\partial^2\Psi_{x_1}}{\partial x_2^2}\right).
\end{aligned} \tag{9.a,b,c}$$

In the sequel we shall treat propagation of harmonic waves only. By using Fourier transform, the Cauchy's problem of propagation of arbitrary wave forms of wave equations (6,a,b) can be studied [4]. This topic is highly interesting but lies far beyond the scope of this paper. The ansatzes for harmonic wave of the scalar potential and the components of the vector potential are of the form

$$\begin{aligned}
\varphi(x_1,x_2,t)&=f(x_2)e^{i(kx_1-\omega t)}, &&\left(i=\sqrt{-1}\right),\\
\Psi_{x_j}(x_1,x_2,t)&=g_j(x_2)e^{i(kx_1-\omega t)}, &&(j=1,2,3),
\end{aligned} \tag{10.a,b}$$

where the parameter k denotes the wavenumber and ω is the angular frequncy of the wave. The harmonic wave does'nt need to fulfill any initial conditions due to the unboudness of the plate in x_1-coordinate direction, that is in the direction of the wave propagation. By puting ansatz (10.a) into wave equattion (6.a) and ansatzes (10.b) into individual components of wave equation (6.b) we get the system of ordinary differential equations from which we can determine unknown functions $f(x_2)$ and $g_j(x_2)$, j=1,2,3:

$$\begin{aligned}
&\frac{d^2f}{dx_2^2}+\left(\frac{\omega^2}{c_L^2}-k^2\right)f=0, && \alpha^2=\frac{\omega^2}{c_L^2}-k^2,\\
&\frac{d^2g_j}{dx_2^2}+\left(\frac{\omega^2}{c_T^2}-k^2\right)g_j=0, && \beta^2=\frac{\omega^2}{c_T^2}-k^2, \qquad (j=1,2,3)
\end{aligned} \tag{11.a,b}$$

where two new parameters α and β are introduced denoting the pressure- and shear wavenumber, respectively. General solutions of Eqs. (11.a,b) are

$$\begin{aligned} f\left(x_2\right) &= A_1\cos\left(\alpha x_2\right)+A_2\sin\left(\alpha x_2\right) \\ g_j\left(x_2\right) &= B_{j,1}\cos\left(\beta x_2\right)+B_{j,2}\sin\left(\beta x_2\right), \qquad \left(j=1,2,3\right), \end{aligned} \tag{12.a,b}$$

where A_1, A_2, $B_{j,1}$, $B_{j,2}$ (j=1,2,3) represent 8 unknown constants that need to be determined. The number of unknown constants is for two constants greater than the number of equations obtained by fulfilling the boundary conditions (8). Therefore, two equations are missing for the solvability of the system of equations, which can be obtained if the divergence conditions provided by Eq. (4.b) are included. We have to set the divergence conditions on both boundary surfaces of the plate, i.e. at $x_2=\pm h$ in the following form

$$\frac{\partial \Psi_{x_1}}{\partial x_1}+\frac{\partial \Psi_{x_2}}{\partial x_2}=0, \qquad \left(x_2=\pm h\right). \tag{13}$$

By using Eqs. (10,b) and (12.b) we can write the divergence conditions in the explicit form:

$$\left[\left(ikB_{1,1}+\beta B_{2,2}\right)\cos\left(\beta x_2\right)+\left(ikB_{1,2}-\beta B_{2,1}\right)\sin\left(\beta x_2\right)\right]e^{i\left(kx_1-\omega t\right)}=0, \qquad \left(x_2=\pm h\right), \tag{14}$$

where we see that two of the four constants, e.g. $B_{1,2}$ and $B_{2,2}$ can be expressed by two other constants and eliminated from the remaining equations of the system. In this way, we obtain a reduced system with six homogeneous transcendental equations containing six unknowns, which can be written in the following matrix form

$$\mathbf{H}\cdot\mathbf{A}=\mathbf{0}, \tag{15}$$

where **H** denotes the matrix of homogeneous system of equations and **A** the column vector consisting of unknown constants, respectively. The column vector **A** has the form $\mathbf{A}=(A_1, A_2, B_{2,1}, B_{3,1}, B_{3,2}, B_{1,1})^{\mathrm{T}}$, where superscript T denotes the vector transposition. Nontrivial solutions of the matrix equation (15) are obtained, when the determinant of the matrix **H** vanishes:

$$Det\left[\mathbf{H}\right]=0. \tag{16}$$

The obtained Eq. (16) is the characteristic equation, the solution of which leads to the generalized dispersion relation of homogeneous isotropic elastic plate.

When determining the unknown constants, as well as to obtain more compact dispersion relations, it is useful to use an identity that can be derived from slightly reformulated Eqs. (11.a,b) and then making use of Eqs. (6.a,b). In this way, we obtain the relation:

$$\alpha^2+k^2=\frac{\omega^2}{c_L^2}, \qquad \beta^2+k^2=\frac{\omega^2}{c_T^2}, \qquad \Rightarrow \qquad \frac{\alpha^2+k^2}{\beta^2+k^2}=\frac{c_T^2}{c_L^2}=\frac{\mu}{\lambda+2\mu}. \tag{17}$$

The obtained Eq. (17) can be further recast to the form

$$\left(\lambda+2\mu\right)\left(\alpha^2+k^2\right)=\mu\left(\beta^2+k^2\right) \qquad \Rightarrow \qquad \lambda\left(\alpha^2+k^2\right)+2\mu\alpha^2=\mu\left(\beta^2-k^2\right), \tag{18}$$

which represents the desired identity.

2.1.1. Symbolic derivation of dispersion relations in programming environment Mathematica®

The Mathematica® software system is one of many software systems that enable symbolic computation, derivations and performing of proof procedures. In this paper, the programming system Mathematica® is used to derivation of generalized dispersion relations (16) in homogeneous isotropic elastic plates by following the procedure, explained in previous sections. It is worth noting that derivation process can be easily implemented on the case of three-layer plate with strongly contrasting geometric and material properties. The derivation process consists of symbolic programming of Eqs. (7-15) and leads in the first step to the output of the matrix **H**, shown in Figure 2.

$$\begin{pmatrix}
(k^2\mu-\beta^2\mu)\,\mathrm{Cos}[h\,\alpha] & (k^2\mu-\beta^2\mu)\,\mathrm{Sin}[h\,\alpha] & 0 & 0 & 2\,i\,k\,\beta\,\mu\,\mathrm{Sin}[h\,\beta] & -2\,i\,k\,\beta\,\mu\,\mathrm{Cos}[h\,\beta] \\
(k^2\mu-\beta^2\mu)\,\mathrm{Cos}[h\,\alpha] & (-k^2\mu+\beta^2\mu)\,\mathrm{Sin}[h\,\alpha] & 0 & 0 & -2\,i\,k\,\beta\,\mu\,\mathrm{Sin}[h\,\beta] & -2\,i\,k\,\beta\,\mu\,\mathrm{Cos}[h\,\beta] \\
-2\,i\,k\,\alpha\,\mu\,\mathrm{Sin}[h\,\alpha] & 2\,i\,k\,\alpha\,\mu\,\mathrm{Cos}[h\,\alpha] & 0 & 0 & (k^2\mu-\beta^2\mu)\,\mathrm{Cos}[h\,\beta] & (k^2\mu-\beta^2\mu)\,\mathrm{Sin}[h\,\beta] \\
2\,i\,k\,\alpha\,\mu\,\mathrm{Sin}[h\,\alpha] & 2\,i\,k\,\alpha\,\mu\,\mathrm{Cos}[h\,\alpha] & 0 & 0 & (k^2\mu-\beta^2\mu)\,\mathrm{Cos}[h\,\beta] & (-k^2\mu+\beta^2\mu)\,\mathrm{Sin}[h\,\beta] \\
0 & 0 & (k^2\mu+\beta^2\mu)\,\mathrm{Cos}[h\,\beta] & \left(-i\,k\,\beta\,\mu-\frac{i\,\beta^3\mu}{k}\right)\mathrm{Sin}[h\,\beta] & 0 & 0 \\
0 & 0 & (k^2\mu+\beta^2\mu)\,\mathrm{Cos}[h\,\beta] & \left(i\,k\,\beta\,\mu+\frac{i\,\beta^3\mu}{k}\right)\mathrm{Sin}[h\,\beta] & 0 & 0
\end{pmatrix}$$

Figure 2: Output of symbolic computation of the matrix **H**

The programming system Mathematica® has embedded functions that can symbolically compute the determinant of the matrix **H** shown in Fig. 2 and then find the solution of the equation *Det*[**H**]=0. The result is the following coupled dispersion relation

$$\begin{aligned} Det[\mathbf{H}] = \Big[& 16\alpha\beta k^2\left(k^2-\beta^2\right)^2+\left(k^4+\beta^4-2k^2\beta(2\alpha+\beta)\right)^2\cos\left[2h(\alpha-\beta)\right] \\ & -\left(k^4+\beta^4+2k^2\beta(2\alpha-\beta)\right)^2\cos\left[2h(\alpha+\beta)\right]\Big]\sin(2h\beta)=0. \end{aligned} \tag{19}$$

The matrix equation (15) can be decoupled to obtain dispersion relations of most well-known types of waves. For this purpose, we perform a series of algebraic manipulations that preserve the value of the determinant, but transform the matrix **H** into a block-diagonal scheme **H***. The symbolically computed block-diagonal matrix **H*** has the form shown in the Fig. 3.

$$\begin{pmatrix}
(2\,k^2\mu-2\,\beta^2\mu)\,\mathrm{Sin}[h\,\alpha] & 4\,i\,k\,\beta\,\mu\,\mathrm{Sin}[h\,\beta] & 0 & 0 & 0 & 0 \\
4\,i\,k\,\alpha\,\mu\,\mathrm{Cos}[h\,\alpha] & 2\,(k^2-\beta^2)\,\mu\,\mathrm{Cos}[h\,\beta] & 0 & 0 & 0 & 0 \\
0 & 0 & -4\,i\,k\,\alpha\,\mu\,\mathrm{Sin}[h\,\alpha] & (2\,k^2\mu-2\,\beta^2\mu)\,\mathrm{Sin}[h\,\beta] & 0 & 0 \\
0 & 0 & 2\,(k^2-\beta^2)\,\mu\,\mathrm{Cos}[h\,\alpha] & -4\,i\,k\,\beta\,\mu\,\mathrm{Cos}[h\,\beta] & 0 & 0 \\
0 & 0 & 0 & 0 & \left(-2\,i\,k\,\beta\,\mu-\frac{2\,i\,\beta^3\mu}{k}\right)\mathrm{Sin}[h\,\beta] & 0 \\
0 & 0 & 0 & 0 & 0 & 2\,(k^2+\beta^2)\,\mu\,\mathrm{Cos}[h\,\beta]
\end{pmatrix}$$

Figure 3: The block-diagonal matrix **H***

In the transformation of the matrix **H** into the block-diagonal matrix **H*** we must recognize that interchanging of individual columns of the original matrix causes shuffling the order of components of the vector **A.** The new order of components corresponds to the vector **A***=(A_2, $B_{3,2}$, A_1, $B_{1,1}$, $B_{3,1}$, $B_{2,1}$)^T. The matrix **H*** consists from three diagonal blocks, to which correspond three determinants D_j, j=1,2,3, whereas equations D_j=0, j=1,2,3 have the meaning of three dispersion relations. These dispersion relations are:

a) in the case that $A_2 \neq 0$, $B_{3,2} \neq 0$ and all remaining constants are equal zero, $A_1=B_{1,1}=B_{3,1}=B_{2,1}=0$, we obtain the Rayleigh-Lamb dispersion relation

$$D_1=\left(k^2-\beta^2\right)^2\sin(\alpha h)\cos(\beta h)+4k^2\alpha\beta\cos(\alpha h)\sin(\beta h)=0, \Rightarrow \frac{\tan(\alpha h)}{\tan(\beta h)}+\frac{4k^2\alpha\beta}{\left(k^2-\beta^2\right)^2}=0. \tag{20}$$

The Rayleigh-Lamb dispersion relation (20) describes the propagation of symmetric waves in respect to the plane x_2=0.

b) in the case that $A_1 \neq 0$, $B_{1,1} \neq 0$ and all remaining constants are equal zero, $A_2=B_{3,2}=B_{3,1}=B_{2,1}=0$, we also obtain the Rayleigh-Lamb dispersion relation, however in this case the relation (21) describes the propagation of asymmetric waves in respect to the plane x_2=0

$$D_2=\left(k^2-\beta^2\right)^2\cos(\alpha h)\sin(\beta h)+4k^2\alpha\beta\sin(\alpha h)\cos(\beta h)=0, \Rightarrow \frac{\tan(\alpha h)}{\tan(\beta h)}+\frac{\left(k^2-\beta^2\right)^2}{4k^2\alpha\beta}=0. \tag{21}$$

Both obtained Rayleigh-Lamb dispersion relations (20) and (21) are homogeneous transcendental equations, whose roots are wavenumbers k in dependence on the angular frequency ω (or vice versa). These roots cannot be obtained analytically in closed forms, but can be computed by means of various numerical methods.

c) in the case that $B_{3,1} \neq 0$, $B_{2,1} \neq 0$ and all remaining constants are equal zero, $A_2=B_{3,2}=A_1=B_{1,1}=0$, we obtain dispersion relation

$$D_3 = \sin(\beta h)\cos(\beta h) = 0, \tag{22}$$

which is solvable analytically in closed form. Roots of Eq. (22) are

$$\beta h = \frac{n\pi}{2}, \qquad (n = 0,1,2,3,\ldots) \tag{23}$$

and they determine the conditions under which the secondary, horizontally polarized waves (SH waves) can propagate in the plate. By choosing the value of angular frequency ω and by computing the shear wavenumber β from Eq. (23) for the selected wave mode n, the wavenumber k is determined with help of Eq. (11.b) as $k=\sqrt{[(\omega/c_T)^2-\beta^2]}$.

All three dispersion relations, Eqs. (20-22) are derived by means of the program, which is written in Mathematica®. By considering relations (11.a,b), these dispersion relations can be presented in the form:

$$D_j(\omega,k) = 0, \qquad (j = 1,2,3). \tag{24}$$

As we have already mentioned, the Mathematica® software system, in addition to the symbolic derivation of dispersion relations, also enables the proof of important theorems. In this article, the following equation is proved in this way:

$$Det[\mathbf{H}] = 16 D_1 D_2 D_3, \tag{25}$$

with the help of which we can justify the claim, that the dispersion relation (19) is a coupled relation.

2.2 Construction of dispersion curves of Rayleigh-Lamb waves in elastic plates

From Eqs. (20) and (21) we can see directly that roots of dispersion equations of Rayleigh-Lamb waves we cannot obtain in closed forms. Due to the importance of the propagation of Rayleigh-Lamb waves in plates for non-destructive testing, many authors offer various numerical methods for constructing the dispersion curves of these waves [5], [6], [7]. In this article, the Newton-Raphson iterative method is proposed for the numerical solving of the dispersion equations (20) and (21), because it represents a natural choice to calculate both real, imaginary and complex wavenumbers in a unified way. The method is basically designed for the calculation of complex wavenumbers $k \in \mathbb{C}$:

$$k = k_{re} + i k_{im}, \qquad \left(i = \sqrt{-1}\right) \tag{26}$$

and in a special case, allows the calculation of real and imaginary wavenumbers by setting either k_{im} or k_{re} equal to zero. For this purpose, the Newton-Raphson method is formulated in the two-dimensional vector space by introducing the vector argument $\mathbf{k}=(k_{re},k_{im})$ and vector function $\mathbf{D}_j=(\mathrm{Re}[D_j(\omega,\mathbf{k})],\mathrm{Im}[D_j(\omega,\mathbf{k})])$,j=1,2. By considering the fact that real part k_{re} and imaginary part k_{im} of the complex wavenumber k are independent of each other, it follows that equations $\mathrm{Re}[D_j(\omega,\mathbf{k})]=0$, $\mathrm{Im}[D_j(\omega,\mathbf{k})]=0$ hold simultaneously. Then the vector argument **k** can be computed in the iterative procedure

$$\mathbf{k}_{n+1} = \mathbf{k}_n - \mathbf{J}^{-1}(\omega,\mathbf{k}_n)\cdot\mathbf{D}_j(\omega,\mathbf{k}_n), \qquad (j=1,2), \tag{27}$$

where the index n denotes the iteration number and $\mathbf{J}(\omega,\mathbf{k})$ means the Jacobean matrix

$$\mathbf{J}(\omega,\mathbf{k}) = \begin{bmatrix} \dfrac{\partial \mathrm{Re}\left[D_j(\omega,\mathbf{k})\right]}{\partial k_{re}} & \dfrac{\partial \mathrm{Re}\left[D_j(\omega,\mathbf{k})\right]}{\partial k_{im}} \\ \dfrac{\partial \mathrm{Im}\left[D_j(\omega,\mathbf{k})\right]}{\partial k_{re}} & \dfrac{\partial \mathrm{Im}\left[D_j(\omega,\mathbf{k})\right]}{k_{im}} \end{bmatrix}. \tag{28}$$

The iterative procedure is repeated until the norm of the difference of two subsequent iterates is less than the prescribed tolerance

$$\left\|\mathbf{k}_{n+1}-\mathbf{k}_n\right\| = \left\|-\mathbf{J}^{-1}\left(\omega,\mathbf{k}_n\right)\cdot\mathbf{D}_j\left(\omega,\mathbf{k}_n\right)\right\| < \mathrm{tol}, \qquad \left(j=1,2\right). \tag{29}$$

The vector space Newton-Raphson method fails if the Jacobean matrix **J**(ω,**k**) is singular. Beside of this, the procedure converges only if the initial guess to the solution is good enough. By the successful employment of the described procedure we obtain one point of the dispersion curve.

In principle, the entire dispersion curve can be constructed by the homotopy process. This means that with a solution corresponding to a point on the dispersion curve, we can obtain an adjacent solution by slightly changing the value of the wavenumber k (or the angular frequency ω) and performing the Newton-Raphson procedure, in which we choose the initial value of the angular frequency ω (or the initial value of the wavenumber k) which is the same as the value in the previously computed solution. Unfortunately, due to the multivalued roots of the dispersion equation, jumps between the dispersion curves occur in this process. An example of the homotopy process is depicted in Fig. 4, where an unsuccessful attempt to construct a dispersion curve of real wavenumbers for the first asymmetric wave mode is shown. The homotopy procedure is flexible enough to start at the top or bottom of the curve. In Fig. 4, for example, it starts at the top of the first asymmetric mode, where the first (highest lying) point is computed by Newton-Raphson iterative procedure. The homotopy procedure then decrements the wavenumber k for a prescribed value (of course, the incrementing the wavenumber k would be applied, when starting from the bottom of the curve) and uses the computed value of frequency ω as the starting value for the next iterative step. In Fig. 4, the homotopy procedure is successful in 10 subsequent points, but then it follows an unexpected jump to the curve of the next asymmetric mode.

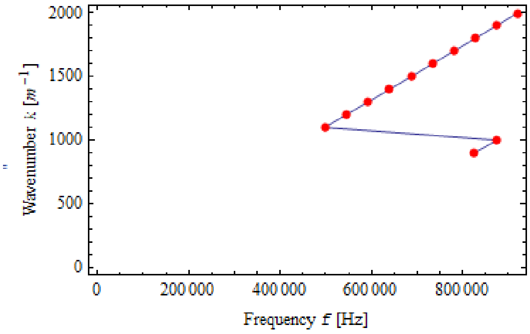

Figure 4: Jumping between dispersion curves of asymmetric wave modes during a homotopy process

After two points on this dispersion curve are computed, the Newton-Raphson iterative process no longer converges and the construction cannot continue.

2.2.1. Arc-length continuation

In order to prevent undesired jumping between wave modes, but in the same time to reduce the number of iterations required that the solution converges, an arc-length continuation combined with cubic extrapolation is used to predict the next point of the dispersion curve. Let $\mathbf{p}_0=(\omega_0,\mathbf{k}_0)$, $\mathbf{p}_1=(\omega_1,\mathbf{k}_1)$, $\mathbf{p}_2=(\omega_2,\mathbf{k}_2)$ and $\mathbf{p}_3=(\omega_3,\mathbf{k}_3)$ be known points, computed by the homotopy process to predict the next point $\mathbf{p}_4=(\omega_4,\mathbf{k}_4)$ by extrapolation, whereat the prescribed arc length Δs is chosen. To achieve this, the arc length l is used as parameter so that l_i corresponds to $\mathbf{p}_i$, $i=0,1,\ldots,3$ and corresponding arc lengths are l_0, $l_1=s_1$, $l_2=l_1+s_2$, $l_3=l_2+s_3$, $l_4=l_3+\Delta s$. The extrapolated point $\mathbf{p}_4$ is then calculated by help of the formula

$$\mathbf{p}_4=\sum_{i=0}^{3}\left(\prod_{\substack{j=0,\\ j\neq i}}^{3}\frac{l_4-l_j}{l_i-l_j}\right)\mathbf{p}_i, \tag{30}$$

where the arc-length increments s_i (i=1,2,3) are computed as

$$s_i=\left|\mathbf{p}_i-\mathbf{p}_{i-1}\right|=\sqrt{\sum_{j=1}^{N_f+1}\left[\mathbf{p}_i\left(j\right)-\mathbf{p}_{i-1}\left(j\right)\right]^2} \tag{31}$$

and N_f denotes the number of components of the wavenumber vector **k**. It is obvious that $N_f=1$ in the case of real or imaginary wavenumbers and $N_f=2$ for complex wavenumbers. The choice of the incremental length Δs is determined by the principal curvature of the hyperspace curve.

3 RESULTS AND DISCUSSION

In this section, the results of the presented numerical method for construction of dispersion curves of Lamb waves in a plate are shown. Analyzed are dispersion curves of real, imaginary and complex wavenumbers in an aluminum plate with the longitudinal wave velocity c_L =6300 m/s, the transverse wave velocity c_T=3100 m/s and half- thickness of the plate h=4 mm. The construction of dispersion curves is carried out in the frequency range 0 - 1 MHz, whereby the circular frequency ω is converted into frequency f using equation $\omega=2\pi f$. In all figures, the symmetric modes of Lamb waves are shown by continuous and asymmetric modes by dashed curves, respectively. The dispersion curves are computed in Mathematica programming environment, using the strong support of symbolic computing.

3.1 Dispersion curves of Lamb waves for real wavenumbers

Lamb waves with real wavenumbers represent harmonic traveling waves, which propagate with constant amplitude in x_1-coordinate direction. Dispersion curves of Lamb waves for real wavenumbers are easily obtained if the vector argument is replaced by only one component, i.e. $\mathbf{k}=k=k_{re}$ (k_{im}=0). Furthermore, the Jacobean matrix (28) is reduced to a single element, $\mathbf{J}(\omega,k_{re})=\partial D_j(\omega,k_{re})/\partial k_{re}$, ($j$=1,2) so that iterates of Eq. (27) takes the form

$$k_{re,n+1}=k_{re,n}-\frac{D_j\left(\omega,k_{re,n}\right)}{\frac{\partial D_j\left(\omega,k_{re,n}\right)}{\partial k_{re}}},\qquad \left(j=1,2\right), \tag{32}$$

In general, there is a multiplicity of dispersion curves in each selected frequency interval, the calculation of which is time consuming. To keeping the processing time within a reasonable limit, the computer program prescribes the number of symmetric and corresponding asymmetric modes of Lamb waves that we want to calculate. In the Fig. 5, first three symmetric and corresponding asymmetric modes of real wavenumbers are shown.

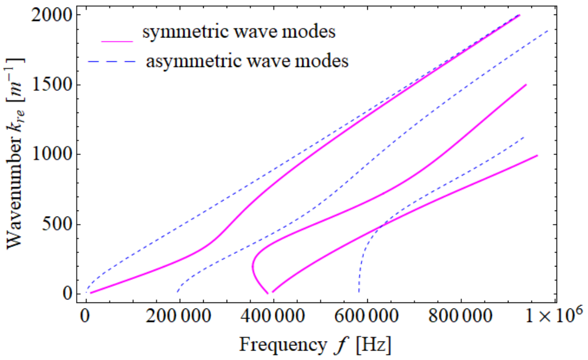

Figure 5: Dispersion curves of Lamb waves for real wavenumbers

3.2 Dispersion curves of Lamb waves for imaginary wavenumbers

Lamb waves with imaginary wavenumbers are called evanescent waves, because they do not propagate but only oscillate depending on the time in such a manner that the amplitude of the oscillation is exponentially decayed in x_1-coordinate direction. In section 2.2 it was mentioned that dispersion curves for imaginary wavenumbers can be constructed as the special case of the vector space method. However, there exists an alternative way, which enables that the construction of dispersion curves can proceed in the same way as for real wavenumbers. If wavenumber is pure imaginary, it can be written as $k=i\cdot k_{im}$. Inserting this substitution into Eqs. (11.a,b) and rename α and β as α_{im} and β_{im}, we get

$$\begin{gathered}\alpha_{im}=\sqrt{\left(\frac{\omega}{c_L}\right)^2+k_{im}{}^2},\quad \beta_{im}=\sqrt{\left(\frac{\omega}{c_T}\right)^2+k_{im}{}^2},\\ \frac{\tan\left(\beta_{im}h\right)}{\tan\left(\alpha_{im}h\right)}+\left\{\frac{4k_{im}{}^2\alpha_{im}\beta_{im}}{\left[2k_{im}{}^2+\left(\frac{\omega}{c_T}\right)^2\right]^2}\right\}^{\pm1}=0.\end{gathered} \tag{33}$$

First three symmetric and corresponding asymmetric modes of imaginary wavenumbers are shown in Figure 6.

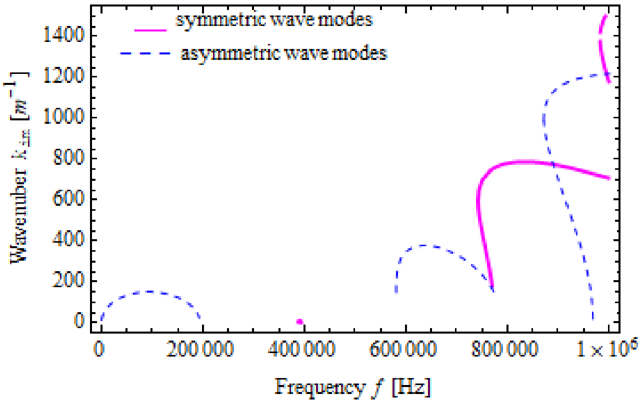

Figure 6: Dispersion curves of Lamb waves for imaginary wavenumbers

3.3 Dispersion curves of Lamb waves for complex wavenumbers

Lamb waves with complex wavenumbers are traveling waves, which propagate with exponentially decayed amplitude in x_1-coordinate direction. For complex wavenumbers, the presented vector space method is used for the construction of dispersion curves. However, in this case is necessary to separately present the course of the real and imaginary part of the complex wavenumber as a function of frequency. An example of dispersion curves with complex wavenumbers is presented in Fig. 7. Figures 7.a and 7.b, respectively show only an individual symmetric wave mode, depicted by continuous line and a corresponding asymmetric wave mode, depicted by dashed line. Unlike the finite number of wave modes appearing in the selected frequency interval for real and imaginary wavenumbers, there are infinitely many wave modes for complex wave numbers [8].

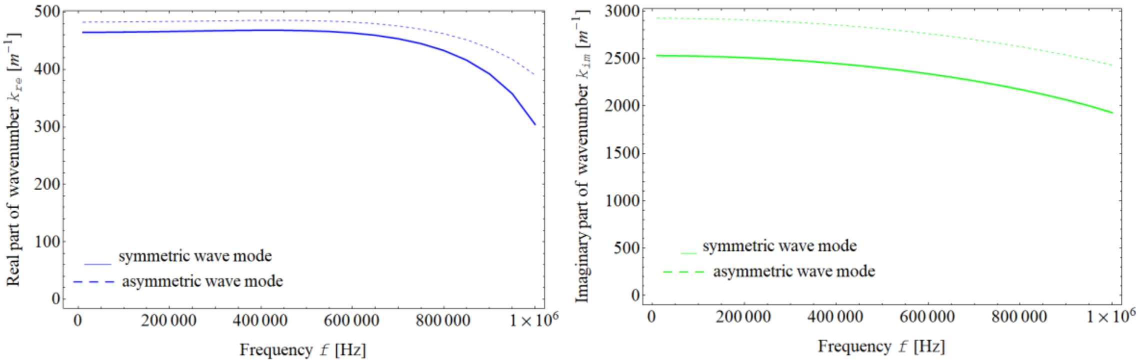

a) b)

Figure 7: Dispersion curves of Lamb waves for complex wavenumbers
a) real part of complex wavenumbers, b) imaginary part of complex wavenumbers

4 CONCLUSION

In the article, a generalized route to derivation of dispersion relations in homogeneous isotropic elastic plates is developed that is implemented by means of symbolic computing. The presented methodology can be upgraded to derivation of dispersion relations in three-layered plates with strongly inhomogeneous geometric and material properties. The derived dispersion relations have the form of homogeneous transcendental equations, which solutions are a multiplicity of roots, representing wavenumbers at selected angular frequency or vice versa. In construction of dispersion curves of Rayleigh-Lamb waves an advanced vector space Newton-Raphson method is used, which is supplemented for branch tracing of curves by means of an arc-length continuation method.

REFERENCES

[1] HARB, M. S.,.YUAN, F. G. Non-contact ultrasonic technique for Lamb wave characterization in composite plates. *Ultrasonics*. 2016, 64, 162-169.
[2] PODDAR, B., GIURGIUTIU, V. Complex modes expansion with vector projection using power flow to simulate Lamb waves scattering from horizontal cracks and disbounds. *J. Ac. Soc. of America*. 2016, 140, 2123-2133.
[3] PUŠENJAK, Rudolf. Computation of dispersion curves of Rayleigh-Lamb waves by Newton-Raphson method.

Anali PAZU. 2023, 13(1), 15-32.

[4] ACHENBACH, J. D. Wave propagation in elastic solids. Fourth impression. New York: North Holland, 1984. ISBN: 0 7204 0325 1.

[5] HAKODA, C., ROSE, J., SHOKOUHI, P. and LISSENDEN, C. Using Floquet periodicity to easily calculate dispersion curves and wave structures of homogeneous waveguides. AIP Conference Proceedings 1949. 2018, 020016; https://doi.org/10.1063/1.5031513.

[6] HORA, P., ČERVENA, O. Determination of Lamb wave dispersion curves by means of Fourier transform. *App. Mech. And Com. Mech*. 2012, 6, 5-2133.

[7] GALAN-PINILLA, C. A., E-QUIROGA, J., PEÑA-BALLESTEROS, D. Y., ACOSTA-MINOLI, C. and GONZALEZ-ESTRADA, O. A. Comparative Study of Dispersion Curves for LAMB Waves Using Analytical Solutions and Semi-Analytical Methods. *Appl. Sci.* 2023, 13, 1706. https://doi.org/10.3390/app13031706.

[8] PODDAR, B.,.GIURGIUTIU, V. Scattering of Lamb waves from a discontinuity: An improved analytical approach. *W. Motion*. 2016, 65, 79-91.

Numerical analysis of the velocity field of fluid in a micro calibration bath

Marko Rožič[1], Simon Muhič[2,3]

[1]*School center Novo mesto, Šegova ulica 112, 8000 Novo mesto, Slovenia*
E-mail: marko.rozic@sc-nm.si

[2]*Faculty of Industrial Engineering Novo mesto, Šegova ulica 112, 8000 Novo mesto, Slovenia*
E-mail: simon.muhic@fini-unm.si

[3]*SIMUTEH, Dr. Simon Muhič s.p., Stična 113, 1295 Ivančna Gorica, Slovenia*
E-mail: simon.muhic@simuteh.si

Abstract: *The micro calibration bath OBM is used to calibrate temperature probes. The velocity field of the liquid with which the bath is filled plays an important role in the calibration. The homogeneity of the temperature field in which the temperature probes are calibrated depends on the velocity field. For optimum calibration conditions, we need a stationary and homogeneous temperature field. The paper presents a steady-state simulation of the velocity field using TCAE computational fluid dynamics software for the given bath geometry. In the numerical simulation, the k-ω SST turbulence model with a second order numerical scheme is used. As a result, a stationary and homogeneous velocity field near the centre of the micro bath was calculated. The results are independent of the mesh size and show a low turbulence intensity, confirming a laminar flow in the centre of the micro bath with low turbulent kinetic energy or small velocity fluctuations.*

Keywords: *computational fluid dynamics, numerical simulation, micro calibration bath, velocity field, homogeneity*

Article Classification: *Scientific paper*

1 INTRODUCTION

The portable micro calibration bath OBM is designed for sensor calibration in fluids (Figure 1). Silicone oil is used as the fluid due to its excellent heat transfer properties [1]. Previous work on the micro bath focused on temperature stability and homogeneity [2, 3] as well as testing different types of fluids [4, 5]. In our research, the velocity field in the micro bath is investigated. Velocity field and the temperature field of the fluid are connected. If the velocity field around the probe is turbulent during mixing, temperature fluctuations may occur. This would indicate that the temperature field is unstable, making it difficult to calibrate the probes. Using silicone oil instead of water in the micro bath reduces turbulence because silicone oil at 100 °C is much more viscous (μ_{oil} = 26.781·10^{-3} Pa·s, [6]) than water (μ_{water}= 0.282·10^{-3} Pa·s, [7]) and the viscosity reduces the kinetic energy of the flow [8]. Due to its high viscosity, silicone oil takes longer, about 30 minutes, to stabilize in the micro bath to reach the set temperature of 100°C.

Figure 1: Micro calibration bath OBM

Since the micro bath is not optically transparent, conventional methods for visualizing velocity fields such as adding foreign material, heat and energy or using optical techniques [9] are not easy to use. To calculate and visualize the velocity field of the micro bath TCAE software for computational fluid dynamics was used.

2 METHOD

Computational Fluid Dynamics (CFD) is an important tool in engineering for solving fluid-related problems. It enables the testing and optimization of products prior to production. Computer-aided engineering (CAE) helps to reduce costs, improve quality and speed up time to market. Advances in computers and algorithms have shortened calculation times, making virtual prototyping in modern engineering more cost-effective and efficient [10, 11]. Similarly, CFD is used to analyze the velocity field of a calibrating micro bath. The numerical calculations were performed using TCAE software, which works on the finite volume method discretization technique. The basic relations for the calculation of an incompressible fluid are the law of conservation of mass [12]:

$$\frac{\partial \rho}{\partial t} + \nabla \cdot (\rho \vec{v}) = 0 \tag{1}$$

where ρ represents density of fluid and $\vec{v}$ velocity vector. Law of conservation of momentum is defined [12]:

$$\rho \frac{D\vec{v}}{Dt} = \frac{\partial}{\partial t}(\rho \vec{v}) + \nabla \cdot (\rho \vec{v} \vec{v}) \tag{2}$$

where $D\vec{v}/Dt$ represents material derivative. TCAE software solves Reynolds time-averaged Navier-Stokes equations (RANS) with $k - \omega\ SST$ turbulence model. Steady-state model with second-order numerical scheme was used in the presented calculations. Numerical calculations were considered converged when the average velocity was constant, and the residuals decreased below the order of magnitude limit of 10^{-5}. Since the numerical experiment is considered adiabatic, analysis was made without solving the energy equation.

The temperature field in fluids depends on the velocity field of the fluid. The heater in the analyzed micro bath is located at the bottom of the chamber. When the magnetic stirrer at the bottom rotates pushes the silicone oil near the heater. At the top of the bath, the oil flows towards the centre and then moves downwards in the middle. The 3D model of the micro bath was prepared and imported into TCAE software (Figure 2). Boundary conditions for simulations were:

- the viscosity of the silicone oil at 100°C (μ_{oil} = 26.781·10^{-3} Pa·s) and its density (ρ_{oil} = 899.88 kg/m³) [6],
- stirrer rotation speed 800 RPM.

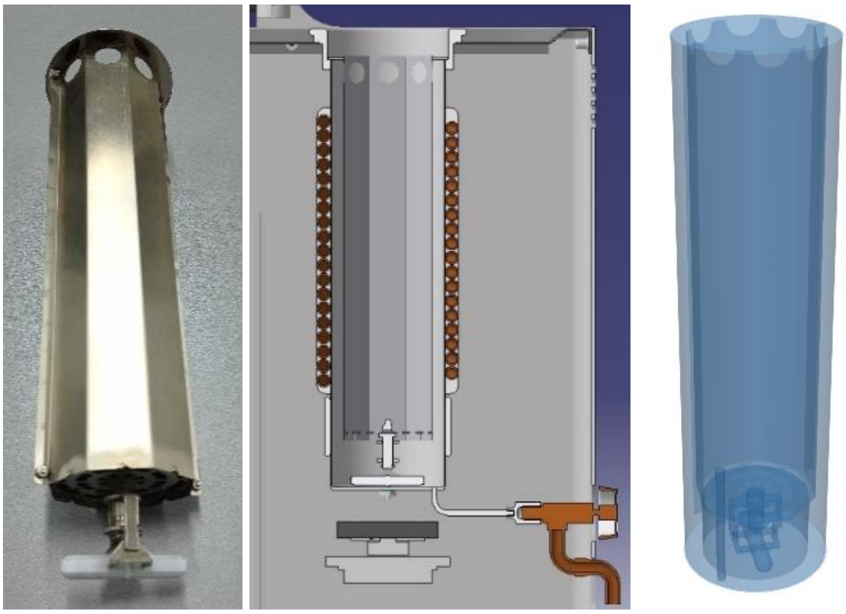

Figure 2: Micro bath chamber (left), cross section (middle), geometry in TCAE (right)

3 RESULTS AND DISCUSSION

An analysis of the independence of the result from the computational mesh was made. Table 1 shows the details of three different mesh types, including parameters such as skewness, non-orthogonality and the maximum y^+ parameter. With y^+ values well below 1, the generated meshes and the chosen $k - \omega\ SST$ turbulence model with Low Reynolds wall treatment is appropriate [13], making the results reliable. Figure 4 shows the details of the mesh near the magnetic stirrer at the bottom of the micro bath, with a constant grid refinement ratio of r = 1.5 for all mesh sizes.

Table 1: Numerical mesh details

mesh	coarse	medium	fine
mesh size (m)	0.009	0.006	0.004
number of mesh cells	248414	614895	1390487
skewness	2.60	6.55	10.74
non-orthogonality	64.88	65.00	64.99
$\overline{y^+}$ (average value)	$1.09 \cdot 10^{-7}$	$0.245 \cdot 10^{-7}$	$0.121 \cdot 10^{-7}$
y^+ (maximum value)	$3.48 \cdot 10^{-7}$	$2.76 \cdot 10^{-7}$	$2.64 \cdot 10^{-7}$

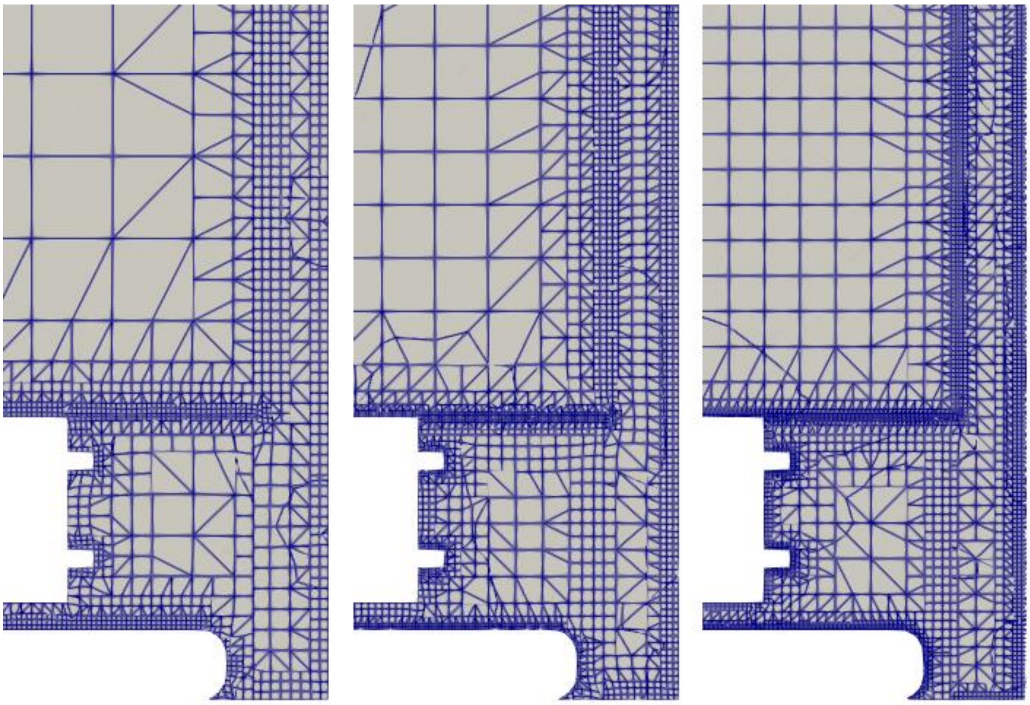

Figure 4: Mesh detail for coarse (left), medium (middle) and fine mesh (right)

Three monitoring probes were positioned in the centre of the micro bath volume (Figure 5). The first probe was located 40 mm above the bottom, the second at 100 mm and the third at 160 mm.

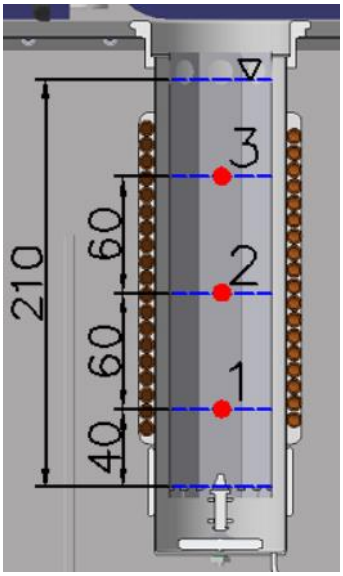

Figure 5: Positions of monitored probes in micro bath

Table 2 shows the velocity components for each monitored probe and mesh type. For example, the velocity component in the z-direction is about 2.5 cm/s in the centre of the chamber and 3.8 cm/s near the bottom (near the magnetic stirrer) and the surface. The high angular velocity of the magnetic stirrer significantly influences the oil velocity near the bottom, while near the surface the direction of the oil flow changes.

Table 2: Numerical results for the average velocity components and the net velocity for each monitored probe

		mesh		
	velocity component	coarse	medium	fine
probe 1	v_x [m/s]	-0.0014	-0.0013	-0.0020
	v_y [m/s]	0.0014	0.0010	0.0016
	v_z [m/s]	-0.0310	-0.0377	-0.0330
	v [m/s]	0.0311	0.0377	0.0331
probe 2	v_x [m/s]	-0.0002	0.0002	-0.0002
	v_y [m/s]	0.0001	-0.0001	0.0003
	v_z [m/s]	-0.0285	-0.0262	-0.0261
	v [m/s]	0.0285	0.0262	0.0261
probe 3	v_x [m/s]	0.0006	-0.0002	0.0003
	v_y [m/s]	-0.0011	-0.0009	-0.0003
	v_z [m/s]	-0.0336	-0.0388	-0.0348
	v [m/s]	0.0336	0.0388	0.0351

To check whether the velocity field is laminar or not, and if it is turbulent, what degree of turbulence it has, the turbulence intensity I must be determined using equation [8]:

$$I = \frac{1}{v} \cdot \sqrt{\frac{2}{3} \cdot k} \tag{3}$$

where v is the absolute velocity (Table 2) and k is turbulence kinetic energy. The prediction of the turbulent kinetic energy in the micro bath chamber is about $2.2 \cdot 10^{-6}$ m^2/s^2 everywhere (Figure 6). The turbulent kinetic energy has a very small value, which means that the fluctuations in velocities are very small [14]. The turbulent kinetic energy is higher in the vicinity of the magnetic stirrer. The velocity fluctuations are more intense there because the silicone oil is mixed very intensively.

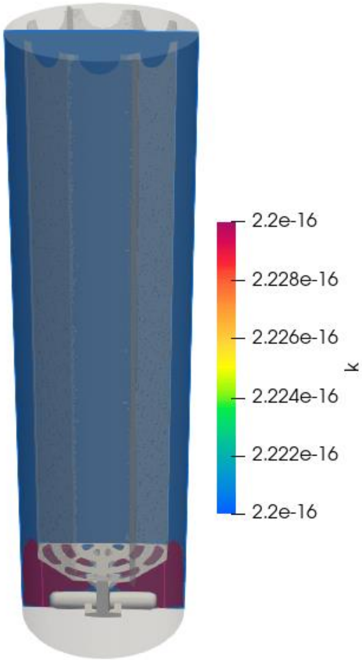

Figure 6: Turbulent kinetic energy in micro bath for fine mesh

Using Equation (3) and the net velocities (Table 2), the turbulence intensity is calculated (Table 3). Since the velocity values fluctuate only minimally in the steady state, the turbulence intensity I is very low (Table 3) and is less than 1 %, indicating low turbulence [8]. This means that the velocity field is fairly laminar and a homogeneous velocity field prevails in the centre of the micro bath chamber.

Table 3: Turbulence intensity for fine mesh

	probe		
	probe 1	probe 2	probe 3
turbulence intensity for fine mesh [10^{-7}]	3.66	4.64	3.45

Figure 7 shows the streamlines of the oil in the micro bath during operation at simulated boundary conditions for a fine numerical mesh. The horizontal planes are located where monitored probes are (Figure 5) and on the surface. It can be clearly seen that a strong vortex flow of the silicone oil occurs at the bottom and on the surface of the micro bath. The reason for this is the rotating magnetic stirrer, which mixes the fluid while the fluid on the surface changes the direction of flow. Near the centre of the micro bath chamber, the liquid flow is laminar and homogeneous. Therefore, we can assume that the silicone oil is well mixed and we do not expect large temperature gradients. These findings make the calibration of the temperature probe more reliable.

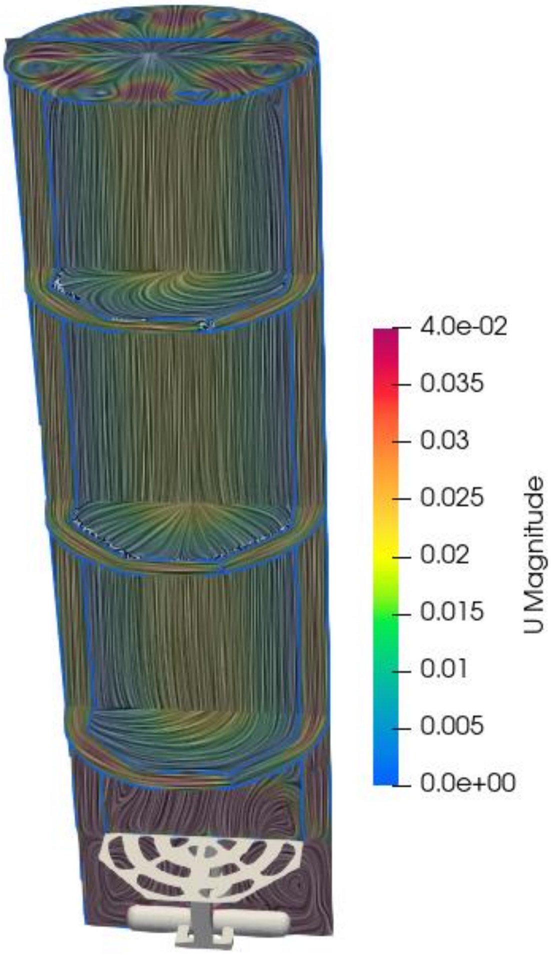

Figure 7: The streamlines of the oil in micro bath during operation of micro bath

4 CONCLUSION

The velocity field of silicone oil in a calibration micro bath was calculated. The grid independence study was made for fluid properties, which corresponds to silicone oil at temperature 100 °C and maximal rotational speed of the analyzed calibration micro bath, 800 RPM.

Vortexes occur in the vicinity of the magnetic stirrer and the oil surface, so that one cannot speak of a homogeneous liquid flow here. The comparison between the net velocity at medium and fine mesh (Table 2) near the point where probe 2 is monitored (Figure 5) shows that the velocity values differ by less than 1 %. Here the flow is laminar and near probe 2, so we can say that the flow is homogeneous, and the results are independent of the mesh size. The kinetic turbulence energy is very low for all points in the micro bath chamber (Figure 6), which shows that the velocity fluctuations are very small. This means that a steady state of the fluid flow is calculated. A small kinetic turbulence energy results in a small turbulence intensity (Table 3), which confirms a laminar flow. The parameter y^+ is also very small (Table 1), which means that the correct $k - \omega\, SST$ turbulence model with Low Reynolds wall treatment was chosen. All these numerical results show that the geometry of the micro calibration bath was prepared correctly, the volume of the micro bath was meshed appropriately and all other settings in the CFD are appropriate.

The simulation focused on high viscosity oil at temperature 100 °C, but future research will include simulations at different temperatures and numerical simulations with different magnetic stirrer speeds will be made. Also, numerical results will be validated by experiment.

REFERENCES

[1] Kambič. *Micro calibraton bath* [Online]. Semič, 2024 [28. 8. 2024]. Available: https://kambicmetrology.com/micro-calibration-bath/.
[2] Pagtalunan, V. C. Establishment of a System for Uniformity and Stability Characterization of Liquid Calibration Bath Used Above Ambient Conditions: 50ºC to 75ºC Settings. *Asia pacific higher education research journal (APHERJ).* 2018, vol. 5, no. 1, pp. 26-35.
[3] Estacio, A. G., Pagtalunan, V. C., Pagtalunana, R. S., Valenzuela, I. C., Tolentino, L. K. S., Dela Cruz, J. C. Characterization of High Temperature Calibration Bath through Stability and Uniformity Tests with Data Acquisition using Standard Platinum Resistance Thermometer and Precision Multimeter. *International Journal of Emerging Trends in Engineering Research.* 2019, vol. 7, no. 10, pp. 388-392.
[4] Rangkuti, W., Tarigan. K., Humaidi, S., Situmorang, M., Frida, E., Darmawan, Y. The Effect of Different Liquid on Temperature Uniformity and Stability in Microbath 7102. *Prisma Sains: Jurnal Pengkajian Ilmu dan Pembelajaran Matematika dan IPA IKIP Mataram*. 2023, vol. 11, no. 2, pp. 550-560.
[5] Pagtalunan, V. C., Tolentino, L. K. S., Estacio A. G., Pagtalunan, R. S. Characterization of Silicon Oil Calibration Bath Through Stability and Uniformity Tests Using Standard Platinum Resistance Thermometer and Precision Multimeter. *International Journal of Engineering Research and Technology*. 2019, vol. 12, no. 5, pp. 705-710.
[6] Anton Paar. *Anton Paar SVM 3001 - Measurement Results* [own archive]. Graz, 2022.
[7] Çengel, Y. A., Ghajar, A. J. *Heat and Mass Transfer: fundamentals & applications*. Fifth Edition. New York: McGraw-Hill Education, 2015. ISBN 978-0-07-339818-1.
[8] Ferziger, J. H., Perić, M., Street, R. L. *Computational Methods for Fluid Dynamics*. Fourth Edition. Switzerland: Springer, 2020. ISBN 978-3-319-99691-2.
[9] Post, F. H., Walsum, T. Fluid flow visualization. *Focus on Scientific Visualization* (Hagen, H., Müller, H., Nielson, G. M. (eds.)), Berlin: Springer Verlag, 1993, pp. 1-40. ISBN 3-540-54940-4.
[10] Andersson, B., Andersson, R., Håkansson, L., Mortensen, M., Sudiyo, R., Wachem, B. *Computational Fluid Dynamics for Engineers*. First edition. United Kingdom: Cambridge University Press. ISBN 978-1-107-01895-2.
[11] Kolbasin, A., Husu, O. Computer-aided design and Computer-aided engineering. *MATEC Web of Conferences.* 2018, vol. 170, pp. 1-6.
[12] Greenshields, C. J., Weller, H. G. *Notes on Computational Fluid Dynamics: General Principles*. CFD Direct Limited, 2022. ISBN: 978-1-3999-2078-0.
[13] Králik, J., Konečna, L., Lavrinčíková, D. Experimental Validation of Computer Fluid Dynamics Simulation aimed on Pressure Distribution on Gable Roof of Low-rise Building. *Procedia Engineering*. 2017, vol. 190, pp. 377-384.
[14] Munson, B. R., Okiishi, T. H., Huebsch, W. W., Rothmayer, A. P. *Fundamentals of Fluid Mechanics*. Seventh Edition. Hoboken: John Wiley & Sons, Inc. 2013. ISBN 978-1-118-11613-5.

Performance analysis of a model-free VRFT method for tuning PID controllers

Damir Tisaj[1], Damir Vrančić[1,2]

[1]*Faculty of Industrial Engineering, Novo mesto, Šegova 112, 8000 Nov mesto, Slovenia*
E-mail: damir.tisaj@fini-unm.si

[2]*Jožef Stefan Institute, Jamova cesta 39, Ljubljana, Slovenia*
E-mails: damir.vrancic@fini-unm.si, damir.vrancic@ijs.si

***Abstract**: Most industrial processes require control loops to run smoothly. However, every control loop requires a properly tuned controller. The parameters of the controller can be tuned using parametric and non-parametric tuning methods. Parametric methods are based on the explicit knowledge of the process model, while non-parametric methods do not require the mentioned model. In this paper, we present a model-free VRFT method for tuning controller parameters, which is based on measuring the change of the process operating point in the time domain and can be easily performed by an operator. The advantage of this tuning method is the simplicity of the experiment on the process and the calculation procedure, which does not require any additional parameters from the user. The calculation of the parameters is computationally simple and can even be performed on a simple hardware. In this paper, the tuning method is tested on several process models with measurement noise. It turns out that the closed-loop responses are fast for most of the tested processes, with very little overshoot, even though the method is based only on measuring the open-loop responses of the process in the time domain.*

Keywords: process control, PID controller, controller tuning, non-parametric method, VRFT method

Article Classification: *Scientific paper*

1 INTRODUCTION

Product quality is important for the competitiveness of a production company. However, the reproducibility of a product is crucial for achieving the right level of quality. To maintain quality, it is therefore necessary to control important process or physical variables such as temperature, pressure, speed, flow, etc. during production. These parameters are controlled via control loops, the key components of which are controllers. The most common controllers found in the industry are Proportional-Integral-Derivative (PID) controllers. Each PID controller contains parameters that must be set appropriately in order to control (regulate) the selected process variable or process efficiently enough. Of course, these parameters are highly dependent on the process to be controlled.

The first methods for setting parameters for PID controllers were developed in the 1940s, when the first PID controllers, which were still pneumatic at the time, came onto the market [1]. In the following decades, many setting methods were developed, which can be divided into parametric and non-parametric depending on the process to be controlled [2]. Parametric methods for setting controller parameters require a parametric model of the process, such as a transfer function of the process or the process state space model. Non-parametric tuning methods are based on direct measurements of the process response to an excitation, such as the process response to a change in the input signal of the process or the frequency response of the process, such as a Nyquist or Bode plot. The advantage of non-parametric methods is that the process model does not have to be identified in order to determine the controller parameters.

Typical representatives of non-parametric methods are Virtual Reference Feedback Tuning (VRFT) [3-6], Fictitious Reference Iterative Tuning (FRIT) [7-8], Direct Adaptive Controller (DIRAC) [9], Magnitude Optimum Multiple Integration (MOMI) [10-11], and so on. All these methods require measurements of the input and output of the process when the input signal of the process changes. In all methods except MOMI, we also need to determine the desired closed loop transfer function. The latter is difficult to determine in practice, especially with an unknown process to be controlled. The disadvantage of the MOMI method is that multiple integrations of input and output signals are sensitive to disturbances that often occur in industrial processes.

Recently, a model-free VRFT method (BVRFT) [2] has been developed that does not require an explicit definition of the closed-loop transfer function, thus overcoming the main drawback of VRFT, FRIT and DIRAC methods. This is because the desired closed-loop response is implicitly defined by the open-loop response of the process or can be automatically adjusted according to the measured input and output signal. Another advantage of the method is that when calculating the controller parameters, it does not take into account the measurements when the process is not yet responding to the input excitation signal. This further stabilizes the response of the closed-loop for delayed processes.

In this paper, we test the performance of the BVRFT method on different process models and evaluate the sensitivity of the method to measurement noise. In the following, we briefly introduce the BVRFT method in Section 2. In Section 3, we test the performance of the method on some typical process models that may be encountered in industry. The sensitivity of the BVRFT method to measurement noise is verified in Section 4 and some conclusions and guidelines for future work are given in Section 5.

2 THE MODEL-FREE VRFT METHOD

The BVRFT method for setting the parameters of the controllers is based on measuring the input and output signals of the process, as shown in Figure 1.

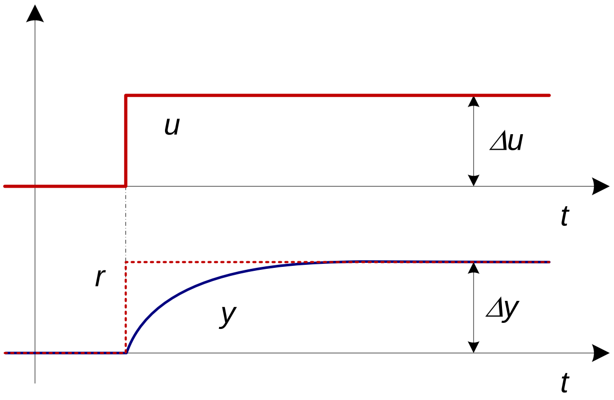

Figure 1: Typical process input (*u*) and output (*y*) signals

The signal *r* is equal to the scaled signal *u*, so that the magnitude of the signal *r* is equal to the magnitude of the signal *y*.

The BVRFT method is based on the structure of a PID controller, which has two degrees of freedom so that the transfer functions from the reference (*r*) and the output of the process (*y*) are not equal:

$$U = R\left(K_P + \frac{K_I}{s}\right) - Y\left(K_P + \frac{K_I}{s} + \frac{K_D s}{1 + sT_F}\right), \tag{1}$$

where K_P, K_I, K_D and T_F are the proportional gain, the integral gain, the derivative gain and the filter time constant of the controller. The variables U, R and Y are the Laplace transforms of the signals *u*, *r* and *y*. The parameters of the controller can be calculated for a selected value of the filter T_F as follows [2]:

$$\begin{bmatrix} K_I \\ K_P \\ K_D \end{bmatrix} = [\Psi^T \Psi]^{-1} \Psi^T u\,, \tag{2}$$

Where u is input signal and Ψ is regression matrix:

$$\Psi = \begin{bmatrix} i_F(1) & e_F(1) & y_F(1) \\ i_F(2) & e_F(2) & y_F(2) \\ \vdots & \vdots & \vdots \\ i_F(n) & e_F(n) & y_F(n) \end{bmatrix}. \tag{3}$$

Signals E_F, I_F and Y_F are as follows:

$$E_F(s) = K_{PR} U - Y, \qquad I_F(s) = \frac{K_{PR} U - Y}{s}, \qquad Y_F(s) = -\frac{sY}{1 + sT_F} \tag{4}$$

The parameter K_{PR} represents the static gain of the process, which can be easily calculated from the following ratio (see Figure 1):

$$K_{PR} = \frac{\Delta y}{\Delta u} \tag{5}$$

In order to better match the response of the open and closed control loops, only measurements from the moment in which the output of the process changes by 10 % compared to the steady-state difference were taken into account in the matrix Ψ and the vector u [2].

In addition to the BVRFT method mentioned above, we have also tried the adaptive BVRFT method [2], where we vary the desired closed-loop speed to obtain the optimal closed- loop response. This is possible because the desired closed-loop speed can be changed by filtering the reference signal accordingly. In this way, the closed loop response can be accelerated to a point where the closed loop and filtered open loop responses of the process begin to differ by a predetermined factor. The advantage of the adaptive BVRFT method is that it automatically finds the optimal closed-loop response and, like the basic BVRFT method, requires no additional prior knowledge of the process to be controlled.

It should be noted that the calculation of the parameters of the PID controller based on the BVRFT method can be performed by running the Matlab/Octave script, which is freely available on the Internet [2,12]. When you run the script, you must click on the "Add 15 seconds" link at the bottom right of the window while the script is running. The "Add 15 seconds" link must be clicked several times for the script to complete.

3 CLOSED-LOOP PERFORMANCE OF THE BVRFT METHOD

The BVRFT method has been tested on a large set of process models representing some of the processes that can be found in industry:

$$\begin{aligned} G_{P1} &= \frac{1}{1+10s} \\ G_{P2} &= \frac{e^{-s}}{1+9s} \\ G_{P3} &= \frac{e^{-8s}}{1+2s} \\ G_{P4} &= \frac{1}{(1+5s)^2} \\ G_{P5} &= \frac{1}{(1+2.5s)^4} \\ G_{P6} &= \frac{1-2s}{(1+4s)^2} \end{aligned} \tag{6}$$

The selected models represent first and higher order processes, processes with low or high time delay and a phase non-minimum process. The parameters of the process models are chosen so that they have the same average residence time $t_P = 10\ s$, i.e. all open loop process responses are approximately equally fast. The process responses were measured with a sampling time $T_S = 0.1\ s$.

The parameters of the PID controller were calculated for both the BVRFT method and the adaptive BVRFT method. They were calculated directly using the Matlab/Octave script [12] mentioned above and are listed in Table 1. For all calculations and experiments, we set the filter time constant of the controller $T_F = 0.2\ s$.

Table 1: PID controller parameters and speed factor K_S

Process	**BVRFT method**			**adaptive BVRFT method**			
	K_I	***K_P***	***K_D***	***K_I***	***K_P***	***K_D***	***K_S***
G_{P1}	0.100	1.03	0.305	0.996	9.951	0.105	9.85
G_{P2}	0.100	0.941	0.370	0.431	4.439	1.133	7.40
G_{P3}	0.034	0.115	0.090	0.0725	0.296	0.280	0.387
G_{P4}	0.100	0.981	2.31	0.177	1.72	4.09	1.77
G_{P5}	0.100	0.796	1.910	0.120	0.925	2.35	1.21
G_{P6}	0.100	0.787	1.485	0.133	0.995	2.10	1.33

Table 1 shows that in the BVRFT method the integral gain of the controllers (K_I) is equal to $K_I = 0.1$ for almost all processes. This is understandable since the basic BVRFT method aims to achieve a closed-loop response similar to the open-loop response. This is because the average residence (reaction) time of the closed-loop response (T_{ZZ}) is inversely proportional to the integral gain of the controller and the steady-state gain of the process (K_{PR}):

$$t_{ZZ} = \frac{1}{K_I K_{PR}} \tag{7}$$

Since the static gains of all selected process models are $K_{PR} = 1$, $t_{ZZ} = t_P = 10$ only if $K_I = 0.1$. In Table 1, only the calculated value of K_I for G_{P3} differs. The process G_{P3} is a process with a large time delay. In fact, the calculation of the controller parameters only takes into account the measurement of the open loop response of the process when it starts to react to a change in the input signal (after the delay time has elapsed). Due to such a high time delay, the calculated integral gain of the controller is correspondingly lower. This is even desirable, as a closed loop response at $K_I = 0.1$ would be unstable.

The closed-loop responses for all six selected process models are shown in Figures 2 to 7. All closed-loop responses obtained with the conventional and adaptive BVRFT methods are stable despite very different process models. All closed-loop responses of the BVRFT method, with the exception of G_{P3}, are practically identical to the open-loop process responses. As mentioned above, the average closed-loop residence time t_{ZZ} is much higher than the process residence time t_P for G_{P3} due to the reduced K_I. The adaptive BVRFT method proves to be very efficient as it accelerates the closed-loop responses in all cases without noticeable oscillations.

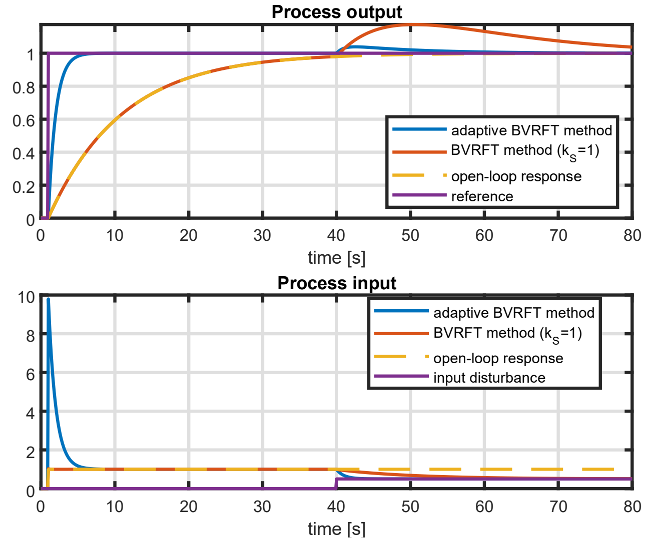

Figure 2: Open- and closed-loop responses of G_{P1} when using the BVRFT method (conventional and adaptive)

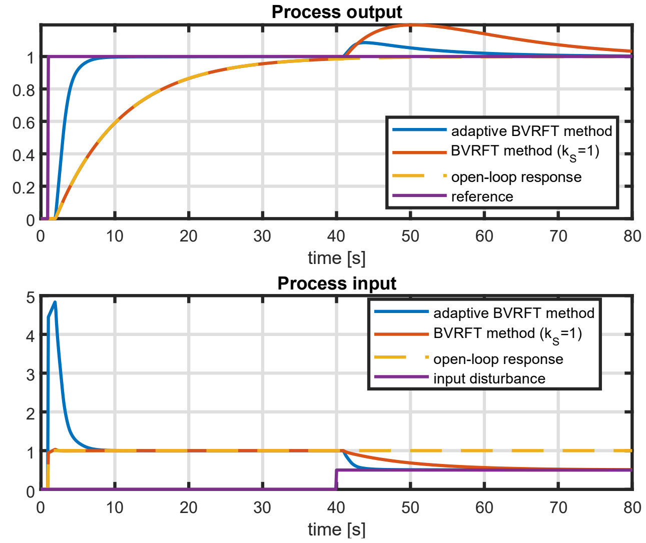

Figure 3: Open- and closed-loop responses of G_{P2} when using the BVRFT method (conventional and adaptive)

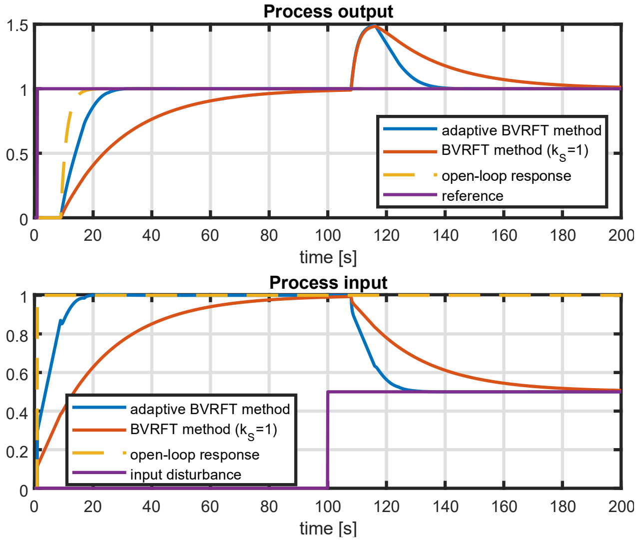

Figure 4: Open- and closed-loop responses of G_{P3} when using the BVRFT method (conventional and adaptive)

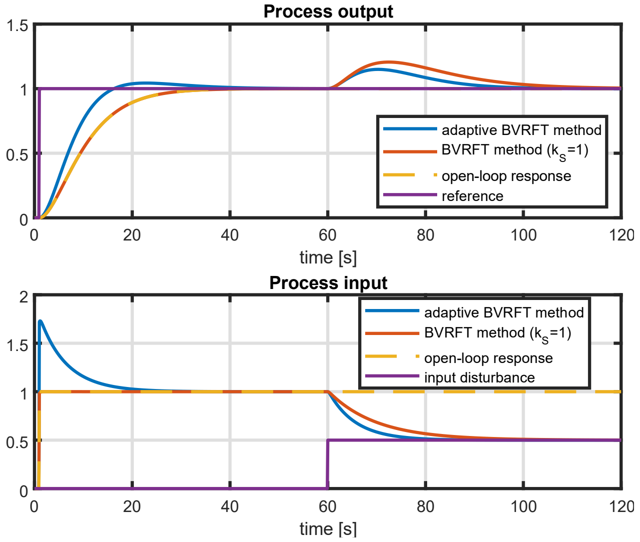

Figure 5: Open- and closed-loop responses of G_{P4} when using the BVRFT method (conventional and adaptive)

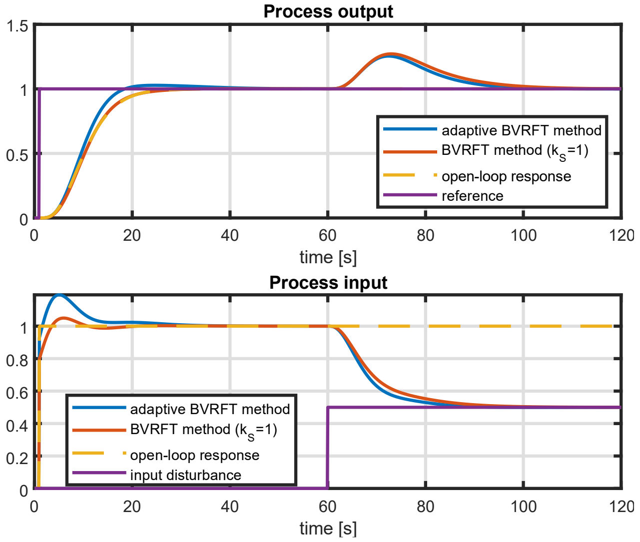

Figure 6: Open- and closed-loop responses of G_{P5} when using the BVRFT method (conventional and adaptive)

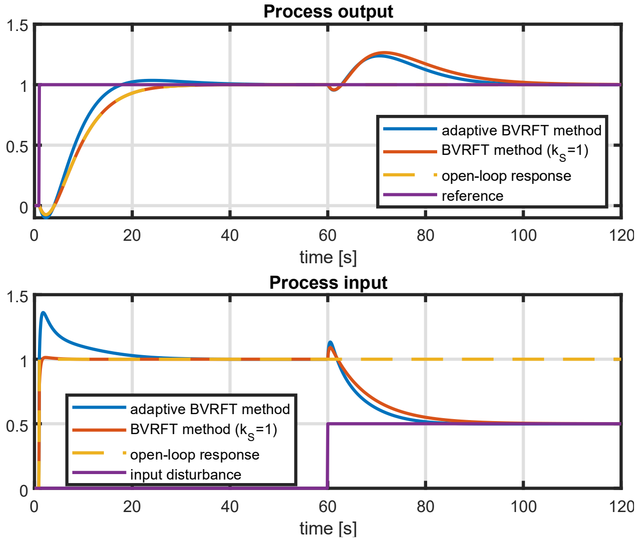

Figure 7: Open- and closed-loop responses of G_{P6} when using the BVRFT method (conventional and adaptive)

4 SENSITIVITY OF THE BVRFT METHOD TO MEASUREMENT NOISE

In practice, measurement noise and other disturbances are always present. We have therefore tested the BVRFT method on measurement signals to which we have added artificially generated measurement noise with a normal distribution. The noise signal was generated in Matlab using the randn function. The resulting noise was multiplied by a factor of 0.0002 at a sampling time of $T_S = 0.1\ s$ and added to the open-loop and closed-loop response of the process.

The parameters of the PID controller with the filter time constant $T_F = 0.2\ s$ were then calculated again using the Matlab/Octave script [12]. Despite the measurement noise, we were unable to detect any significant differences in the calculation of the controller parameters. Only for the process G_{P1} the gain of the derivative term in the basic BVRFT method increase from practically zero to $K_D = 0.287$. However, the time constant of the derivative term ($T_D = K_D/K_P$) is still negligible compared to the time constant of the process (10 s). Therefore, we do not expect large differences in the closed loop response.

Tabel 2: PID controller parameters and speed factor K_S with additional measurement noise

Process	BVRFT method			adaptive BVRFT method			
	K_I	K_P	K_D	K_I	K_P	K_D	K_S
G_{P1}	0.100	1.03	0.287	0.994	9.85	0.00	9.85
G_{P2}	0.100	0.941	0.365	0.431	4.437	1.13	7.40
G_{P3}	0.034	0.115	0.090	0.0725	0.296	0.280	0.387
G_{P4}	0.100	0.981	2.31	0.177	1.72	4.09	1.77
G_{P5}	0.100	0.796	1.911	0.120	0.925	2.35	1.21
G_{P6}	0.100	0.787	1.483	0.133	0.995	2.09	1.33

This is confirmed in Figure 8, where the closed-loop response of the conventional BVRFT method, when the noise is removed, is virtually identical to the response in Figure 2. Figure 8 also shows that the degree of noise we have added to the measurement is relatively high and may reflect the situation in practice where significant measurement noise is present.

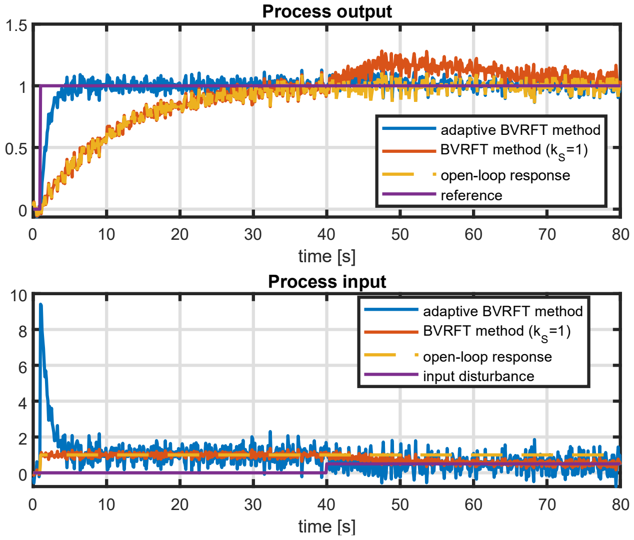

Figure 8: Open- and closed-loop response of the process G_{P1} when using the BVRFT method (conventional and adaptive) in the presence of measurement noise

Of course, the sensitivity of a tuning method to measurement noise cannot be based on a single noise sample. For this purpose, we decided to use different noise signal samples with normal distribution and equal variance. In further experiments, we used 100 statistically identical noise signals for each process model, as shown in Figure 8. All 100 open-loop responses are shown in Figure 9 above. For each individual response, we calculated the controller parameters and then performed a closed-loop experiment. To better recognize the "spread" of the closed-loop responses, we intentionally removed the measurement noise. All 100 closed-loop responses, without additional noise, are shown in Figure 9 below. It can be seen that the responses are very similar. The tuning method is therefore relatively insensitive to measurement noise. This is confirmed by the histogram of the controller parameters in Figure 10, where the variance is relatively low. The red circles in Figure 10 represent the controller parameters without measurement noise.

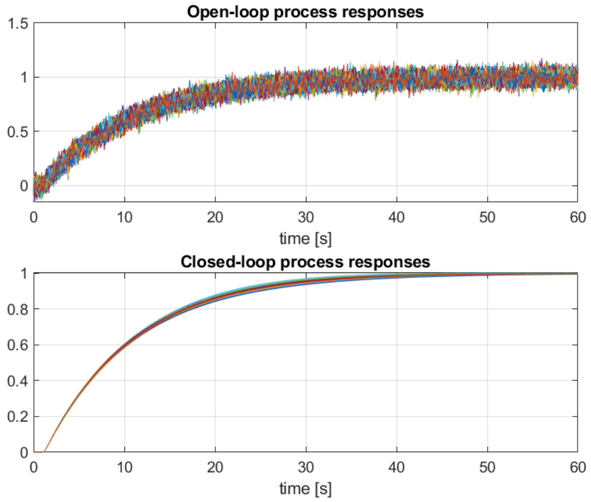

Figure 9: Open- and closed-loop responses of the process G_{P1} using the conventional BVRFT method in the case of 100 open-loop response measurements with measurement noise

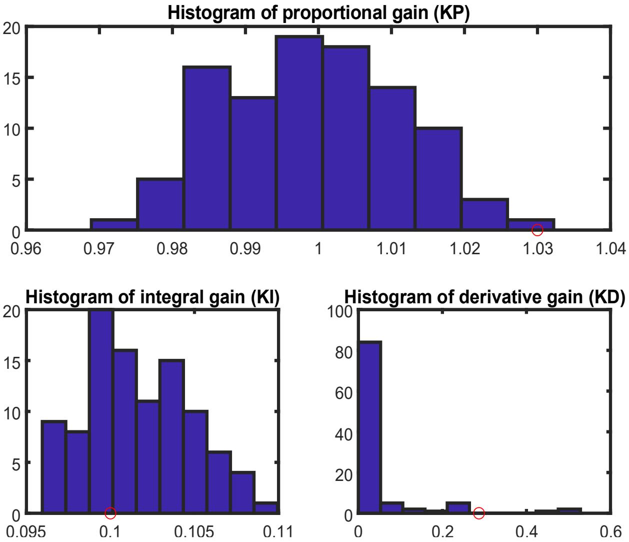

Figure 10: Histogram of the PID controller parameters for the process G_{P1} using the conventional BVRFT method in the case of 100 open-loop response measurements with measurement noise

The responses of processes G_{P2} to G_{P6} in the open and closed control loop are shown in Figures 11 to 15. Similar to process G_{P1}, the dispersion of the closed-loop responses for processes G_{P2} to G_{P6} is relatively low.

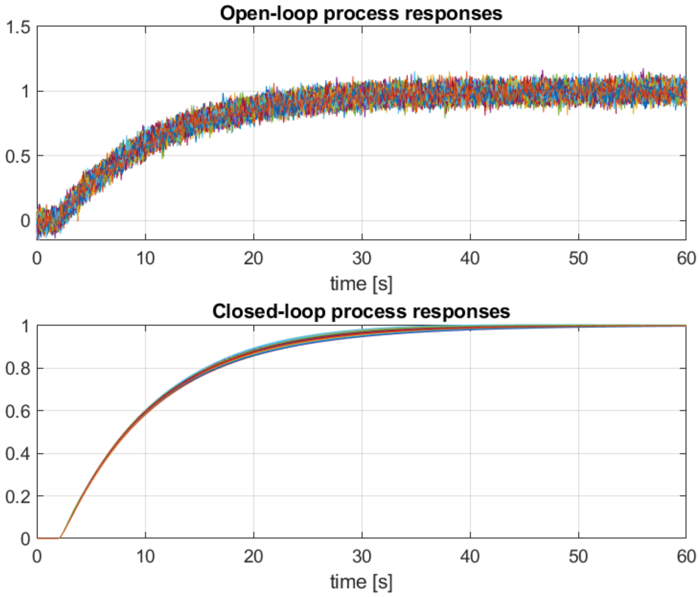

Figure 11: Open- and closed-loop responses of the process G_{P2} using the conventional BVRFT method in the case of 100 open-loop response measurements with measurement noise

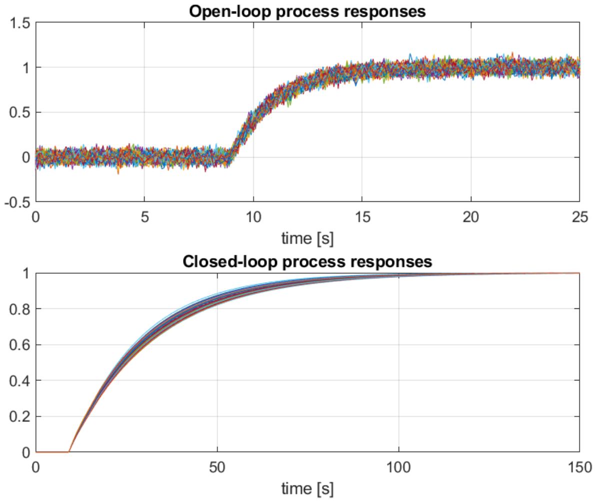

Figure 12: Open- and closed-loop responses of the process G_{P3} using the conventional BVRFT method in the case of 100 open-loop response measurements with measurement noise

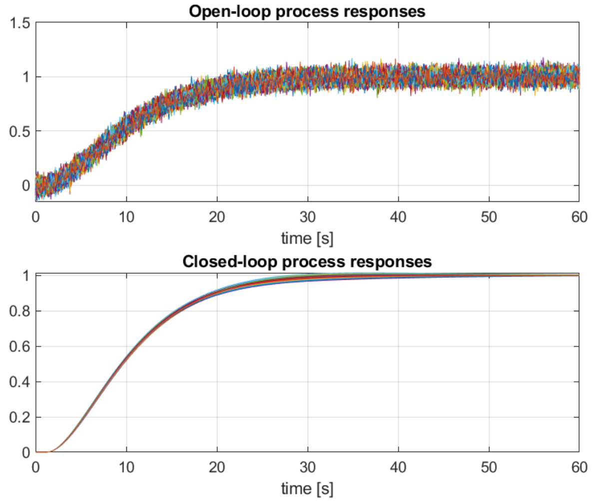

Figure 13: Open- and closed-loop responses of the process G_{P4} using the conventional BVRFT method in the case of 100 open-loop response measurements with measurement noise

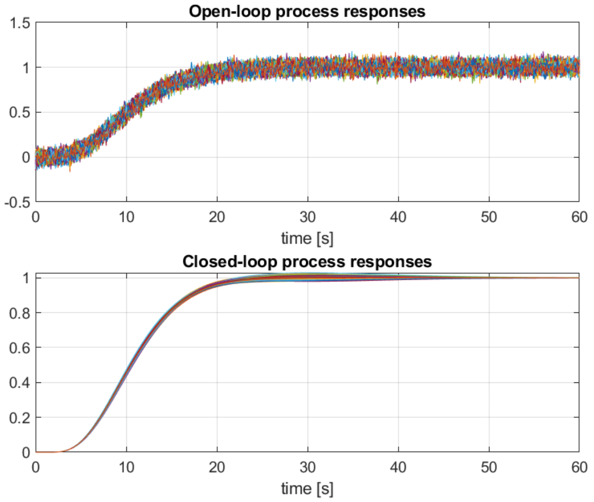

Figure 14: Open- and closed-loop responses of the process G_{P5} using the conventional BVRFT method in the case of 100 open-loop response measurements with measurement noise

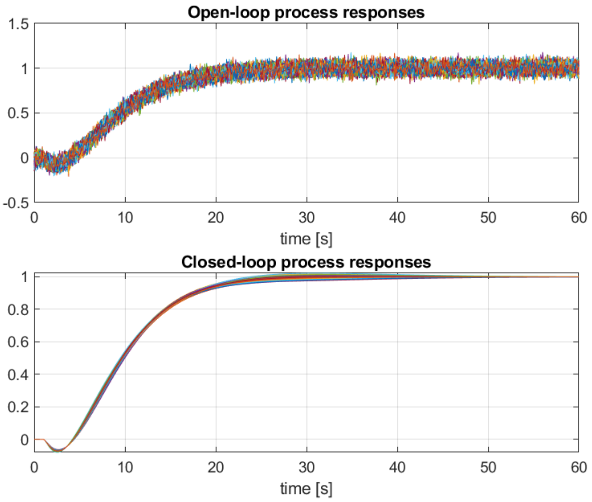

Figure 15: Open- and closed-loop responses of the process G_{P6} using the conventional BVRFT method in the case of 100 open-loop response measurements with measurement noise

5 CONCLUSION

In this paper, we discuss the BVRFT method for setting the PID controller parameters, which does not require any additional information about the process or the desired closed-loop response other than the open-loop time response of the process. In fact, the BVRFT method sets the desired closed-loop response of the process equal to the open-loop response. In industrial practice, this is often a desirable feature of the tuning method as it does not cause large changes in the control signal when the reference signal changes. In addition to the basic BVRFT method, we have also tested an adaptive BVRFT method that can be used to accelerate the closed-loop response.

Both methods were tested on six process models that represent typical processes occurring in industry. The closed-loop responses of the processes showed that the BVRFT method is very efficient and that the closed-loop responses are almost identical to the open-loop responses. The only major difference occurred for a process model with a large dead time (much larger than the main time constant of the process). In this case, the closed-loop response was slower than the open-loop response. However, such a response proved to be an advantage of the tuning method. This is because with such a delayed process and a PID controller, it is not possible to obtain a stable closed-loop response as fast as the open-loop response.

In addition to the performance of the method on selected process models, we also tested the method on open-loop signals to which we added measurement noise with a normal distribution. For a more in-depth analysis, we added 100 signals with normally distributed noise and the same statistical parameters to each open-loop response. Despite the relatively high noise level of the process output signal, the dispersion of the PID controller parameters was relatively low for all process models. All closed-loop responses based on the BVRFT method were stable and similar.

In this paper, we have confirmed that the parameter tuning method discussed is suitable for further testing in an industrial environment, which will be our next research goal.

REFERENCES

[1] ZIEGLER, J.G. and N. B. Nichols. Optimum Settings for Automatic Controllers. *Transactions of the ASME*, 1942, 64, pp. 759-768.
[2] VRANČIĆ, Damir. Model-free VRFT-based tuning method for PID controllers. *Mathematics*. 2023, Vol. 11, 715. https://doi.org/10.3390/math11030715
[3] CAMPI, M.; A. Lecchini and S. Savaresi. Virtual reference feedback tuning: A direct method for the design of feedback controllers. *Automatica.* 2002, 38, pp. 1337–1346.
[4] CAMPESTRINI, L., D. Eckhard, L. A. Chía and E. Boeira. Unbiased MIMO VRFT with application to process control. *J. Process. Control*. 2016, 39, pp. 35–49.
[5] JENG, J.-C. *Data-Based Tuning of PID Controllers: A Combined Model- Reference and VRFT Metho*d. V: *PID Control for Industrial Processes*; London, IntechOpen, 2018. https://www.intechopen.com/chapters/63028
[6] FORMENTIN, S., M. C. Campi, A. Carè and S. M. Savaresi. Deterministic continuous-time Virtual Reference Feedback Tuning (VRFT) with application to PID design. *Syst. Control. Lett*. 2019, 127, pp. 25–34.
[7] MASUDA, S. PID controller tuning based on disturbance attenuation FRIT using one-shot experimental data

due to a load change disturbance, V: *IFAC Proceedings Volumes*, Volume 45, Issue 3, 2012, pp. 92-97. ISBN 9783902823182, https://doi.org/10.3182/20120328-3-IT-3014.00016
[8] KUROKAWA, R. et al., Closed-loop Data-driven Trade-off PID Control Design, V: *IFAC-PapersOnLine*, Volume 51, Issue 4, 2018, 244-249, ISSN 2405-8963, https://doi.org/10.1016/j.ifacol.2018.06.073
[9] DeKEYSER R., DIRAC: A direct adaptive controller. V: *Preprints of the IFAC Workshop on Digital Control*, 2000,199-204. Terrassa, 2000.
[10] VRANČIĆ, D., S. Strmčnik and Đ. Juričić. A magnitude optimum multiple integration method for filtered PID controller. *Automatica*. 2001, Vol. 37, pp. 1473-1479.
[11] VRANČIĆ, D. et al. Improving disturbance rejection of PID controllers by means of the magnitude optimum method. *ISA transactions*, 2010, vol. 49, no. 1, pp. 47-56. ISSN 0019-0578
[12] Octave Online Bucket: Software package for calculating PID controller parameters based on the BVRFT method. Available: https://octav.onl/gvbic444 (Accessed 16 September 2024).

Challenges of green transition: Application of life cycle assessment in the energy sector

Jelena Topić Božič[1,2] Simon Muhič[1,2,3]

[1]*Rudolfovo - Science and Technology Center Novo mesto, Podbreznik 15, 8000 Novo mesto, Slovenia*
E-mail: jelena.topic.bozic@rudolfovo.eu

[2]*Faculty of Industrial Engineering Novo mesto, Šegova ulica 112, 8000 Novo mesto, Slovenia*
E-mail: simon.muhic@fini-unm.si

[3]*INOVEKS, Cesta 2. grupe odredov 17, 1295 Ivančna Gorica, Slovenia*
E-mail: simon.muhic@inoveks.si

Abstract: *The green transition towards the low-carbon energy sector stems from dual sustainable development challenges and climate change. It is a long-term process that implies a shift towards economically sustainable growth based on low-carbon solutions, which requires socio-technical changes. The energy sector is a significant player facing the dual challenge of meeting the world's increasing energy demand while mitigating greenhouse gas emissions (GHGE). The selection criteria for the development of sustainable energy transition should consider socio-economic, environmental, and dimension. Life cycle assessment (LCA) is a methodology that addresses a product's or system's potential environmental impact throughout its life cycle, i.e., raw material acquisition through production, use, end-of-life, recycling, and final disposal. It goes beyond the sole quantification of GHGE as it considers several other categories, including possible impacts on soil, water, and air. The article utilizes LCA to compare the potential environmental impact of different electricity mix scenarios in Slovenia, Croatia, and Bosnia. It shows how the country's electricity profiles play an important role in the environmental impact of services and systems. Different electricity mix scenarios were modeled, including increased renewables share. The electricity mix profile's role was shown in the use of electric bicycles in modeled countries, as its environmental impact is lower in scenarios with a higher share of renewable energy sources in the category global warming.*

Keywords: *green transition, renewable energy, life cycle assessment, electricity profile scenarios, energy sector*

Classification: *Scientific contribution*

1 INTRODUCTION

The energy sector faces dual challenges of meeting the increasing energy demand while simultaneously decreasing greenhouse gas emissions (GHGE) [1]. Many of the present energy systems still rely on fossil resources. The Paris Agreement [2] and the European Green Deal [3] require the reduction of GHGE and switching to renewable energy sources (RES) [4]. Achieving the energy transition targets will demand a change in the energy systems' design and supporting infrastructure [4]. The Intergovernmental Panel on Climate Change (IPCC) has identified the decarbonization of electricity systems worldwide as a significant measure for reducing GHGE and keeping global warming below 1.5 °C to 2 °C [5, 6].

Countries globally, among them the EU members and EU candidate countries, face the same energy and environmental challenges; however, the energy systems and their performances vary significantly from one country to another [7]. The energy balance sheets of each EU Member State and EU candidate countries depend largely on their geographical location, energy policy, the structure of the energy system, the availability of energy resources for primary energy production, and the structure and development of the economy. As a result, countries significantly differ in the use of fossil fuels, renewables, energy intensity, and CO_2 emissions [7]. The electricity mix of Slovenia, Croatia and Bosnia is presented in Figure 1.

According to the latest available data from International Energy Agency (IEA) the two largest sources of electricity generation are nuclear (41 %) and hydro (25 %). Compared to Slovenia, Croatia's two main sources of electricity generation are hydro (48 %) and natural gas (20 %). In contrast to Slovenia and Croatia, the largest source of electricity generation in Bosnia and Herzegovina is coal, presenting 60 % share [8–10]. Life cycle assessment (LCA) provides detailed information on a wide range of environmental indicators by taking full account of the impact of an energy technology on the environment from cradle-to-grave based on the life cycle inventory (LCI) [11]. Several articles in the international LCA literature assessed the decreasing environmental impacts of the transition to electricity mix scenarios consistent with decarbonization plan and targets [12–14]. The LCA importance as a suggested key method for the assessment of environmental impacts of products or services in European legislations and policies increased over time since the first regulations [15], and LCA is a part of the methods in the adoption of the Circular Economy Action Plan [16].

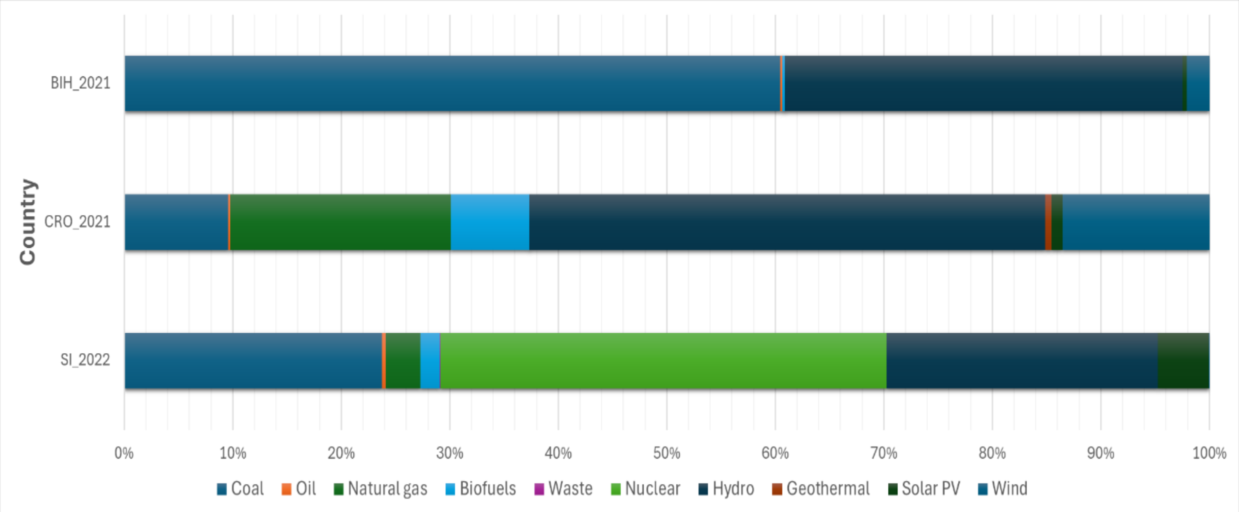

Figure 1: Electricity generation sources for Slovenia, Croatia, Bosnia and Herzegovina (data source: IEA [8–10])

Transportation is also a significant contributor to the GHGE [17, 18] and important part of green transition initiatives. Currently, car transport accounts for almost half of transport emissions, and to get on track with the 2050 Net Zero Emission scenario, emissions from the transport sector must fall more than 3 % per year by 2030 [19]. Several options and alternatives have been proposed to solve this issue, the main one being a transition to electric mobility solutions and electric lightweight vehicles (ELV), as a part of the micromobility offer, numerous advantages over conventional internal combustion engines [18, 20].

Micromobility is defined as the low use speed, small vehicles with mass below 350 kg and a speed up to 45 km/h with battery capacities requirements in the 0.4 – 10 kWh range. They cover different types of vehicles, including electric stand-up scooters, driven in a standing position; electric bicycles; electric moped scooters; or light four wheeled vehicles [17, 18]. The transition to electric bicycles present an alternative in the urban context of low-carbon mobility options and the e-bike industry has experienced significant growth in recent years [20].

According to EC (2021) electric bicycles are the fastest-growing e-mobility segment in Europe, with a 52% increase in sales in 2020 [21]. With the current trend, the EU is also developing a stronger bike and two wheels industrial base. From a life cycle perspective, ELV and electric vehicles generally require electric power. Previous studies have shown that the magnitude of the GHGE reductions is determined by the electricity mix and the efficiency of electricity transmission and reduction [22].

This LCA study aims to assess the potential environmental impacts of electricity production from different countries (Slovenia, Croatia, Bosnia and Herzegovina) to ascertain their environmental impact per unit of electricity generated (kWh). The second goal was to demonstrate the difference in potential environmental impacts on using electric bicycle for transport in the case of different electricity mixes.

2 MATERIALS AND METHODS

2.1 Life cycle assessment (LCA)

LCA is a standardized methodology regulated by the 14040 and 14044 ISO standards that allows the quantification of the potential environmental impact of products, processes or activities through the whole life cycle stages. The LCA analysis has four main steps: definition of the goal and scope of the study, life cycle inventory analysis, life cycle impact assessment, and life cycle interpretation as shown in Figure 2 [12].

The software SimaPro and Ecoinvent 3.9.1 database were used for modeling. Ecoinvent is a comprehensive life cycle inventory database. ReCiPe Midpoint (H) was the impact assessment method used [23, 24].

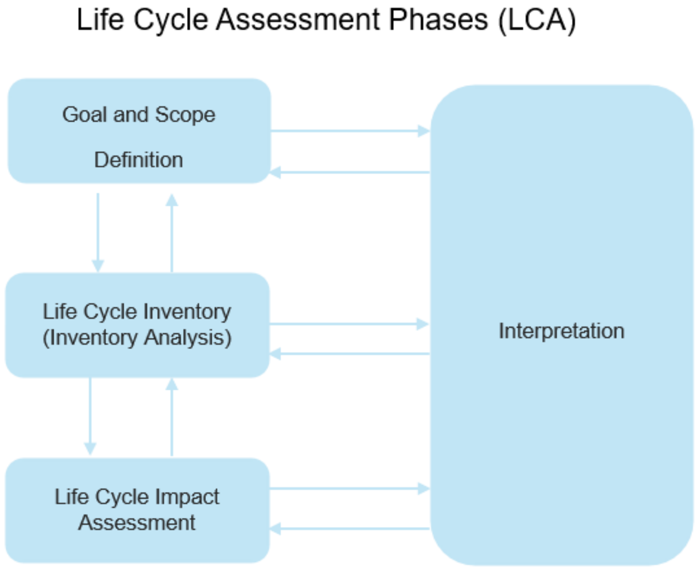

Figure 2: Life cycle assessment phases according to ISO 14040 – 14044 [25, 26]

2.2 System definition, Functional Unit, and Processes included

The functional unit of the assessment used was 1 kWh of electricity produced for modelling of virtual electricity production mix for countries based on the data from International Energy Agency as shown in Figure 1. The life cycle inventory data about single electricity production sources for Slovenia, Croatia and Bosnia were used from the Ecoinvent database to create virtual production mix scenario with different shares of production sources.

Dataset for the electric bicycle production was used with the geographical denomination Europe was used from the Ecoinvent. The dataset assumes life span of 15000 km and 24 kg of weight for the bicycle [27]. The system boundaries included electric bicycle production, maintenance, use and disposal. The process “electric bicycle production with geographical denomination rest of Europe” was used which is available in the Ecoinvent database. Low voltage mix datasets for Slovenia, Croatia and Bosnia were used from the Ecoinvent database for electricity needed as it represents the electricity used in households. The maintenance and the use of roads were also included in the boundaries. For the end-of-life, the process market for used electric bicycle (GLO) was used. The modeled processes in the Ecoinvent also include the imports [27]. The functional unit was 1 person km (pkm) journey with an electric bicycle. Yearly average electricity production mix was used, which is common practice in LCA studies.

3 RESULTS AND DISCUSSION

3.1 Lifecycle impact assessment in selected categories for electricity production mixes (1 kWh)

The life cycle impact assessment results for the categories considered are presented in Table 1. The impact in the category global warming for 1 kWh of produced electricity is the highest for Bosnia with 200 % and 121 % higher value compared to Croatia and Slovenia, respectively. The higher impact can be attributed to the high share of electricity production from coal-based sources. Slovenia has a 35.5 % higher impact in category global warming than Croatia, which can be attributed to the high share of thermal power plants using lignite [28]. In contrast, the main share in the electricity production in Croatia is hydro energy which results in the highest value in the impact category water consumption among the three countries. 1 kWh of produced electricity in Croatia results in 82 % and 62.8 % increase in the value of impact water consumption compared to Slovenia and Bosnia, respectively. On the other hand, the highest value in impact category ionizing radiation can be seen in the Slovenian electricity production mix due to the production of electricity from nuclear power plant. The values correspond to a 98.9 % and 98.5 % increase in the impact category ionizing radiation compared to values for Croatia and Bosnia, respectively.

Table 1: Lifecycle impact assessment for categories considered for electricity production (1 kWh of produced electricity in Slovenia (SLO), Croatia (CRO) and Bosnia and Herzegovina (BIH)

Impact category	**Unit**	**SLO**	**CRO**	**BIH**
Global warming	kg CO_2 eq	0.362551	0.267594	0.801752
Ionizing radiation	kBq Co-60 eq	0.263450	0.002949	0.003793
Ozone formation, Human health	kg NOx eq	0.000872	0.000656	0.001830
Fine particulate matter formation	kg PM2.5 eq	0.001962	0.000247	0.005147
Ozone formation, Terrestrial ecosystems	kg NOx eq	0.000876	0.000677	0.001833
Terrestrial acidification	kg SO_2 eq	0.006237	0.000674	0.014365
Terrestrial ecotoxicity	kg 1,4-DCB	0.302818	0.300457	0.475364
Freshwater ecotoxicity	kg 1,4-DCB	0.020555	0.005309	0.044322
Marine ecotoxicity	kg 1,4-DCB	0.028110	0.007079	0.060907
Human carcinogenic toxicity	kg 1,4-DCB	0.039730	0.011820	0.088008
Human non-carcinogenic toxicity	kg 1,4-DCB	0.801426	0.160598	1.777980
Land use	m^2a crop eq	0.001137	0.018028	0.002813
Mineral resource scarcity	kg Cu eq	0.000419	0.000369	0.000210
Fossil resource scarcity	kg oil eq	0.078656	0.081449	0.162493
Water consumption	m^3	0.002397	0.014038	0.005221

3.2 Lifecycle impact assessment in selected categories of transport with electric bicycle in different countries

The results shown in Figure 3 demonstrate the impact of electricity mix on the environmental impact of the use of electric bicycle. In the category global warming, the lowest impact has a journey in Slovenia, which can be attributed to the lower share of fossil fuel-based electricity sources compared to Bosnia, in which, the primary electricity production source is coal (60 %) which results in the 33.5 % higher value of the impact category. Croatia has 3 % % increase compared to Slovenia. Although Croatia has lower share of electricity production from thermal power plant than Slovenia (9.6 % and 23.7 %), it has significantly higher share of electricity production from natural gas. In Croatia, electricity production from natural gas has the second highest share with 20.4 %, compared 3.2 % in Slovenia [8–10]. Although the result from electricity production show higher value in the global warming category for Slovenia, compared to Croatia, the modelled electricity mix scenario used in the transport with electric bicycle also considers electricity imports for Slovenia, Croatia and Bosnia. Croatia imports primarily electricity from Hungary, Slovenia, Bosnia and Herzegovina, Serbia and Bulgaria [29]. The impact in category ionizing radiation is the highest for using the electric bicycle in Slovenia due to the nuclear power plant share. Compared to the electricity production mixes, the differences in values are lower, as the difference between Slovenia and Croatia is 3 %. Croatia co-owns the nuclear power plant in Slovenia and the electricity from the nuclear power plant is considered in its energy mix as imported electricity [30]. In Slovenia, cross-border interconnections also exist towards Italy and Austria, from where the electricity is imported in Slovenia [31]. Similarly, to category global warming, the highest value in the impact category fine particulate matter is in the case of the electric bicycle in Bosnia due to the highest share of electricity production from coal.

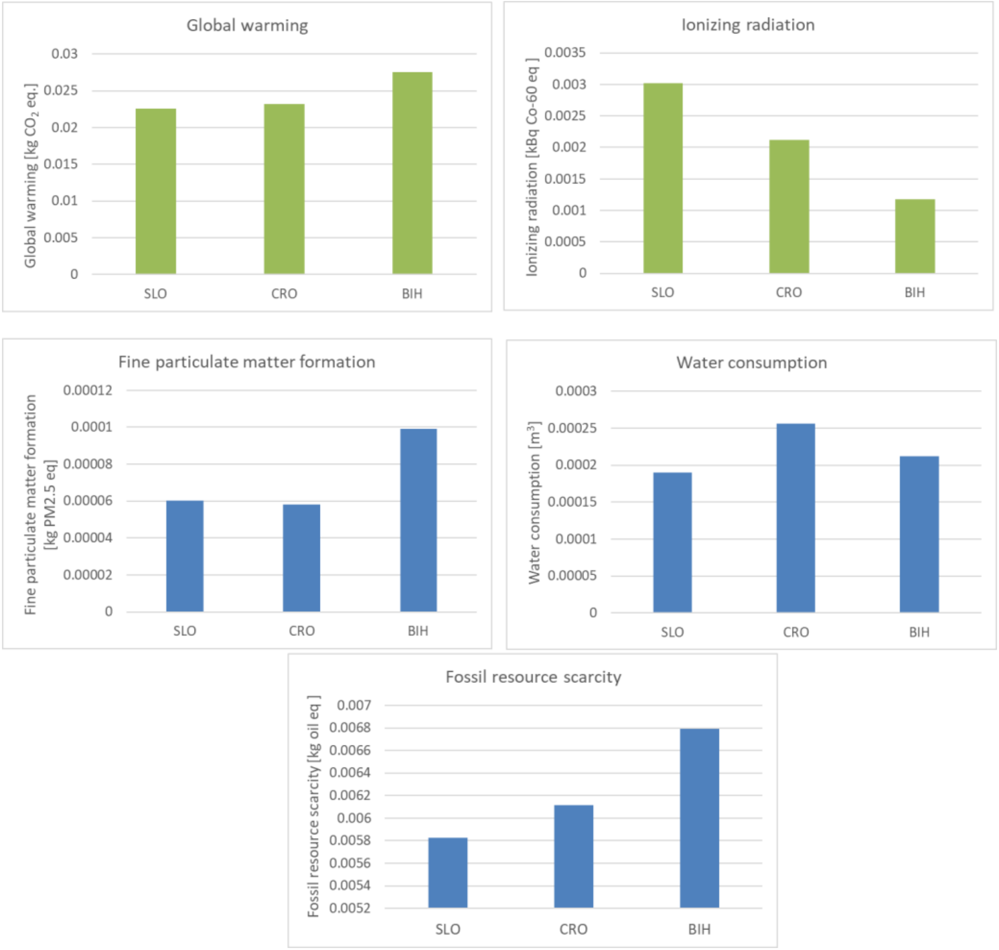

Figure 3: Environmental impact assessment in selected categories of 1 km journey with electric bicycle in Slovenia (SLO), Croatia (CRO), and Bosnia and Herzegovina (BIH)

Results from Huang et al. [22] show that electric bicycles can reduce GHGE significantly, and the reduction has room for increase with a change in the electricity generation mix. Elliot et al. [32] assessed the potential environmental impact of electric bicycles in New Zealand. The electric bicycle had lower environmental impacts compared to the car for eleven of the fifteen impact categories considered when the functional unit was one kilometer travelled in Wellington. A sensitivity analysis on variability in electricity generation sources throughout the day for charging the electric bicycle had little influence on the LCIA results, however in the electricity mix, no photovoltaic was present, and the percentages of the sources in the studied generation profile were stable, and did not vary significantly. De Bortoli [33] modeled a wide range of electricity mixes, average USA, China, Spain, the UK, Germany, Norway, the Netherlands, Australia, Denmark, Italy, and Canada, to assess environmental performances of shared light electric vehicles. The results showed that the electricity mix impacts electric scooters and electric mopeds' performances, except in countries with a very low-carbon intensity electricity mix. The electricity mix influences the impact of the use stage as well as the servicing stage, as electric vehicles are assumed to be used to maintain, balance, and charge the vehicles. The results also showed that the environmental performances of shared electric bicycles were not sensitive to the type of electricity mix on the five indicators due the low electricity use of electric bicycles bikes and the fact that the shared bike fleet is considered half electric and half mechanical, cutting the electricity consumption by a factor of two. However, in the case of shared environmental scooters and electric mopeds, the environmental performance was highly influenced by the electricity mix.

4 CONCLUSIONS AND FUTURE OUTLOOKS

In this research, LCA of electricity production mixes for Slovenia, Croatia, and Bosnia was performed to assess environmental performances od 1 kWh of produced electricity. Due to the nature of different primary sources of electricity production, the impact in category global warming for 1 kWh of produced electricity was the highest in Bosnia with 200 % and 121 % higher value compared to Croatia and Slovenia, respectively due to the predominant share of electricity production from coal-based sources. On the other hand, the category values for impact category ionizing radiation were the highest in Slovenia due to the nuclear power plant as an electricity production source.

The impact of country electricity mix on the environmental performance of an electric bicycle was assessed with LCA, and the functional unit was determined to be 1 personkm. The electricity mixes at low voltage from Ecoinvent was used for the energy use process (charging of bicycle) for Slovenia, Croatia and Bosnia and Herzegovina, which include imported electricity. The low voltage dataset models the use of electricity in households. The results showed that in impact category global warming, the lowest impact has a 1 km journey with electric bicycle in Slovenia, which can be attributed to the lower share of fossil fuel-based electricity sources compared to Bosnia, in which, the primary electricity production source is coal (60 %) which results in the 33.5 % higher value of the impact category. On of the limitations of the study is the use of average yearly electricity production mix, which can in some cases lead to underestimation or overestimation of potential environmental impacts due to variations in the electricity production mix.

Micromobility modes exhibit minimal direct emissions during urban vehicle use compared to fossil-powered vehicles and present a way to reduce GHGE especially in urban environments. Still, transportation electrification poses a challenge in the energy transition. Transportation electrification and the measures for decarbonization of electricity should go hand in hand as the GHGE emission of transport will be lower in the power system with larger share of renewable energy sources.

Funding

This research was funded by the Slovenian Research and Innovation Agency Research Program, Public call ARRS-RPROJ/2023/Appl. 375.

REFERENCES

[1] GENÇER, Emre, Sarah TORKAMANI, Ian MILLER, Tony Wenzhao WU a Francis O'SULLIVAN. Sustainable energy system analysis modeling environment: Analyzing life cycle emissions of the energy transition. *Applied Energy* [online]. 2020, **277**, 115550. ISSN 0306-2619. Available at: doi:10.1016/j.apenergy.2020.115550

[2] UNFCC. *Paris Agreement* [online]. B.m.: UN Climate Change Conference (COP21). 2016 [vid. 2024-09-09]. Available at: https://eur-lex.europa.eu/legal-content/EN/TXT/?uri=CELEX:22016A1019(01)

[3] EUROPEAN COMMISSION. *The European Green Deal* [online]. 2019 [vid. 2024-03-05]. Available at: https://eur-lex.europa.eu/legal-content/EN/TXT/?uri=CELEX:52019DC0640

[4] YAVOR, Kim Maya, Vanessa BACH a Matthias FINKBEINER. Resource Assessment of Renewable Energy Systems—A Review. *Sustainability* [online]. 2021, **13**(11), 6107. ISSN 2071-1050. Available at: doi:10.3390/su13116107

[5] DAS, Jani, Atta UR REHMAN, Rahul VERMA, Gurcan GULEN a Michael H. YOUNG. Comparative Life-Cycle Assessment of Electricity-Generation Technologies: West Texas Case Study. *Energies* [online]. 2024, **17**(5), 992. ISSN 1996-1073. Available at: doi:10.3390/en17050992

[6] ROGELJ, J., D. SHINDELL, K. JIANG, S. FIFITA, P. FORSTER, V. GINZBURG, C. HANDA, H. KHESHGI, S. KOBAYASHI, Elmar KRIEGLER, L. MUNDACA, R. SÉFÉRIAN, M. V. VILARINO, K. CALVIN, J. C. DE OLIVEIRA DE PORTUGAL PEREIRA, O. EDELENBOSCH, J. EMMERLING, S. FUSS, T. GASSER, N. GILLETT, C. HE, E. HERTWICH, L. HÖGLUND-ISAKSSON, D. HUPPMANN, Gunnar LUDERER, A. MARKANDYA, M. MEINSHAUSEN, D. MCCOLLUM, R. MILLAR, Alexander POPP, P. PUROHIT, K. RIAHI, A. RIBES, H. SAUNDERS, C. SCHÄDEL, C. SMITH, P. SMITH, E. TRUTNEVYTE, Y. XU, W. ZHOU a K. ZICKFELD. Mitigation Pathways Compatible with 1.5°C in the Context of Sustainable Development. In: *Global warming of 1.5 °C* [online]. B.m.: Intergovernmental Panel on Climate Change, 2018 [vid. 2024-09-09], s. 93–174. Available at: https://www.ipcc.ch/site/assets/uploads/sites/2/2018/07/SR15_Chapter2_High_Res.pdf

[7] RENOU-MAISSANT, Patricia, Rafik ABDESSELAM a Jean BONNET. Trajectories for Energy Transition in EU-28 Countries over the Period 2000–2019: a Multidimensional Approach. *Environmental Modeling & Assessment* [online]. 2022, **27**(3), 525–551. ISSN 1573-2967. Available at: doi:10.1007/s10666-022-09816-7

[8] INTERNATIONAL ENERGY AGENCY (IEA). Energy system of Slovenia. *IEA* [online]. 2024 [vid. 2024-04-15]. Available at: https://www.iea.org/countries/slovenia

[9] IEA. Croatia - Countries & Regions. *IEA* [online]. 2024 [vid. 2024-09-10]. Available at: https://www.iea.org/countries/croatia

[10] IEA. Bosnia and Herzegovina - Countries & Regions. *IEA* [online]. 2024 [vid. 2024-09-10]. Available at: https://www.iea.org/countries/bosnia-and-herzegovina/electricity

[11] JUNNE, Tobias, Sonja SIMON, Jens BUCHGEISTER, Maximilian SAIGER, Manuel BAUMANN, Martina HAASE, Christina WULF a Tobias NAEGLER. Environmental Sustainability Assessment of Multi-Sectoral Energy Transformation Pathways: Methodological Approach and Case Study for Germany. *Sustainability* [online]. 2020, **12**(19), 8225. ISSN 2071-1050. Available at: doi:10.3390/su12198225

[12] GHISELLINI, Patrizia, Renato PASSARO a Sergio ULGIATI. Environmental assessment of multiple "cleaner electricity mix" scenarios within just energy and circular economy transitions, in Italy and Europe. *Journal of Cleaner Production* [online]. 2023, **388**, 135891. ISSN 0959-6526. Available at: doi:10.1016/j.jclepro.2023.135891

[13] MENG, Linghao a Jusen ASUKA. Impacts of Energy Transition on Life Cycle Carbon Emission and Water Consumption in Japan’s Electric Sector. *Sustainability* [online]. 2022, **14**(9), 5413. ISSN 2071-1050. Available at: doi:10.3390/su14095413

[14] RAMIREZ, A. D., A. BOERO, B. RIVELA, A. M. MELENDRES, S. ESPINOZA a D. A. SALAS. Life cycle methods to analyze the environmental sustainability of electricity generation in Ecuador: Is decarbonization the right path? *Renewable and Sustainable Energy Reviews* [online]. 2020, **134**, 110373. ISSN 1364-0321. Available at: doi:10.1016/j.rser.2020.110373

[15] SALA, Serenella, Andrea Martino AMADEI, Antoine BEYLOT a Fulvio ARDENTE. The evolution of life cycle assessment in European policies over three decades. *The International Journal of Life Cycle Assessment* [online]. 2021, **26**(12), 2295–2314. ISSN 1614-7502. Available at: doi:10.1007/s11367-021-01893-2

[16] EC, European Commission. *COMMUNICATION FROM THE COMMISSION TO THE EUROPEAN PARLIAMENT, THE COUNCIL, THE EUROPEAN ECONOMIC AND SOCIAL COMMITTEE AND THE COMMITTEE OF THE REGIONS A new Circular Economy Action Plan For a cleaner and more competitive Europe, COM/2020/98 final* [online]. 2020 [vid. 2023-11-06]. Available at: https://eur-lex.europa.eu/legal-content/EN/TXT/?uri=COM%3A2020%3A98%3AFIN

[17] EWERT, Amelie, Mascha BROST, Christine EISENMANN a Sylvia STIELER. Small and Light Electric Vehicles: An Analysis of Feasible Transport Impacts and Opportunities for Improved Urban Land Use. *Sustainability* [online]. 2020, **12**(19), 8098. ISSN 2071-1050. Available at: doi:10.3390/su12198098

[18] SCHELTE, Nora, Semih SEVERENGIZ, Jaron SCHÜNEMANN, Sebastian FINKE, Oskar BAUER a Matthias METZEN. Life Cycle Assessment on Electric Moped Scooter Sharing. *Sustainability* [online]. 2021, **13**(15), 8297. ISSN 2071-1050. Available at: doi:10.3390/su13158297

[19] IEA. Transport and Environment Report 2022. *European Environment Agency* [online]. 2022 [vid. 2024-09-11]. Available at: https://www.eea.europa.eu/publications/transport-and-environment-report-2022/term-2022

[20] MINA, Giorgio, Alessandro BONADONNA, Giovanni PEIRA a Riccardo BELTRAMO. How to improve the attractiveness of e-bikes for consumers: Insights from a systematic review. *Journal of Cleaner Production* [online]. 2024, **442**, 140957. ISSN 0959-6526. Available at: doi:10.1016/j.jclepro.2024.140957

[21] EC, European Commission. *COMMUNICATION FROM THE COMMISSION TO THE EUROPEAN PARLIAMENT, THE COUNCIL, THE EUROPEAN ECONOMIC AND SOCIAL COMMITTEE AND THE COMMITTEE OF THE REGIONS The New EU Urban Mobility Framework* [online]. 2021 [vid. 2024-09-12]. Available at: https://eur-lex.europa.eu/legal-content/EN/TXT/?uri=CELEX%3A52021DC0811

[22] HUANG, Yue, Like JIANG, Haibo CHEN, Kaushali DAVE a Tony PARRY. Comparative life cycle assessment of electric bikes for commuting in the UK. *Transportation Research Part D: Transport and Environment* [online]. 2022, **105**, 103213. ISSN 1361-9209. Available at: doi:10.1016/j.trd.2022.103213

[23] BOŠNJAKOVIĆ, Mladen a Vlado TADIJANOVIĆ. Environment impact of a concentrated solar power plant. *Tehnički glasnik* [online]. 2019, **13**(1), 68–74. ISSN 1846-6168, 1848-5588. Available at: doi:10.31803/tg-20180911085644

[24] HUIJBREGTS, Mark A. J., Zoran J. N. STEINMANN, Pieter M. F. ELSHOUT, Gea STAM, Francesca VERONES, Marisa VIEIRA, Michiel ZIJP, Anne HOLLANDER a Rosalie VAN ZELM. ReCiPe2016: a harmonised life cycle impact assessment method at midpoint and endpoint level. *The International Journal of Life Cycle Assessment* [online]. 2017, **22**(2), 138–147. ISSN 1614-7502. Available at: doi:10.1007/s11367-016-1246-y

[25] ISO. ISO 14044:2006. *ISO* [online]. 2022 [vid. 2024-04-16]. Available at: https://www.iso.org/standard/38498.html

[26] ISO. ISO 14040:2006. *ISO* [online]. 2022 [vid. 2024-04-16]. Available at: https://www.iso.org/standard/37456.html

[27] ECOINVENT. ecoinvent - Data with purpose. *ecoinvent* [online]. 2024 [vid. 2024-04-16]. Available at: https://ecoinvent.org/

[28] DIMNIK, Jože, Jelena TOPIĆ BOŽIČ, Ante ČIKIĆ a Simon MUHIČ. Impacts of High PV Penetration on Slovenia’s Electricity Grid: Energy Modeling and Life Cycle Assessment. *Energies* [online]. 2024, **17**(13), 3170. ISSN 1996-1073. Available at: doi:10.3390/en17133170

[29] OEC. *Electricity in Croatia | The Observatory of Economic Complexity* [online]. 2024 [vid. 2024-09-12]. Available at: https://oec.world/en/profile/bilateral-product/electricity/reporter/hrv

[30] INTERNATIONAL TRADE ADMINISTRATION. *Croatia - Energy* [online]. 2023 [vid. 2024-09-12]. Available at: https://www.trade.gov/country-commercial-guides/croatia-energy

[31] DIMNIK, Joze, Peter NOVAK a Simon MUHIC. Decarbonising power system with high share of renewables and optionally with or without nuclear: Slovenia case. *Thermal Science* [online]. 2022, **26**(2 Part B), 1593–1602. ISSN 0354-9836, 2334-7163. Available at: doi:10.2298/TSCI201117342D

[32] ELLIOT, Thomas, Sarah J. MCLAREN a Ralph SIMS. Potential environmental impacts of electric bicycles replacing other transport modes in Wellington, New Zealand. *Sustainable Production and Consumption* [online]. 2018, **16**, 227–236. ISSN 2352-5509. Available at: doi:10.1016/j.spc.2018.08.007

[33] DE BORTOLI, Anne. Environmental performance of shared micromobility and personal alternatives using integrated modal LCA. *Transportation Research Part D: Transport and Environment* [online]. 2021, **93**, 102743. ISSN 1361-9209. Available at: doi:10.1016/j.trd.2021.102743

9th International Conference on the Development of Industrial Engineering
21. November 2024
Novo mesto, Slovenia

Computational fluid dynamics study of the pressure recovery coefficient along the wall of an axial annular diffuser

Pratima Vishwakarma[1], Anubhav Vishwakarma[2], Simon Muhič[1,3]

[1]*Rudolfovo – Science and Technology Centre Novo mesto, Podbreznik 15, 8000 Novo mesto, Slovenia*
E-mails: simon.muhic@rudolfovo.eu, erpratima00@gmail.com

[2]*Jozef Stefan institute, Jamova cesta 39, Ljubljana, Slovenia*
E-mail: anubhav.vishwakarma@ijs.si

[3]*Faculty of Industrial Engineering Novo mesto, Šegova ulica 112, 8000 Novo mesto, Slovenia*
E-mail: simon.muhic@fini-unm.si

Abstract: *The characteristics of a swirl-free flow with a different type of annular diffuser at same area ratio by carrying out simulations in the frame of computational fluid dynamics (CFD) were investigated. The RNG $k - \varepsilon$ turbulence model is applied. The investigation is carried out for different experimentally obtained inlet velocity profiles in the flow regime. The flow is analyzed numerically by calculating the axial velocity and the pressure-recovery coefficient as a function of the position within the diffuser. Pressure coefficients have been calculated along the casing and hub walls of an axial annular diffuser. A decrease in the velocity and a consequent increase in the pressure along the flow direction is found in agreement with experimental data. The result was represented from the contour of pressure recovery, and the contour of velocity magnitude. The results justify the numerical approach and call for further tests of alternative turbulence models.*

Keywords: *Annular diffuser, Area ratio, Axial velocity, Pressure recovery coefficient, Computational fluid dynamics.*

Article Classification: *Scientific paper*

1 INTRODUCTION

A diffuser is an essential fluid dynamic device used to reduce the kinetic energy of the fluid by pressure work, resulting in reduced velocity and increased static pressure. Furthermore, diffusers are used to achieve a uniform flow at the exit by keeping the contribution of the transversal-velocity components below 10%. The inner-wall configuration of annular diffusers affects the flow dynamics within the device, increasing the design complexity. The performance of a diffuser depends on its geometric and dynamic characteristics. In the application, the diffuser recuperates kinetic energy from the turbine and compressor discharge in turbomachinery, enhancing the overall isentropic pressure efficiency [1]. Renewable energy production is a recent accomplishment, as there is a growing demand for environmentally friendly energy production. There is an increasing demand for machinery advancement, and the production of machine parts is complex yet necessary to meet these geometric manufacturing needs [2]. Efficient turbomachinery depends on the transfer of energy between the fluid and the rotor, which consists of two major components, the turbine and the compressor, and various factors influence the overall efficiency [3]. A number of diffusers are available to match the area of growth or deflect at the output. They are designed to minimize the velocity of the outlet in relation to the inlet to achieve the lowest possible pressure drop while maximizing the pressure recovery [4]. Diffusers can be categorized based on their geometry and provide uniform flow at the outlets. To achieve optimal combustor performance, it is necessary to design and optimize the shape of the diffuser to meet specific essentials. The annular diffuser for the exhaust comprises an inner wall with an outer surface and an outer element with an inner surface [5]. These two components are connected through the annular diffuser, which facilitates the assembly of the diffuser. The outer component governs the flow towards the exhaust and is supported by the inner associate surface [6].

In order to have a better understanding of the flow behavior of diffusers, several theoretical investigations have been carried out in the late 20th century. The efficiency of an axial annular diffuser with a parallel diverging hub and casing was experimentally examined with and without swirl. The values used were Rh_i = 38.0 mm, Rci = 77.5 mm, θ_h = 0°, θ_c = 20° and L= 158.67 cm The pressure recovery coefficient (C_P) was estimated, and it was found that the diffuser length increased without swirl flow [7]. Furthermore, the efficiency of a leverage annular diffuser was investigated, taking into account different swirl quantities $(0.0, 0.4, 0.8)$ and compared to those with almost identical swirl numbers, the diffusers without struts had remarkably high-pressure recovery coefficients and the influence of struts was addressed [8].

Latest research results observed and evaluated the effectiveness variety of annular diffusers with various divergence angles $(9°, 15°, 21°, 27°)$ and the results revealed that the pressure coefficient grew with an increasing divergence angle up to the value of $21°$ at which a drop was observed [9]. A further increase of the angle above $21°$, and $27°$ produced no meaningful improvements [10]. Another research was performed to evaluate the outcome characteristics of S-shaped diffusers by vertical and horizontal offsets [11]. Another investigation was analyzed two different cross-section shapes for the S-shaped diffuser by vertical and horizontal offsets and two-outlet-cross-section geometries, semi-circular and rectangular, as well as four-vertical-offset heights relative to the characteristic dimension $(\mathrm{z} = 0.25, 0.5, 0.75\ , 1)$, were studied too [12]. This previous study indicated that the pressure recovery was reduced when the vertical offset increased. Furthermore, the magnitude of the velocity contours increased with higher degrees of vertical offsetting and many annular diffuser geometries, including parallel diverging hub and casing (PDHC), unequal diverging hub and casing (UDHC), straight hub and diverging casing (SHDC) and converging hub and diverging casing (CHDC), were implemented, and an equivalent cone angle of 15° cone angle of the identical length (278 mm) [13]. The Parallel-diverging-hub-and-casing annular diffuser performs better when subjected to an inlet swirl, with an ideal swirl angle between 20° and 30° and the convergent-hub-diverging-and-casing diffuser shows the worst performance in terms of swirl effects [14]. The study examined the impact of offset on an S-shaped diffuser using semicircular and rectangular inlet and the centerline length was $4.0625\ \mathrm{mm}$, and the radius of curvature was measured to be $1.1938D$ [15]. The CFD simulations were performed using miscellaneous turbulence models for an annular axial diffuser through identical geometry and flow circumstances, and the RNG $k-\varepsilon$turbulence model was adopted due to its relative agreement with experimental impacts [9].

This work employs a parametric approach to investigate how design affects diffuser performance and the relationship between coefficients of static pressure gain (Cps) and offset distances. The Cps decreased at all measuring stations along the center line with increasing distance, resulting in a decrease in effectiveness. The CFD software engaged to analyze the flow characteristics of these diffusers with 10^{o}cone angle and 4.25 area ratio.

2 CFD MODELING

The geometry of the annular diffuser was designed and applied using ANSYS software, and an appropriate mesh was constructed. This analysis involves the development and comparison of $k-\varepsilon$ turbulence models using geometries with empirical results, and the equations are compared using traditional renormalization group (RNG) and realizable techniques. The inlet velocity profile associated with the diffuser reached the 5% turbulence specification, and the inlet sketch diffuser hydraulic diameter was identified. The equation governing the momentum of turbulent flow includes second-order terms for kinetic energy and turbulence dissipation. The diffuser outlet layout was determined based on the hydraulic diameter, with the outlet boundary set to zero-gauge pressure and turbulence intensity.

The analysis converged the CFD model and determined the velocities of continuity, including components (v_x, v_r, v_z). To ensure grid independence, this research has been conducted multiple times with mesh sizes ranging from 57786 to 129987 finite volumes. The RNG $k-\varepsilon$ turbulence model for 2D axisymmetric cases demonstrates explicit division along the central axis and closely matches experimental results [13].

2.1 Problem Description and Modelling of Annular Diffuser

The performance of an annular diffuser is significantly impacted by miscellaneous parameters (e.g. casing, hub, area ratio, and axial length) and dynamic parameters (e.g. velocity profile, Reynolds number, swirl conditions, and boundary layer) [16]. There are four configurations illustrated in Figure 1 and the inlet diameter of the diffuser to evaluate and improve the efficiency of these configurations and specific parameters (Rhi = 3.8 cm, Rci = 7.75 cm, θh = −2.81°, θc = 3.53°, Li = 5 cm, and L = 77.20 cm). The CFD has been used for the evaluation of several parameters. Details of numerical mesh, boundary conditions and geometry are presented in the Table 1 and 2**.**

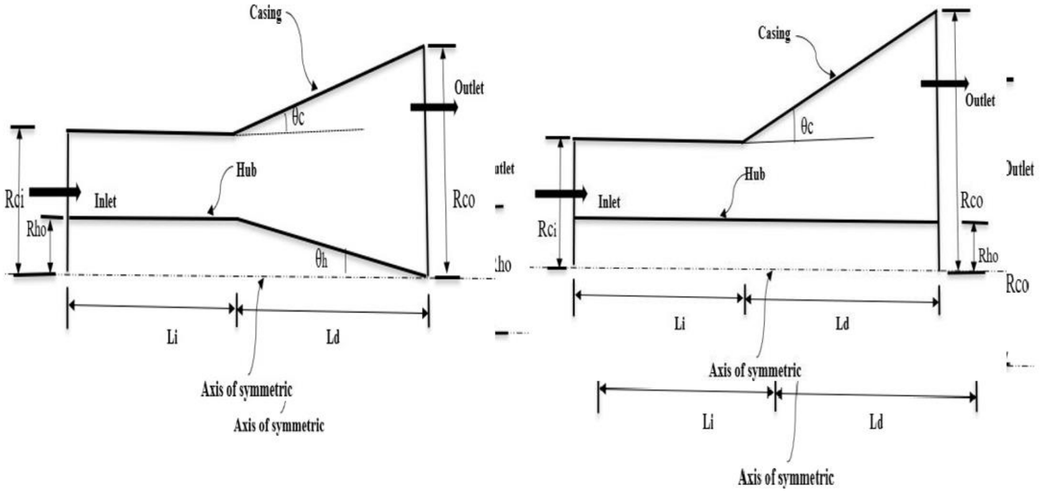

Figure 1: Various annular diffuser geometries (in axis of symmetric form) analyzed AR = 4.25

2.2 Meshing of Annular Diffuser

The inlet diameter is 3.8 cm, and the inlet length is 5 cm, whereas the outlet diameter depends on different geometry types and the total length taken in this analysis and geometry with the details given in Figure 1.

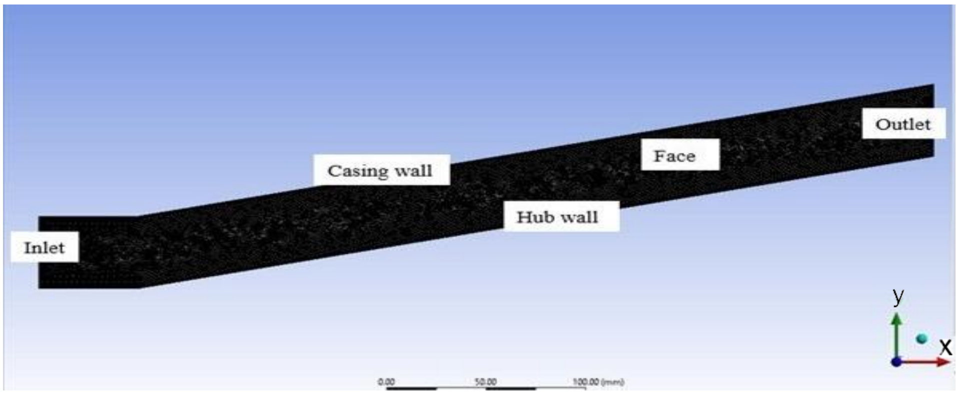

Figure 2: The mesh of the PDHC diffuser geometry

Figure 2 shows the geometry of the diffuser. The X-Y plane was selected for the sketch, and the axial length of the diffuser was measured along the X axis. The meshing, which refers to the division of each model into a number of finite volumes, is a method known as discretization. The mesh was created in the Ansys 15 software environment and used quadrilateral type of mesh.

Table 1: Diffuser dimensions and, meshing details

Inlet and outlet (edge)	Number of divisions = 100
Casing and hub (edge)	Number of divisions = 110
Face	Element sizing = 0.5 mm
Number of nodes/elements	130840/130025
Material	Fluid = air, Density =1.225 kg/m^3
Boundary condition	Inlet = flat velocity, 50 m/s Outlet = gauge pressure 0 Pa, Turbulence intensity = 5 %

Table 2: Details of the analyzed geometries

Geometrical parameters	Different types of diffusers			
	Diverging casing and Converging Hub	Diverging casing and Straight Hub	Parallel diverging Casing and Hub	Unequal Diverging and Converging hub
Area ratio	4.25	4.25	4.25	4.25
Equivalent cone angle	10°	10°	10°	10°
Hub inlet radius (cm)	3.8	3.8	3.8	3.8
Hub outlet radius (cm)	0	3.8	22.56	10.55
Casing inlet radius(cm)	7.75	7.75	7.75	7.75
Casing exit radius (cm)	13.92	14.3	26.51	17.47
Hub angle	-2.8°	0°	12.64°	5°
Casing angle	4.57°	4.64°	12.64°	7.17°

3 GOVERNING FLUID EQUATIONS

The fluid-dynamics problem is described by fundamental governing equations for 2D axisymmetric design with swirl [12], [13]. The continuity equation is written as:

$$\frac{\partial \rho}{\partial t} + \nabla .(\rho \vec{v}) = S_m \tag{1}$$

Equation (1) is the general form of the conservation of mass equation and is valid for both incompressible and compressible flows. The source S_m is the mass added to the continuous phase from the dispersed second phase (e.g. due to evaporation of liquid droplets) and any user defined sources. In the 2-D axisymmetric geometry is rewritten as:

$$\frac{\partial \rho}{\partial t} + \frac{\partial (\rho v_x)}{\partial x} + \frac{\partial (\rho v_r)}{\partial r} = S_m \tag{2}$$

Here are x and r axial and radial directions, respectively, while v_x illustrates axial velocity and v_r radial velocity. Momentum equation in the common form can be written as follows:

$$\frac{\partial}{\partial t}(\rho \vec{v}) + \nabla \vec{v}.(\rho \vec{v}) = -\nabla p + \nabla .(\bar{\tau}) + \rho . \vec{g} + \vec{F} \tag{3}$$

Here, p denotes static pressure, $\bar{\tau}$ designates the stress tensor, $\rho . \vec{g}$ acceleration of gravity, and $\vec{F}$ represents external forces density. The stress tensor is defined as:

$$\bar{\tau} = \mu \left[\left(\nabla \vec{v} + \nabla \vec{v}^{r} - \frac{2}{3} \nabla . \vec{v} I \right) \right] \tag{4}$$

with the viscosity μ and the unit tensor I. The axial and radial momentum equations for 2D symmetric geometries can be written as:

$$\frac{\partial (\rho v_x)}{\partial t} + \frac{1}{r}\frac{\partial (r \rho v_x v_x)}{\partial x} + \frac{1}{r}\frac{\partial}{\partial r}(r \rho v_r v_x) = -\frac{\partial \rho}{\partial x} + \frac{1}{r}\frac{\partial}{\partial x}\left[r\mu \left(\left\{ 2\frac{\partial v_x}{\partial x} - \frac{2}{3}(\nabla . \vec{v}) \right\} \right) + \frac{1}{r}\frac{\partial}{\partial r}\left(r\mu \frac{\partial v_x}{\partial r} + \frac{\partial v_r}{\partial x} \right) \right] + F_x \tag{5}$$

$$\frac{\partial}{\partial t}(\rho v_r) + \frac{1}{r}\frac{\partial}{\partial x}(r\rho v_x v_r) + \frac{1}{r}\frac{\partial}{\partial r}(r\rho v_r v_r) = -\frac{\partial p}{\partial r} + \frac{1}{r}\frac{\partial}{\partial x}\left[r\mu\left(\frac{\partial v_r}{\partial x} + \frac{\partial v_x}{\partial r}\right)\right] + \frac{1}{r}\frac{\partial}{\partial r}\left[r\mu\left(2\frac{\partial v_r}{\partial r} - \frac{2}{3}(\nabla . \vec{v})\right)\right] - 2\mu\frac{v_r}{r^2} + \frac{2}{3}\frac{\mu}{r}(\nabla . \vec{v}) + \rho\frac{v_z^2}{r} + F_r \tag{6}$$

where,

$$\nabla . \vec{v} = \frac{\partial v_x}{\partial x} + \frac{\partial v_r}{\partial r} + \frac{v_z}{r}$$

Here $v_z$is the swirl velocity. The tangential momentum equation for 2D swirling flows may be written as:

$$\frac{\partial}{\partial t}(\rho v_z) + \frac{1}{r}\frac{\partial}{\partial x}(r\rho v_x v_z) + \frac{1}{r}\frac{\partial}{\partial x}(r\rho v_x v_z) = \frac{1}{r}\frac{\partial}{\partial x}\left[r\mu\frac{\partial v_z}{\partial x}\right] + \frac{1}{r^2}\frac{\partial}{\partial r}\left[r^3\mu\frac{\partial}{\partial r}\left(\frac{v_z}{r}\right)\right] - \rho\frac{v_x v_z}{r} \tag{7}$$

3.1 Performance Evaluation of Annular Axial Diffuser

The investigation on the standard diffuser model performed for the RNG $k - \varepsilon$ turbulence model presented more pertinent results for swirling and non-swirling flows [18]. The RNG $k - \varepsilon$ turbulence model establishes a more significant connection, ultimately mathematically generating velocity profiles indicating the transverse velocity profile and pressure recovery coefficient. Because of their small magnitude and high frequency, modeling the corresponding oscillations accurately can be computationally demanding. To simplify the problem, the governing equations can be modified using techniques such as time-averaging or ensemble-averaging to eliminate small scales.

Coefficient of Pressure Recovery C_p is represented as the proportion between the work of pressure and the transformed kinetic energy as an influence of the diffusion effort:

$$C_p = \frac{2(P_2 - P_{in})}{\rho v_i^2} \tag{8}$$

The absolute pressure ratio is a dimensionless parameter that illustrates the ratio of outlet total pressure to inlet total pressure. It is primarily used for supersonic flows:

$$\eta = \frac{C_p}{C_{pi}} \tag{9}$$

4 GRID INDEPENDENCE TEST

In the computational model for the proposed geometry, the construction of the mesh and the finer mesh significantly impact the results. The finer mesh consists of nodes or a grid structure and size, affecting the physical model, and the smoother mesh ensures more additional computation times [17]. Grid size optimization plays a crucial role in maintaining accuracy in less time and improving performance, and the RNG $k - \varepsilon$ turbulence model was used in the analysis, and resilience was investigated using five different grid sizes [18].

Table 3: Grid Independence in Terms of Node Count

S.N.	Mesh size (mm)	Number of nodes	Number of elements	Cp at the outlet (%)
1	0.8	58376	57786	0.61
2	0.7	74417	73773	0.62
3	0.6	96959	96226	0.63
4	0.5	130805	129987	0.64
5	0.4	203847	202870	0.64

Various types of meshes were studied for the independence test and symmetry-adjusted mesh size to the solution, and the annular diffuser element size was varied between 0.4mm and 0.8mm to ensure mesh symmetry. The analysis examined the impact of element size on research results and the computational time required to obtain them.

5 RESULTS AND DISCUSSION

The impact of mesh size (0.8, 0.7, 0.6, 0.5 and 0.4 mm) when employing the RNG $k-\varepsilon$ turbulent model is illustrated in Figure 3 and Table 3. The value was used because the mesh size parameters (0.4 and 0.5 mm) presented almost identical results. The equal turbulence model has been used for the evaluation of the performance of miscellaneous axial annular diffusers with exact area ratios. The pseudo velocity (y/Ym) was specified by crossing the non-dimensional length of diffuser at different shape. The different diffuser hub positions y/Ym = 0, the transverse casing is y/Ym = 1, and all the transverses routing is shown in the class x/L = 0.1, 0.2, 0.4, 0.6, 0.8 and 0.9. x/L represents traverse of the full length of diffuser.

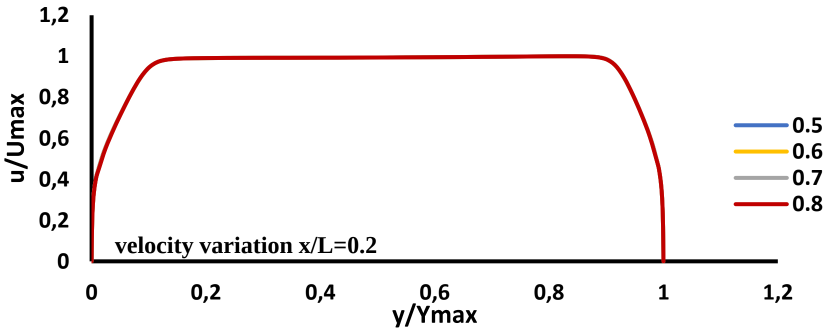

Figure 3: Representation of Mesh independence on size of the element

5.1 Converging Hub and Diverging Casing

The availability of more CHDC annular diffusers can affect the spread or diffusion, and this has been attributed to the centrifugal force causing energy to flow toward the casing wall. Figures 4(i) and (ii) illustrate the distribution of the static pressure coefficient and velocity variation along the diffuser. Different colors indicate the fluid characteristics, including pressure and velocity. A particular color does not give the single value of these characteristics but shows the range of these values. If the value of a characteristic at a particular point falls in this range, there will be color of that range. These results have practical applications in understanding and optimizing the performance of diffusers in various engineering applications.

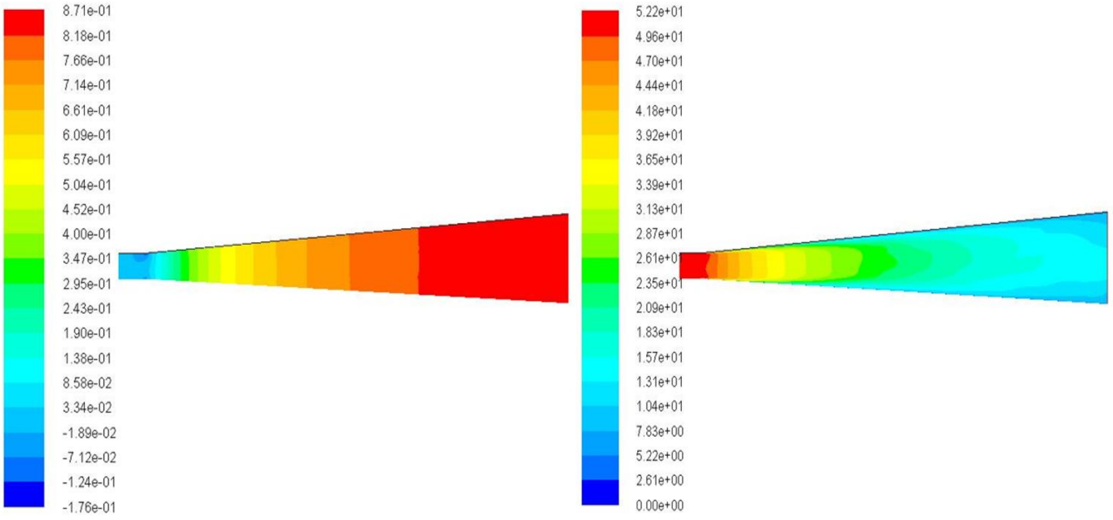

(i) (ii)

Figure 4: (i) shows the contours of the pressure coefficient distribution (dimensionless), and (ii) represents the contours of the velocity variation (m/s) for CHDC

Figure 5 shows the pressure recovery curve along the wall, indicating the minimum high pressure along the casing wall and elevated pressure along the hub wall. It was observed that reducing the peak velocity to y/Ym = 0.82, 0.78, 0.71, 0.53, and 0.50 for x/L = 0.1, 0.2, 0.4, 0.6, and 0.8 respectively resulted in backflow occurring at the segment (x/L = 0.9). Figure 6 shows the nature of the tangential velocity distribution of the forced vortex.

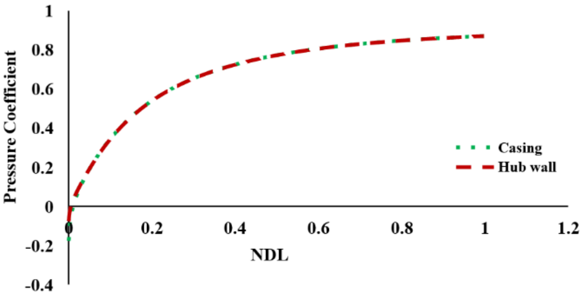

Figure 5: Pressure Coefficient for AR=4.25 in CHDC

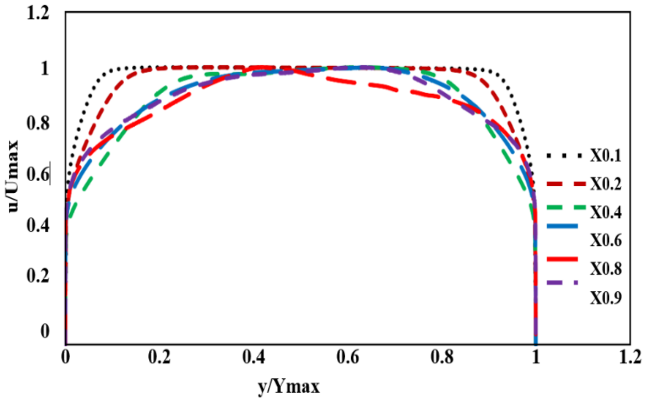

Figure 6: Velocity variation for AR=4.25 in CHDC

5.2 Straight hub and Diverging casing

Figures 7(i) and (ii) show the distribution of static pressure coefficients and velocity variation along the diffuser. The various colors represent fluid properties such as pressure and velocity distribution. It should be noted that a given hue does not represent a single value for these attributes but rather the range of these values. If the value of a characteristic at a certain point fall within this range, that range's color will be displayed. SHDC gave better results, and Figure 8 illustrates the pressure recovery curve along the wall, representing the lowest pressure along the casing wall and the increased pressure along the hub wall.

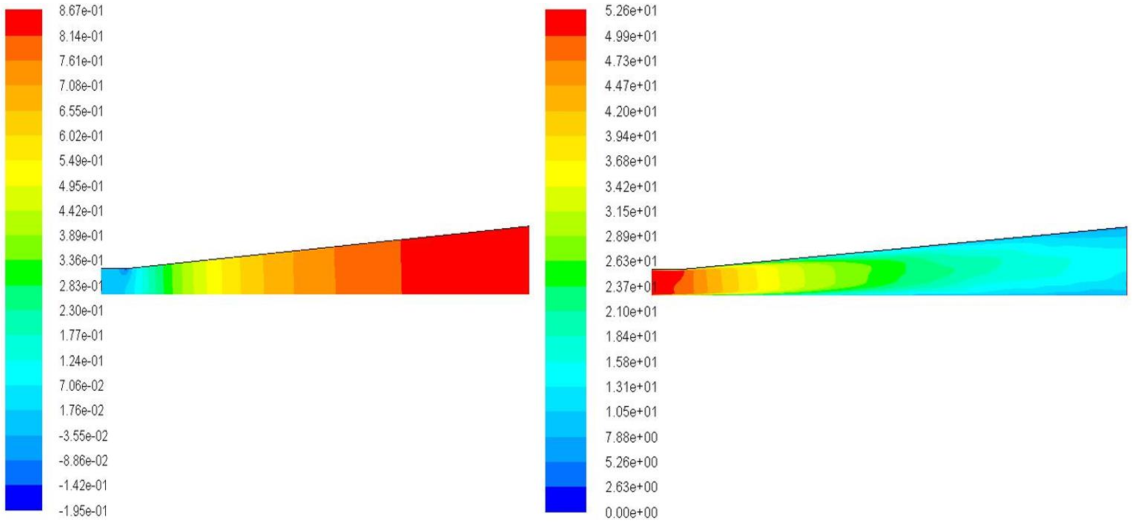

(i) (ii)

Figure 7: (i) illustrates the contours of the pressure coefficient distribution (dimensionless), while figure (ii) depicts the contours of the velocity variation (m/s) for SHDC

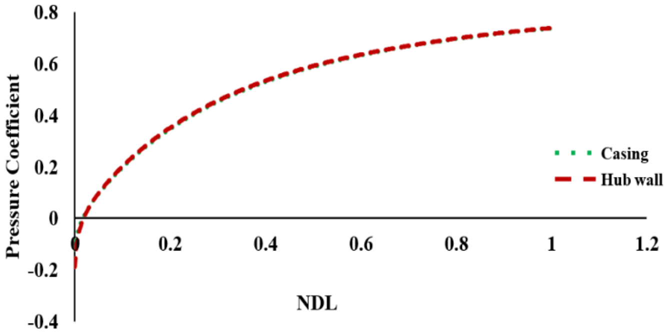

Figure 8: Pressure Coefficient for AR=4.25 in SHDC

Figure 9 displays the nature of the tangential velocity distribution of the forced vortex, which shows an identical trend to that observed in the previous cases. Similarly, analyses on annular diffusers with DCSH have revealed that reducing the peak velocity to y/Ym = 0. 82, 0.78, 0.71, 0.53, and 0.50 for x/L = 0.1, 0.2, 0.4, 0.6, 0.8 respectively, results in backflow occurring at the segment (x/L = 0.9).

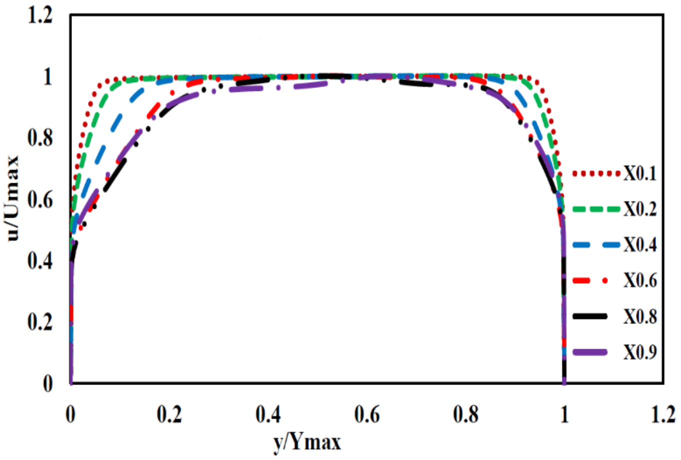

Figure 9: Velocity variations plots at AR = 4.25 in SHDC

5.3 Parallel diverging Hub and casing

The tangential velocity circulation and pressure distribution in a Parallel Diverging hub and Casing (PDHC) with an annular diffuser shows a higher pressure along the casing wall than along the hub wall.

Figures 10(i) and (ii) demonstrate the distribution of static pressure coefficients and velocity variation along the diffuser. The different colors denote fluid qualities like pressure and velocity variance.

The pressure recovery coefficient increases continuously, and Figure 11 shows the static pressure distribution along the wall. The normalized peak velocity decreases continuously from y/Ym = 0.47 and 0.34 for x/L = 0.6 and 0.8, respectively. The flow is directed towards the casing for x/L = 0.1, 0.2, 0.4, and 0.6, and the flow is reversed up to y/Ym = 0.15, 0.24, 0.33, and 0.47, respectively. The velocity variation plots show that the dimensionless velocity is highest near the casing wall and decreases toward the hub wall. Figure 12 shows the tangential velocity variation profile, showing different shapes with different points.

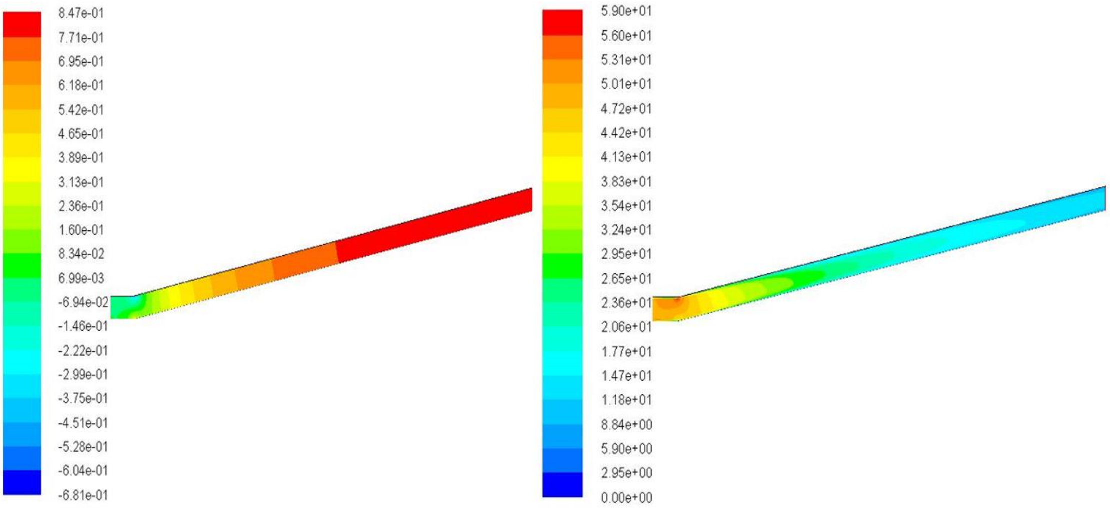

(i) (ii)

Figure 10: (i) depicts the contours of the pressure coefficient distribution (dimensionless), while (ii) shows the contours of the velocity variation (m/s) for the PHDC

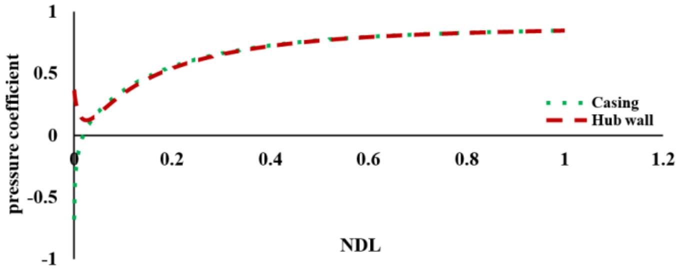

Figure 11: Pressure Coefficient for AR=4.25 in PDHC

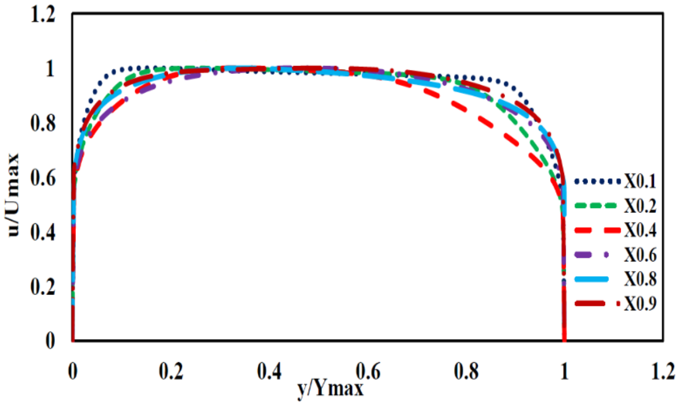

Figure 12: Velocity variation graph for AR=4.25 in PDHC

5.4 Unequal diverging casing and hub

Figures 13(i) and (ii) show the distribution of static pressure coefficients and velocity variation over the diffuser. The varied colors represent fluid properties such as pressure and velocity variation. Figures 14 and 15 depict the pressure and velocity profiles in the UDCH. The calculations for this case are identical to those in the previous case.

For x/L values of 0.1, 0.2, and 0.4, there is a steady increase in peak velocity observed at y/Ym values of 0.15, 0.23, and 0.48, and the peak velocity is y/Ym = 0.48 for x/L values of 0.6, 0.8, and 0.9. Table 3 exhibits an analysis of the performance of various types of diffusers, including pressure coefficient and velocity variations. The CHDC annular diffuser is more efficient than the SHDC annular diffuser, possibly due to increased flow and other variables, making it the most efficient of the four different-shaped diffusers.

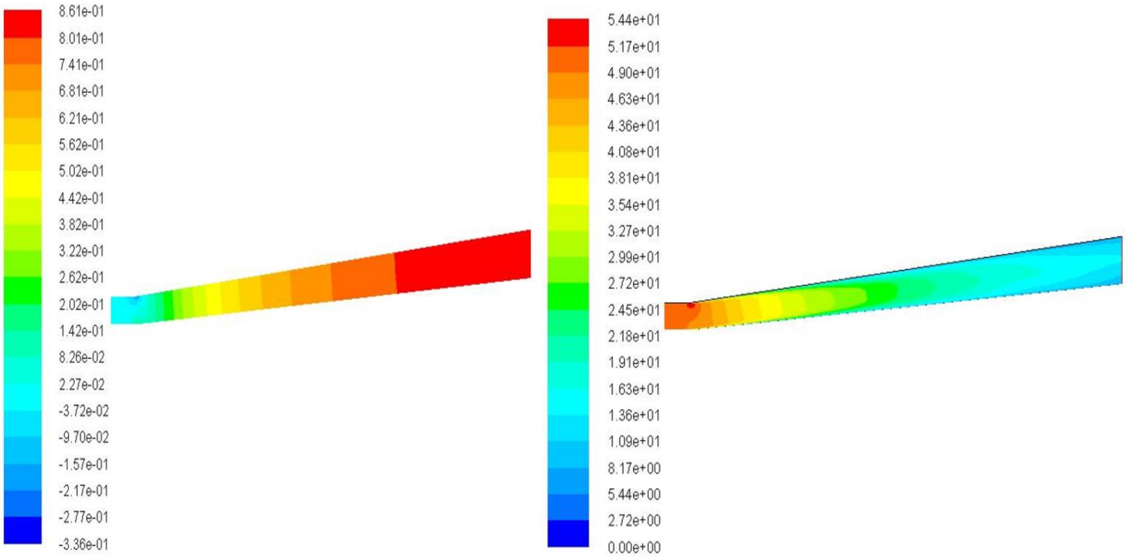

(i) (ii)

Figure 13: (i) depicts the contours of the pressure coefficient distribution (dimensionless), while (ii) shows the contours of the velocity variation (m/s) for the UDCH

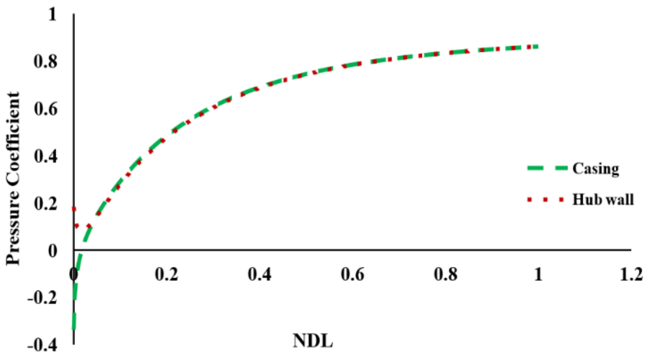

Figure 14: Pressure Coefficient for AR=4.25 in UDHC

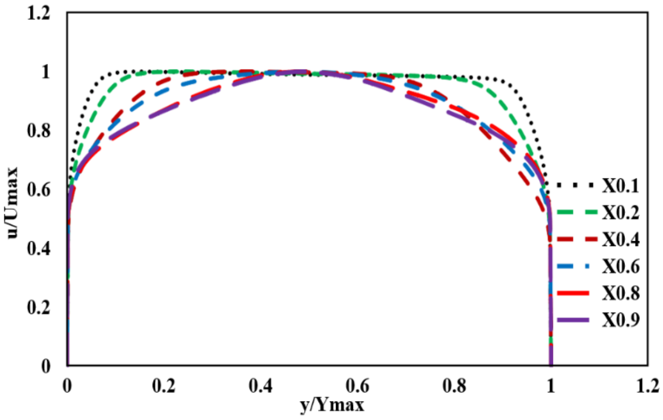

Figure 15: Velocity variation graph for AR=4.25 in UDHC

Table 4: Investigated C_p and velocity variation at the outlet of the annular diffusers

Performances	Pressure coefficient		Velocity variation (m/s)	
	Max.	Min.	Max.	Min
CHDC	0.87	-0.1758	52.2	13.1
SHDC	0.86	-0.1213	52.6	13.1
PDHC	0.84	-0.686	59.0	11.9
UDHC	0.85	-0.3365	54.4	13.6

Figure 16 shows that the CHDC diffuser has the highest threshold cp, with the PDHC diffuser displaying a slightly lower value of 0.84. The graph plot shows the relationship between the Pressure coefficients and diffuser passage height in the form of NDL. This graph shows the performance of the four diffuser types along the casing wall. This figure shows that the Pressure coefficient decreased first and then after slightly increasing along the wall, respectively, for the proposed diffuser.

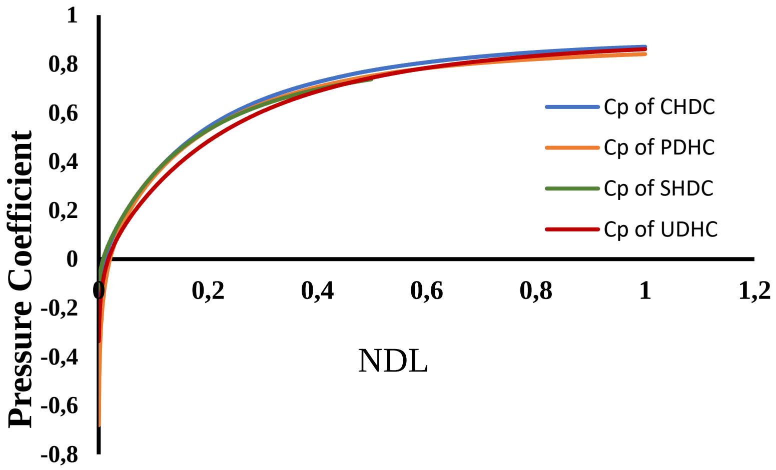

Figure 16: Comparison results of proposed CHDC, SHDC, PHDC and UDHC of Pressure coefficient along the casing wall for area ratio (AR=4.25)

6 CONCLUSION

The performance of the annular diffuser has been studied within the framework of computational fluid dynamics by using the RNG $k-\varepsilon$turbulence model. The focus was on annular diffusers with an area ratio of 4.25 and without swirl flow. The results revealed a close agreement with experimental data, which justifies the use of the turbulence model. The velocity profile calculation showed the various positions, shapes, and changes in fluid movement regions directed along the boundary layers. The velocity initially increases at the beginning of the diffuser and then gradually decreases as the momentum at the outlet is minimal. The pressure recovery coefficient increases, and the velocity decreases uniformly along the flow direction of the diffuser. The CFD simulation results suggest that the RNG $k-\varepsilon$ turbulence model is suitable for estimating the pressure recovery coefficient in an equivalent diffuser. Although the DCCH annular diffuser performed the best, testing other turbulence models in future research is advisable.

REFERENCES

[1] J. Walter, D. Wurz, S. Hartig, and M. Gabi, ‘Experimental investigation of an annular diffuser for axial fans at different inflow profiles’, *Therm. Sci.*, vol. 21, pp. S553–S564, 2017, doi: 10.2298/TSCI160408183W.
[2] S. Ubertini and U. Desideri, ‘Experimental performance analysis of an annular diffuser with and without struts’, *Exp. Therm. Fluid Sci.*, vol. 22, no. 3–4, pp. 183–195, 2000, doi: 10.1016/S0894-1777(00)00025-X.
[3] E. S. Shukri, ‘Numerical Comparison of Temperature Distribution in an Annular Diffuser Fitted with Helical Screw-Tape Hub and Pimpled Hub’, *Energy Procedia*, vol. 141, pp. 625–629, 2017, doi: 10.1016/j.egypro.2017.11.083.
[4] S. Rasidi *et al.*, ‘Numerical investigation of 180o curved diffuser performance by varying geometrical and operating parameters’, *CFD Lett.*, vol. 12, no. 7, pp. 100–109, 2020, doi: 10.37934/cfdl.12.7.100109.
[5] E. S. Shukri, B. H. Abdullah, and O. M. Mohammed Ali, ‘Velocity Distribution in an Annular Diffuser Fitted with Twisted Hub for Different Area Ratios’, *Energy Procedia*, vol. 141, pp. 639–643, 2017, doi: 10.1016/j.egypro.2017.11.086.
[6] K. Jeyachandran and V. Ganesan, ‘Numerical modelling of turbulent flow through conical diffusers with uniform and wake velocity profiles at the inlet’, *Math. Comput. Model.*, vol. 10, no. 2, pp. 87–97, 1988, doi: 10.1016/0895-7177(88)90070-2.
[7] B. B. Arora, ‘Performance analysis of parallel hub diverging casing axial annular diffuser with 20° equivalent cone angle’, *Aust. J. Mech. Eng.*, vol. 12, no. 2, pp. 179–194, 2014, doi: 10.7158/m11-823.2014.12.2.
[8] R. Prakash, V. K. Srinivas, H. Anand, G. Adithya, and N. Lakshmi Narayanan, ‘Effect of Swirl on the Performance of an Annular Diffuser’, *Appl. Mech. Mater.*, vol. 787, pp. 318–321, 2015, doi: 10.4028/www.scientific.net/amm.787.318.
[9] R. Keerthana and G. J. Rani, ‘Flow Analysis of Annular Diffusers’, *Int. J. Eng. Res. Appl.*, vol. 2, no. 3, pp. 2348–2351, 2012.
[10] M. A. Alvarenga, C. R. Andrade, and E. L. Zaparoli, ‘Compressible subsonic flow in gas turbine annular

diffusers’, *Int. Rev. Mech. Eng.*, vol. 10, no. 7, pp. 474–481, 2016, doi: 10.15866/ireme.v10i7.8994.
[11] E. M. Cherry, A. M. Padilla, C. J. Elkins, and J. K. Eaton, ‘Three-dimensional velocity measurements in annular diffuser segments including the effects of upstream strut wakes’, *Int. J. Heat Fluid Flow*, vol. 31, no. 4, pp. 569–575, 2010, doi: 10.1016/j.ijheatfluidflow.2010.02.029.
[12] M. Kumar, B. B. Arora, S. Maji, and S. Maji, ‘Effect of area ratio and inlet swirl on the performance of annular diffuser’, *Int. J. Appl. Eng. Res.*, vol. 7, no. 13, pp. 1493–1506, 2012.
[13] S. N. Singh, V. Seshadri, K. Saha, K. K. Vempati, and S. Bharani, ‘Effect of inlet swirl on the performance of annular diffusera having the same equivalent cone angle’, *Proc. Inst. Mech. Eng. Part G J. Aerosp. Eng.*, vol. 220, no. 2, pp. 129–143, 2006, doi: 10.1243/09544100G05004.
[14] B. Dr Salim, ‘Effect of Goemeterical Parameters on the Performance of Wide Angle’, *Int. J. Innov. reasearch Sci. Eng. Technol.*, vol. 2, no. 9, pp. 4178–4191, 2013.
[15] M. Kumar Gopaliya, M. Kumar, S. Kumar, and S. Manjaree Gopaliya, ‘Analysis of performance characteristics of S-shaped diffuser with offset’, *Aerosp. Sci. Technol.*, vol. 11, no. 2–3, pp. 130–135, 2007, doi: 10.1016/j.ast.2006.11.003.
[16] V. Ganesan, ‘Flow and boundary layer development in straight core annular diffusers’, *Int. J. Eng. Sci.*, vol. 18, no. 2, pp. 287–304, 1980, doi: 10.1016/0020-7225(80)90051-8.
[17] D. C. and K. K. R. Prakash, ‘CFD analaysis of flow through a conical exhaust’, *Int. J. Res. Eng. Technol.*, vol. 3, no. 11, pp. 239–248, 2014.
[18] K. Saha, S. N. Singh, V. Seshadri, and S. Mukhopadhyay, ‘Computational analysis on flow through transition S-diffusers: Effect of inlet shape’, *J. Aircr.*, vol. 44, no. 1, pp. 187–193, 2007, doi: 10.2514/1.22828.

Vpliv načina vožnje na hitrost regeneracije filtra trdnih delcev v dizelskem motorju

Matej Fike[1], Andrej Predin[1], Andraž Roger[1]

[1]*Univerza v Mariboru, Fakulteta za energetiko, Hočevarjev trg 1, 8270 Krško, Slovenija*
E-naslovi: matej.fike@um.si, andrej.predin@um.si, andraz.roger@um.si

Povzetek: *Namen strokovnega prispevka je analizirati vpliv načina vožnje na hitrost regeneracije filtra trdnih delcev (angl. DPF – Diesel Particulate Filter, poznan tudi kot fr. FAP - Filtres à Particules) v vozilih z dizelskim motorjem. DPF je ključna komponenta v sodobnih dizelskih motorjih, zasnovana za zmanjšanje onesnaženja okolice z zajemanjem sajastih delcev. DPF filtri zahtevajo občasno regeneracijo, kar pomeni, da se nabrani delci z uporabo toplote izpušnih plinov sežgejo, s tem pa se obnovi učinkovitost filtra. Na proces regeneracije lahko vplivajo različni dejavniki, vključno z močjo motorja med fazo regeneracije.*

Naša raziskava posebej preučuje, kako različne ravni moči motorja vplivajo na trajanje regeneracije DPF. Predvidevamo, da višja moč motorja med regeneracijo vodi k hitrejšemu in bolj učinkovitemu procesu regeneracije, medtem ko nižja moč motorja podaljšuje trajanje regeneracije. Za preverjanje te hipoteze smo zbrali in analizirali podatke o vožnji med dogodki regeneracije DPF pri različnih močeh.

Podatki so bili zabeleženi med več vožnjami, zajemajoč primere tako nizke kot visoke moči motorja med regeneracijo. Ti nabori podatkov vključujejo parametre kot so hitrost vozila, obremenitev motorja ter temperatura izpušnih plinov. S primerjavo trajanj regeneracije pri različnih ravneh moči ugotavljamo korelacijo med močjo motorja in hitrostjo aktivne regeneracije.

V zaključku naša raziskava poudarja pomen načina vožnje na regeneracijo DPF in izpostavlja potencialne koristi vzdrževanja višje moči motorja med dogodki regeneracije za bolj učinkovit nadzor emisij.

Ključne besede: *filter trdnih delcev, dizel motor, OBD podatki, regeneracija*

Razvrstitev: *Strokovni prispevek*

1 UVOD

Filter trdnih delcev (angl. Diesel Particulate Filter - DPF) je z uvedbo standarda EURO 5 od leta 2009 obvezna komponenta sodobnih dizelskih motorjev, ki zmanjšuje onesnaženje zraka s PM (angl. Particulate Matter) delci z zajemanjem sajastih delcev v izpušnih plinih. Delci v izpušnih plinih so predvsem produkt nepopolnega zgorevanja goriva in so sestavljeni iz saj, ogljikovodikov in pepela.

DPF je nameščen v izpušnem sistemu in je običajno izdelan iz porozne keramične strukture. Struktura DPF je oblikovana v satasto mrežo kanalov, ki so izmenično zaprti na enem od koncev. Ta oblika prisili izpušne pline, da prehajajo skozi porozne stene filtra, kjer se delci ujamejo, medtem ko prečiščeni plini potujejo naprej skozi izpušni sistem. Poroznost in velikost kanalov sta natančno izračunani, da omogočata optimalno filtracijo delcev, hkrati pa vzdržujeta učinkovit pretok izpušnih plinov [1].

Med obratovanjem motorja se saje in drugi delci, ki nastajajo pri zgorevanju goriva, kopičijo na stenah kanalov znotraj DPF. Ta proces postopoma vodi do povečanja tlaka v izpušnem sistemu, kar lahko povzroči zmanjšano učinkovitost motorja in povečano porabo goriva. Visoka obremenitev filtra z delci povzroči večje izgube pri pretoku izpušnih plinov, kar ima za posledico zmanjšanje zmogljivosti motorja [2]. To nalaga potrebo po redni regeneraciji DPF, ki obnavlja njegovo zmogljivost filtracije. Za izdelavo DPF se najpogosteje uporabljata kordierit in silicijev karbid, ki sta odporna proti visokim temperaturam in kemičnim vplivom. Poleg teh materialov DPF vključuje tudi katalizator, ki je prekrit s plemenitimi kovinami, kot sta platina in paladij, s katerimi se pospešujejo kemične reakcije med regeneracijo filtra [1]. Njegova osnovna funkcija je znižanje temperature, potrebne za oksidacijo nabranih delcev, in izboljšanje učinkovitosti regeneracije. Katalizator pospešuje reakcijo dušikovih oksidov (NO) v izpušnih plinih v dušikov dioksid (NO_2), ki je močan oksidant in omogoča oksidacijo saj pri nižjih temperaturah [1, 2].

Med pasivno regeneracijo se zgorevanje saj odvija ob prisotnosti NO_2 pri temperaturah v območju 200–500 °C. Pri reakciji ogljik (C) v sajah oksidira v ogljikov dioksid (CO_2), medtem ko se dušikov dioksid (NO_2) reducira v dušikov oksid (NO). Ta proces poteka kontinuirano, dokler so prisotne ustrezne temperature in koncentracije NO_2, kar omogoča pasivno regeneracijo brez posredovanja motornega krmilnega sistema [1, 2].

Če pasivna regeneracija ni zadostna, se sproži aktivna regeneracija, kjer je potrebna višja temperatura za oksidacijo saj. Katalizator pri tej obliki regeneracije omogoča, da se ob dodatnem vbrizganju goriva temperatura v izpušnem sistemu poveča do približno 600 °C, kar je dovolj za oksidacijo saj v prisotnosti kisika (O_2). Katalizator dodatno pospešuje pretvorbo dušikovega monoksida (NO) v NO_2 prek reakcije z uporabo plemenitih kovin na površini katalizatorja. Ta reakcija je pomembna, saj omogoča tvorbo NO_2, ki je bistven za učinkovitost pasivne regeneracije pri nižjih temperaturah. Prisotnost katalizatorja omogoča, da se proces regeneracije sproži pri nižjih temperaturah in hitreje poteka, kar je še posebej pomembno pri vozilih, ki se uporabljajo za kratke mestne vožnje, kjer temperature izpušnih plinov pogosto niso dovolj visoke za spontano zgorevanje saj [1, 2].

Zamašitev DPF zaradi pretiranega kopičenja saj je eden največjih izzivov pri uporabi teh sistemov. Pogoji vožnje, kot so kratke mestne vožnje z nizkimi hitrostmi in nizko temperaturo izpušnih plinov, otežujejo pasivno regeneracijo. V takih primerih se večinoma sproži aktivna regeneracija, ki zahteva dodatne ukrepe, kot so povišanje temperature izpušnih plinov s povečano obremenitvijo motorja ali dodatno vbrizgavanje goriva. Pogosta aktivna regeneracija pa lahko vodi do povečanih emisij ogljikovega dioksida (CO_2) in večje obrabe DPF, kar vpliva na skupno življenjsko dobo sistema .

Za dolgoročno ohranjanje učinkovitosti DPF je potrebno redno spremljanje stanja filtra preko senzorjev, ki beležijo tlak, temperaturo in pretok izpušnih plinov. Poleg tega je priporočljivo občasno izvajati vožnje pri višjih obremenitvah (npr. vožnja na avtocesti), kar omogoča pasivno regeneracijo in zmanjšuje potrebo po aktivnem posegu. To je še posebej pomembno za vozila, ki se večinoma uporabljajo za mestno vožnjo, kjer so pogoji za pasivno regeneracijo pogosto neustrezni.

Da bi ohranili učinkovito delovanje DPF, je potrebno izvajati periodični proces regeneracije. Regeneracija DPF vključuje oksidacijo nabranih saj v ogljikov dioksid (CO_2) pri visokih temperaturah (običajno med 500 °C in 600 °C). Obstajata dva osnovna tipa regeneracije: pasivna in aktivna.

Na proces regeneracije DPF vplivajo številni dejavniki, vključno s temperaturo izpušnih plinov, načinom vožnje (npr. mestna ali avtocestna vožnja), obremenitvijo motorja ter vrsto goriva in dodatkov.
Namen te raziskave je analizirati vpliv načina vožnje na hitrost regeneracije DPF. Osredotočili smo se na kombinirano vožnjo in preučevali, kako različne ravni moči motorja vplivajo na trajanje regeneracije. Hipoteza raziskave je, da višja moč motorja med regeneracijo vodi k hitrejši in bolj učinkoviti regeneraciji filtra. V ta namen smo zbrali podatke iz več voženj z različnimi obremenitvami motorja ter analizirali njihovo korelacijo z učinkovitostjo regeneracije.

2 METODE

2.1 Opis vozila in merilnega postopka

Za analizo podatkov je bil uporabljen dizelski motor modularnega dizelskega sistema MDB s prostornino 1,6 litra, ki je bil v vozilih znamke Škoda Auto prvič vgrajen v modelu Škoda Octavia tretje generacije. Motor je na voljo v dveh zmogljivostnih izvedbah - z močjo 66 kW in 81 kW. Uporabljena je bila najbolj priljubljena različica z močjo 81 kW oziroma 110 KM. Avtomobil je bil testiran v realnih pogojih, pri čemer je bila pozornost namenjena različnim obremenitvam motorja ter spremljanju ustreznih podatkov. Značilnosti motorja 1.6 TDI so prikazane v tabeli 1.

Tabela 1: Značilnosti motorja 1.6 TDI

Zasnova	dizelski motor z neposrednim visokotlačnim vbrizgavanjem goriva, turbopolnilnik z nastavljivo geometrijo lopatic, tekočinsko hlajenje, 2 x OHC, prečna vgradnja spredaj
Število valjev	4
Gibna prostornina	1598 cm^3
Število ventilov na valj	4
Največja moč	81 kW
Največji navor	250 Nm
Vbrizgavanje goriva	elektronsko krmiljeno visokotlačno vbrizgavanje goriva prek skupnega voda
Sistem mazanja	krožno dovajanje olja pod tlakom, s filtriranjem celotnega pretoka
Gorivo	dizelsko gorivo
Emisijski standard	EU 6

2.2 Zajem podatkov preko OBD vmesnika

Za zajem podatkov smo uporabili OBD2 ELM327 vmesnik, ki omogoča dostop do različnih informacij o delovanju motorja in izpušnega sistema ter aplikacijo za zajem podatkov »CarScanner«. Na ta način smo iz glavnega računalnika vozila zajemali podatke o senzorjih ter preračunane podatke na podlagi senzorjev.
Zajemali smo podatke o preračunani moči motorja (na podlagi vbrizganega goriva), temperature izpušnih plinov na treh različnih lokacijah, temperaturo DPF filtra, preračunane podatke o masi saj v DPF filtru, vrtljaje motorja, hitrost vozila, porabo goriva, status regeneracije, pretok zraka in količine naknadnih vbrizgov.
Podatki so bili beleženi med kombinirano vožnjo, ki vključuje različne vrste cestnih pogojev (mesto, podeželje, avtocesta) in s tem različne načine obremenitve motorja.

2.3 Analiza podatkov

Zbrani podatki so bili analizirani s poudarkom na ugotavljanju korelacije med močjo motorja in hitrostjo regeneracije. Raziskava ima določene omejitve, predvsem zaradi uporabe le enega tipa vozila in kombinirane vožnje.

Od 1. septembra 2017 poteka homologacijski postopek za določena nova vozila skladno z WLTP (Worldwide Harmonized Light Vehicles Test Procedure). To je globalno usklajen preizkusni postopek za lahka vozila, ki omogoča realnejši prikaz porabe goriva in emisij CO_2.

S 1. septembrom 2018 je postopek WLTP nadomestil predhodno veljavni preizkusni postopek, imenovan novi evropski vozni cikel (NEVC). Zaradi realnejših preizkusnih pogojev so vrednosti porabe goriva in emisij CO_2, izmerjene po postopku WLTP, v mnogih primerih višje od vrednosti, izmerjenih po postopku NEVC. Tudi davek na motorna vozila se obračunava v skladu z WLTP vrednostmi emisij CO_2.

Podatki so bili obdelani v programu spisanem v Matlab okolju. Podatki, ki smo jih beležili z vozila, se zelo hitro spreminjajo. Zato smo podatke povprečili na 10 s intervalu.

3 REZULTATI

Prikazani rezultati obdelave vožnje se nanašajo na eno vožnjo z začetkom v okolici Maribora, skozi mesto Maribor, po avtocesti do kraja Dramlje. Dolžina poti je znaša 67 km, čas vožnje je znašal 49 minut. Povprečna poraba goriva je znaša 4,93 l/100 km. Povprečna hitrost je bila 82,5 km/h. Med samo vožnjo se je slabih 16 minut izvajala aktivna regeneracija DPF filtra in v tem času je bilo prevoženih 17,6 km.

Slika 1 prikazuje potek hitrosti in mase saj v DPF filtru v odvisnosti od časa. Čas je podan v urah. Aktivna regeneracija se je začela ob 6,928 uri in je trajala do 7,243 ure. Količina delcev v filtru se je začela zmanjševati ob 6,993 uri. Po opravljeni regeneraciji pa je začela ponovno naraščati ob 7.299. Na začetku vožnje je bil filter napolnjen z 23,53 g saj. Te so naraščale do vrednosti 24,15 g, nato pa so začele zaradi aktivne regeneracije zmanjševati do vrednosti 6,52 g. Na koncu opazovane vožnje je masa saj v filtru znašala 6,99 g. Vožnja se je začela v ruralnem okolju, nadaljevala skozi mesto in ob času 7,102 se je začela vožnja po avtocesti.

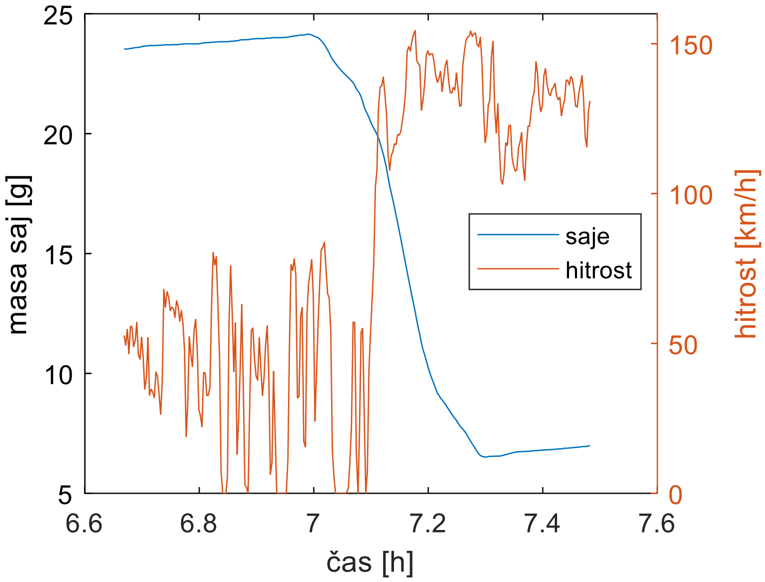

Slika 1: Hitrost avtomobila ter masa saj v DPF v odvisnosti od časa

Slika 2 prikazuje potek moči motorja in hitrost vozila v odvisnosti od časa. Razvidno je, da je bila potrebna moč motorja v ruralnem okolju nizka in je znašala okoli 20 KM. Konice moči pa so znašale do 100 KM. Na avtocesti je povprečna moč višja, okoli 40 KM. Iz slike je razvidna tudi primerjava iz nepovprečenih in povprečenih vrednosti na intervalu 10 sekund. Korelacijski faktor med močjo in hitrostjo znaša 0,71 kar nakazuje na relativno visoko pozitivno linearno povezavo.

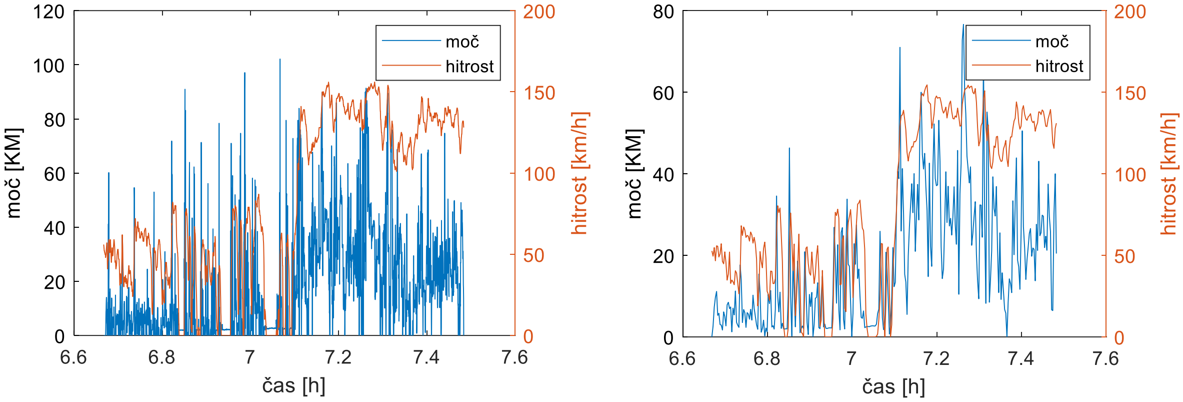

Slika 2: Potek moči motorja in hitrosti vozila v odvisnosti od časa. Levo nepovprečene vrednosti, desno povprečene vrednosti

Na sliki 3 je prikazan potek moči in sprememba mase saj v DPF filtru v odvisnosti od časa. Razvidno je, da se je aktivna regeneracija začela že pri vožnji skozi mesto, torej pred prihodom na avtocesto. Razvidno, da je v času od 7,031 do 7,058 avto miroval, moč motorja je bila minimalna, kljub temu pa se je masa saj zmanjševala. V času mirovanja se je masa zmanjševala počasneje kot pred in za tem. Iz slike ni razvidne odvisnosti moči motorja in hitrost regeneracije filtra.

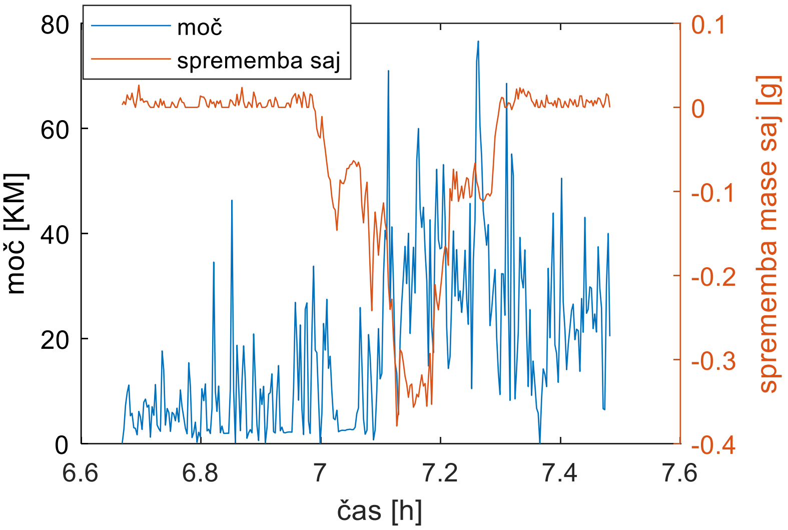

Slika 3: Moč motorja in sprememba mase saj v DPF v odvisnosti od časa

Slika 4 prikazuje spremembo mase saj v filtru in temperaturo DPF filtra. Razvidno je, da se masa saj v filtru začne zmanjševati, ko temperatura DPF filtra doseže 450 °C in se konča, ko temperatura pade pod to vrednost. Razvidno je tudi, da čeprav nadaljujemo vožnjo po avtocesti temperatura filtra pade na 300 °C.

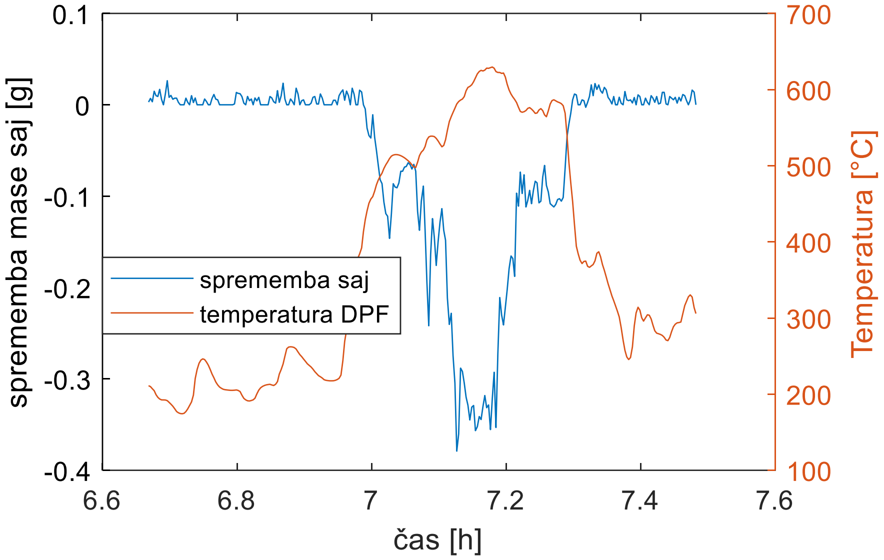

Slika 4: Temperatura DPF filtra in sprememba mase saj v DPF v odvisnosti od časa

Slika 5 prikazuje spremembo mase saj v filtru in količino naknadno vbrizganega goriva v valj. Osnovni namen naknadnega vbrizga je dvig temperature izpušnih plinov in posledično DPF filtra. Iz slike je razvidno, da se začne naknadno vbrizgavanje goriva ob času 6,955 h, nato pa se šele z zakasnitvijo, ob času 6,990 h, začne masa saj v filtru zmanjševati. Toliko časa je bilo potrebnega, da se je filter segrel na ustrezno temperaturo.

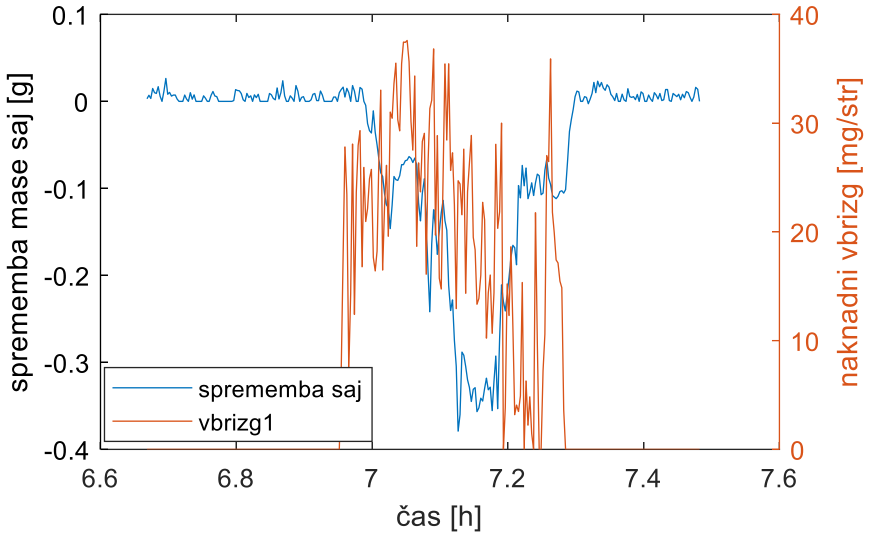

Slika 5: Naknadni vbrizg in sprememba mase saj v odvisnosti od časa

Slika 6 prikazuje količino naknadno vbrizganega goriva in moč motorja. Iz slike je razvidno, da se v teku aktivne regeneracije in času nizke moči motorja količina naknadno vbrizganega goriva poveča in obratno, ko je moč motorja visoka, se količina naknadno vbrizganega goriva zmanjša.

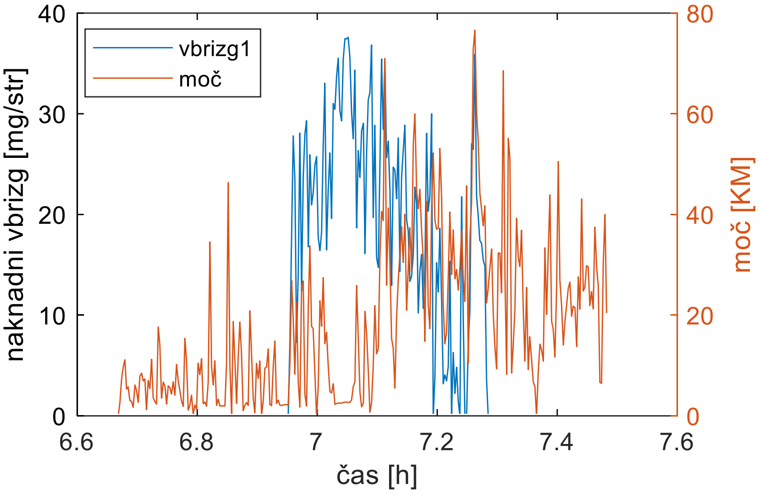

Slika 6: Korelacija med količino naknadnega vbrizga in močjo motorja v odvisnosti od časa

4 ZAKLJUČEK

V prispevku je analizirana vožnja z vozilom, ki ga poganja 1.6 TDI motor z DPF filtrom, ki se uvrša v standard EURO 6. Med vožnjo se je izvršila aktivna regeneracija, kjer se je količina saj zmanjšala iz začetnih 24,15 g na 6,52 g. Iz analize je razvidno, da ima največji vpliv na hitrost oziroma učinkovitost regeneracija količina naknadno vbrizganega goriva. Na količino naknadno vbrizganega goriva pa pomembno vpliva moč motorja. Večja kot je moč motorja manjša je količina naknadno vbrizganega goriva.

LITERATURA

[1] BAI, Shuzhan, et al. Soot loading estimation model and passive regeneration characteristics of DPF system for heavy-duty engine. *Applied Thermal Engineering*. 2016, vol.(100), 1292-1298.
[2] FANG, Jia, et al. The influence of ash on soot deposition and regeneration processes in diesel particular filter. *Applied Thermal Engineering*. 2017, vol.(124), 633-640.

Analiza in optimizacija preoblikovalnega procesa vtiskovanja tolerančno zahtevnega detajla v pločevino

Domen Gnidovec[1], Jurij Švegelj[1], Rajko Marinčič[2], Matic Muc[1], Davor Tramte[1], Tomaž Habinc[1], Vili Malnarič[1]

[1]TPV Automotive d.o.o., Brezina 101, 8250 Brežice, Slovenija
E-naslovi: d.gnidovec@tpv.si, j.svegelj@tpv.si, matic@biro-bonus.si, d.tramte@tpv.si, t.habinc@tpv.si, v.malnaric@tpv.si

[2]SIEVA d.o.o., Slovenija
E-naslov: r.marincic@tpv.si

Povzetek: *Študija se osredotoča na analizo in optimizacijo vtiskovanja zobcev v jekleno pušo iz pločevine, ki ima sicer konstantno debelino, vendar ta niha od šarže do šarže znotraj tolerančnega polja. Puša se uporablja v sestavu nosilca zadnjega kolesa za platformo vozil BMW. Raziskava zajema celoten razvojni cikel, od začetne zasnove in numeričnih simulacij do testiranja prototipa in validacije, pri čemer je v tem delu podrobno predstavljena strukturna analiza po metodi končnih elementov. Jeklena puša skupaj z vtisnjenim gumijastim paketom predstavlja gumijasto uležajenje, preko katerega je nosilec kolesa uležajen na karoserijo. Namen vtisnjenih zobcev v jekleni puši je zagotoviti ustrezen oblikoven zaklep v sestavu, ki zagotavlja minimalno aksialno iztisno silo gumijastega paketa. Geometrija zobcev, ki smo jo nadzorovali z ustrezno zapolnitvijo materiala v matrici in pestiču, mora dosegati tolerančne zahteve neodvisno od nihanja debeline vhodne pločevine. Pri tem se v materialu med procesom vtiskovanja ne sme pojaviti razpoka. Analizirane so bile različne spremembe zasnove orodja, ki so privedle do boljšega polnjenja materiala in porazdelitve kontaktnega tlaka po površini zobcev. Vzporedno smo identificirali tudi delež preoblikovalne sile v orodju, potreben za vtis zobcev. Nadalje študija vključuje pripravo in kalibracijo duktilnega poškodbenega kriterija v materialni model, ki omogoča napovedovanje nastanka poškodbe zaradi iniciacije, propagacije in združevanja praznin v materialu. Na podlagi rezultatov analize smo izdelali prototipne modele. Ugotovitve kažejo, da lahko z optimizirano geometrijo orodja dosežemo ustrezno zapolnitev zobcev z uporabo materiala s standardnim tolerančnim poljem debeline. Rezultirajoči zobci v jekleni puši robustno zagotavljajo zahtevano aksialno iztisno silo gumijastega paketa. Na podlagi identificiranega deleža preoblikovalne sile v orodju smo določili ustrezno stiskalnico.*

Ključne besede: *modeliranje preoblikovalnega procesa, vtiskovanje, tolerančno zahteven detajl, numerična analiza, duktilni poškodbeni kriterij, degradacija materiala, preoblikovalno orodje*

Razvrstitev: *Strokovni prispevek*

1 UVOD

Vzmetenje je izraz za sistem vzmeti, dušilke in vezi, ki povezuje kolo s karoserijo vozila na način, da omogoča relativno neodvisno gibanje kolesa. Ključna funkcionalnost vzmetenja je preprečiti prenos udarcev s ceste na okvir vozila, ohraniti stabilnost vozila pri nagibanju ali bočenju, zaščititi potnike pred udarci s ceste, zagotoviti stabilnost krmiljenja, dobro vodljivost in oprijem na cesti med vožnjo, zavijanjem in zaviranjem. Danes večina osebnih avtomobilov uporablja neodvisni sistem vzmetenja, ki omogoča relativno gibanje posameznega kolesa glede na okvir, ne da bi vplivalo na preostala kolesa. Najpogosteje uporabljeno vzmetenje za zadnje kolo je sistem vzmetenja z nihajno roko. Glavna naloga nihajne roke je prenašati delujoče obremenitve z zanemarljivo deformacijo, da lahko vzmetenje učinkovito deluje.

Predstavljena študija v tem delu je del razvoja nihajne roke za platformo vozil BMW. Gre za zvarjenec kompleksne oblike, ki sestoji iz trinajstih odpreškov visoko trdnostnega jekla, odkovka, dveh matic ter gumijastega blažilca. Priključna mesta, preko katerih se funkcija nihajne roke prenaša na okolico, so prikazana na sliki 1.

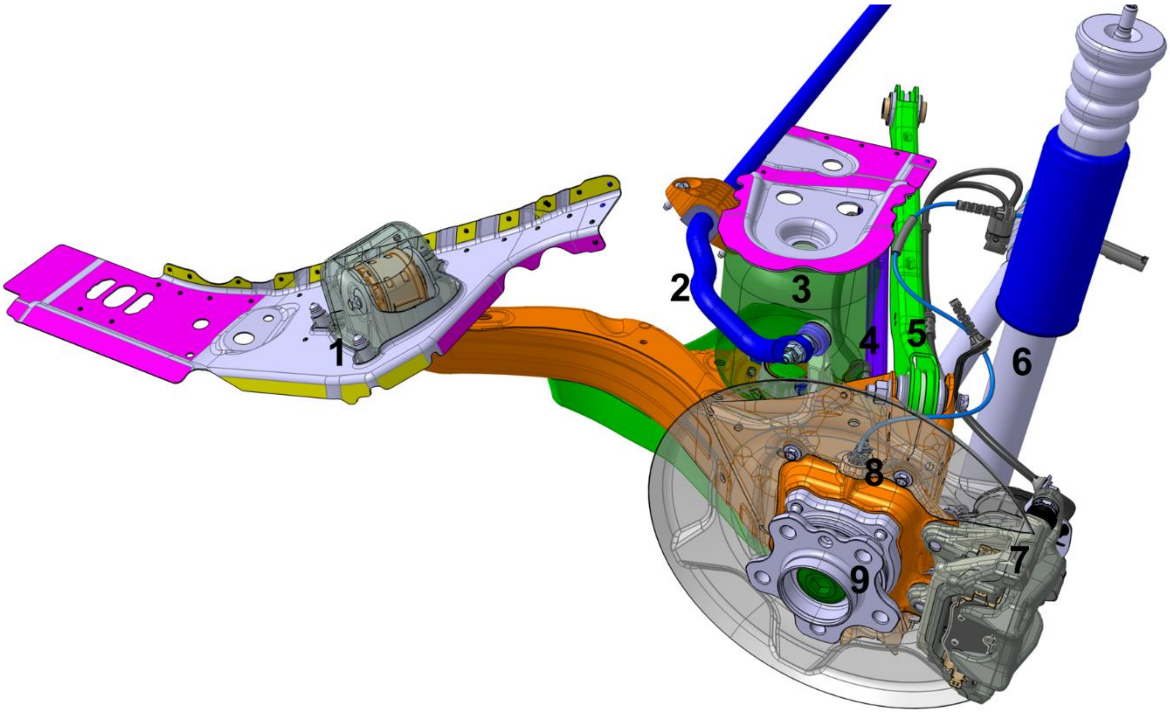

Slika 1: Nihajna roka v sistemu vzmetenja [interni vir podjetja TPV Automotive]. Ključne funkcionalnosti: 1) vpetje na karoserijo, 2) povezava s stabilizatorjem, 3) povezava z vzmetjo, 4) vpetje spodnje kontrolne ročice, 5) vpetje zgornje kontrolne ročice, 6) povezava z amortizerjem, 7) pritrditev zavorne čeljusti, 8) ABS senzor, 9) kolesni ležaj

Predmet obravnave se nanaša na mesto vpetišča na karoserijo (številka 1 na sliki 1), kjer je nosilec kolesa uležajen preko gumijastega paketa in jeklene puše. »Gumijasti ležaj« je sestavljen iz paketa aluminijastega jedra, gumijastega vložka in polimernega obroča, ki se ga vtisne v jekleno pušo (slika 2). Tak način prožnega vpetja na karoserijo skrbi za pasivno krmiljenje zadnjih koles (»Weissach axle« [1]), ob enem pa disipira absorbirano energijo s cestišča. Med obratovanjem vozila je gumijasti ležaj izpostavljen visokim dinamičnim aksialnim silam, ki gumijasti paket silijo iz jeklene puše. To preprečujejo ustrezne torne razmere v kontaktu med jekleno pušo in polimernim obročem. Zato je bila ključna naloga razvoja definirati in fizikalno popisati oblikoven zaklep gumijastega paketa v jekleni puši in minimizirati njegovo odvisnost od vhodnih spremenljivk problema.

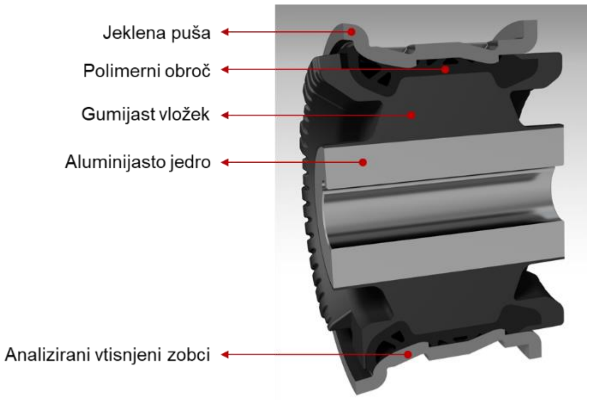

Slika 2: "Gumijasti ležaj" - jeklena puša z gumijastim paketom in aluminijastim jedrom

Izpad gumijastega paketa iz jeklene puše preprečujejo vtisnjeni zobci v jekleni puši, ki s primerno tolerirano geometrijo zagotavljajo ustrezno oblikovno trdnost tako, da sestav dosega predpisano minimalno aksialno iztisno silo gumijastega paketa $F_{out} = 10\,kN$. Zobce se izdela s procesom preoblikovanja pločevine - vtiskovanjem, primarna spremenljivka katerega je debelina vhodne pločevine, ki neposredno vpliva na sile v preoblikovalnem orodju in posledično na geometrijo vtisnjenega zobca. Namen predstavljene numerične analize je analizirati odvisnost končne geometrije zobca od spreminjanja vhodne pločevine, vzporedno pa identificirati minimalno potrebno preoblikovalno silo v orodju.

Cilj raziskave je s pomočjo numerične analize in optimizacije v prototipnih fazah ohraniti standardno tolerančno polje debeline vhodne pločevine $(3 \pm 0{,}1\,mm)$, s čimer so doseženi tako gospodarski kot tudi trajnostni in okoljski učinki. S tem namenom je potrebno določiti optimalno geometrijo preoblikovalnega orodja, t.j. pestiča in matrice ter izračunati odvisnost preoblikovalne sile od pomika preoblikovalnega orodja, na podlagi katere se lahko določi ustrezno stiskalnico za proces preoblikovanja. Proces mora biti definiran tako, da se v materialu med procesom vtiskovanja ne pojavi razpoka. Pojav nastanka razpoke v materialu smo matematično popisali z duktilnim poškodbenim kriterijem v materialnem modelu, ki omogoča napovedovanje nastanka poškodbe zaradi iniciacije, propagacije in združevanja praznin v materialu.

2 METODE

V tem poglavju je predstavljena metodologija matematičnega modeliranja vtiskovalnega procesa. Vodilni sistem enačb problema je rešen po metodi končnih elementov. Analize so tematsko razdeljene v dva sklopa glede na definicijo materialnega modela. Prvi sklop zajema primarne analize, v katerih ni upoštevan razvoj poškodbe v materialu. Namen teh analiz je bilo spremljati kako nihanje debeline vhodne pločevine vpliva na zapolnjenost materiala v matrici, razporeditev kontaktnega tlaka po površini zobca in maksimalno preoblikovalno silo. Drugi sklop analiz zajema materialni model z vključenim kriterijem duktilne poškodbe, s katerim poskušamo napovedati iniciacijo in propagacijo poškodbe na mestu maksimalne degradacije materiala.

2.1 Primarne analize

2.1.1 Geometrijski model

Jeklena puša je produkt zaporednih operacij preoblikovanja, v katerem se najprej naredi obrez, formira prirobnico, vtisne zobce in nato krivi v končno formo. Izhodiščna geometrija pred vtiskovanjem zobcev je prikazana skrajno levo na sliki 3. V pločevino se vtisne šest parov zobcev, ki po dolžini puše (kasneje po obodu) predstavljajo periodično ponovljive geometrijsko simetrične segmente. Zaradi navedenih lastnosti lahko izvedemo redukcijo geometrije in obravnavamo samo en ponovljiv segment (sredina na sliki 3). Ker so poleg simetrične geometrije posameznega segmenta, simetrični tudi robni pogoji in obremenitve, matematično domeno predstavlja le polovica enega segmenta (skrajno desno na sliki 3).

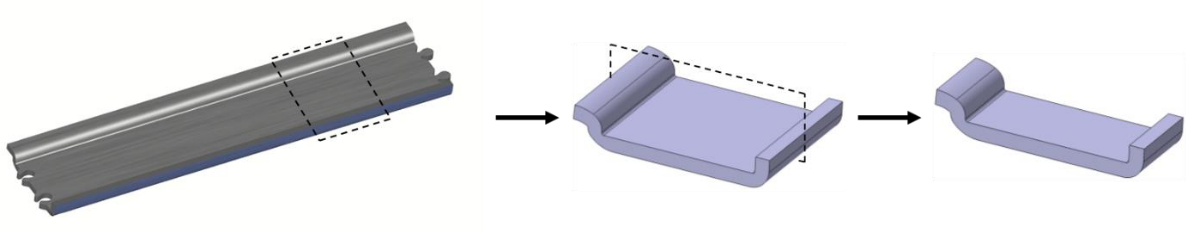

Slika 3: Redukcija geometrije do geometrijskega modela

2.1.2 Fizikalni in numerični model

Fizikalno dogajanje je povezano z mehaniko deformabilnih teles. Ker nas v dani analizi zanima le mehansko stanje v pločevini, je kot deformabilno telo modelirana le domena puše, za pestič in matrico pa predpostavimo, da sta idealno toga. Pri vtiskovanju zobca prihaja lokalno do velikih pomikov, zato je upoštevana teorija velikih deformacij. Čas preoblikovalnega procesa je kratek (0.01 s), zato dinamični učinki, kot sta hitrost deformacije in masna vztrajnost, niso zanemarljivi. Fizikalno dogajanje je zato časovno spremenljivo.

Na podlagi fizikalnega modela je definiran numerični model, t.j. *Abaqus Explicit* – vsesplošni reševalnik po metodi končnih elementov za eksplicitno dinamiko. Sistem vodilnih enačb numeričnega modela zagotavlja dinamično ravnotežje [2]:

$$M^{NJ}\,\ddot{u}^{N}_{(i)} = P^{J}_{i} - I^{J}_{i}, \tag{1}$$

kjer $\boldsymbol{M}$ predstavlja masno matriko, $\ddot{\boldsymbol{u}}$ vektor vozliščnih pospeškov, P vektor zunanjih vozliščnih sil, $\boldsymbol{I}$ vektor notranjih vozliščnih sil, i indeks časovnega inkrementa, N in J pa sta vozliščna indeksa. Gibalne enačbe se po času integrirajo z uporabo eksplicitne časovne integracije po centralni diferenčni shemi [2]:

$$\dot{u}^{N}_{\left(i+\frac{1}{2}\right)} = \dot{u}^{N}_{\left(i-\frac{1}{2}\right)} + \frac{\Delta t_{(i+1)} + \Delta t_{(i)}}{2}\ddot{u}^{N}_{(i)}, \tag{2}$$

$$u^{N}_{(i+1)} = u^{N}_{(i)} + \Delta t_{(i+1)}\dot{u}^{N}_{\left(i+\frac{1}{2}\right)}, \tag{3}$$

kjer je $\dot{u}$ vektor vozliščnih hitrosti in $\boldsymbol{u}$ vektor vozliščnih pomikov. Centralni diferenčni integracijski operator je ekspliciten v smislu, da kinematično stanje napreduje v času z uporabo znanih vrednosti $\dot{u}^{N}_{(i-1/2)}$ in $\ddot{u}^{N}_{(i)}$ iz prejšnjega časovnega inkrementa. Začetek časovne integracije je predpisan z začetnimi pogoji, ki so definirani v skladu z izbranim numeričnim modelom, medtem ko robni pogoji izpopolnjujejo robni problem.

2.1.3 Materialni model

Pločevina za preoblikovanje je izdelana iz materiala S500MC - vroče valjanega konstrukcijskega jekla visoke trdnosti. Fizikalno obnašanje materiala je popisano z elasto-plastičnim modelom, parametre katerega smo pridobili z nateznim preizkusom. Vztrajnostni učinki so popisani z gostoto materiala $\rho = 7.85E - 09\ t/mm^3$, elastični del z modulom elastičnosti $E = 210E03\ MPa$ in Poissonovim količnikom $\nu = 0.3$, plastični del pa je popisan s krivuljo utrjevanja $\sigma(\varepsilon_{\mathrm{pl}})$, kjer velja $\sigma(\varepsilon_{\mathrm{pl}} = 0) = R_{p,0}$. Diskretizirana krivulja utrjevanja $\sigma(\varepsilon_{\mathrm{pl}})$ je podana v tabeli 1.

Tabela 1: Diskretizirana krivulja utrjevanja $\sigma(\varepsilon_{\mathrm{pl}})$ za popis plastičnega dela v materialnem modelu

$\boldsymbol{\sigma}\ [\boldsymbol{MPa}]$	$\boldsymbol{\varepsilon}_{\mathbf{pl}}\ [/]$
488	0
510	0.022
660	0.077
770	0.150
780	0.180
1100	0.442

2.1.4 Mreža končnih elementov

Matematična domena pločevine je diskretizirana z volumskimi končnimi elementi, ki imajo v vsakem vozlišču tri translacijske prostostne stopnje pomika. Uporabljenih je 79670 elementov tipa C3D8R (Abaqus) – linearni heksaeder z 8 vozlišči in reducirano integracijo in 496 elementov tipa C3D6 (Abaqus) – linearna trikotna prizma s 6 vozlišči. Karakteristična dolžina elementov na mestih velikih gradientov in kontaktnih površin znaša 0.2 mm – 0.3 mm, izven kontaktnih površin pa 0.5 mm. Skupno število vozlišč v domeni pločevine je približno $90E03$, kar skupno pomeni $90E03 \cdot 3 = 270E03$ translacijskih prostostnih stopenj. Pestič in matrica sta modelirana kot togi telesi, ki sta diskretizirani z elementi tipa R3D4 (Abaqus) – 3D bilinearni togi štirikotnik s štirimi vozlišči in R3D3 (Abaqus) – 3D togi trikotnik s tremi vozlišči. Število elementov in vozlišč togih teles se skozi razvojne iteracije spreminja. Diskretizacija geometrijska modela v mrežo končnih elementov je prikazana na sliki 4.

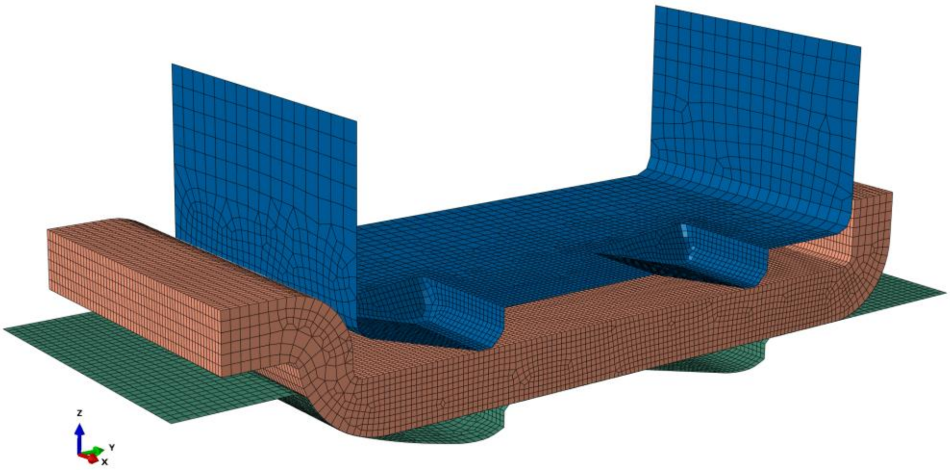

Slika 4: Diskretizacija geometrijska modela v mrežo končnih elementov

2.1.5 Robni pogoji

Analiza vtiskovanja je izvedena v dveh korakih: 1) zaprtje orodja in 2) razprtje orodja. V prvem koraku smo spremljali zapolnitev materiala v matrici, v drugem pa elastični povratek in končno geometrijo vtisnjenih zobcev. Definicija robnih pogojev je prikazana na sliki 5. Matrica ima v referenčni točki togega telesa omejene vse prostostne stopnje v obeh korakih. Pestič ima podobno omejene vse prostostne stopnje, razen pomik v z-smeri, ki predstavlja hod orodja: v prvem koraku pomik v negativni smeri z-osi, v drugem pa pomik v pozitivni smeri z-osi do začetnega položaja. Pločevina ima na prereznih ravninah aplicirane simetrijske robne pogoje, kar v primeru volumskih končnih elementov pomeni, da so vsi pomiki v normalni smeri prerezne ravnine enaki nič.

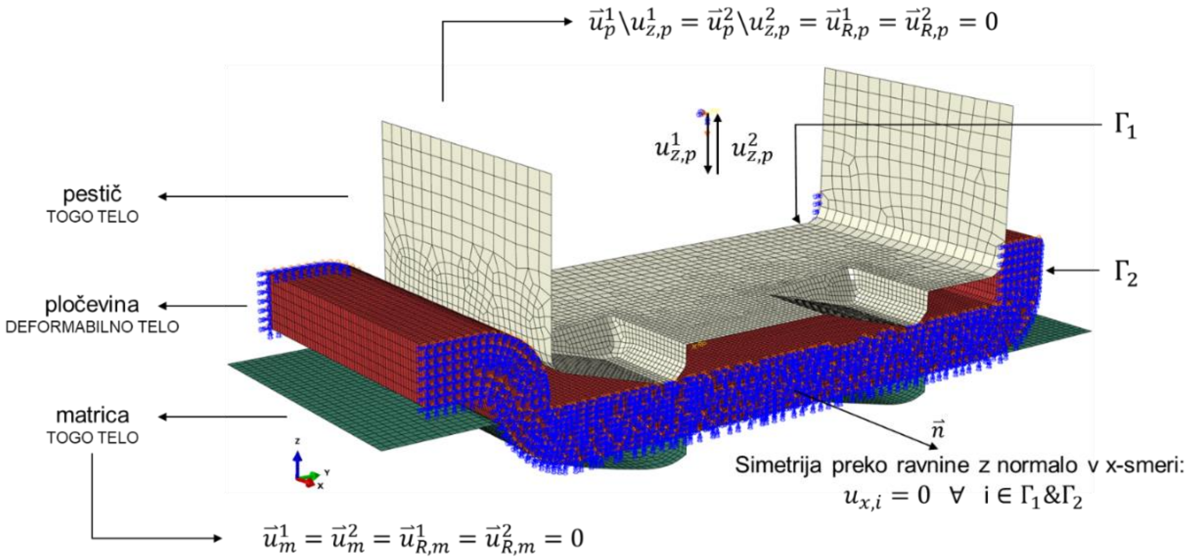

Slika 5: Numerični model z definicijo robnih pogojev

2.2 Vključitev duktilnega poškodbenega kriterija v materialni model

Poškodba materiala pomeni popolno izgubo nosilnosti, ki je posledica postopne degradacije togosti materiala. Proces degradacije togosti se modelira z uporabo poškodbene mehanike. Mehanizem porušitve je določen v skladu s pravim odzivom napetost-deformacija iz treh posameznih sklopov (slika 6) [3]:

1) opredelitev efektivnega (ali nepoškodovanega) elasto-plastičnega odziva materiala ($a - b - c - d'$),
2) kriterij za iniciacijo poškodbe (točka c),
3) zakon za propagacijo poškodbe ($c - d$).

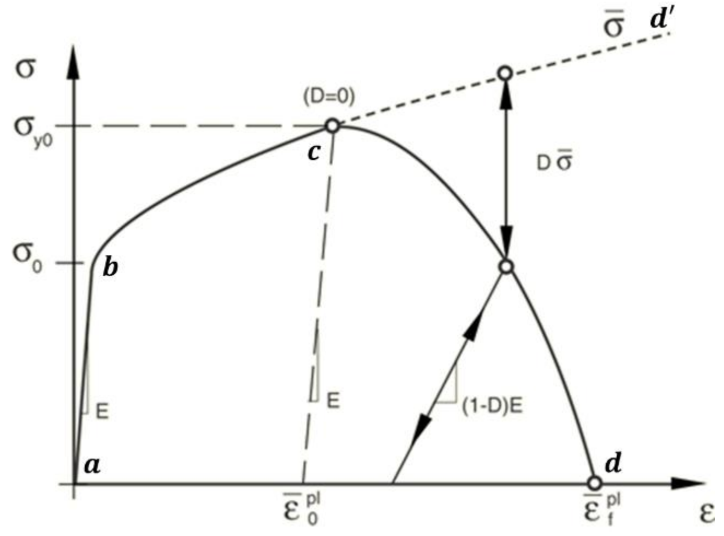

Slika 6: Prava krivulja napetost-deformacija s progresivno degradacijo poškodbe v kritični točki porušitve [4]

Iniciacijo poškodbe v duktilnih kovinah lahko v splošnem povzročita dva glavna mehanizma: duktilna porušitev zaradi nastajanja, rasti in združevanja praznin v materialu ter strižna porušitev zaradi lokalizacije strižnega pasu. Na podlagi fenomenoloških opažanj ta dva mehanizma zahtevata različne oblike meril za nastanek poškodbe [5]. V tej študiji je upoštevana le zmožnost iniciacije poškodbe zaradi duktilne porušitve. Model predpostavlja, da je ekvivalentna plastična deformacija ob nastanku poškodbe funkcija triosnosti napetosti η in hitrosti plastične deformacije $\dot{\bar{\varepsilon}}^{pl}$ [6]:

$$\bar{\varepsilon}_D^{pl} = \bar{\varepsilon}_D^{pl}(\eta, \dot{\bar{\varepsilon}}^{pl}), \tag{4}$$

v kateri predpostavimo $\eta = konst.$, $\dot{\bar{\varepsilon}}^{pl} = konst.$ Pogoj za nastanek poškodbe je izpolnjen, ko je dosežen naslednji pogoj [6]:

$$\omega_D = \int \frac{d\bar{\varepsilon}_D^{pl}}{\bar{\varepsilon}_D^{pl}(\eta, \dot{\bar{\varepsilon}}^{pl})} = 1, \tag{5}$$

kjer je ω_D spremenljivka stanja, ki monotono narašča s plastično deformacijo. Prirastek ω_D v vsakem inkrementu se izračuna kot [6]:

$$\Delta\omega_D = \frac{\Delta\bar{\varepsilon}_D^{pl}}{\bar{\varepsilon}_D^{pl}(\eta, \dot{\bar{\varepsilon}}^{pl})} \geq 0. \tag{6}$$

Zakon za propagacijo poškodbe predpostavlja, da je poškodba povezana s progresivno degradacijo togosti materiala, kar vodi do porušitve (slika 6). σ_{y0} in $\bar{\varepsilon}_0^{pl}$ sta napetost tečenja in ekvivalentna plastična deformacija ob nastanku poškodbe in $\bar{\varepsilon}_f^{pl}$ je ekvivalentna plastična deformacija pri porušitvi, t.j. ko poškodbeni parameter doseže vrednost $D = 1$. Vrednost ekvivalentne plastične deformacije pri porušitvi $\bar{\varepsilon}_f^{pl}$ je močno odvisna od karakteristične dolžine elementa, zato je ni mogoče neposredno opredeliti kot materialni parameter za specifikacijo zakona o propagaciji poškodbe. Namesto tega je Hillerborg [7] predlagal lomno energijo G_f, t.j. energija potrebna za odprtje enotske površine razpoke, s katero je odziv materiala po nastanku poškodbe opisan z odzivom napetost-pomik in ne z odzivom napetost-deformacija, ki je močno odvisen od mreže. Lomna energija je podana z enačbo [4]:

$$G_f = \int_{\bar{\varepsilon}_0^{pl}}^{\bar{\varepsilon}_f^{pl}} L\,\sigma_y\, d\bar{\varepsilon}_D^{pl} = \int_0^{\bar{u}_f^{pl}} \sigma_y\, d\bar{u}^{pl}, \tag{7}$$

v kateri je L karakteristična dolžina elementa. S tem izrazom je vpeljana definicija ekvivalentnega plastičnega pomika $\bar{u}^{pl}$, kot lomnega dela, ki je povezano z napetostjo tečenja po iniciaciji poškodbe (delo na enoto površine razpoke). Pred iniciacijo poškodbe velja $\dot{\bar{u}}^{pl} = 0$, po iniciaciji poškodbe pa je efektivni plastični pomik opredeljen z evolucijsko enačbo $\dot{\bar{u}}^{pl} = L\,\dot{\bar{\varepsilon}}_D^{pl}$. V analizi predpostavimo linearni razvoj poškodbenega parametra D v odvisnosti od efektivnega plastičnega pomika $\bar{u}^{pl}$ (slika 7). Vrednost efektivnega plastičnega pomika pri porušitvi $\bar{u}_f^{pl}$ je kalibrirana na podlagi nateznega preizkusa za dani material in znaša $\bar{u}_f^{pl} = 0.5\,mm$. Takrat je $D = 1$. Vrednost $\bar{u}^{pl} = 0$ je definirana pri $\bar{\varepsilon}_0^{pl} = 0.182$.

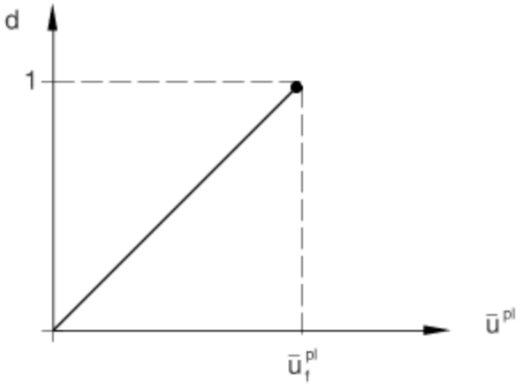

Slika 7: Linearna degradacija togosti oziroma linearna rast poškodbe [4]

Materialna točka odpove, ko doseže največjo dovoljeno degradacijo D_{max}. Takrat se element izbriše oziroma odstrani iz mreže, kar pomeni, da v integracijskih točkah elementa ni nadaljnje akumulacije poškodbe, preostala togost pa se izniči. Z namenom boljše konvergence v analizi predpostavimo $D_{max} = 0.95$. To pomeni, da se tekom analize iz mreže odstranijo vsi elementi, ki jim togost pade pod 5% začetne togosti. To vpliva tudi na definicijo kontaktnih razmer, saj se kontaktna površina tekom analize spreminja v odvisnosti od brisanja elementov. V območjih največje poškodbe kot potencialne kontaktne površine definiramo tudi ploskve elementov v notranjosti, ki v določenem časovnem trenutku postanejo zunanje površine v kontaktu z orodjem, dokler ne pride do porušitve elementa (slika 8).

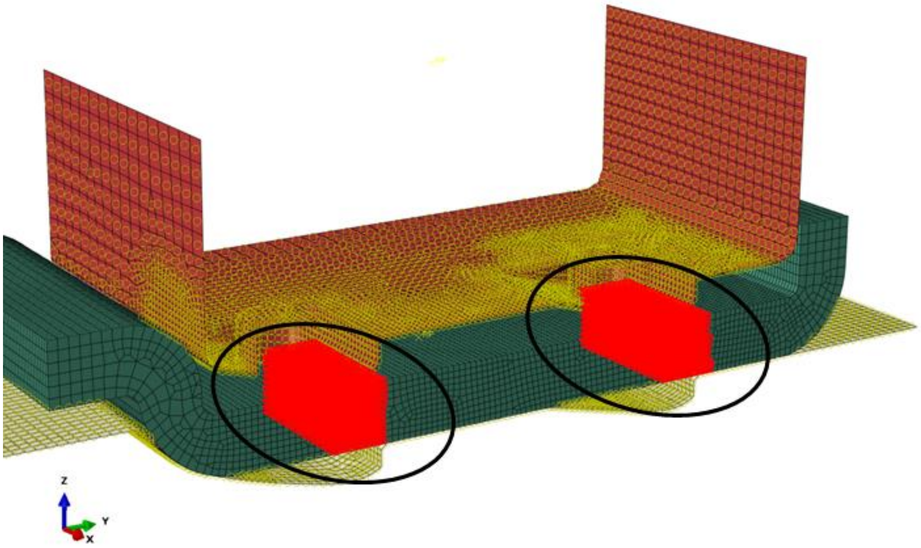

Slika 8: Definicija kontaktnih razmer med brisanjem elementov: ploskve elementov v notranjosti (rdeči coni) prevzemajo vlogo kontaktnih površin

3 REZULTATI IN DISKUSIJA O REZULTATIH

Poglavje zajema pregled rezultatov primarnih analiz, skozi katere smo nadzorovali ustrezno zapolnitev materiala v matrici pri minimalni in maksimalni debeline vhodne pločevine. Spremljali smo tudi porazdelitev kontaktnega tlaka po površini vtisnjenega zobca, saj z njim zagotavljamo plastifikacijo funkcijsko najpomembnejše cone zobca, zato smo želeli maksimalno ponovljivost kontaktnega tlaka neglede na vhodno pločevino. Identificirana je odvisnost preoblikovalne sile od pomika preoblikovalnega orodja. Nadalje so ovrednoteni rezultati analize z vključenim duktilnim poškodbenim kriterijem v materialni model.

3.1 Rezultati primarnih analiz

3.1.1 Analiza 1: Izhodiščna geometrija matrice in pestiča

Iz rezultatov analize z izhodiščno geometrijo na sliki 9 je razvidno, da je zapolnitev materiala v levem zobcu manjša kot v desnem. Razlog predstavlja nepodprta prirobnica puše, zaradi česar obstoja cona prostega tečenja, v katero se material umakne med vtiskovanjem.

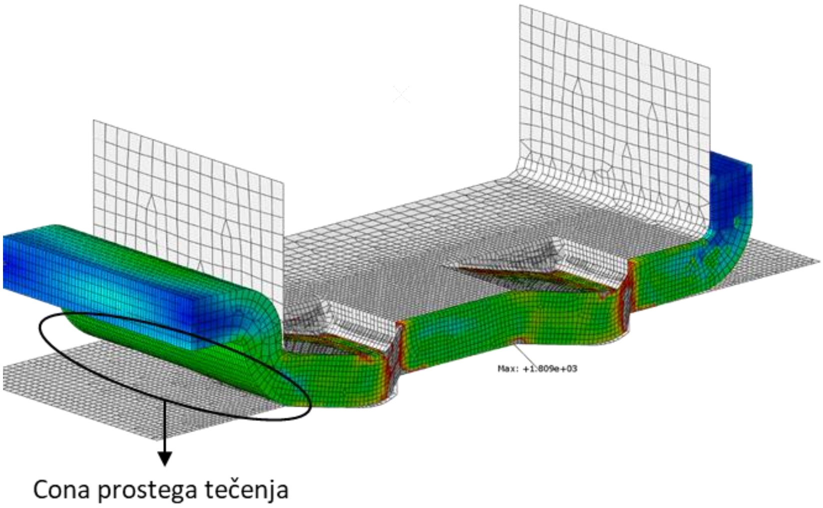

Slika 9: Vtis zobcev na izhodiščni geometriji orodja

Iz neenakomerne porazdelitve kontaktnega tlaka na sliki 10, kjer je velikost tlaka na površini levega zobca občutno manjša kot na površini desnega, lahko sklepamo, da je zapolnjenost materiala v levem zobcu neprimerna.

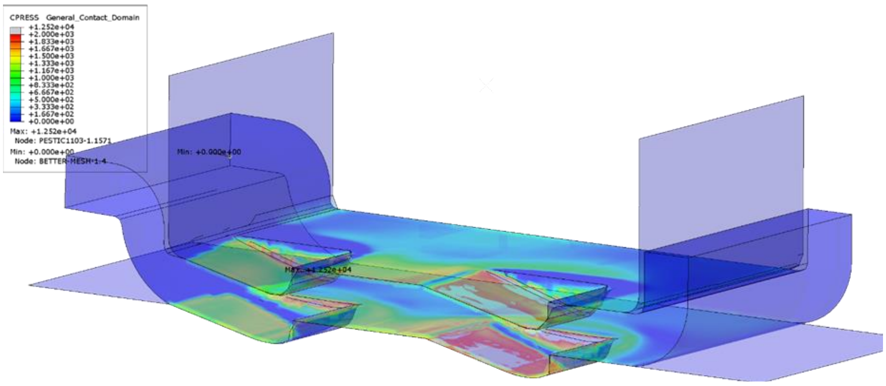

Slika 10: Razporeditev kontaktnega tlaka – izhodiščna geometrija

Rezultati analize vtiskovanja v pločevino minimalne ($3^{-0.1}\ mm$) in maksimalne ($3^{+0.1}\ mm$) debeline (slika 11) kažejo na to, da je zapolnitev materiala pri maksimalni debelini sprejemljiva, medtem ko pri minimalni debelini pride do nepopolne zapolnitve, iz česar zaključimo, da predlagana geometrija orodja ni primerna.

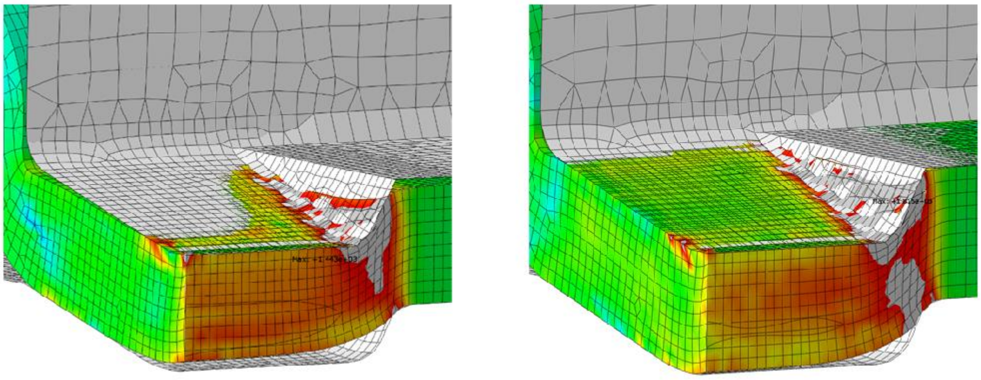

Slika 11: Zapolnitev materiala v matrici pri minimalni (levo) in maksimalni (desno) debelini vhodne pločevine

Na sliki 12 je prikazana odvisnost preoblikovalne sile od pomika pestiča. Dokler sta v kontaktu le skrajni površini zobcev na pestiču je naraščanje sile dokaj linearno. Ko pride do zaprtja orodja se začne proces kovanja materiala, gradient močno naraste in sila skokovito naraste. Za izdelavo polovice para zobcev znaša približno 33 ton, kar pomeni, da za izdelavo 12 zobcev potrebujemo približno 400 ton preoblikovalne sile.

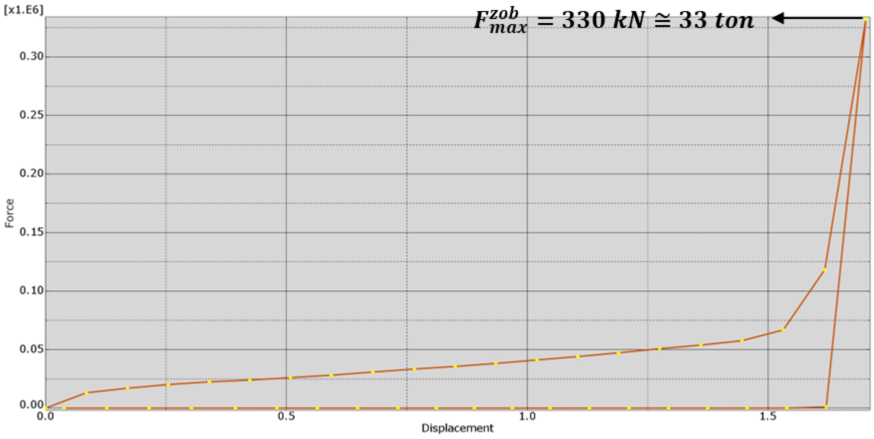

Slika 12: Graf odvisnosti preoblikovalne sile od pomika pestiča - izhodiščna geometrija

3.1.2 Analiza 2: Podprtje radija na matrici

V naslednji iteraciji smo odpravili cono prostega tečenja s podprtjem radija na matrici. Zapolnitev materiala v levem in desnem zobcu je tako primerljiva. Prikazana je na sliki 13.

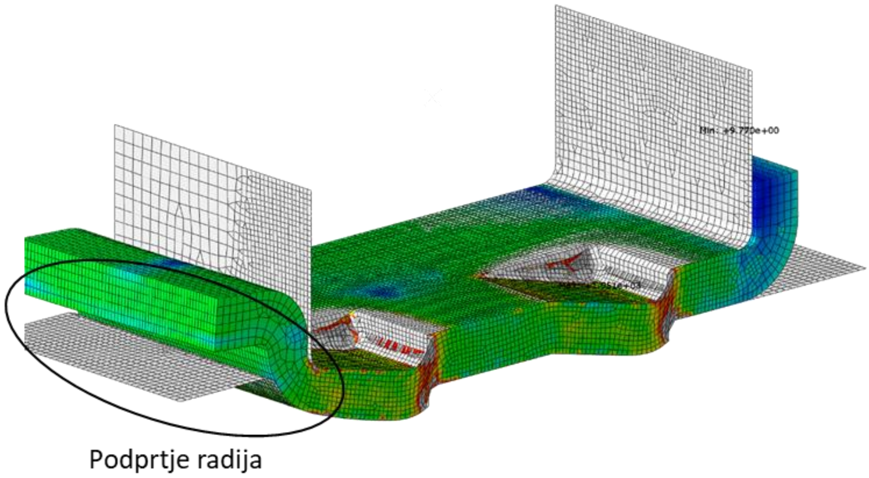

Slika 13: Popravljena oblika matrice

Kontaktni tlak, prikazan na sliki 14, je v tem primeru med levim in desnim zobcem bolj homogeno razporejen. Nekoliko večji tlak je opaziti na levem zobcu, kar je posledica geometrije pestiča, katero smo optimizirali v nadaljnjih razvojnih iteracijah.

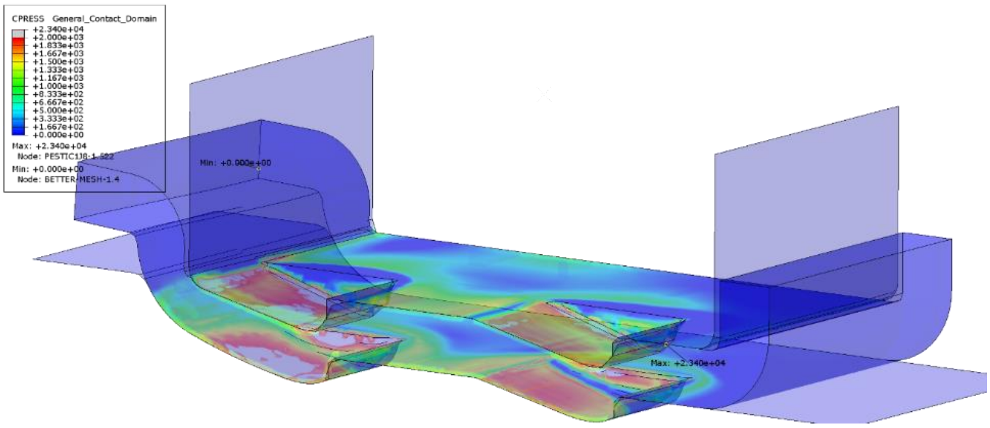

Slika 14: Razporeditev kontaktnega tlaka - popravljena matrica

Podprtje radija na matrici je močno izboljšalo zapolnitev materiala tudi pri minimalni debelini pločevine do sprejemljive mere. Je pa iz slike 15 razvidno, da bi lahko material bolje zapolnili predvsem v bočnem radiju zobca.

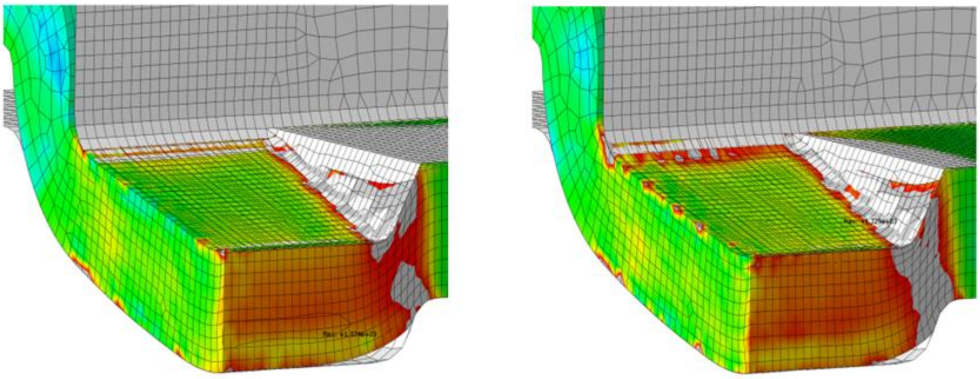

Slika 15: Zapolnitev materiala v spremenjeni obliki matrici pri minimalni (levo) in maksimalni (desno) debelini vhodne pločevine

Zaradi odprave cone prostega tečenja je bilo pričakovati porast maksimalne preoblikovalne sile. V tem primeru za izdelavo polovice para zobcev potrebujemo 35 ton preoblikovalne sile, kar za 12 zobcev pomeni približno 420 ton (slika 16).

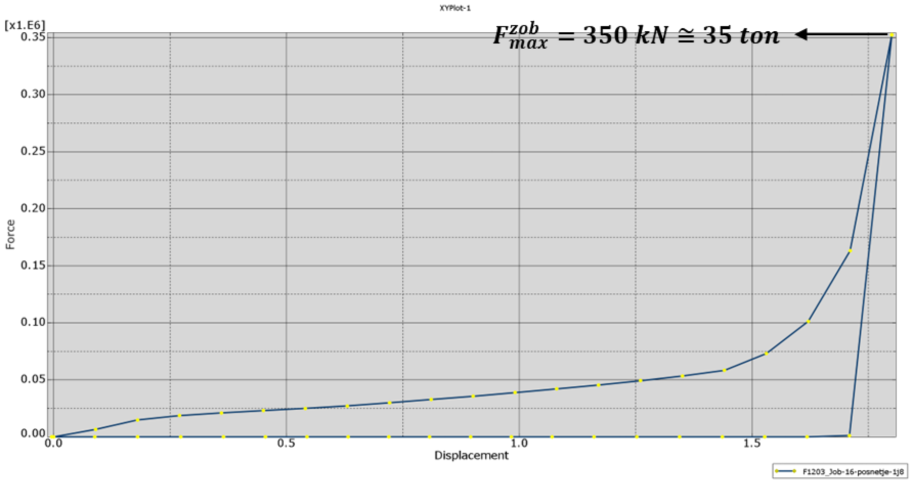

Slika 16: Graf odvisnosti preoblikovalne sile od pomika pestiča – spremenjena geometrija matrice

3.1.3 Analiza 3: Sprememba naklona zobčka na pestiču

Z namenom enakomerne porazdelitve tlaka med levim in desnim zobcem ter njegove homogene porazdelitve po površini zobca smo v nadaljnjih analizah spreminjali geometrijo pestiča. V tej analizi smo povečali naklon spodnje površine zobca na 18°, kot prikazano na sliki 17. Površini zobca na pestiču in v matrici tako nista bili več vzporedni.

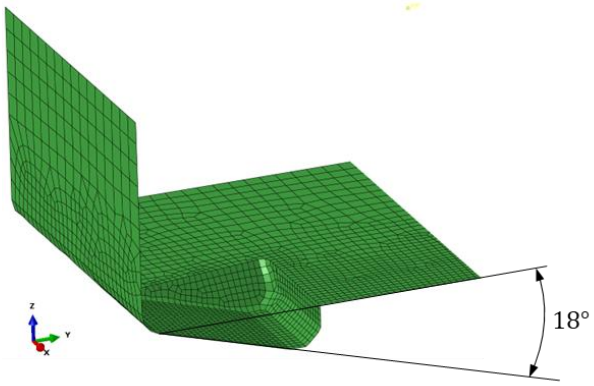

Slika 17: Spremenjen naklon spodnje površine zobca na pestiču na 18°

Iz razporeditve tlakov na sliki 18 je razvidno, da je razporeditev med levim in desnim zobcem enaka, velikost kontaktnega tlaka pa se je skoraj razpolovila. To je posledica lokalne deformacije pod konico zobca, ki zmanjša silo kovanja materiala, saj material steče v prosto cono bočnega radija zobca. To izboljša tudi zapolnitev materiala v matrici v primerjavi s prejšnjo analizo tako pri minimalni kot pri maksimalni debelini pločevine (slika 19).

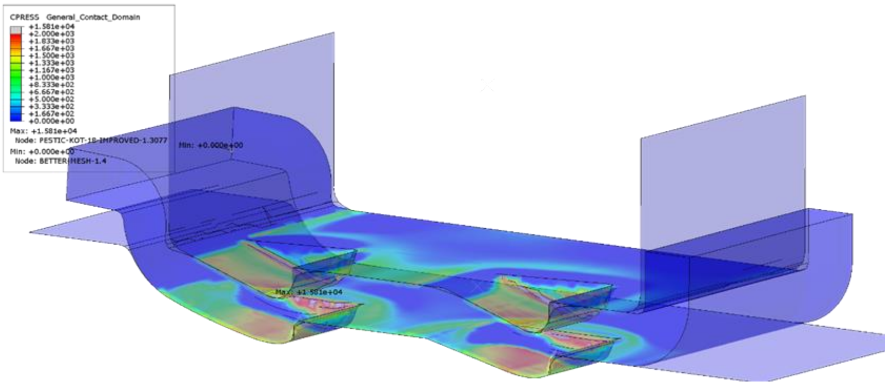

Slika 18: Razporeditev kontaktnega tlaka - spremenjen naklon pestiča

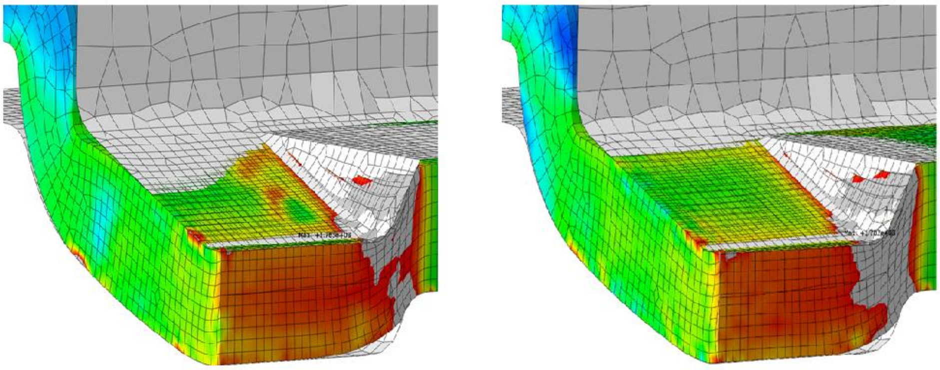

Slika 19: Zapolnitev materiala ob spremenjeni obliki pestiča pri minimalni (levo) in maksimalni (desno) debelini vhodne pločevine

Potek preoblikovalne sile v odvisnosti od pomika pestiča je prikazan na sliki 20. Zaradi povečanega naklona zobca, ki lokalizira deformacijo pod konico zobca, je maksimalna preoblikovalna sila za vtis polovice enega para zobcev upadla na približno 22 ton. Za izdelavo 12 zobcev to pomeni 260 ton preoblikovalne sile.

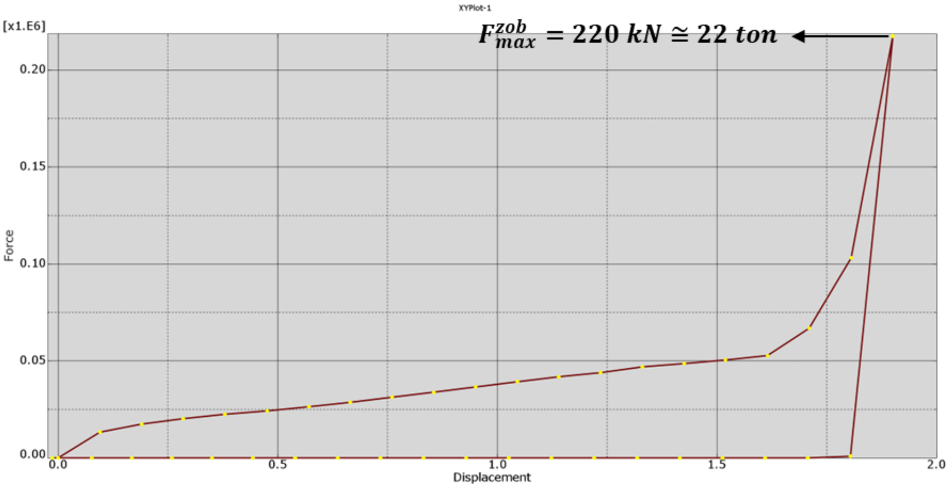

Slika 20: Graf odvisnosti preoblikovalne sile od pomika pestiča – sprememba naklona zobca na pestiču

3.1.4 Analiza 4: Optimizacija naklona zobčka na pestiču

V predhodni analizi smo ugotovili, da smo z večjim naklonom spodnje površine zobca na pestiču močno znižali kontaktni tlak in posledično potrebno preoblikovalno silo. Z namenom boljše ponovljivosti geometrije v serijski proizvodnji smo želeli povečati kontaktni tlak in s tem plastično deformacijo materiala. Zato smo naklon zobca rahlo zmanjšali, t.j. na 16°, in analizirali rezultirajoče razmere. Velikost kontaktnega tlaka na sliki je kot predvideno nekoliko višja od prejšnje analize (slika 18), vendar še vedno nižja od analize 2, v kateri sta bili površini zobca v matrici in na pestiču vzporedni (slika 14). Razporeditev tlaka med zobcema je enaka, izboljšala pa se je tudi homogenost porazdelitve tlaka po površini posameznega zobca. Od tod rezultira tudi še boljša zapolnjenost materiala v matrici tako pri minimalni kot pri maksimalni debelini vhodne pločevine, kot prikazano na sliki 22.

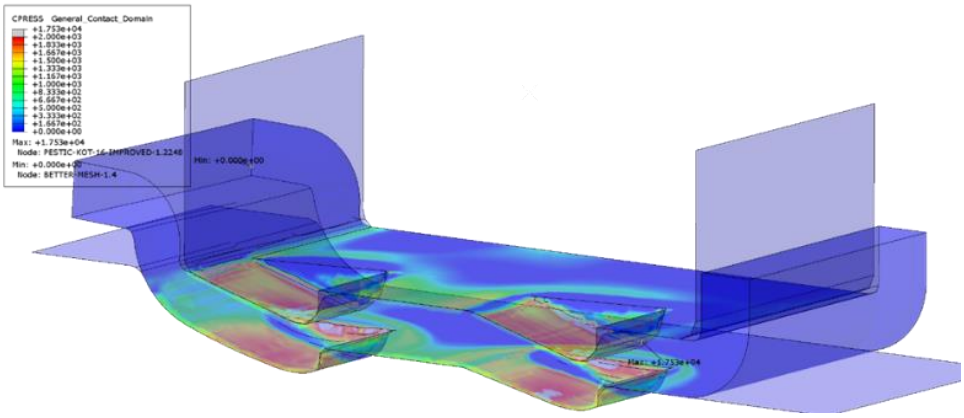

Slika 21: Razporeditev kontaktnega tlaka - optimizirana geometrija zobca na pestiču

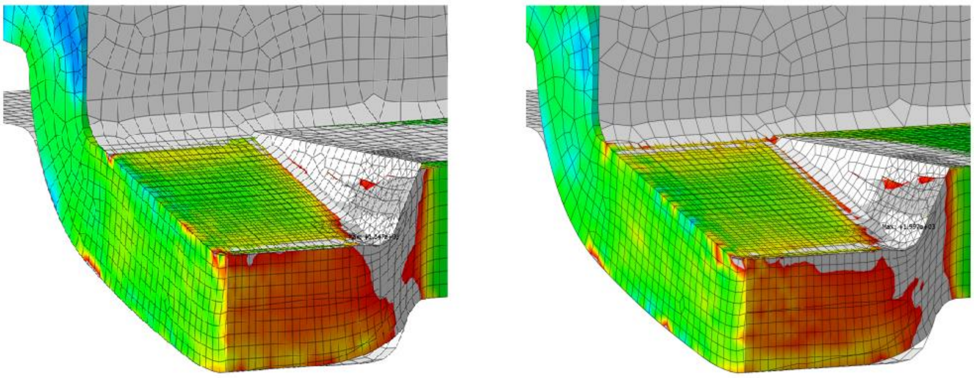

Slika 22: Zapolnitev materiala pri optimizirani obliki pestiča pri minimalni (levo) in maksimalni (desno) debelini vhodne pločevine

Maksimalna preoblikovalna sila se je, kot pričakovano, nekoliko povečala (slika 23). V primerjavi s prejšnjo analizo (slika 20) je narasla za dobrih 5 ton na polovico para zobcev, kar skupno za izdelavo 12 zobcev pomeni približno 320 ton preoblikovalne sile, kar napram izhodiščnim analizam pomeni redukcijo sile za približno 25%.

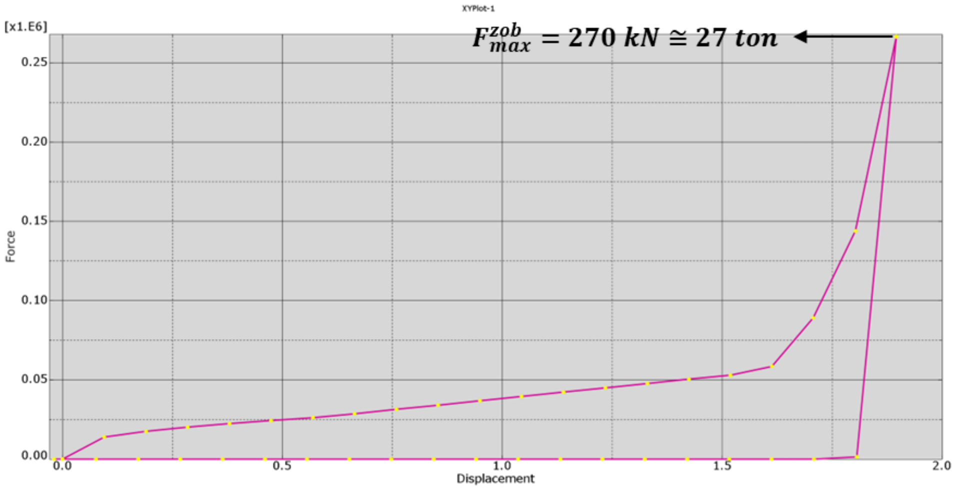

Slika 23: Graf odvisnosti preoblikovalne sile od pomika preoblikovalnega orodja - optimizirana oblika pestiča

3.2 Eliminacija razpoke skozi razvojne iteracije

Vzporedno z izvajanjem numeričnih analiz se je v fazi prototipiranja preizkušalo različne geometrije preoblikovalnega orodja, ki so bile izdelane na podlagi napovedi rezultatov iz analiz. Eden izmed bolj pomembnih pojavov, ki smo ga opazovali, je bil nastanek razpoke v kritični strižni ravnini. Razpoko v materialu smo identificirali s postopkom makrografije. Na sliki 24 je prikazan pojav razpoke v začetnih prototipnih fazah in njena eliminacija v serijskem izdelku ter primerjava z napovedjo numerične analize z optimizirano geometrijo preoblikovalnega orodja.

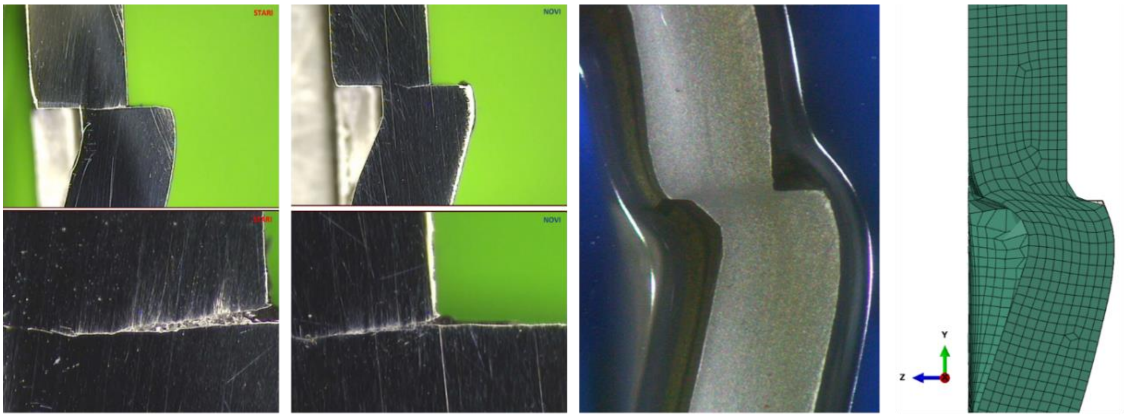

Izhodiščni prototip
Nadgrajen prototip
Serijski izdelek
Napoved numerične analize

Slika 24: Eliminacija razpoke skozi razvojne iteracije in primerjava z napovedjo numerične analize

V primarnih analizah s prvotno postavljenim materialnim modelom nismo uspeli napovedati nastanek razpoke v začetnih fazah, zato smo se kasneje ukvarjali z lomno mehaniko, s pomočjo katere lahko popišemo iniciacijo in propagacijo poškodbe do porušitve materialne točke.

3.3 Rezultati analize z vključenim duktilnim poškodbenim kriterijem

V analizi z vključeno lomno mehaniko so nas v prvi vrsti zanimala predvsem kritična mesta materialnih točk, v katerih pride do porušitve. Ko poškodbeni parameter D doseže vrednost $D = 1$, materialna točka odpove in pripadajoči končni element se odstrani iz mreže. Na sliki 25 je prikazana vrednost poškodbenega parametra D v trenutku popolnega zaprtja orodja, ko je preoblikovalna sila maksimalna. Iz rezultatov je razvidno, da materialni model ustrezno napove kritične ravnine, ki predstavljajo potencialna mesta za nastanek razpok. Opaziti je moč, da pride na desnem zobcu do popolnega pretrga materiala, medtem ko na levem zobcu razpoka rezultira zgolj na zgornji strani pločevine. Iniciacija razpoke se tako pri levem kot pri desnem zobcu pojavi na vogalih spodnje površine samega zobca, kjer je napetostno stanje najbolj nehomogeno in nadaljnji razvoj poškodbe najhitrejši.

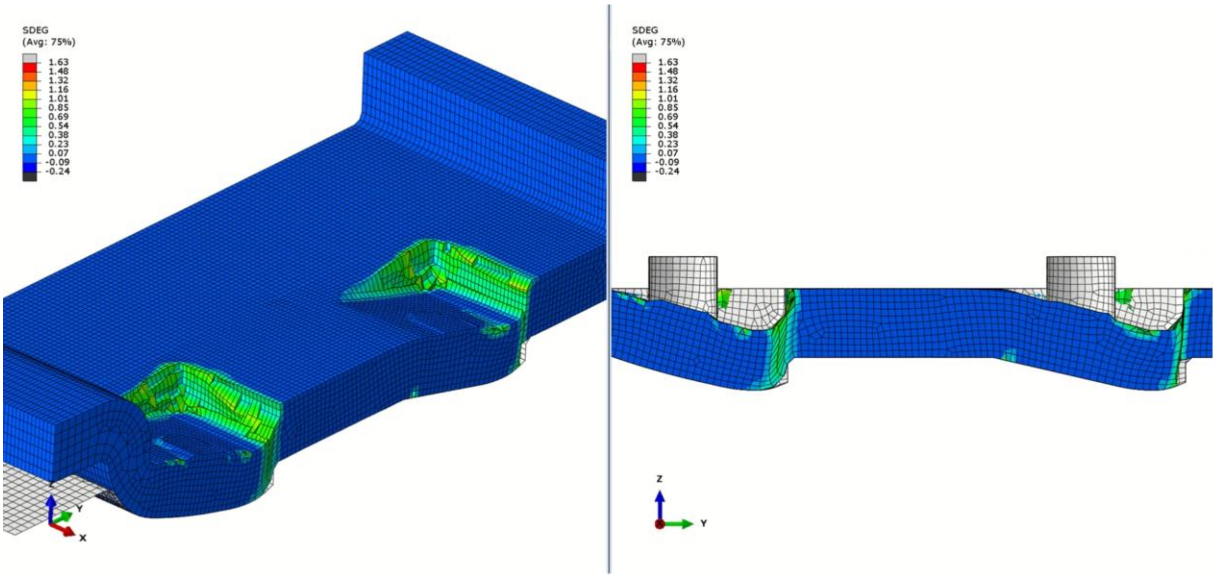

Slika 25: Vrednost poškodbenega parametra D (SDEG) v materialnih točkah, v katerih ni prišlo do porušitve

Na sliki 26 je levo prikazano stanje materiala v preseku v trenutku popolnoma zaprtega orodja in desno pripadajoč potek pritisne sile v odvisnosti od relativnega pomika pestiča. Fizikalno razumevanje te odvisnosti je pomembno za razumevanje samega procesa vtiskovanja. V prvem inkrementu je sila enaka nič, saj se pestič pomakne za dolžino zračnosti med pločevino in pestičem. Nato je odziv konsistenten z elasto-plastičnim odzivom materiala do trenutka, ko odpove prva materialna točka. V tistem trenutku se togost materiala zaradi nastanka razpoke oziroma izbrisa elementa iz mreže zmanjša in v nadaljevanju prirast sile zaradi pomika pestiča in degradacija togosti materiala narekujeta dokaj konstantno korelacijo preoblikovalna sila – pomik pestiča. Pred samim zaprtjem orodja je opaziti rahel upad sile, kar je posledica pretrga materiala v kritični strižni ravnini. Ko se orodje zapre in material zakuje, preoblikovalna sila skokovito naraste. Vrednost maksimalne preoblikovalne sile za vtis polovice para zobcev znaša okoli $80\,kN$, kar je več kot trikrat manj od $270\,kN$, kar smo napovedali v analizi 4 brez vključenega poškodbenega kriterija. Razlog za tako odstopanje je poseben obremenitveni primer, ki je odvisen od mreže. Med procesom vtiskovanja se na čelu zobca pojavi kritična strižna ravnina v kateri se pojavi razpoka. Debelina te razpoke je v realnosti ničelna, v analizi pa je ponazorjena z debelino strižnega stolpca končnih elementov, ki se med analizo iz mreže izbrišejo. Odstranjeni elementi predstavljajo zračnost v materialu oziroma cono prostega tečenja, v katero material pri zapiranju orodja steče in se takrat ne kuje, kar seveda ni fizikalno. V limiti, ko gre karakteristična dolžina strižnega stolpca končnih elementov proti nič, se cona prostega tečenja ne bi pojavila in popis razpoke bi bil fizikalen. Takrat bi morala biti maksimalna preoblikovalna sila v rangu z analizo 4 ($\cong 270\,kN$), a nekoliko nižja zaradi degradacije togosti, ki jo povzroči razpoka. To bi lahko dokazali s študijo neodvisnosti mreže, zato jo vključujemo med predloge za nadaljnje delo.

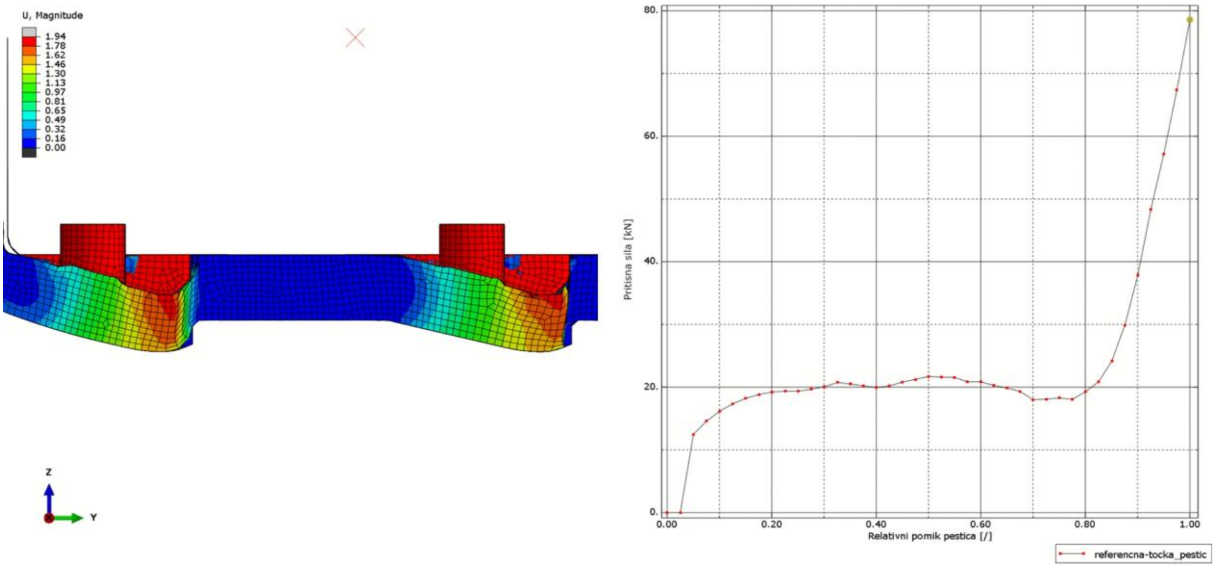

Slika 26: Magnituda pomika v trenutku popolnoma zaprtega orodja (levo) in pripadajoč potek pritisne sile v odvisnosti od relativnega pomika pestiča (desno)

4 ZAKLJUČEK

Z numerično analizo vtiskovanja zobcev v pločevino spremenljive debeline smo optimizirali tolerančno zahteven geometrijski detajl zobca, ki je prikazan na sliki 27. Določili smo pripadajočo geometrijo matrice in pestiča, s katero v procesu vtiskovanja zagotavljamo ustrezno zapolnitev zobcev z uporabo materiala s standardnim tolerančnim poljem debeline ($3 \pm 0.1\,mm$). Zobci v sestavu robustno zagotavljajo zahtevano aksialno iztisno silo gumijastega paketa iz jeklene puše $F_{out} > 10\,kN$. Na podlagi rezultatov analize smo identificirali delež preoblikovalne sile v orodju, potreben za vtis 12 zobcev, ki znaša približno $320\ ton$. Tako zmoremo celotno jekleno pušo izdelati v 1000 tonski stiskalnici. V prototipnih fazah smo spremljali pojav razpoke v materialu in jo v kombinaciji z analizami do serijskega procesa eliminirali. Z namenom napovedovanja razpoke že v virtualnih analizah, smo postavili materialni model z vključenim duktilnim poškodbenim kriterijem. Z njim smo uspešno identificirali materialne točke, v katerih pride do porušitve. Ugotovili smo, da je napoved razpoke v danem obremenitvenem primeru odvisna od karakteristične dolžine končnih elementov, kar je razlog za odstopanja od rezultatov primarnih analiz.

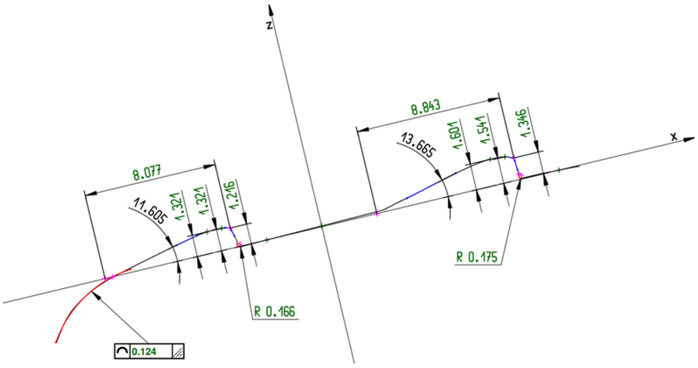

Slika 27: Optimizirana geometrija površine zobcev z določenim tolerančnim poljem (meritev s konturografom)

LITERATURA

[1] Peitzmeier, Klaus-Achim. Dawn of a New Axle Era. [Datum ogleda: 4. 9. 2024]. Dostopno: https://www.porsche.com/international/_iceland_/aboutporsche/christophorusmagazine/archive/386/articleoverview/article05/

[2] ABAQUS Online Documentation: Version 6.6-1. Explicit dynamic analysis. [Datum ogleda: 4. 9. 2024]. Dostopno: https://classes.engineering.wustl.edu/2009/spring/mase5513/abaqus/docs/v6.6/books/usb/default.htm?startat=pt03ch06s03at07.html

[3] ABAQUS Online Documentation. General Framework for Modelng Damage and Failure. [Datum ogleda: 6. 9. 2024]. Dostopno: https://help.3ds.com/2023/english/dssimulia_established/SIMACAEMATRefMap/simamat-c-damageoverview.htm?contextscope=all&id=3945854c24b54572a7a454fa83ee5691

[4] ABAQUS Online Documentation. Damage Evolution. [Datum ogleda: 6. 9. 2024]. Dostopno: https://help.3ds.com/2023/english/dssimulia_established/SIMACAEMATRefMap/simamat-c-damageevolductile.htm?contextscope=all&id=2ac2fbe9bba841109eaae681b5fac03d
[5] Hooputra, H., H. Gese, H. Dell, and H. Werner. A Comprehensive Failure Model for Crashworthiness Simulation of Aluminium Extrusions. International Journal of Crashworthiness. 2004, vol. 9, no.5, strani 449-464.
[6] ABAQUS Online Documentation. Damage Initiation Criteria for Fracture of Metals. [Datum ogleda: 6. 9. 2024]. Dostopno: https://help.3ds.com/2023/english/dssimulia_established/SIMACAEMATRefMap/simamat-c-damageinitductile.htm?contextscope=all&id=54e92e6346c44125a0c66daa597a264e
[7] Hillerborg, A., M. Modeer, and P. E. Petersson. Analysis of Crack Formation and Crack Growth in Concrete by Means of Fracture Mechanics and Finite Elements. Cement and Concrete research. 1976, vol. 6, strani 773-782.

9th International Conference on the Development of Industrial Engineering
21. November 2024
Novo mesto, Slovenia

Zmanjševanje ogljičnega odtisa z uporabo električnih vozil v urbani mikro mobilnosti

Aleš Jelen[1], Damjan Balabanič[1]

[1]Fakulteta za industrijski inženiring Novo mesto, Šegova ulica 112, 8000 Novo mesto, Slovenija
E-naslova: ales.jelen@students.fini-unm.si, damjan.balabanic@fini-unm.si

***Povzetek:** V zadnjih desetletjih se ogljični odtis človeštva in s tem pritiski na okolje vztrajno povečujejo. Od začetka sedemdesetih let 20. stoletja, ko je človeštvo prvič prekoračilo obnovitvene zmožnosti planeta, je ogljični odtis stalno presegal biokapaciteto ekosistemov na Zemlji, zlasti še na račun hitro rastočega ogljičnega odtisa zaradi rabe fosilnih goriv. Namen prispevka je ugotoviti ali električna mikro mobilnost v urbanih okoljih prispeva k zmanjšanju ogljičnega odtisa mest, ali je izbor primerne električne mobilnosti glede na značilnosti urbanega okolja ključnega pomena za učinkovitost in priljubljenost, ali ima električna mikro mobilnost poleg zmanjšanja ogljičnega odtisa tudi druge koristi za urbano okolje in ali je izračun ogljičnega odtisa električnega vozila za mikro mobilnost manjši od odtisa klasičnega vozila. Predstavljena so električna vozila, njihove prednosti in slabosti ter bolj podrobno predstavljena vozila, ki se uporabljajo za urbano mikro mobilnost. Opisane so omejitve pri uporabi električnih vozil in težava ogljičnega odtisa visokonapetostnih baterij za električna vozila. V poglavju o mikro mobilnosti je predstavljena definicija trajnostne mobilnosti, varnostni vidik le-te in izračun ogljičnega odtisa z uporabo električne mikro mobilnosti. Prikazani so primeri dobrih praks in projekte mikro mobilnosti v urbanem okolju iz različnih držav po svetu. Predstavljene so tudi inovacije na tem področju, ki bodo v prihodnosti oblikovale mikro mobilnost. Na koncu študije je narejena primerjava med izračunom ogljičnega odtisa, če za vožnjo po opravkih uporabljamo vozilo na klasična goriva in če uporabljamo električna vozila, medtem ko ostale aktivnosti ostanejo enake. Ugotovljeno je, da je skupni ogljični odtis veliko manjši v primeru uporabe električnega mikro vozila.*

***Ključne besede:** električna mobilnost, električna vozila, mikro mobilnost, ogljični odtis, urbano okolje*

***Razvrstitev:** Strokovni članek*

1 UVOD

Ogljični odtis predstavlja skupno količino izpustov toplogrednih plinov, ki jih posameznik, organizacija, država, dogodek, izdelek ali storitev povzroči neposredno ali posredno. Izračun ogljičnega odtisa, izraženega v tonah CO_2 (če gre za neposredne CO_2 izpuste) ali tonah CO_2 ekvivalenta (če so vključeni izpusti vseh toplogrednih plinov), predstavlja družbeno odgovornost posameznika ali organizacije ter služi pri načrtovanju zmanjšanja emisij v okolju. V Sloveniji nastane letno 15 650 Gg CO_2, od tega ga 17,2 % prispeva promet [1]. Države si zato prizadevajo z različnimi ukrepi in spodbudami zmanjšati ogljični odtis oziroma emisije CO_2. Evropski parlament je sprejel Uredbo (EU) 2021/1119 Evropskega parlamenta in Sveta z dne 30. junija 2021 o vzpostavitvi okvira za doseganje podnebne nevtralnosti in spremembi uredb (ES) št. 401/2009 in (EU) 2018/1999 (evropska podnebna pravila) [2], ki zvišuje cilj EU glede zmanjšanja neto emisij toplogrednih plinov za vsaj 55 % do leta 2030 in ki je spremenil podnebno nevtralnost v zavezo.

V EU več kot 70 % prebivalcev živi v mestih, ki proizvedejo 23 % vseh toplogrednih plinov zaradi prometa. Rešitev je bolj trajnostna, pametna in zdrava mobilnost, zato EU predlaga novo strategijo urbane mobilnosti. Ena od strategij je povečanje podpore za uporabo in skupno rabo trajnostnih načinov prevoza ter urbane logistike, ki ne povzroča emisij, ter integracijo inovativnih storitev mobilnosti v urbane transportne sisteme [3].

Električna mobilnost v mestih pa ne obsega samo uporabe električnih vozil za vožnjo prebivalcev, ampak tudi za nadomestitev drugih prevoznih sredstev (avtobus, taksi, dostavne službe, …), ki bolj obremenjujejo okolje. V zadnjih letih smo v Sloveniji in tujini priča hitremu porastu mikro mobilnosti. Ko govorimo o mikro mobilnosti, mislimo na prevozna sredstva manjše velikosti s kapaciteto prevoza ene osebe (el. mopedi, el. kolo, el. skiro). Naša ideja je, da bi z uporabo električne mikro mobilnosti lahko zmanjšali ogljični odtis prometa v urbanih okoljih in hkrati izboljšali zdravje ljudi, ki bi se z uporabo teh vozil več časa zadrževali na zraku in več gibali, hkrati pa tak način prevoza tudi omogoča več medosebnih stikov. Vse to naj bi imelo pozitiven vpliv na prihodnost urbanih okolij in njihovih prebivalcev.

2 MIKRO MOBILNOST

Pod pojmom električna mikro mobilnost razumemo mikro prevozna sredstva na električni pogon. Gre za električna kolesa, skiroje in skuterje. Namen električne mikro mobilnosti je zmanjšati ogljični odtis prometa v mestih.

2.1 Trajnostna mobilnost

Izraz trajnostna mobilnost se nanaša na prevoz z okoljskega vidika. Ko govorimo o trajnostni mobilnosti, mislimo na vse od hoje in kolesarjenja do javnega potniškega prometa in drugih oblik mobilnosti. Trajnostna mobilnost bo zagotovila enakopraven dostop do mobilnosti za vse uporabnike, spodbujala k alternativnim načinom potovanja in hkrati omejila uporabo osebnih motornih vozil in rabo energije. S tem bo trajnostna mobilnost zmanjšala emisije toplogrednih plinov, izboljšala kakovost zraka v mestih ter izboljšala javno zdravje [4, 5].

Eden od ciljev trajnostne mobilnosti je tudi, da se zmanjša čas, ki ga porabimo v prometnih zamaških. Ta ne vpliva slabo samo na okolje, ampak tudi na zdravje ljudi. Za ta namen se mobilnost čedalje bolj avtomatizira in digitalizira, uvajajo se inteligentni sistemi za upravljanje prometa, ki naj bi prinesli bolj pretočen promet, napovedovali prometne zamaške in upravljali potrebe po javnem prevozu in souporabi vozil. Čedalje več mest prebivalcem ponuja tudi souporabo koles, skirojev in skuterjev, ki ne proizvajajo izpustov. Po raziskavi inštituta MIT iz ZDA naj bi souporaba mobilnosti močno zmanjšala število parkirnih mest v mestih in tako sprostila prostor za pešce in kolesarje [6].

Številni strokovnjaki trdijo, da bi moral vsak poskus strategije trajnostne mobilnosti vključevati najmanj osnovne tri vidike trajnostnega razvoja: zadostiti potrebam uporabnikov, zagotoviti socialno pravičnost in spoštovati okoljske omejitve. Avtorji so te tri vidike prevedli v kriterije za vrednotenje trajnosti takih strategij, ki so zagotavljanje dostopnosti osnovnih transportnih sredstev (potrebe), zagotavljanje enakega dostopa do transportnih storitev (socialna pravičnost) in zagotavljanje, da transport ne ogroža okolja (okoljske omejitve) [7].

2.2 Definicija mikro mobilnosti

Elektromobilnost je definirana kot zamenjava obstoječih vozil, ki imajo pogon na fosilna goriva, z električnimi vozili. Ko združimo izraza elektro mobilnost in mikro mobilnost, dobimo električno mikro mobilnost. Gre za vozila z najvišjo hitrostjo 25 km/h, ki jih upravlja voznik.

Olabi idr. (2023) navajajo naslednje prednosti mikro mobilnosti: zmanjšanje števila nesreč, zmanjšanje vodnega odtisa prometa, zmanjšanje energijskega odtisa prometa, povečanje dostopnosti prevoza, zmanjšanje prometnih zastojev, zmanjšanje hrupa, izboljšanje kakovosti zraka, večja učinkovitost virov in izboljšanje trajnosti mest. Kot slabosti mikro mobilnosti pa navajajo varnost, logistične izzive, komunikacijo, infrastrukturo, življenjski cikel vozil, spreminjajočo se zakonodajo ter vedenje voznikov mikro vozil [8].

2.3 Izračun ogljičnega odtisa z uporabo električne mikro mobilnosti

Prikazan je izračun ogljičnega odtisa štiričlanske družine iz Ljubljane, ki za vožnjo po mestu uporablja mikro vozila, in sicer kolesa, električna kolesa in električne skiroje, za daljše vožnje izven Ljubljane pa lasten avtomobil in vlak (Primer 1). Primerjali ga bomo z ogljičnim odtisom iste družine, ki za vožnjo po mestu uporablja avtomobil namesto mikro vozil (Primer 2). Za izračun bomo uporabili kalkulator ogljičnega odtisa na spletni strani Umanotera [9]. Za Primer 1 smo torej vnesli podatke, ki so prikazani v Tabeli 1.

Tabela 1: Izračun ogljičnega odtisa za vožnjo z avtomobilom [9]

Podatek	Vrednost
Število članov v gospodinjstvu	4
Poraba električne energije iz omrežja letno	420 kWh
Mesečna poraba kurilnega olja za ogrevanje	200 l
Povprečno število potnikov v avtomobilu	2
Mesečna poraba dizelskega goriva	200 l
Potovanja z letalom v letu dni	1 povratni let (Egipt – Kairo)

Izračun ogljičnega odtisa je pokazal skupno porabo na osebo na leto 6 ton CO_2.

Rezultati prikazujejo, da je Ravnotežna vrednost izpustov povprečno 1,5 ton CO_2/leto na osebo v obdobju 2018–2050. Ob tej vrednosti bi glede na število zemljanov dosegli omejitev globalnega segrevanja na 1,5 stopinje C glede na predindustrijsko obdobje, kar je cilj Pariškega sporazuma. Izpusti posameznika so lahko razporejeni neenakomerno, tako da je osebni ogljični odtis v začetku večji, proti sredini stoletja pa ustrezno manjši.
V tem primeru je ravnotežna vrednost presežena za 4 ton CO_2/leto.«

Za Primer 2 smo spremenili samo podatek za porabo dizelskega goriva in povprečno število potnikov v avtomobilu, saj se namesto z avtomobilom po mestu vozimo z mikro vozili, na daljše relacije pa je povprečno število potnikov v vozilu 4 namesto 1. Rezultati so prikazani v Tabeli 2.

Tabela 2: Izračun ogljičnega odtisa za vožnjo z električnim skirojem [9]

Podatek	Vrednost
Število članov v gospodinjstvu	4
Poraba električne energije iz omrežja letno	420 kWh
Mesečna poraba kurilnega olja za ogrevanje	200 l
Povprečno število potnikov v avtomobilu	4
Mesečna poraba dizelskega goriva	40 l
Potovanja z letalom v letu dni	1 povratni let (Egipt – Kairo)

V tem primeru se je skupna letna poraba na osebo zmanjšala na 3,1 tone CO_2. V tem primeru presegamo ravnotežno vrednost za: 1,1 tone CO_2/leto.

3 PRIMERI REŠITEV ZA MIKRO MOBILNOST V URBANIH OKOLJIH PO SVETU

3.1 Sistem za analizo prometa Asistobe EXPLORE

Podjetje Asistobe je razvilo sistem za analizo mobilnosti v mestih, ki na podlagi podatkov pokaže, kako, kdaj in kje se ljudje premikajo po mestu. Upošteva javni prevoz, osebne avtomobile in mikro mobilnost. Sistem zbira in analizira različne vire podatkov in upravljalcem prometne strategije omogoča iskanje, raziskovanje, kombiniranje in vizualizacijo podatkov v realnem času. Kot vir podatkov lahko uporablja tudi podatke o uporabnikih mobilnih telefonov, ki jih dajo na voljo mobilni operaterji. Upravljalci prometa lahko s pomočjo sistema spremljajo prometno omrežje (stroške, zasedenost, učinkovitost) in analizirajo pretok potnikov skozi čas, s pomočjo teh podatkov pa lahko načrtujejo bolj učinkovit prometni sistem [10].

Sistem analizira tudi obstoječe podatke o mobilnosti in v njih ugotavlja trende, prepoznava prometne vzorce po območjih in prikaže učinek dogodkov (koncerti, športni dogodki) in večjih motenj v mobilnosti. S temi podatki lahko upravljalci prometa raziskujejo, kako ljudje potujejo, predvidijo trende v mobilnosti ter optimizirajo in načrtujejo prihodnja prometna omrežja [10].

3.2 Postaja za parkiranje skirojev Trap

Postaja Trap omogoča, da uporabniki vozil za osebno mobilnost, kot so skiroji, kolesa ali rolke, varno parkirajo svoje vozilo. Stojala podpirajo vse modele električnih skirojev in so lahko priključena na obnovljivi vir električne energije, kot so fotovoltaična talna obloga ali solarni paneli. Stojala imajo tehnološko dovršen sistem za zaklepanje in zaščito. Postaje so enostavne za uporabo in praktične, saj se uporabljajo prek mobilne aplikacije in tipkovnice, v stojala pa je integriran tudi čip RFID in sistem za geolociranje [11].

3.3 Sistem za varno mobilnost SpotBeam

Namen tehnologije SpotBeam je izboljšanje varnosti pešcev in drugih udeležencev v prometu s pomočjo pasivnega zbiranja podatkov iz mobilnih telefonov in drugih povezanih naprav, hkrati pa zagotoviti zasebnost uporabnikov. SpotBeam je tehnologija zaznavanja povezanih naprav (WiFi, Bluetooth, mobilni podatki), ki uporabnike opozarja na bližajoče srečanje s pešci in vozniki mikro vozil. Uporaba ne zahteva namestitve mobilne aplikacije in deluje s pomočjo senzorjev ne glede na razdaljo in vreme. S to tehnologijo želi podjetje povečati varnost pešcev, tekačev, kolesarjev in vozil [12].

3.4 Jonna

Jonna je švedska spletna platforma za nakup in prodajo obnovljenih električnih koles. Jonna kupuje električna kolesa višje kakovosti od podjetij ter jih obnovi in proda končnim uporabnikom in podjetjem po načelu leasinga. Uporabljena električna kolesa se prodajajo končnim uporabnikom po strogih pregledih, uporabnik pa dobi transparentne informacije o garanciji na dele ter ponudbe za servisiranje in zavarovanje. Vsi deli, ki jih uporablja Jonna, se lahko diagnosticirajo elektronsko in imajo dolgo življenjsko dobo [13].

3.5 Dostavni električni skiro Bruntor

Bruntor se imenuje električni skiro in hkrati podjetje, ki ga izdeluje. Skiro je namenjen »last-mile« dostavi, torej dostavi končnemu uporabniku v mestnih območjih, kjer z običajnimi dostavnimi vozili ne moremo. Skiro brez sedeža ima štiri kolesa in je enostaven za uporabo. Nanj lahko naložimo do 600 litrov oziroma 100 kg tovora, poleg tega pa podpira še voznika do 100 kg teže. Širok je 65 cm in dolg 140 cm. Z enim polnjenjem lahko prevozi 120 km, prostor za tovor pa je možno popolnoma prilagoditi potrebam uporabnikov. Ima ločeno vzmetenje, zato je vožnja po tlakovanih in neravnih površinah udobna za voznika in varna za tovor. Prevozi lahko tudi do 15 cm visoke ovire. Proizvajalec trdi, da so dostave z dostavnimi skiroji do 20 % bolj učinkovite kot z električnimi dostavnimi kolesi [14].

3.6 Mobilna platforma NUDGD: Smart Nudges Mobility

Marsikdo si želi potovati na okolju bolj prijazen način, vendar ne zna narediti prvega koraka. Smart Nudges Mobility ali NUDGD je mobilna platforma po načelu mobilnosti kot storitve (angl. *mobility-as-a-service, MaaS*), ki uporabnike spodbuja k uporabi okolju prijaznih potovalnih navad. Zasnovana je na podlagi psiholoških dognanj glede vedenja potrošnikov. Podjetje, ki je razvilo aplikacijo, trdi, da je 43 % uporabnikov po zaslugi platforme spremenilo način potovanja ali pa to še načrtuje, promet z avtomobilom med zaposlenimi pa se je v švedski regiji, kjer so preskušali platformo, zmanjšal za 14 % [15]. Platforma deluje po načelu svežega začetka in uporablja potencial za vedenjsko spremembo, ki ga prinesejo novi začetki. Platforma na primer tistim, ki so se na novo priselili v neko območje ali na novo zaposlili v nekem območju, prikaže njim prilagojene informacije glede na okoliščine. Po SMS jim pošlje sporočilo in edinstveno povezavo z informacijami, nato pa uporabnika z različnimi načini spodbuja k bolj okolju prijaznim potovalnim navadam. Na koncu se celoten proces izmeri in analizira, da lahko uporabnik enostavno ovrednoti svoj okoljski učinek [15]. Upravljalec platforme trdi, da se dvakrat več njihovih uporabnikov odloča za hojo v službo v primerjavi z drugimi, da se je 76 % več njihovih uporabnikov odločilo za kolesarjenje v službo, da se je 62 % več njihovih uporabnikov odločilo za nakup električnega, plinskega ali hibridnega vozila ali souporabo vozila v prihodnje, 33 % njihovih uporabnikov pa trdi, da se je za to odločilo po zaslugi platforme NUDGD [15].

3.7 Varna parkirišča za kolesar RASTEL.IO

RASTEL.IO je sistem za kontrolo dostopa, ki lahko pretvori vsak zaprt prostor v pametno parkirno postajo za kolesa. Upravitelji postaj za kolesa lahko s tem sistemom upravljajo dostop, spremljajo zasedenost in spodbujajo kolesarjenje. Aplikacija Rastel.io omogoča tudi izdelavo poročil ter odklepanje enot na daljavo v nujnih primerih. Vse to uporabnikom zagotavlja višjo varnost in enostaven dostop. Hkrati pa aplikacija vključuje akcije, ki kolesarje nagrajujejo in spodbujajo bolj zdrav in zelen razvoj [16].

3.8 Sistem umetne inteligence R.O.A.D.

Sistem R.O.A.D. temelji na umetni inteligenci, ki skenira in zbira podatke vzdolž kolesarskih poti. Naprava analizira in ovrednoti kakovost infrastrukture za mikro mobilnost na podlagi različnih parametrov, ki jih pridobi s pomočjo senzorjev, nameščenih na kolesih, ter iz podatkov, ki jih zbirajo sateliti v sistemu Copernicus. Sistem z IoT-senzorji in mobilno aplikacijo prepozna lokacijo, zazna anomalije na cestni površini in spremlja ključne parametre, ki vplivajo na mikro mobilnost, npr. svetlobne pogoje, promet, kakovost zraka in onesnaženost s hrupom. Nato s tehnologijo 4G/5G prenese podatke v oblak ter jih obdela in ustvari podatkovne nize GIS. Hkrati iz evropske satelitske mreže Sentinel 5P zbere okoljske podatke, kot so onesnaženost zraka z delci velikosti PM1.0, PM2.5 in PM10 ter drugimi onesnaževalci (O_3, NO_2, CO, CH_2O, SO_2, CH_4) in jih združi s podatki iz senzorjev. Analizirane podatke nato prikaže na nadzorni plošči in s tem omogoča hitro in učinkovito analizo stanja infrastrukture [17]. Sistem se uporablja za analizo kakovosti in varnosti cestne infrastrukture. Njegove funkcije omogočajo tudi spremljanje stanja cestnih površin, zaznavanje lukenj na cesti, zaznavanje ovir, spremljanje osvetljenosti kolesarskih poti in zaznavanje ledu na cestnih površinah, s podatki pa lahko upravljalci infrastrukture tudi načrtujejo izboljšave in posodobitve, da izboljšajo kakovost površin za kolesarje in zmanjšajo onesnaženost okolja s hrupom in drugimi onesnaževalci.

3.9 Postaja LEVOX za izmenjavo baterij za mikro vozila

Postaje LEVOX so postavljene na različnih lokacijah in so oblikovane kot paketniki. V predalih so zaklenjene baterije za mikro vozila in uporabnik se pripelje, zamenja baterijo v predalu in se odpelje dalje. Deluje po načelu baterije kot storitev. Postaje so na voljo 24 ur na dan in vsebujejo različne baterije za različna mikro vozila, so pa tudi zavarovane pred krajo [18].

3.10 Podaljšana zelena luč za kolesarje v Odense, Danska

V mestu Odense na Danskem so na semaforje, ki so postavljeni na cesti Super Bike Highway, namestili senzorje za dež, ki zaznavajo padavine. Ko dežuje, bo zelena luč za kolesarje svetila 20 sekund dlje, zato da kolesarjem ne bo treba predolgo čakati na dežju. Senzor za dež je povezan z dvema senzorjema gibanja, ki zaznavata, ko se kolesarji približajo semaforju na 70 metrov. Na semaforju je nameščena tudi škatla, ki s svetlobo obvešča kolesarje kdaj je sistem aktiven. Ko se sistem vklopi, imajo avtomobili na križišču 20 sekund daljši postanek ob rdeči luči. Sistem temelji na ideji, da je treba kolesarjem olajšati vožnjo s pomočjo tehnologije [19].

3.11 Kolesarske avtoceste na Danskem

Danska je uvedla avtoceste za kolesarje (Cycle Superhighways), s katerimi želi ustvariti mrežo kolesarskih poti po osrednji regiji. Cilj je ustvariti boljše pogoje za tiste, ki se na delo vozijo s kolesom, in s pomočjo novih in inovativnih rešitev spodbuditi ljudi, da za prevoz na delo uporabljajo kolo. Kolesarske avtoceste naj bi povečale število tistih, ki za prevoz na delo uporabljajo kolo, za več kot 30 %. Od odprtja prve kolesarke avtoceste Farum leta 2012 se je število tistih, ki kolesarijo na delo, povečalo za 52 %. Pri projektu je regijska vlada sodelovala s 23 občinami, vse skupaj pa je koordinirala regijska agencija [20]. Po izgradnji vseh 28 kolesarskih avtocest na Danskem, naj bi se na letni ravni zmanjšalo število dni odsotnosti z dela zaradi bolniške za 34 000 in med prometno konico zmanjšalo število vozil za 1,4 milijona. Izračunali so, da imajo kolesarske avtoceste družbeno-ekonomski učinek oziroma donosnost naložbe 19 %, medtem ko je imela investicija v danski sistem podzemne železnice donosnost naložbe samo 3,1 % [20].

3.12 Zložljive kolesarske čelade Newton-Rider

Zložljive kolesarske čelade so prve polmehke čelade, ki se natančno prilagajo glavi in so hkrati debele le 16 mm. Čelado lahko uporabniki zložijo v torbo. Material iz katerega je narejen zunanji del, je 40 % tanjši od običajnih čelad, blazinice v notranjosti pa so narejene iz polmehkega materiala in fleksibilne, zato jih je možno zviti. Namen čelade je izboljšati varnost uporabnikov (kolesarjev in voznikov drugih mikro vozil in zmanjšati število pretresov možganov, ki so najpogosteje posledica neuporabe čelade) [21].

3.13 Mobilnost kot storitev v Sloveniji (Care4climate)

Mikro mobilnost bi se tudi v Sloveniji morda še bolj razširila, če bi bila smiselno povezana z drugimi prometnimi sistemi. Temu danes rečemo mobilnost kot storitev (MaaS). Gabrovec, Bole, Goluža in Tiran (2022) so v dokumentu Zasnova mobilnosti kot storitve v Sloveniji, ki je nastal v okviru projekta Care4Climate, predlagali zasnovo mobilnosti kot storitve v Sloveniji glede na tuje izkušnje in slovenske posebnosti. Mobilnost kot storitev dobiva vse večjo pozornost, saj ponuja možen odgovor na sodobne izzive na področju osebnih potovanj, zlasti glede učinkovitosti prometnih sistemov in zmanjševanja vplivov prometa na podnebne spremembe [22]. V projektu LIFE IP CARE4CLIMATE je v okviru akcije C3.1 (Integriranje javnega potniškega prometa) predvidena vzpostavitev spletne platforme po vzoru sistema MaaS v Sloveniji. Eno od izhodišč projektne akcije je bilo, da je ena od poti do bolj konkurenčnega in pogosteje uporabljanega javnega potniškega prometa (JPP) prav povezovanje vseh oblik JPP in drugih trajnostnih potovalnih načinov. Na takšni platformi bi bile na enem mestu zbrane informacije o JPP in drugih trajnostnih potovalnih načinih, kakor so na primer souporaba koles in avtomobilov, sopotništvo ter alternativne oblike JPP (prevoz na klic, taksi, stalni izvenlinijski prevoz in podobno). Platforma bi pokrivala območje celotne države in omogočila uporabnikom, da izberejo (večmodalno) optimalno pot od začetka do cilja ter tudi naročijo in plačajo prevoz [23]. Takšna platforma bi uporabnikom ponudila zadovoljivo alternativo uporabi lastnega avtomobila, ki je v Sloveniji s 67,5 % opravljenih poti še vedno močno prevladujoči potovalni način. Vendar je pot do tja, kakor kažejo tuje izkušnje, dolga, težavna in negotova, saj je MaaS razmeroma nov, hitro razvijajoč, še ne v celoti preizkušen in za vključene akterje pomeni številna tveganja, na njegov uspeh pa vplivajo številni dejavniki. MaaS spodbuja večmodalnost oziroma kombiniranje različnih oblik mobilnosti, ki jih ponujajo zasebni in javni ponudniki prevozov. To so lahko javni avtobusni in železniški prevoz, souporaba avtomobila, taksi, najem avtomobila, sopotništvo, najem ali souporaba kolesa, najem ali souporaba skiroja in drugi. MaaS spodbuja tudi aktivno mobilnost, zlasti kolesarjenje in hojo. S povezovanjem različnih oblik prevoza se poveča privlačnost uporabe tega sistema za končne uporabnike [23]. Sistem MaaS zahteva sodelovanje številnih akterjev, ki imajo v sistemu različne vloge in odgovornosti. Ena od organizacijskih zgradb sistem MaaS členi na štiri ravni: zakonodajna raven, raven izvajanja prevoznih storitev, raven integracije in ponudbe storitev mobilnosti ter raven končnih uporabnikov. Vse so prikazane v naslednji Tabeli 3.

Tabela 3: Organizacija mobilnosti kot storitve [23]

Raven	Akterji	Vloge in odgovornosti
Zakonodajna raven	Ministrstvo, pristojno za promet	Pripravlja predpise, oblikuje prometno politiko in prometne strategije, spodbuja pilotne projekte, je odgovorno za investicije.
	Javne agencije in podjetja na področju prometa	Izvajajo prometno politiko in strategije, zagotavljajo izvedbo investicij, izdajajo dovoljenja, soglasja in mnenja; v to skupino spadajo tudi upravljavci JPP.
	Lokalni uradi na področju prometa	Odgovorni za lokalno prometno infrastrukturo, prostorsko in prometno načrtovanje na lokalni ravni. Načrtujejo, organizirajo in upravljajo mestni promet in z njim povezano infrastrukturo.
Izvajanje storitev mobilnosti	Avtobusni potniški promet	Podjetja, ki zagotavljajo izvajanje avtobusnih prevozov na določenih progah v skladu z voznimi redi. Zbirajo voznine, zagotavljajo

		informacije o storitvi, po možnosti v realnem času.
	Železniški potniški promet	Odgovorni za izvajanje železniških prevozov na določenih progah v skladu z voznimi redi. Zbirajo voznine, zagotavljajo informacije o storitvi, po možnosti v realnem času.
	Taksi in prevoz na zahtevo (klic)	Odgovorni za izvajanje prevozov na zahtevo ali klic. Zagotavljajo informacije o lokaciji vozil, tarifah, omogočajo rezervacijo in plačilo.
	Podjetja za souporabo avtomobilov	Zagotavljajo floto vozil. Zagotavljajo informacije o vozilih, njihovi lokaciji, stroških ter omogočajo rezervacijo in plačilo.
	Podjetja za souporabo koles	Zagotavljajo floto koles, informacije o kolesih, njihovi lokaciji, stroških ter omogočajo rezervacijo in plačilo.
	Posredniške platforme za sopotništvo	Zagotavljajo informacije o prevozih in vozninah ter omogočajo rezervacijo.
Integracija in ponujanje storitev mobilnosti	Upravljavec/povezovalec MaaS	Odgovoren za organizacijo in združevanje ponudbe mobilnostnih storitev v okviru enotne platforme po sistemu »vse na enem mestu«. Zagotavlja celostno storitev mobilnosti, prilagojeno potrebam uporabnikov.
	Ponudnik MaaS (podjetje za izvajanje podpornih storitev)	Zagotavlja tehnologijo, ki omogoča ključne dele MaaS, kakor so mobilna aplikacija, spletno plačevanje in pomoč uporabnikom.
Končni uporabniki	Uporabniki	Uporabljajo aplikacijo MaaS za načrtovanje, rezervacijo in plačevanje svoje poti.

Avtorji so raziskali domače in tuje primere mobilnosti kot storitve in ugotovili, da obstajajo številne ovire pri vpeljavi. Pomemben izziv so birokratske ovire pri uvajanju sistema MaaS. Od zakonskih podlag je namreč odvisno, kako odprti in dostopni so podatki, kako poteka usklajevanje med različnimi ponudniki prometnih storitev in podobno. V sistemu MaaS lahko pride tudi do velikega razkoraka med javnim in zasebnim sektorjem, saj je prvi usmerjen zlasti v doseganje ciljev javnih politik, drugi pa v dobiček. Zelo pomembni sta vizija ter močna in dolgoročna politična podpora takšnim projektom, saj lahko država oziroma lokalne oblasti le tako privabijo investitorje in zasebne operaterje k sodelovanju [23].

Uvajanje sistema MaaS je praviloma povezano tudi z visokimi stroški organizacije in delovanja sistema. Zahtevni poslovni modeli, pogodbe, delovanje sistema, promocije in številni drugi stroški zahtevajo velike finančne vložke. Na drugi strani so finančna tveganja zelo visoka, saj so dobički le hipotetični, kar potencialne investitorje odvrača od sodelovanja. Ker je MaaS izjemno kompleksen sistem, ki zahteva usklajevanje in povezovanje številnih akterjev, so pomemben izziv tudi tehnične ovire. Te nastajajo predvsem na področju digitalne povezljivosti različnih podsistemov, na primer pri zagotavljanju in usklajevanju voznih redov različnih ponudnikov JPP v realnem času. Dosedanje izkušnje tudi kažejo, da so sistemi MaaS bolj uporabni in učinkoviti na območjih z visoko gostoto prebivalstva, torej na urbanih območjih. Uporabniki, ki se pogosteje odločajo za uporabo storitev MaaS, so praviloma tisti, ki živijo v bližini ponudbe prevozov. Ker sistemi MaaS praviloma vključujejo tudi ponudbo voženj z osebnimi avtomobili – na primer taksije, souporabo avtomobila ali platforme za prevozne storitve, kakor na primer Uber, obstaja nevarnost, da MaaS doseže nasprotni učinek od želenega in še poveča uporabo osebnih vozil [23].
MaaS odpira tudi pereča vprašanja glede digitalne in socialne izključenosti določenega dela prebivalstva. Nekateri ljudje oziroma družbene skupine se težje navajajo na digitalne tehnologije. MaaS temelji skoraj izključno na uporabi aplikacije ali spletne platforme. To je ključni komunikacijski kanal, ki zahteva znanje o uporabi aplikacije, dostop do interneta, lastništvo pametnega telefona ali računalnika. Pogosto uporaba MaaS zahteva tudi uporabo bančne kartice. Dostop do storitev MaaS torej ni samoumeven ter dostopen za vse sloje in segmente družbe enako [23].
Ker se naloga osredotoča na mikro mobilnost, smo si podrobneje pogledali podatke o souporabi koles in e-skirojev, ki jih omenjajo avtorji. Sistemi souporabe koles so sestavni del večine MaaS-ov po svetu, saj so v pomoč pri reševanju težav glede t. i. zadnjega kilometra, njihova vključitev pa je smiselna tudi zaradi spodbujanja aktivne mobilnosti. Potem ko je bil v Ljubljani leta 2011 uveden sistem BicikeLJ, so se v Sloveniji sistemi souporabe koles, zlasti po izdelavi občinskih celostnih prometnih strategij, precej razmahnili. Na začetku leta 2022 je bila namreč vsaj ena postaja samopostrežne izposoje koles že v 44 občinah. Avtorji predlagajo, da je v MaaS zaradi povečanja privlačnosti ponudbe pod določenimi pogoji smiselno vključiti tudi souporabo e-skirojev in drugih lahkih motornih vozil, ki so prav tako ena izmed rešitev za zadnji kilometer poti. V zadnjih letih se je njihova uporaba precej razširila, jo pa spremljajo prometnovarnostni in javnozdravstveni pomisleki. V Sloveniji je ta ponudba še razmeroma omejena; za zdaj deluje samo en ponudnik (GoGiro), ki deluje po sistemu prostega parkiranja, ki omogoča prevzem in vrnitev skirojev kjer koli na območju delovanja sistema. Deluje v Ljubljani, v manjšem obsegu pa tudi v nekaterih turističnih krajih [23].

Kot lahko vidimo, se v mobilnosti kot storitvi daje večji poudarek javnemu potniškemu prometu in souporabi vozil kot souporabi mikro vozil. Tudi sicer avtorji pravijo, da mora biti javni potniški promet hrbtenica MaaS, in celo predlagajo, da MaaS upravlja upravljalec javnega potniškega prometa ali njegov pogodbeni partner. Na koncu avtorji podajo tri predloge mobilnostnih paketov, ki so lahko jedro ponudbe MaaS in so prilagojeni skupinam uporabnikom z različnimi mobilnostnimi potrebami in potovalnimi navadami. Izpostavljamo Urbani paket ali »Meščanc«, ki je namenjen predvsem tistim, ki nimajo stalnega dostopa do osebnega vozila oziroma jim je pri izbiri potovalnega načina blizu večmodalnost. Lastnosti takšnega paketa so:

- mesečna naročnina;
- cena paketa je dobropis, ki se lahko uporabi za vse vključene storitve;
- dobropis se lahko prenese v naslednji mesec;
- jamstvo najnižje cene za JPP (seštevek enkratnih vozovnic ne sme preseči cene dnevne oziroma mesečne vozovnice na ravni mesta in države);
- jamstvo najnižje cene pri izposoji koles; popust pri souporabi vozil in taksi prevozih pri izbranih ponudnikih;
- vključitev souporabe e-skirojev pri izbranih ponudnikih [23].

Iz poročila in priporočil lahko ugotovimo, da v Sloveniji trenutno še nimamo pogojev za vzpostavitev sistema mobilnosti kot storitve, saj nam manjka učinkovit javni potniški promet. Hkrati je za uporabo MaaS in mikro mobilnosti treba poskrbeti za digitalno pismenost prebivalcev, saj se souporaba koles in skirojev večinoma upravljata prek mobilnih aplikacij ali računalnikov.

3.14 Primer trajnostne uporabe mikro mobilnosti v Šentjurju

Šarlah (2021) je v svojem diplomskem delu predstavil in analiziral primer uporabe mikro mobilnosti v Šentjurju. Kot primera dobre prakse je navedel mesti Zűrich in Berlin, kjer so se avtomobili umaknili kolesom in kjer imajo učinkovit sistem javnega potniškega prometa. Šarlah ugotavlja, da mikro mobilnost najpogosteje ni storitev, ki bi upravičila samo sebe. Poleg pozitivnih učinkov mikro mobilnosti omenja tudi negativne [24]. Pravi, da mikro vozila sicer sama ne ustvarjajo CO_2 med delovanjem, so pa povzročila velik izpust CO_2 med proizvodnjo. Hkrati mnoga mesta ugotavljajo, da se mikro vozila že po enem letu uporabe precej hitro obrabijo in uničijo, kar povzroča težave (in izpust CO_2) zaradi odlaganja mikro vozil med smeti. Omenja tudi varnost pešcev in voznikov. Kot primer navede ozke ulice mest, kjer se srečajo pešci z vozniki mikro vozil, ki vozijo z višjo hitrostjo kot se pešci premikajo. Pravi, da je problem še najbolj pereč za šibkejše člane družine, kot so majhni otroci in starejše osebe z okvaro sluha in vida. Taki udeleženci v prometu lahko v primeru nesreče dobijo tudi zelo hude poškodbe. Poleg tega pa parkiranje mikro vozil pomeni tudi oviro za pešce, kadar jih je na kupu več [24]. Šarlah med negativne učinke uporabe mikro mobilnosti šteje tudi zmanjšanje fizične aktivnosti, čeprav se mikro mobilnost običajno oglašuje kot način prevoza, ki poveča fizično aktivnost. Pravi, da se uporabniki zdaj namesto za hojo odločijo za uporabo električnih skirojev in koles, kar zmanjša njihovo fizično aktivnost namesto poveča. Tako kot smo že sami omenili, tudi avtor z raziskavo ugotavlja, da mora biti storitev mikro mobilnosti cenejša alternativa drugim načinom prevoza, da izpolni svoj potencial, ter da je pogosto omejena na tiste, ki so lastniki kreditnih kartic in imajo usvojene veščine digitalne pismenosti. Prav tako ugotavlja, da mora biti obstoj storitve mikro mobilnosti razširitev javnega potniškega prometa, saj sama po sebi ne opravičuje svojega obstoja [24].

Pri uvedbi mikro mobilnosti avtor omenja še en dejavnik, na katerega pogosto pozabimo – vreme. Vožnja z mikro vozili je omejena v dežju in večinoma ne pride v poštev v snežnih razmerah, medtem ko se pri visokih vročinah vozila hitreje obrabijo in so neudobna. To pomeni, da so mikro vozila bolj primerna za lokacije v zmernem podnebnem pasu, kar je že ena velika omejitev pri uvedbi [24].

V nalogi je avtor analiziral stroške implementacije mikro mobilnosti v občini Šentjur. Ker gre za manjši kraj, je implementacija težja kot v večjem mestu zaradi potreb in izzivov manjših mest. Med drugim je ugotovil, da naložba ekonomsko ni dobičkonosna, saj bodo prihodki od delovanja ob načrtovani rasti prihodkov presegli odhodke delovanja šele po 27 letih obratovanja. Skupaj s stroški izgradnje, torej uvedba takega sistema ekonomsko ni upravičena. Z vidika celovitih učinkov mikro mobilnosti se prav tako ni izkazalo, da je uvedba izključno pozitivna. Je pa kot pozitivno ocenil splošno spodbujanje kolesarjenja za povečanje fizične aktivnosti, kar je običajno samo en del mikro mobilnosti. Pravi, da lahko morda prav promocija tradicionalnega kolesarjenja izboljša zdravje prebivalstva [24].

3.15 Agencija za trajnostno dostavo v mestu New York

Zaradi velikega povečanja uporabe električnih koles, skirojev in mopedov za dostavo paketov in hrane so se v mestu New York v ZDA odločili v letu 2024 ustanoviti posebno agencijo za trajnostno dostavo. Naloge agencije bodo vključevale reguliranje storitev komercialne dostave, ki uporabljajo dvo- in trikolesna vozila. V mestu so prepričani, da so mikro vozila na električni pogon ključnega pomena za boj proti onesnaženem zraku in prometnim zastojem. Hkrati pa želijo regulirati tudi pravila za uporabo teh vozil na pločnikih in prometnih površinah, saj se prebivalci New Yorka pritožujejo nad divjo vožnjo in nevarnimi samovžigi baterij na teh vozilih. New York je znan po 24-urni dostavi vse dni v tednu in s tem ukrepom želijo še spodbuditi razvoj panoge, ki je že zdaj zelo dobičkonosna [25].

3.16 Umetna inteligenca v električnih mikro vozilih

Na sejmu CES 2024 so prikazali novosti na področju električnih mikro vozil, med njimi je bila najbolj izpostavljena uporaba umetne inteligence. Električna mikro vozila postajajo čedalje pametnejša in nekateri jih imenujejo kar pametna mikro vozila. Na trg so prišla električna kolesa, ki imajo vgrajen ChatGPT, ki se ga upravlja z glasom. Ta nam med vožnjo ponuja različne informacije, kot so prilagojeni plani treningov s kolesom ali izleti v okolici. Na voljo so tudi že električna kolesa z dvojno pogonsko baterijo, gorska električna kolesa in kolesa z naprednim sistemom zaklepanja. Velik problem namreč predstavljajo tatvine koles. Velik poudarek se daje tako preprečevanju kot zaznavanju tatvin. Moderna električna kolesa imajo vgrajeno zavoro na pestu in vgrajeno sledenje GPS v realnem času [26].
Podjetje Segway-Ninebot je predstavilo pametno električno kolo z aktivnim zaznavanjem okolja, ki spremlja prometne razmere in vedenje kolesarja in sprejema odločitve, podprte z umetno inteligenco, na primer prilagodi izhodno moč baterije ter vklopi ali izklopi sprednjo luč [26].

4 RAZPRAVA

Iz raziskav in izračuna ogljičnega odtisa smo ugotovili, da uporaba avtomobila z notranjim izgorevanjem za kratke vožnje, kadar se vozimo večinoma sami, ni okolju prijazna. Zaradi trenutnih in prihodnjih podnebnih sprememb, ki nas še čakajo, moramo najti bolj primerne načine mobilnosti v Sloveniji.

Ugotovili smo, da je mikro mobilnost okolju bolj prijazna alternativa vozilom na notranje izgorevanje, prav tako pa zmanjšuje gnečo na cestah. Kljub vsem prednostim (in nekaterim slabostim) pa je še vedno primerna in izvedljiva samo v urbanih okoljih. Ker ima Slovenija zaradi razpršene poseljenosti več ruralnih območij kot urbanih, se mikro mobilnost uporablja v glavnem v nekaj večjih mestih in na počitnicah (npr. električni skiro). Za ruralna okolja mikro mobilnost ni tako primerna zaradi večjih razdalj med lokacijami pa tudi zaradi slabše prometne infrastrukture, kot so pomanjkanje pločnikov in kolesarskih stez ter neurejene bankine cest.

Kot že rečeno, ima električna mikro mobilnost kar nekaj prednosti, njena največja slabost pa je proizvodnja električnih baterij. Ta povzroča velike izpuste in ni okolju prijazna, saj se sestavine za baterije pridelujejo včasih tudi na zelo krut način. Prav tako je problematično odlaganje baterij, ki bo kmalu postalo še večja težava kot proizvodnja, saj je že zdaj na trgu ogromno mikro vozil z električno baterijo, ki jih bo v naslednjih nekaj letih treba obnoviti ali zavreči. Trenutno še ni veliko ponudnikov, ki bi obnavljali električne baterije, dogajajo pa se tudi nevarne eksplozije baterij, ki so izpostavljene visokim temperaturam in mrazu. Predvidevamo torej, da se bo o trajnostni proizvodnji in odlaganju baterij ter njihovi ponovni uporabi v naslednjih letih še veliko govorilo.

Veliko je bilo že povedanega tudi o varnosti udeležencev v cestnem prometu – tako pešcev kot voznikov mikro električnih vozil. Nekatere raziskave kažejo, da električna mikro vozila ne povzročajo več in težjih nesreč v primerjavi s kolesarji, vendar hkrati priznavajo, da se številne nesreče z mikro vozili ne prijavijo, razen kadar gre za težjo poškodbo. Zagotovo pa bo treba posvetiti veliko časa izobraževanju uporabnikov teh vozil in pešcev glede vedenja v prometu. Verjetno bo spet zelo pomembna zakonodaja, ki bo določala uporabo čelad in drugih varnostnih elementov.

Naslednji pomislek, o katerem doslej v Sloveniji ni bilo veliko govora, je glede parkirnih mest. Čeprav so električna mikro vozila manjša, vseeno zahtevajo parkirno mesto, kjer lahko vozniki varno pustijo svoje vozilo in pri tem ne ovirajo mimoidočih. Trenutno mikro vozila puščajo na pločnikih in ob stavbah, tam pa so lahko napoti mimoidočim in se lahko prevrnejo ter s tem poškodujejo še druga vozila. Verjetno jim bo treba načrtovati in zgraditi ustrezna parkirišča, kot jih imamo za kolesa.

Tudi v urbanih okoljih je mikro mobilnost še vedno povezana z javnim potniškim prometom. Vse raziskave in strategije poudarjajo, da mikro mobilnost ne more zaživeti, če javni potniški promet ni učinkovit in dovolj razvejan. V idealnem primeru bi lahko na primer oseba iz Krškega prišla do Ljubljane z vlakom, tam pa si izposodila električni skiro ali kolo in se odpeljala do končne lokacije, nato pa vrnila do vlaka. Žal v Sloveniji medkrajevni javni potniški promet ni dovolj pogost in učinkovit, da bi ljudem omogočal tako mobilnost, zato se tak način potovanja po našem mnenju še ne bo kmalu prijel, razen za osebe, ki tudi živijo znotraj urbanega okolja in lahko uporabljajo električno mikro mobilnost od svojih vrat do končne lokacije.

Kot za vsako bolj napredno orodje, bomo uporabniki električne mikro mobilnosti morali razvijati tudi digitalno pismenost. Brez aplikacije na mobilnem telefonu si danes ni možno izposoditi električnega mikro vozila. Drugače je za lastna mikro vozila, vendar so tehnološki dodatki tudi na teh danes povezani z mobilnimi aplikacijami, recimo za merjenje prevožene razdalje, navigacijo in podobno. Uporabniki brez pametnega telefona in predznanja bodo električna mikro vozila čedalje težje uporabljali. Hkrati se z uporabo mobilnih aplikacij na mikro vozilih zmanjša tudi varnost v cestnem prometu, saj vozniku odvrača pozornost od dogajanja.
V tujini obstaja že ogromno ponudnikov električne mikro mobilnosti, saj to tudi mesta večja in imajo več prebivalcev, torej večji nabor uporabnikov. Zna pa se zgoditi, da trg postane nasičen s preveč ponudniki, zaradi česar bo spet težava, da bo za vsakega ponudnika treba namestiti drugo mobilno aplikacijo. Zaradi tega bodo uporabniki porabili več časa za preklapljanje med operaterji in bodo prej opustili vožnjo z mikro vozili in sedli v avtomobil. V Evropi je sicer že v uporabi mobilna aplikacija, ki povezuje ponudbo številnih operaterjev mikro mobilnosti.

Na koncu pa omenimo še zelo vsakdanji razlog, zaradi katerega je uporaba mikro mobilnosti omejena. To je vreme. V nasprotju z avtomobilom in avtobusom je vožnja z električnim skuterjem pozimi in po snegu ne samo neprijetna, ampak tudi nevarna. Poleti voznike mikro vozil med vožnjo hladi veter v laseh, vendar so baterije zaradi visokih temperatur manj vzdržljive in znajo tudi eksplodirati. Idealni pogoji za uporabo električnih mikro vozil so torej zmerne temperature s čim manj odkloni, kar pa je za naše podnebje težko doseči. Glede na podnebne spremembe zadnjih let je take pogoje povsod po svetu težko najti, zato bo baterije treba pogosteje menjati in jih bo več treba obnoviti ali zavreči. Tukaj pa smo spet pri problemu okoljskega odtisa.

5 SKLEP

Kot smo že večkrat omenili, električna mikro vozila res niso popolnoma okolju prijazna, saj v fazi pridobivanja surovin in proizvodnje povzročajo številne negativne vplive na okolje in ljudi. Kljub temu pa v urbanih okoljih pripomorejo k boljšemu zraku, uporabnikom pa omogočajo bolj brezskrbno vožnjo brez čakanja v prometnih zamaških ter jim omogočajo še gibanje na prostem. Ugotovili pa smo tudi, da električna mikro mobilnost sama ne zmore rešiti vseh prometnih težav v urbanih okoljih. Poleg primerne strategije za uvedbo elektro mikro mobilnosti je treba tako poskrbeti tudi za učinkovit sistem javnega potniškega prometa, ki dopolnjuje električno mikro mobilnost. Hkrati je treba določiti pravila glede uporabe električnih vozil mikro mobilnosti (vožnja po kolesarskih stezah ali cestah, parkiranje na pločnikih) in varnosti uporabnikov teh vozil (uporaba čelade) ter zagotoviti tudi digitalno podporo tako starejšim kot mlajšim uporabnikom (aplikacije), da se bo električna mikro mobilnost prijela in razširila. Ne smemo pa pozabiti na strategijo odlaganja odsluženih baterij, ki so zaradi svojih sestavnih delov nevarni odpadki.

Ljudje, ki danes živijo v urbanih okoljih, že precej dobro poznajo električno mikro mobilnost in njene prednosti in slabosti. Žal pa so njene prednosti še vedno bolj omejene na urbana okolja kot ruralna, kar pa se bo tudi v prihodnosti spremenilo. Na trg namreč že prihajajo tudi električna mikro vozila, ki so namenjena tudi slabšim prometnim pogojem izven mest. Za učinkovito uvedbo električne mikro mobilnosti v slovenskih urbanih okoljih bo zelo pomembno, da se povežejo in uskladijo različni organi in zasebni ponudniki na lokalni in nacionalni ravni. Številna mesta po svetu dokazujejo, da je uvedba možna in da je to ena od dolgoročnih rešitev za trajnostno mobilnost, boljši zrak in dobro počutje prebivalcev urbanih okolij.

LITERATURA

[1] Borzen, d.o.o.. (n.d.). »Trajnostna energija.« *Borzen* [splet]. Dosegljivo: https://www.trajnostnaenergija.si/Trajnostna-energija/Ohranite-okolje-%C4%8Disto/Oglji%C4%8Dni-odtis. [28. 4. 2023].
[2] *Uredba (EU) 2021/1119 Evropskega parlamenta in Sveta z dne 30. junija 2021 o vzpostavitvi okvira za doseganje podnebne nevtralnosti in spremembi uredb (ES) št. 401/2009 in (EU) 2018/1999 (evropska podnebna pravila).* Uradni list Evropske unije, št. 64, str. 1–18.
[3] Evropska komisija. (14. 12. 2021). »Questions and Answers: European Urban Mobility Framework.« *Evropska komisija* [splet]. Dosegljivo: https://ec.europa.eu/commission/presscorner/detail/en/qanda_21_6729. [28. 4. 2023].
[4] R. L. Abduljabbar, S. Liyanage in H. Dia, »The role of micro-mobility in shaping sustainable cities: A systematic literature review.« *Transportation research part D: transport and environment*, vol. 92, 2021.
[5] B. Sengül in H. Mostofi, »Impacts of E-Micromobility on the Sustainability of Urban Transportation—A Systematic Review,« Applied Sciences, vol. 11, št. 13, 2021.
[6] MIT. (n.d.). »Unparking – A project by MIT Senseable City Lab.« *MIT SCL* [splet]. Dosegljivo: https://senseable.mit.edu/unparking/. [30. 10. 2023].
[7] OECD. (17. 2. 2020). »Safe Micromobility.« *International Transport Forum* [splet]. Dosegljivo: https://www.itf-oecd.org/safe-micromobility. [3. 11. 2023].
[8] A. G. Olabi et al., »Micromobility: Progress, benefits, challenges, policy and regulations, energy sources and storage, and its role in achieving sustainable development goals,« International Journal of Thermofluids, št. 17, 2023.
[9] Umanotera. (n.d.). »Izračunajte svoj ogljični odtis.« Umanotera [splet]. Dosegljivo: https://www.umanotera.org/izracunaj-svoj-ogljicni-odtis/. [15. 11. 2023].
[10] EIT Urban Mobility. (n.d.). »Mobility Innovation Marketplace.« EIT Urban Mobility [splet]. Dosegljivo: https://marketplace.eiturbanmobility.eu/. [28. 4. 2023].
[11] YUP Mobility. (n.d.). »Regenerating mobility.« YUP Mobility [splet]. Dosegljivo: https://yupmicromobility.com/. [3. 11. 2023].
[12] A.D Knight. (n.d.). »A.D Knight. Enhancing Road Safety and Reducing Congestion.« A.D Knight [splet]. Dosegljivo: https://www.ad-knight.com/. [3. 11. 2023].
[13] Jonna. (n.d.). »A bike that always works. Bike as a subscription.« Jonna [splet]. Dosegljivo: https://jonnabike.se/?lang=en. [3. 11. 2023].
[14] Bruntor. (n.d.). »Cargo Scooter.« Bruntor [splet]. Dosegljivo: https://bruntor.com/. [3. 11. 2023].
[15] Nudgd. (n.d.). »Smart nudges mobility - establishes smart travel habits.« Nudgd [splet]. Dosegljivo: https://nudgd.io/smartnudgesmobility/. [3. 11. 2023].
[16] Rastel.io. (n.d.). »Are you looking for a safe and accessible solution for bicycle parking?«Rastel.io [splet].

Dosegljivo: https://www.rastel.io/en. [3. 11. 2023].

[17] Social Tech Projects ApS. (n.d.). »AI-driven bike lanes assessment as a service.« Road System [splet]. Dosegljivo: https://roadsystem.io/. [3. 11. 2023].

[18] Levox. (n.d.). »Energía ilimitada. En segundos.« Levox [splet]. Dosegljivo: https://itslevox.com/. [3. 11. 2023].

[19] Cycling Embassy of Denmark. (n.d.). »Welcome to Cycling Embassy of Denmark.« Cycling Embassy of Denmark [splet]. Dosegljivo: https://stateofgreen.com/en/solution-providers/cycling-embassy-of-denmark/. [3. 11. 2023].

[20] Sekretariatet for Supercykelstier. (n.d.). »Cycle Superhighways.« Super Cykelstier [splet]. Dosegljivo: https://supercykelstier.dk/english/. [3. 11. 2023].

[21] Newton-Rider. (n.d.). »Home.« Newton-Rider [splet]. Dosegljivo: https://newton-rider.com/. [3. 11. 2023].

[22] M. Gabrovec et al. (26. 4. 2022). »Zasnova mobilnosti kot storitve v Sloveniji.« Care4Climate.si [splet]. Dosegljivo: https://www.care4climate.si/_files/1668/Zasnova_MaaS_koncna.pdf. [28. 4. 2023] .

[23] M. Gabrovec et al., Zasnova mobilnosti kot storitve v Sloveniji. Ljubljana: Ministrstvo za okolje in prostor, 2022.

[24] A. Šarlah, Primer trajnostne uporabe mikro mobilnosti v manjšem kraju. Maribor: Ekonomsko-poslovna fakulteta, 2021.

[25] J. Surico. (24. 1. 2024). »New York City Set to Launch ‘Department of Sustainable Delivery’.« Bloomberg [splet]. Dosegljivo: https://www.bloomberg.com/news/articles/2024-01-24/nyc-launches-city-office-to-regulate-e-bike-delivery-boom. [22. 12. 2023].

[26] European Institute of Innovation and Technology. (21. 9. 2021). »Living lab e-micromobility -MOBY Guideline of best practices, and results of e-micro mobile integration potentials.« EIT [splet]. Dosegljivo: https://eit.europa.eu/library/living-lab-e-micromobility-moby-guideline-best-practices-and-results-e-micro-mobile. [30. 1. 2024].

Trajnostno 3D tiskanje: predelava plastenk v filament

Matic Morgan[1]

[1]Inštitut Jožef Stefan, Jamova cesta 39, 1000 Ljubljana, Slovenija
E-naslov: matic.morgan@gmail.com

***Povzetek**: S povečano ozaveščenostjo o vplivu plastičnih odpadkov na planet nenehno iščemo nove in inovativne načine za reševanje problematike ogromne količine odpadne plastike za enkratno uporabo. Ena takšnih nekonvencionalnih rešitev je uporaba odpadlih plastenk za proizvodnjo filamenta za 3D tiskanje. Ustvaril in preizkusil sem preprost postopek preoblikovanja PET plastenk, ki se običajno uporabljajo za prodajo pijač, v uporaben filament za 3D tiskanje. Princip delovanja je zelo enostaven: sprva plastenko segrejemo, da postane njena oblika čim bolj simetrična. Nato jo razrežemo v trak. Trak nato vlečemo skozi segreto šobo ustrezne velikosti, da se preoblikuje v filamenta. V duhu okoljevarstva sem stremel po tem, da projekt deluje z uporabo čim več odvečnih elektronskih in mehanskih delov. Stroj sestavljajo grelni blok 3D tiskalnika z ustreznim grelcem in termistorjem, modificirana šoba, NEMA17 koračni motor in nekaj 3D natisnjenih zobnikov. Komplementarna elektronika vključuje Arduino Nano, krmilnik za koračne motorje in katerikoli 12V napajalnik, ki lahko zagotavlja vsaj 50 vatov. Vse je povezano z doma zasnovanim tiskanim vezjem in programom, ki nadzoruje temperaturo in upravlja motor. Ena 1,5-litrska plastenka se predela v približno 45 minutah. Preizkusi kažejo, da je material primerljivo močan s PETG, z manjšimi prilagoditvami nastavitev tiskanja.*

***Ključne besede:** recikliranje, FDM tiskanje, 3D tiskanje, ekologija, DIY*

***Razvrstitev:** Strokovni prispevek*

1 UVOD

Po več desetletjih pospešenega vzbujanja ekološke zavesti smo vedno znova pretreseni nad neodgovornim in neiskrenim ravnanjem odgovornih entitet v zvezi z gospodarjenjem z odpadki [1] [2]. Zemljani vsako leto uporabimo 13 milijard plastenk in jih le 9% recikliramo, kar predstavlja milijardo dolarjev finančnih izgub [3] [4]. Naraven odziv na tako situacijo je, da se ljudje poskusijo znajti sami, da njihovo razočaranje ne zavisi od situacij na katere nimajo vpliva. Raba 3D tiskalnika za pomoč pri izdelavi uporabnih in nadomestnih delov za vsakdan, kot tudi za profesionalno rabo se je v zadnjem desetletju izkazala za izjemno uporabno in samozadostno rešitev [3]. Sledilo je še vprašanje rabe plastike – ali obstaja tudi za to okoljsko odgovorna rešitev? Izkazalo se je, da so plastenke za vode in sokove izdelane iz polietilen tereftalat (PET), ki je kemijsko podoben enemu najpopularnejših materialov za 3D tisk – polietilen tereftalat glikol (PETG).

Namenili smo se izdelati napravo, s katero bi odpadne plastenke iz PET predelali v uporaben filament za 3D tiskalnik. Želeli smo si tudi, da bi bil dizajn naprave čimbolj enostaven in bi bila sestavljena iz vseh enostavno dobavljivih kosov elektronike, da jo lahko vsakdo s primernim znanjem podvoji. Cilj je seveda tudi to, da so iz doma narejenega filamenta natisnjeni izdelki primerljive kvalitete natisnjenim s kupljenim filamentom.

Ta ideja ni nova [4] [5] [6] [7]. Primanjkljaj, ki ga tu izboljšujemo je pomanjkanje enostavnosti in ekonomičnosti, ker že obstoječe rešitve pogosto potrebujejo specifično, drago ali pa nepotrebno komplicirano opremo, kot so namenska tiskana vezja [4], namensko elektroniko in načrte [8], kar oboje drastično podraži končni izdelek.

2 METODE

Na podlagi teh smernic smo si zamislili sledeči dizajn: najprej se plastenko nareže na enakomeren, nekaj milimetrov debel trak, kot kaže Slika 1. Ta trak se vstavi v prilagojeno šobo za 3D tiskalnik z luknjo velikosti 1,7 mm. Šoba je vstavljeno v grelni blok 3D tiskalnika z grelcem in termistorjem. Vstavljen trak plastike nato pričvrstimo na zobniški sistem, preko katerega koračni motor vleče trak skozi šobo. Mikrokrmilnik Arduino Nano bo deloval kot PID krmilnik za vzdrževanje temperature šobe in krmilnik za koračni motor.

Slika 1: rezalnik (levo) in narezan trak (desno)

2.1 Nadzor temperature šobe

Uporabili smo generičen aluminijast grelni blok 3D tiskalnika z 12-voltnim, 40-vatnim keramičnim grelcem in 100 kΩ NTC termistorjem. Šobo smo povrtali z 1,7-milimetrskim svedrom, saj ciljamo na filament, ki je primerljiv 1,75-milimetrskemu filamentu. Za lažje drsenje plastičnega traku smo povrtali tudi aluminijast blok skozi katerega potuje trak v šobo.

Za merjenje temperature z mikrokrmilnikom moramo vezati NTC v delilnik napetosti, saj s tem lineariziramo njegov odziv na temperaturo, ki je sicer eksponenten. Dobro vrednost upora za delilnik napetosti za 100 kΩ NTC dobimo z enačbo $R = \sqrt{R\_max \;-\; R\_min}$, kjer je R_{max} vrednost NTC pri minimalni temperaturi, ki jo želimo izmeriti in R_min vrednost NTC pri maksimalni temperaturi, ki jo želimo izmeriti. Glede na to, da se PET topi pri okoli 260 °C smo izbrala 4,7 kΩ upor. Z 10-bitno resolucijo analogno-digitalnega pretvornika izbranega mikrokrmilnik [4] je natančnost s katero lahko merimo temperaturo v intervalih velikosti 0,2 °C, kar je več kot dovolj natančno za naše potrebe. Naredili smo umeritveno krivuljo, kjer smo za temperaturno referenco vzeli spajkalnik z nastavljivo temperaturo, na katerega smo prilepili NTC.

V tandemu z merilcem temperature deluje grelec. Skupaj tvorita enostaven PID sistem lovljenja temperaturnega ravnotežja. V ta namen moramo grelec nadzirati digitalno. Z mikrokrmilnikom to najlažje izvedemo z pulzno-širinsko modulacijo. Izhod mikrokrmilnika torej uporabimo za preklapljanje MOSFET-a, ki bo prižigal in ugašal napetost na grelcu. Tok skozi mikrokrmilnik omejimo z uporom ter na vrata MOSFET-a dodam še upor, ki pripne napetost na 0 V, da se MOSFET zanesljivo izključi, ko je mikrokrmilnik izključen. Izbrali smo IRFZ44N, ker se ga lahko vklopi in izklopi s 5-voltnim signalom iz mikrokrmilnika.

2.2 Nadzor koračnega motorja

Koračni motor, ki bo vrtel zobnike za vlečenje filamenta, nadziramo z gonilnikom za koračne motorje A4988, ker je enostaven in cenovno ugoden ter zmogljiv znotraj naših zahtev. Večine njegovih funkcij sploh ne bomo koristili: zvežemo le napajanje za motor, v našem primeru 12 V, napajanje za gonilnik, 5 V, ter STP nogico z poljubno nogico na mikrokrmilniku. Na nogici za napajanje vežemo še elektrolitska kondenzatorja v izogib težavam zaradi prehodnih pojavov. Ostale nogice so zvezane med sabo ali pa na 5 V, kot kaže Slika 2.

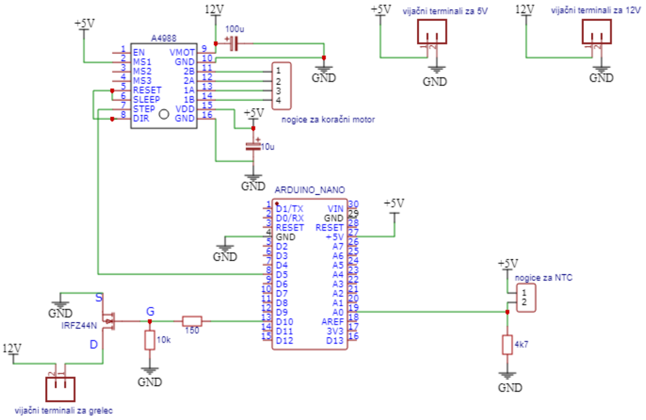

Slika 2: shema vezja

2.3 Napajanje

Uporabili smo napajalnik za stacionarni računalnik. Tudi najslabši napajalniki za stacionarne računalnike zmorejo zagotoviti več, kot 100 vatov moči in ponujajo 5 V in 12 V priključke, kar potrebujemo. Za si še dalje olajšati delo smo uporabili komercialni priključek [5], ki 24-pinski računalniški priključek pretvori v vijačne terminale za vse potrebne napetosti, ter doda stikalo s katerim napetost priključimo in izključimo.

2.4 Strojna oprema

Za čim manj preglavic smo uporabili natisnjene zobnike iz odprtokodnega projekta [6]. Vstavili smo jih med dva kosa lesa ter vse privili z navojnimi palicami in maticami. Motor je vpet v natisnjen nosilec [7]. Vsi deli so natisnjeni iz PLA s 30 % polnilom. Zaključena naprava z vsemi deli je na Sliki 3.

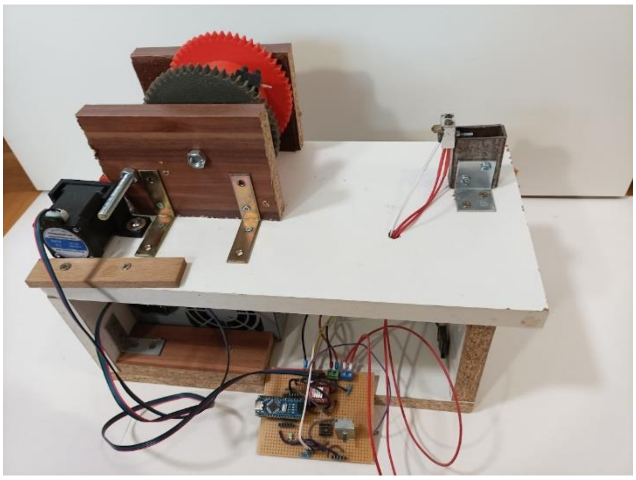

Slika 3: končni izdelek

2.5 Programska oprema

Program, ki se izvaja na Arduino mikrokrmilniku je napisan v C++. Dostopen je na Github odložišču www.github.com/MaticMorgan/petdaktil, vključno s komplementarnim gradivom, ki ni objavljeno tukaj. Program je sestavljen iz dveh ključnih delov: PID temperaturnega krmilnika in krmiljenja motorja.

PID krmilnik uporablja knjižnico *PID_v2* [12], pri kateri moramo nastaviti le vhod in izhod za PID ter temperaturo in seveda P, I in D parametre. Ker je PID odvisen od strojne opreme in okolice naprave moramo biti pozorni pri vsakršni spremembi oblike in materialov grelca ter njegove okolice.

Za krmiljenje koračnega motorja smo uporabili popularno knjižnico *AccelStepper* [13] z vsemi standardnimi nastavitvami, saj potrebujemo le vrtenje motorja v vedno isto smer, s konstantno hitrostjo.

V izogib kakršnimkoli motnjam delovanja programa, ki je zaradi zahtev AccelStepper knjižnice časovno zelo intenziven, so vse komunikacije z računalnikom v programu zakomentirane. Uporabljene so bile zgolj za razhroščevanje programa za nastavitev parametrov PID, ciljne temperature ter hitrosti motorja.

3 REZULTATI IN DISKUSIJA O REZULTATIH

Z ročnim nastavljanjem spremenljivk in sprotnim poskušanjem tiskanja smo prišli do uspešnih rezultatov. 1,5-litrska plastenka se predeluje nekje 1 uro pri temperaturi šobe 225 °C. Nastali filament ima v svoji sredini votlino. Debel je 1,7 mm ± 0,05 mm.

Testno tiskanje je bilo narejeno na predelanem Ender 3. Uporablja originalen hotend z boljšim hlajenjem, *Capricorn* Bowdenovo cev [8], *BTT SKR mini E3* [8] matično ploščo in *Klipper* [9]. Zaradi manjšega premera in votline v filamentu smo morali pri tiskanju povečati volumetrični pretok materiala. V programu Cura Slicer se ta nastavitev imenuje »Flow«. Povečati smo ga morali na 130 %. Temperatura tiskanja je bila 260 °C s temperaturo podlage 80 °C. S testnim tiskalnikom smo uspešno tiskali s temi nastavitvami do hitrosti 100 mm/s. Za hitrejše tiskanje bi potreboval šobo z večjim volumetričnim pretokom. Hlajenje tiskanine je bilo 20 %.

Natisnjeni izdelki so primerljivo lepi izdelkom natisnjenim iz kupljenega PETG [8]. Kot funkcionalni deli tudi delujejo enako uspešno kot običajen PETG [9].

4 ZAKLJUČEK

Glede na začetne želje je bil projekt uspešen. Z orodjem in znanjem povprečnega elektronskega navdušenca je mogoče izdelati napravo, ki pretvarja plastenke v uporaben filament s katerim se lahko tiska povsem operativne kose. Zaradi minimalističnega pristopa ter domače izdelave vseh potrebnih gradnikov se cena ne dvigne nad nekaj deset evrov. Iz vsake plastenke nastane do 15 gramov uporabnega filamenta, iz približno 70-ih plastenk torej pridobimo kilogram filamenta, ki se po kakovosti primerja s filamenti, ki stanejo od 20 €/kg dalje [22] [23].

V bodoče bi bilo potrebno narediti način za efektivno spajanje nastalih kosov filamentov. Trenutno nastanejo kosi z maso do 15 gramov, tako da je pogosto potrebno tiskanje ustaviti in zamenjati kos filamenta. Enostavno segrevanje in stiskanje koncev filamentov enega ob drugega ni zanesljivo spajanje, spoj je prešibak in poči ob stiku s pogonskim zobnikom.

LITERATURA

[1] J. Crowe, "www.waster.com," Waster, 30 11 2023. [splet]. Dosegljivo: https://waster.com.au/australia-waste-export/. [11 9 2024].

[2] K. Kapoor, "www.reuters.com," Reuters, 28 2 2022. [splet]. Dosegljivo: https://www.reuters.com/business/environment/exclusive-after-much-praised-waste-export-ban-australia-under-fire-shipping-2022-02-28/. [11 9 2024].

[3] "www.jerseyislandholidays.com," 2020. [splet]. Dosegljivo: https://www.jerseyislandholidays.com/plastic-bottle-pollution-statistics/.

[4] "www.habitsofwaste.org," [splet]. Dosegljivo: https://habitsofwaste.org/call-to-action/plastic-bottles/.

[5] T. J. Snyder, M. Andrews, M. Weisloge, P. Moeck, J. Stone-Sundberg, D. Birkes, A. L. Madeline Paige Hoffert, J. Morrill, O. Fercak, S. Friedman, J. Gunderson, A. Ha, J. McCollinster, Y. Chen and J. Graft, "3D Systems ' Technology Overview and New Applications in Manufacturing, Engineering, Science, and Education," *3D Printing and Additive Manufacturing,* 2014.

[6] Electronoobs, "https://electronoobs.com/eng_arduino_tut174.php," [splet]. Dosegljivo: https://electronoobs.com/eng_arduino_tut174.php. [13 9 2024].

[7] "https://www.instructables.com/Turn-PET-Bottles-Into-3D-Printer-Filament/," [splet]. Dosegljivo: https://www.instructables.com/Turn-PET-Bottles-Into-3D-Printer-Filament/. [13 9 2024].

[8] "https://petamentor.com/," [splet]. Dosegljivo: https://petamentor.com/. [13 9 2024].

[9] R. Yauri, H. Bermeo, A. Leon and O. Llerena, "Processing System for Plastic Bottle to Obtain Polyethylene Terephthalate Filament in 3D Printers," *WSEAS Transactions on Systems and Control,* vol. 19, 2024.

[10] I. Tylman, "www.cults3d.com," 8 10 2022. [splet]. Dosegljivo: https://cults3d.com/en/3d-model/tool/pet-machine-make-your-own-filament-from-plastic-bottles-at-home-tylman_design-2.

[11] Atmel Corporation, *Atmega328P,* 2015.

[12] D. Prototypes, "www.dangerousprototypes.com/," 15 6 2016. [splet]. Dosegljivo: http://dangerousprototypes.com/docs/ATX_Breakout_Board. [13 9 2014].

[13] Electronoobs, "www.electronoobs.com," 29 7 2022. [splet]. Dosegljivo: https://electronoobs.com/eng_arduino_tut174_stl1.php. [13 9 2024].

[14] ImHuman, "www.thingiverse.com," 11 4 2016. [splet]. Dosegljivo: https://www.thingiverse.com/thing:1482013. [13 9 2024].

[15] M. Ignatenko, "https://github.com/imax9000/Arduino-PID-Library," [splet]. Dosegljivo: https://github.com/imax9000/Arduino-PID-Library. [15 9 2024].

[16] P. Wasp, "https://github.com/waspinator/AccelStepper," [splet]. Dosegljivo: https://github.com/waspinator/AccelStepper. [15 9 2024].

[17] "https://www.captubes.com," [splet]. Dosegljivo: https://www.captubes.com/#!/1-Meter-XS-Low-Friction-1-75mm-Bowden-Tubing/p/82190682/category=23214267. [13 9 2024].

[18] BigTreeTech, "https://github.com/bigtreetech/BIGTREETECH-SKR-mini-E3," [splet]. Dosegljivo: https://github.com/bigtreetech/BIGTREETECH-SKR-mini-E3.

[19] "https://www.klipper3d.org/," [splet]. Dosegljivo: https://www.klipper3d.org/. [13 9 2024].

[20] "www.azurefilm.com," AzureFilm, 2024. [Online]. Dosegljivo: https://azurefilm.com/sl/3d-filamenti/petg-filamenti/. [13 9 2024].

[21] C. Kitchen, "www.youtube.com," 22 1 2022. [splet]. Dosegljivo: https://www.youtube.com/watch?v=N06FWr06iOI. [13 9 2024].

[22] "www.azurefilm.com," [splet]. Dosegljivo: https://azurefilm.com/sl/?s=PETG&post_type=product&lang=sl.

[23] "www.3djake.com," [splet]. Dosegljivo: https://www.3djake.com/3d-printer-filaments/pet-filament.

Pregled trga elektrificiranih osebnih vozil

Mitja Muhič[1]

[1]*Šolski center Novo mesto Višja strokovna šola, Šegova ulica 112, 8000 Novo mesto, Slovenija*
E-naslov: mitja.muhic@sc-nm.si

Povzetek: *V zadnjih desetih letih smo priča elektrifikaciji osebnih vozil z namenom bolj trajnostne mobilnosti. Elektrifikacija naj bi zmanjšala izpuste vozil, tako ogljikovega dioksida, ki dokazano povzroča globalno segrevanje našega planeta, kot tudi ostalih škodljivih izpustov kot so dušikovi oksidi NOx in tudi trdni delci, ki so posledica izgorevanja fosilnih goriv. Prispevek vsebuje pregled prodaje elektrificiranih osebnih vozil med katere sodijo priključni hibridi – PHEV (plug-in hybrid electric vehicle) in popolnoma električna – BEV (battery electric vehicle) vozila. V prispevku je predstavljena rast prodaje elektrificiranih osebnih vozil po različnih regijah EU, ZDA in Kitajske v zadnjem desetletju ter preteklem in tekočem letu. Predstavljena je razpoložljivost in cenovna dostopnost elektrificiranih vozil ter analiza trendov, katere vrste – segmenti elektrificiranih vozil so v porastu. Predstavljena je tudi problematika porabe surovin kot so litij, nikelj, kobalt in mangan ter problematika velikih in težkih baterij in problematika dosega in polnjenja.*

Ključne besede*: trajnostna mobilnost, elektrifikacija osebnih vozil, priključni hibrid – PHEV, elektrificirana vozila – BEV, prodaja elektrificiranih vozil*

Razvrstitev*: Strokovni prispevek*

1 UVOD

Prejšnje leto je bilo skoraj vsako peto novo prodano vozilo elektrificirano. Prodaja elektrificiranih vozil je v zadnjem desetletju iz nič narasla na 14 milijonov. 95 % prodaje predstavljajo Kitajska, Evropa in ZDA (Slika 1 in 2). Leta 2023 je bilo registriranih skoraj 14 milijonov novih elektrificiranih vozil, s čimer se je njihovo skupno število na cestah povzpelo na 40 milijonov. Prodaja elektrificiranih vozil je bila leta 2023 za 3,5 milijona večja kot leta 2022, kar je 35-odstotno povečanje. To je več kot šestkrat več kot leta 2018, kar je samo 5 let prej. V letu 2023 je bilo več kot 250 000 novih registracij na teden, kar je več kot letno skupno število v letu 2013. Elektrificirani avtomobili so leta 2023 predstavljali približno 18 % vseh prodanih vozil, kar je več kot leta 2022 (14 %) in veliko več kot leta 2018 (2 %). Ti trendi kažejo, da rast ostaja močna in da trgi elektrificiranih vozil dozorevajo. Baterijski elektrificirani avtomobili so leta 2023 predstavljali 70 % delež elektrificiranih vozil [1].

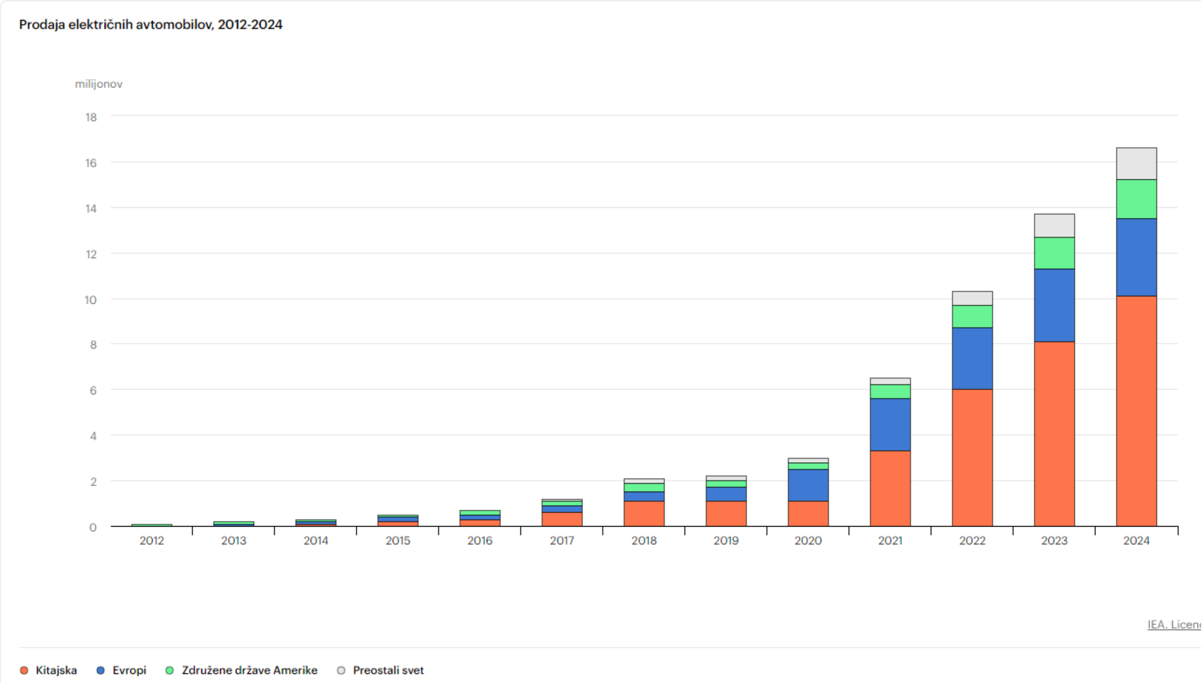

Slika 1: Globalna prodaja elektrificiranih vozil po regijah od 2012 do 2014 [1]

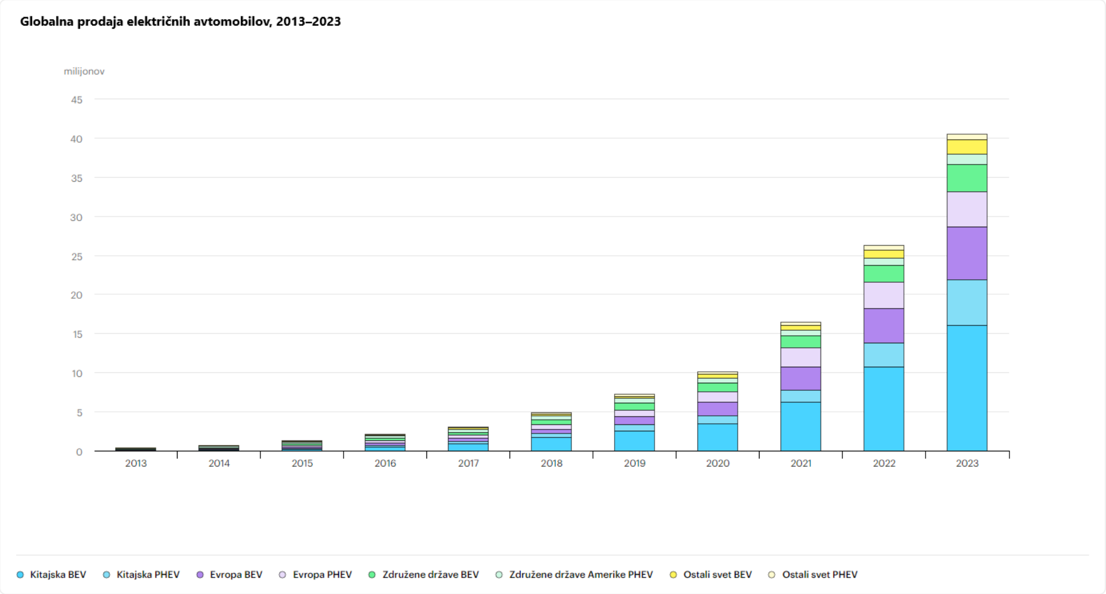

Slika 2: Globalna prodaja elektrificiranih BEV in PHEV vozil od 2013 do 2023 [1]

Prodaja elektrificiranih vozil na svetovni ravni narašča vendar ostaja skoncentrirana le na nekaterih večjih trgih. Leta 2023 je bilo nekaj manj kot 60 % registracij novih elektrificiranih vozil v Ljudski republiki Kitajski (v nadaljevanju Kitajska), slabih 25 % v Evropi in 10 % v Združenih državah Amerike – kar ustreza skoraj 95 % svetovne prodaje elektrificiranih vozil (Slika 3). V teh državah elektrificirani avtomobili predstavljajo velik delež lokalnih avtomobilskih trgov: več kot ena od treh registracij novih vozil na Kitajskem je bila leta 2023 elektrificirana, več kot ena od petih v Evropi in ena od desetih v Združenih državah. Kitajska, Evropa in Združene države predstavljajo približno dve tretjini celotne prodaje in zalog vseh vrst vozil, kar pomeni, da ima prehod na elektrificirana vozila na teh trgih velike posledice v smislu globalnih trendov [1, 2].

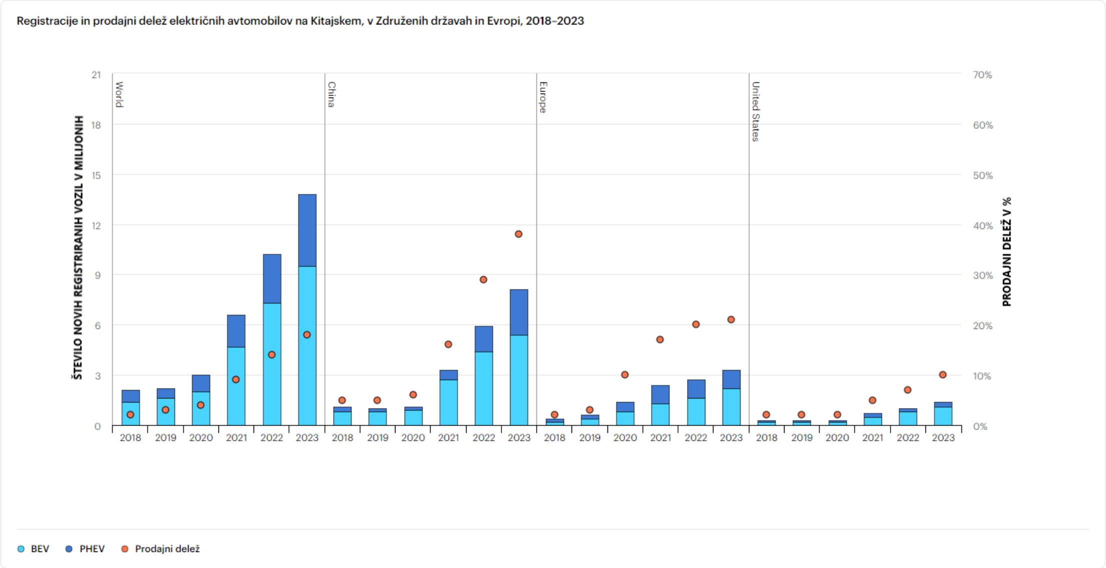

Slika 3: Število novih registriranih elektrificiranih vozil in njihov prodajni delež [1]

2 PRODAJA ELEKTRIFICIRANIH VOZIL V EU

V Evropi so leta 2023 registracije novih elektrificiranih vozil dosegle skoraj 3,2 milijona, kar je skoraj 20-odstotno povečanje glede na leto 2022. V Evropski uniji je prodaja znašala 2,4 milijona s podobnimi stopnjami rasti. Tako kot na Kitajskem visoke stopnje prodaje elektrificiranih vozil v Evropi kažejo, da rast ostaja močna, več evropskih držav pa je leta 2023 doseglo pomembne mejnike. Nemčija je na primer postala tretja država za Kitajsko in Združenimi državami z rekordno pol milijona registracij novih baterijskih elektrificiranih vozil v enem letu, pri čemer je 18 % prodaje vozil BEV (in še 6 % PHEV). Delež elektrificiranih vozil (BEV in PHEV) v % in kumulativna vsota vseh prodanih novih vozil po državah EU je prikazan na sliki 4. Vrste (BEV, PHEV, HEV, dizel in bencin) in delež v % prodanih novih vozil po državah EU v letu 2023 predstavlja slika 5 [1, 2].

Slika 4: Delež elektrificiranih vozil (BEV in PHEV) v % in kumulativna vsota vseh prodanih novih vozil po državah EU [2]

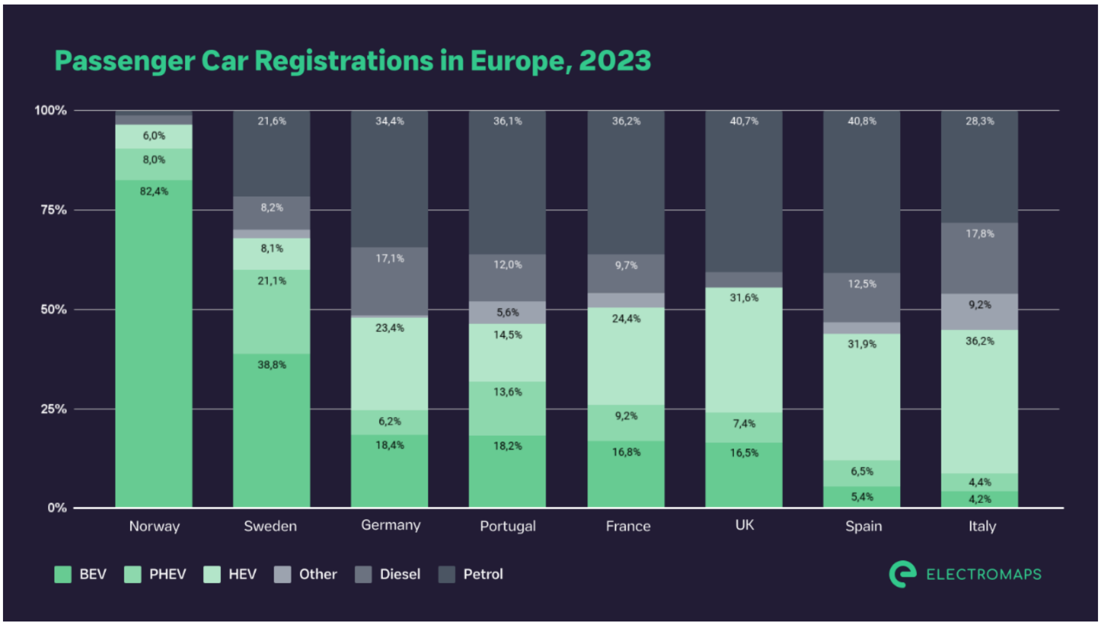

Slika 5: Vrsta (BEV, PHEV, HEV, dizel in bencin) in delež v % prodanih novih vozil po državah EU v letu 2023 [3]

Vendar pa je postopna opustitev več subvencij za nakup v Nemčiji upočasnila splošno rast prodaje elektrificiranih vozil. Na začetku leta 2023 so bile subvencije za PHEV postopno ukinjene, kar je povzročilo nižjo prodajo PHEV v primerjavi z letom 2022, decembra 2023 pa so se vse subvencije za BEV končale po odločitvi sklada za podnebje in preobrazbo. V Nemčiji je delež prodaje elektrificiranih vozil padel s 30 % leta 2022 na 25 % leta 2023. To je vplivalo na skupni delež prodaje elektrificiranih vozil v regiji. V preostalem delu Evrope pa se je prodaja elektrificiranih vozil in njihov prodajni delež povečala. Elektrificiranih je bilo 25 % vseh vozil, prodanih v Franciji in Združenem kraljestvu, 30 % na Nizozemskem in 60 % na Švedskem. Na Norveškem so se prodajni deleži kljub skupnemu krčenju trga nekoliko povečali, njen prodajni delež pa ostaja najvišji v Evropi, skoraj 95-odstoten. [1, 2, 3, 4]

3 PREGLED PRODAJE ELEKTRIFICIRANIH VOZIL 2023 IN 2024

Močna prodaja elektrificiranih vozil v prvem četrtletju leta 2024 presega letno skupno prodajo izpred štirih let (Slika 6). Prodaja elektrificiranih vozil je v prvem četrtletju leta 2024 ostala močna in je presegla prodajo v enakem obdobju leta 2023 za približno 25 % in dosegla več kot 3 milijone vozil. Ta stopnja rasti je bila podobna povečanju, opaženemu v istem obdobju leta 2023 v primerjavi z letom 2022. Večino dodatne prodaje je prinesla Kitajska, ki je prodala približno pol milijona več elektrificiranih vozil kot v enakem obdobju leta 2023. Relativno gledano, največja rast je bila opažena zunaj glavnih trgov elektrificiranih vozil, kjer se je prodaja povečala za več kot 50 %, kar nakazuje, da se prehod na elektro mobilnost krepi v vse večjem številu držav po svetu [1, 2].

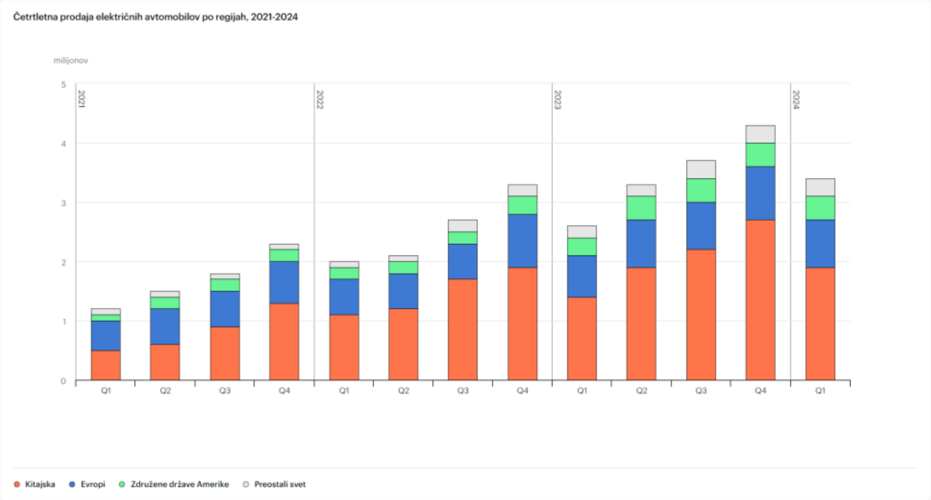

Slika 6: Prodaja elektrificiranih vozi po četrtletjih v različnih regijah od 2021 do 2024. [1, 2]

Od januarja do marca letos je bilo na Kitajskem prodanih skoraj 1,9 milijona elektrificiranih vozil, kar je skoraj 35-odstotno povečanje v primerjavi s prodajo v prvem četrtletju leta 2023. Marca je prodaja elektrificiranih vozil na Kitajskem presegla 40-odstotni delež v skupni prodaji vozil. Kot smo priča leta 2023, prodaja priključnih hibridnih elektrificiranih vozil raste hitreje kot prodaja čisto baterijskih elektrificiranih vozil. Prodaja priključnih hibridnih elektrificiranih vozil se je v prvem četrtletju na Kitajskem medletno povečala za približno 75 % v primerjavi s 15 % prodaje baterijskih elektrificiranih vozil.

V Evropi je prvo četrtletje leta 2024 zabeležilo več kot 5-odstotno medletno rast, ki je nekoliko nad rastjo celotne prodaje vozil in s tem stabilizirala delež prodaje elektrificiranih vozil na podobni ravni kot lani. Še posebej visoka je bila rast prodaje elektrificiranih vozil v Belgiji, kjer je bilo prodanih okoli 60.000 elektrificiranih vozil, kar je skoraj 35 % več kot leto prej. Vendar Belgija predstavlja manj kot 5 % celotne evropske prodaje vozil. Na večjih evropskih trgih – v Franciji, Nemčiji, Italiji in Združenem kraljestvu (ki skupaj predstavljajo približno 60 % evropske prodaje vozil) – je bila rast prodaje elektrificiranih vozil nižja. V Franciji je skupna prodaja elektrificiranih vozil v prvem četrtletju narasla za približno 15%. Združeno kraljestvo je zabeležilo podobno medletno rast (več kot 15 %) prodaje elektrificiranih vozil kot Francija. V Nemčiji, kjer so se leta 2023 končale subvencije za elektrificirane avtomobile na baterije, je prodaja elektrificiranih vozil v prvem četrtletju leta 2024 padla za skoraj 5 %, predvsem zaradi 20-odstotnega medletnega zmanjšanja v marcu. Delež EV v skupni prodaji vozil je bil torej nekoliko nižji kot lani. Tako kot na Kitajskem je bila prodaja PHEV v Nemčiji in Združenem kraljestvu večja od prodaje BEV. V Italiji je bila prodaja elektrificiranih vozil v prvih treh mesecih leta 2024 več kot 20 % nižja kot v enakem obdobju leta 2023, pri čemer se je večina zmanjšala v segmentu PHEV. Vendar bi se ta trend lahko obrnil na podlagi uvedbe nove sheme spodbud.

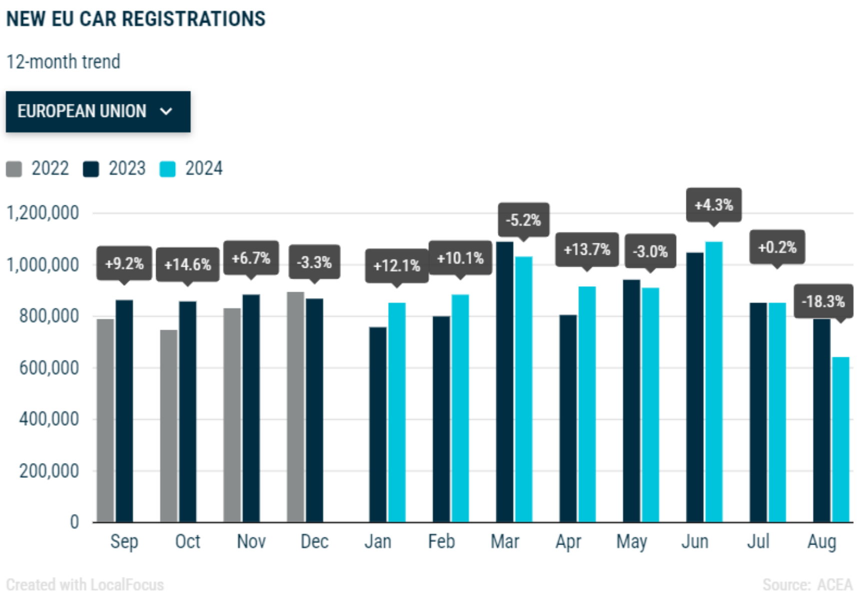

Source: ACEA

Slika 7: Število novih registracij vseh vozil v EU po mesecih v letih 2022, 2023 in 2024 [5]

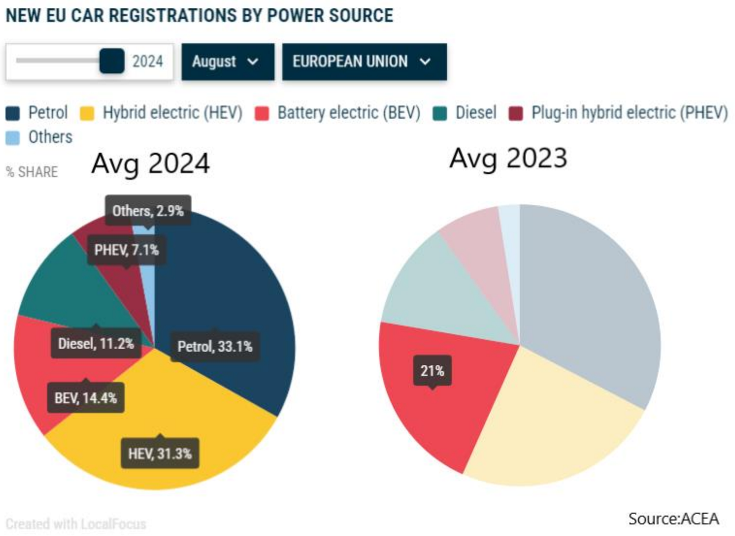

Source:ACEA

Slika 8: Delež novih vozil v EU glede na vrsto pogona. Primerjava Avgust 2023 in 2024 [5]

V Združenih državah je prodaja v prvem četrtletju dosegla okoli 350 000, kar je skoraj 15 % več kot v enakem obdobju leto prej. Tako kot na drugih večjih trgih je bila rast prodaje PHEV še večja, in sicer 50-odstotna. Medtem ko se zdi, da je delež prodaje BEV v Združenih državah v zadnjih nekaj mesecih nekoliko padel, je delež prodaje PHEV narasel.

Na manjših trgih elektrificiranih vozil je bila rast prodaje v prvih mesecih leta 2024 precej višja, čeprav z nizke osnove. Januarja in februarja se je prodaja elektrificiranih vozil v Braziliji skoraj početverila. V Indiji se je prodaja v prvem četrtletju leta 2024 povečala za več kot 50 %. Te številke kažejo, da elektrificirana vozila pridobivajo zagon na različnih trgih po vsem svetu.

Od leta 2021 je prodaja elektrificiranih vozil v prvem četrtletju običajno predstavljala 15-20 % celotne svetovne letne prodaje. Na podlagi tega opaženega trenda, skupaj z zagonom politike in sezonskostjo, ki se običajno pojavlja pri prodaji elektrificiranih vozil, ocenjujemo, da bi lahko prodaja elektrificiranih vozil leta 2024 dosegla približno 17 milijonov. To kaže na močno rast, pri čemer bo prodaja v letu 2024 presegla prodajo v letu 2023 za več kot 20 % in bodo elektrificirana vozila presegla 20 % delež v skupni prodaji vozil.

4 ANALIZA SEGMENTOV ELEKTRIFICIRANIH VOZIL

Na voljo je vse več elektrificiranih modelov, vendar se trend usmerja k večjim vozilom. Število razpoložljivih modelov elektrificiranih vozil se približuje 600, od tega dve tretjini velikih vozil in SUV-jev. Leta 2023 se je število razpoložljivih modelov za elektrificirane avtomobile medletno povečalo za 15 % na skoraj 590, saj so proizvajalci vozil povečali načrte za elektrifikacijo, da bi pritegnili rastočo bazo potrošnikov. Medtem se je število popolnoma opremljenih modelov z motorji z notranjem izgorevanjem v nadaljevanju oznaka – ICE (internal combustion engine) (tj. brez hibridov) zmanjšalo že četrto leto zapored, v povprečju za 2 %. Na podlagi nedavnih objav proizvajalcev (OEM) bi lahko število novih modelov elektrificiranih vozil do leta 2028 doseglo 1000. Če vsi napovedani novi elektrificirani modeli dejansko pridejo na trg in če se bo število razpoložljivih modelov vozil ICE še naprej zmanjševalo za 2 % letno, bi lahko pred letom 2030 bilo toliko elektrificiranih kot modelov vozil ICE.

Kot poroča GEVO-2023 [1], se delež majhnih in srednjih modelov elektrificiranih vozil med razpoložljivimi elektrificiranimi modeli zmanjšuje: leta 2023 sta bili dve tretjini baterijsko-elektrificiranih modelov na trgu SUV,https://www.iea.org/reports/global-ev-outlook-2024/trends-in-electric-cars tovornjaki ali veliki avtomobili. Samo 25 % prodaje baterijskih elektrificiranih vozil v Združenih državah je bilo za majhne in srednje velike modele, v primerjavi s 40 % v Evropi in 50 % na Kitajskem. Elektrificirani avtomobili sledijo istemu trendu kot običajni avtomobili in v povprečju postajajo večji. Leta 2023 so SUV, pick-up tovornjaki in veliki modeli predstavljali 65 % celotne prodaje vozil ICE po vsem svetu ter več kot 80 % v ZDA, 60 % na Kitajskem in 50 % v Evropi. Razčlenitev prodaje baterijskih električnih avtomobilov v izbranih državah in regijah po segmentih, 2018–2023 prikazuje slika 7 [1, 2].

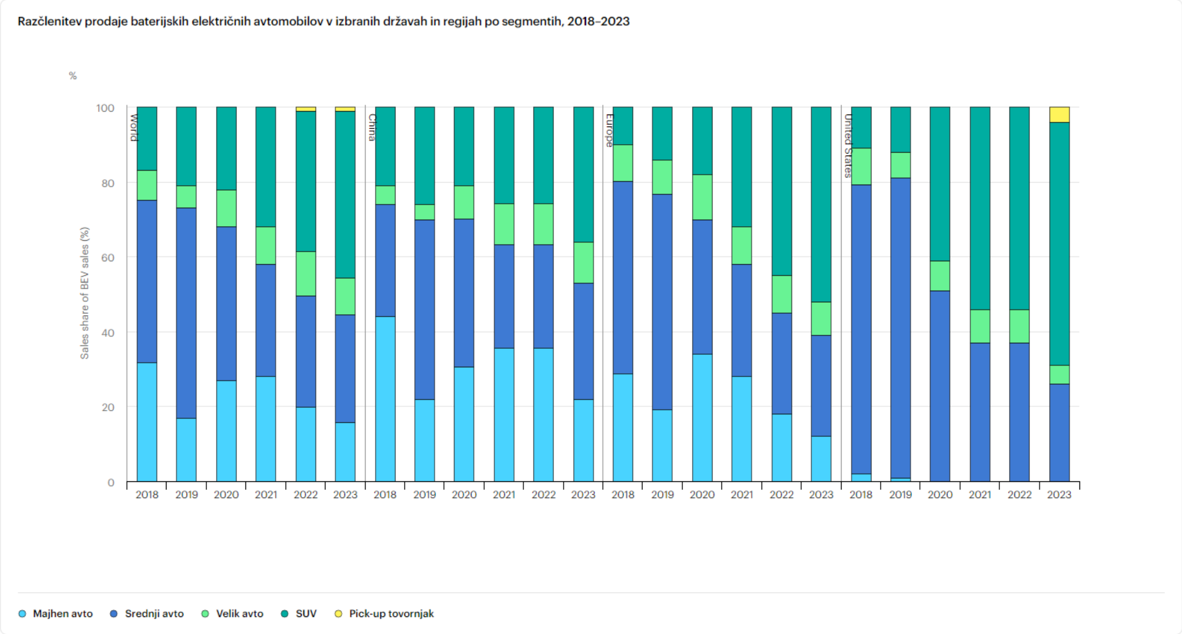

Slika 7: Razčlenitev prodaje baterijskih električnih avtomobilov v izbranih državah in regijah po segmentih, 2018–2023 [1, 2]

4.1 Velikost baterij, poraba energije in surovin

Večji modeli elektrificiranih vozil pomembno vplivajo na dobavne verige baterij in kritično povpraševanje po surovinah. Leta 2023 je imelo povprečno BEV terensko vozilo v Evropi skoraj dvakrat večjo baterijo od tiste v povprečnem majhnem BEV vozilu, kar je sorazmerno vplivalo na kritične potrebe po surovinah. Seveda je doseg majhnih vozil običajno krajši od SUV in velikih vozil. Če pa primerjamo elektrificirane SUV in srednje velike BEV vozila, ki so leta 2023 ponujali podoben doseg, je bila baterija SUV še vedno 25 % večja. To pomeni, da če bi elektrificirane SUV vozila zamenjali za nižja vozila srednjega razreda, bi lahko globalno prihranili 60 GWh energije. Poleg tega bi če upoštevamo porabo surovin, ki se uporabljajo na Kitajskem, v Evropi in Združenih državah, prihranili skoraj 6 000 ton litija, 30 000 ton niklja, skoraj 7 000 ton kobalta in več kot 8 000 ton mangana.

Večje baterije zahtevajo več energije ali daljši čas polnjenja. To lahko povzroči pritisk na elektrificirana omrežja in polnilno infrastrukturo s povečanjem zasedenosti, kar lahko povzroči težave med največjo porabo, na primer na polnilnih mestih na avtocestah v času povečanega prometa.

Večja vozila zahtevajo tudi večje količine materialov, kot so železo in jeklo, aluminij in plastika, z večjim okoljskim in ogljičnim odtisom za proizvodnjo materialov, predelavo in sestavo. Dodatno porabo energije, ki je posledica povečane mase, do neke mere ublaži regenerativno zaviranje.

4.2 Doseg elektrificiranih vozil

Povprečni doseg se povečuje, vendar precej počasi. Pomisleki glede dosega v primerjavi z vozili z motorjem ICE in glede razpoložljivosti polnilne infrastrukture za potovanja na dolge razdalje prav tako prispevajo k povečanju apetita po večjih modelih z daljšim dosegom.

Z naraščajočo velikostjo baterije ter izboljšavami v tehnologiji baterij in dizajnu vozil se je povprečna ponudba BEV elektrificiranih vozil med letoma 2015 in 2023 povečala za skoraj 75 modelov. Povprečni realen doseg majhnih vozil v letu 2023 – okoli 150 km – ni veliko večji kot v letu 2015, kar kaže, da je ta doseg že zelo primeren za mestno uporabo (z izjemo taksijev, ki imajo veliko večjo dnevno porabo). Veliki modeli višjega cenovnega razreda so že leta 2015 ponujali višje dosege od povprečja, njihov realen doseg pa do leta 2023 ni naraščal in je v povprečju znašal okoli 360–380 km. Medtem so bile dosežene znatne izboljšave pri srednje velikih avtomobilih, katerih doseg zdaj znaša okoli 380 km, medtem ko je leta 2015 v povprečju znašal približno 150 km pri srednje velikih avtomobilih in 270 km pri športnih terencih SUV. To je spodbudno za potrošnike, ki želijo kupiti elektrificirani avto za daljša potovanja namesto mestne vožnje [1].

5 ZAKLJUČEK

Za dosego prelomne točke na množičnem trgu so potrebni cenovno dostopnejši elektrificirani avtomobili. Pravičen in vključujoč prehod na elektrificirano mobilnost, tako znotraj držav kot na svetovni ravni, je odvisen od uspešnega lansiranja cenovno dostopnih elektrificiranih vozil. Odločitve o nakupu avtomobila običajno vključujejo upoštevanje maloprodajne cene in razpoložljivih subvencij ter življenjskih obratovalnih stroškov, kot so stroški goriva, zavarovanja, vzdrževanja in amortizacije, ki skupaj sestavljajo celotne stroške lastništva.

Leta 2023 so bile vnaprejšnje maloprodajne cene za elektrificirane avtomobile na splošno višje kot za njihove ekvivalente modele z notranjim izgorevanjem. Tudi izguba vrednosti vozil je bila višja pri BEV in PHEV kot pri modelih z notranjem zgorevanjem. Vendar se lahko trend hitrejše izgube vrednosti elektrificiranih vozil obrne iz več razlogov. Prvič, potrošniki pridobivajo več zaupanja v življenjsko dobo baterij, s čimer se povečuje vrednost pri nadaljnji prodaji elektrificiranih vozil. Drugič, veliko povpraševanje in pozitivna podoba blagovne znamke nekaterih elektrificiranih modelov lahko pomenita, da ohranijo svojo vrednost dlje. V Združenih državah Amerike modelom znamke Tesla pada vrednost počasneje kot ostalim bencinskim avtomobilom. Nazadnje, povišanje cen goriva v nekaterih regijah, uvedba območij z nizkimi emisijami, ki omejujejo dostop za vozila, ki najbolj onesnažujejo okolje, ter davki in parkirnine, posebej usmerjeni na vozila z motorjem z notranjim zgorevanjem, lahko pomenijo, da bodo v prihodnosti deležna hitrejše izgube vrednosti kot elektrificirana vozila.

Subvencije pri nakupu znižajo prvotno maloprodajno ceno in pomagajo znižati celotni strošek lastništva elektrificiranih vozil v primerjavi z ekvivalentnimi modeli z motorji z notranjim izgorevanjem. Doseganje enakosti cen med elektrificiranimi avtomobili in avtomobili z motorjem ICE bo pomembna točka preloma. Tudi če je celotni strošek lastništva za elektrificirane avtomobile ugoden, ima vnaprejšnja maloprodajna cena odločilno vlogo. Raziskave v Združenih državah na primer kažejo, da je bila cenovna dostopnost glavna skrb za potrošnike, ki so leta 2023 razmišljali o uporabi elektrificiranih vozil.

Ko bodo trgi elektrificiranih vozil dozoreli, bo trg rabljenih vozil postal pomembnejši. Podobno kot pri drugih tehnoloških izdelkih se zdaj pojavljajo trgi rabljenih elektrificiranih vozil, ko prihajajo novejše generacije vozil, prejšnji uporabniki pa kupujejo nova. Trgi rabljenih vozil so ključnega pomena za spodbujanje sprejemanja na množičnem trgu, zlasti če novi elektrificirani avtomobili ostajajo dragi, rabljeni pa cenejši. Tako kot pri vozilih z motorjem z notranjim izgorevanjem (ICE) – za katera je nakup rabljenega pogosto glavni način nakupa avtomobila v nastajajočih in razvitih gospodarstvih – se bo podoben vzorec pojavil pri elektrificiranih vozilih.

Ko veliki trgi elektrificiranih vozil dosegajo zrelost, ostaja vse več rabljenih elektrificiranih vozil na voljo za nadaljnjo prodajo. Naše ocene kažejo, da je leta 2023 obseg trga rabljenih elektrificiranih vozil znašal skoraj 800 000 na Kitajskem, 400 000 v Združenih državah in več kot 450 000 v Franciji, Nemčiji, Italiji, Španiji, na Nizozemskem in v Združenem kraljestvu skupaj. Trgi rabljenih vozil že ponujajo cenovno ugodnejše elektrificirane možnosti na Kitajskem, v Evropi in Združenih državah Amerike [1].

V Evropi je mogoče najti rabljene BEV elektrificirane avtomobile med 15.000 in 25.000 EUR, rabljene priključne hibride pa okoli 30.000 EUR. Nekatere evropske države ponujajo tudi subvencije za rabljene elektrificirane avtomobile, na primer Nizozemska (2.000 EUR), kjer subvencija za nove avtomobile od leta 2020 vztrajno upada, za rabljene pa ostaja enaka, in Francija (1.000 EUR). V Sloveniji znaša subvencija za nakup rabljenega električnega vozila 3.000 € za vozila do 45.000 € z DDV in subvencija 2.000 € za nakup rabljenega za vozila vrednosti od 45.000 € do 65.000 € z DDV.

LITERATURA

[1] 2023 edition of the Global EV Outlook (GEVO-2023) [splet]. Dosegljivo: www.iea.org/reports/global-ev-outlook-2023
[2] International Council on Clean Transportation [splet]. Dosegljivo: https://theicct.org/insight-analysis/publications/?_decarbonizing=electrification
[3] Electric car registrations in 2023 in Europe [splet]. Dosegljivo: https://www.electromaps.com/en/blog/electric-car-registrations-europe-2023
[4] Europe EV Sales Analysis: Key Insights on June 2024 Registrations [splet]. Dosegljivo: https://alternative-fuels-observatory.ec.europa.eu/general-information/news/europe-ev-sales-analysis-key-insights-june-2024-registrations
[5] Registracije novih avtomobilov: -18,3 % avgusta 2024; Tržni delež BEV padel za skoraj tretjino [splet]. Dosegljivo: https://www.acea.auto/pc-registrations/new-car-registrations-18-3-in-august-2024-bev-market-share-do

9th International Conference on the Development of Industrial Engineering
21. November 2024
Novo mesto, Slovenia

Mehanske lastnosti jekla 42CrMo4 v toplotno vplivnem področju vara

Matej Petek[1], Matej Pleterski[1]

[1]Fakulteta za industrijski inženiring Novo mesto, Šegova ulica 112, 8000 Novo mesto, Slovenija
E-naslovi: mpetek93@gmail.com, matej.pleterski@gmail.com

Povzetek: *Jeklo 42CrMo4 se uvršča med posebna legirana konstrukcijska jekla namenjena poboljšanju. Uporablja se ga v avtomobilski in letalski industriji za izdelavo strojnih elementov, kot so gredi, zobniki, vijačne in zobate letve, sorniki, itn. in so izpostavljeni visokim in zmernim dinamičnim obremenitvami. V raziskavi smo preiskovali mehanske lastnosti tega jekla v toplotno vplivanem področju (TVP), ki se nahaja tik ob zvaru in med varjenjem ni bilo staljeno. Na tem območju se zaradi vnosa toplote in hitrega ohlajanja pojavi kaljenje, kar jeklu na tem področju spremeni mehanske lastnosti. Obravnavani zvarjenec predstavlja verižnik, na katerega je privarjena prirobnica, skupaj pa sestavljata spodnji del stebra gozdarskega dvigala FK 8500. Namen je tako bil ugotoviti vpliv predgrevanja zvarjenca na mehanske lastnosti v TVP. Zvarjenec 1 smo predhodno predgrevali, varili in nato počasi ohlajali v izolacijski volni. Zvarjenec 2 smo zavarili brez predhodnega predgrevanja ter smo ga po varjenju pustili ohlajati na zraku pri sobni temperaturi. Oba zvarjenca smo uporabili za pridobivanje vzorcev, s pomočjo katerih smo izmerili trdoto, natezno trdnost in žilavost. Izmerjeni rezultati so potrdili predvidevanja, saj so se mehanske lastnosti v TVP na jeklu 42CrMo4 spremenile. Predgrevanje je ugodno vplivalo na mehanske lastnosti v TVP, saj je bila žilavost višja in trdota nižja na predgretem zvarjencu 1 kot pri nepredgretem zvarjencu 2. Obenem smo z rezultati pokazali, da je trenutni tehnološki postopek varjenja verižnika s prirobnico neustrezen.*

Ključne besede*: jeklo 42CrMo4, varjenje, TVP, mehanske lastnosti, trdota, žilavost*

Razvrstitev: *Strokovni prispevek*

1 UVOD

Mehanske lastnosti jekel opisujejo odziv materiala na določeno obremenitev. Obstaja več vrst mehanskih lastnosti. Najpomembnejše mehanske lastnosti jekel so natezna trdnost, trdota in žilavost. Z Njihovimi nazivnimi vrednostmi se glede na konstrukcijske zahteve določi primerno vrsto jekla. Podatek o natezni trdnosti se uporablja pri trdnostnem izračunu konstrukcije, kjer se izračunano natezno trdnost primerja z nazivno natezno trdnostjo določenega jekla. Trdota jekla je pomembna pri tistih jeklih, kjer so elementi neposredno izpostavljeni obrabi. Udarna žilavost predstavlja mehansko lastnost, ki je pomembna pri jeklih, ki so izpostavljena nenadnim obremenitvam ali nizkim temperaturam.

V raziskavi je bil obravnavan steber gozdarskega dvigala. Pri delovanju dvigala ta segment prenaša največjo obremenitev, saj nanj deluje upogibni moment. Med obratovanjem dvigala je v zimskem času, ko je zunanja temperatura padla pod – 15 °C prišlo do zloma stebra na predelu verižnika, kamor je privarjena prirobnica. Vzrok za zlom stebra se je predpisal zvaru. Zaradi neposredne obrabe in prenašanja velike obremenitve, je verižnik izdelan iz jekla 42CrMo4, ki ga odlikujejo visoka trdota, žilavost in natezna trdnost. Obravnavano jeklo spada med jekla za poboljšanje. Za jekla, ki imajo vsebnost ogljika večjo od 0,25 % velja, da so pogojno variva. Legirni elementi v jeklu za poboljšanje dodatno izboljšujejo prekaljivost jekla, kar rezultira v naraščanju trde mikrostrukture s podhlajenim avstenitom. Visok vnos energije, ki se jo v zvarjenec vnaša med varjenjem in hitro ohlajanje sta ključna dejavnika, ki na mestu zvara povzročita nezaželeno lokalno kaljenje in s tem poslabšata mehanske lastnosti jekla do te mere, da lahko v kombinaciji s hladno okolico privedejo do porušitve materiala.

Toplotno vplivano področje (v nadaljevanju TVP) je področje tik ob zvaru. Vnos toplote med varjenjem in hitro ohlajanje povzročita spreminjanje mikrostrukture na mestu, ki je bilo izpostavljeno temperaturi, ki je nekaj stopinj manjša od temperature tališča jekla. Spremenjena mikrostruktura v TVP ima poslabšane mehanske lastnosti kot osnovni material (v nadaljevanju OM). To se kaže v povečani trdoti in manjši žilavosti in pojav krhkosti. S povečanjem vsebnosti ogljika v jeklu je možnost za poslabšanje mehanskih lastnosti v TVP toliko večja. Slika 1 prikazuje spreminjanje žilavosti od vara preko TVP do OM. Iz nje se vidi, da se žilavost v TVP močno zmanjša [1].

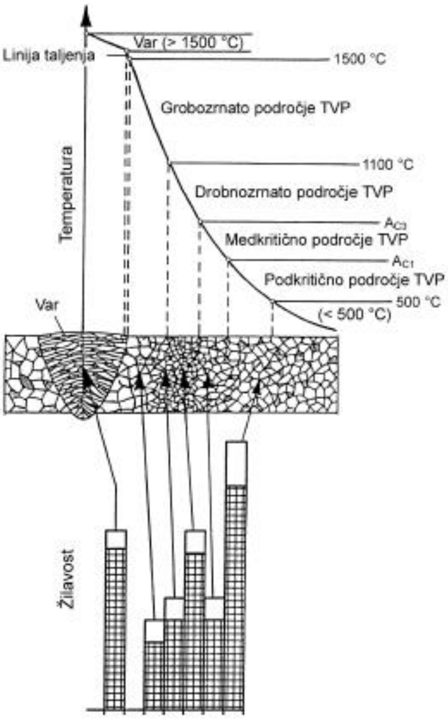

Slika 1: Žilavost v TVP [2]

Bolj ugodno mikrostrukturo se doseže s predgrevanjem zvarjenca, kar pomeni, da se surovec pred izvajanjem varjenja predgreje na določeno temperaturo. Po končanem varjenju pa se zvarjenec postavi v izolacijsko posodo. S tem se doseže manjša hitrost ohlajanja kar ublaži učinek kaljenja. Posledično je mikrostruktura bolj ugodna, mehanske lastnosti pa so zadovoljive do te mere, da material pod obremenitvijo ne poka.

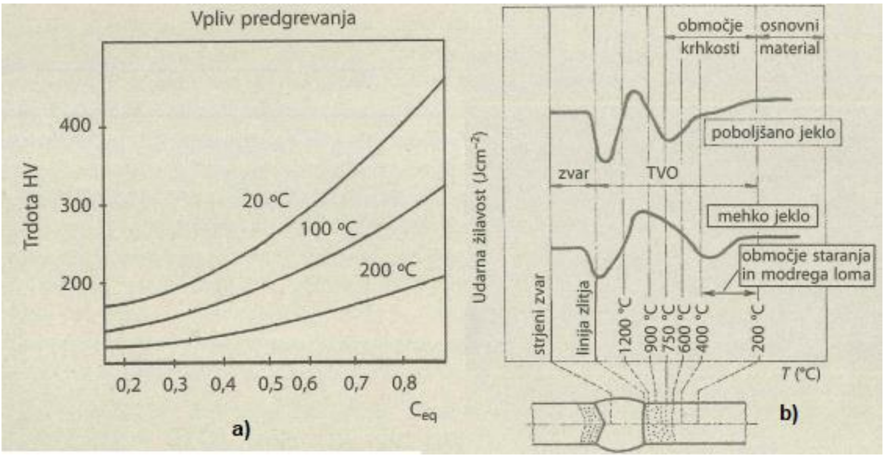

Slika 2: Trdota in žilavost v zvarnem spoju [1]

Točka a) na sliki 2 prikazuje odvisnost trdote od vsebnosti ogljika. S povečevanjem temperature predgrevanja se trdota v TVP zmanjša. Jekla za poboljšanje imajo lahko največjo trdoto 350 HV oziroma med 400 in 450 v TVP. Točka b) na sliki 2 pa prikazuje spreminjanje udarne žilavosti v zvaru poboljšanega jekla.

Ravno tako na zmanjšanje mehanskih lastnosti jekla vpliva tudi zunanja temperatura, saj pri določeni temperaturi material postane krhek, njegova žilavost pa se bistveno poslabša. Kombinacija neustrezno predgretega in hitro ohlajenega zvarjenca lahko pod obremenitvijo pri nizki temperaturi vodi v porušitev materiala.

Namen raziskave je bil ugotoviti, ali so poslabšane mehanske lastnosti v TVP lahko vzrok za zlom stebra. Pri tem nas je zanimalo, kako predgrevanje in počasno ohlajanje vplivata na mehanske lastnosti v TVP. Med drugim smo tudi ugotavljali za koliko se poslabša žilavosti jekla v TVP v primerjavi z žilavostjo OM pri temperaturi – 20 °C.

2 METODE

V teoretičnem delu smo z metodo kompilacije povzeli vire, ki se navezujejo na mikrostrukturo jekel, toplotno obdelavo, varjenje in predgrevanje jekel ter različne preizkuse, s katerimi se ugotavljajo mehanske lastnosti. Z metodo deskripcije je bil opisan obstoječ tehnološki postopek varjenja veržnika s prirobnico.

V raziskovalnem delu smo z metodo analize in pridobivanja podatkov na vzorcih dveh zvarjencev, ki sta bila zavarjena po različnih tehnoloških postopkih, odvzeli različne vzorce, ki so bili potrebni za merjenje natezne trdnosti, trdote iz žilavosti. Na koncu smo z metodo komparacije primerjali rezultate na obeh vzorcih.

2.1 Predgrevanje

Slabo varivost jekel za poboljšanje (C > 0,25 %) se lahko izboljša s predgrevanjem pred varjenem. Predgrevanje je še posebej pomembno pri debelejših zvarjencih in legiranih jeklih. Legirni elementi znižujejo kritično hitrost ohlajanja pri kaljenju jekel, s tem pa še dodatno otežujejo varjenje saj narašča trda mikrostruktura s podhlajenim avstenitom. CCT diagram, ki je prikazan na sliki 3, se uporablja za presojanje kaljenja in varivosti jekla. Pri tem se je potrebno držati težje, ki veleva, da smo z ohlajevalnimi hitrosti čim bolj na desni strani CCT diagrama, saj se s tem dobi mehkejše mikrostrukture, s katerimi se ohranja žilavost v TVP [1].

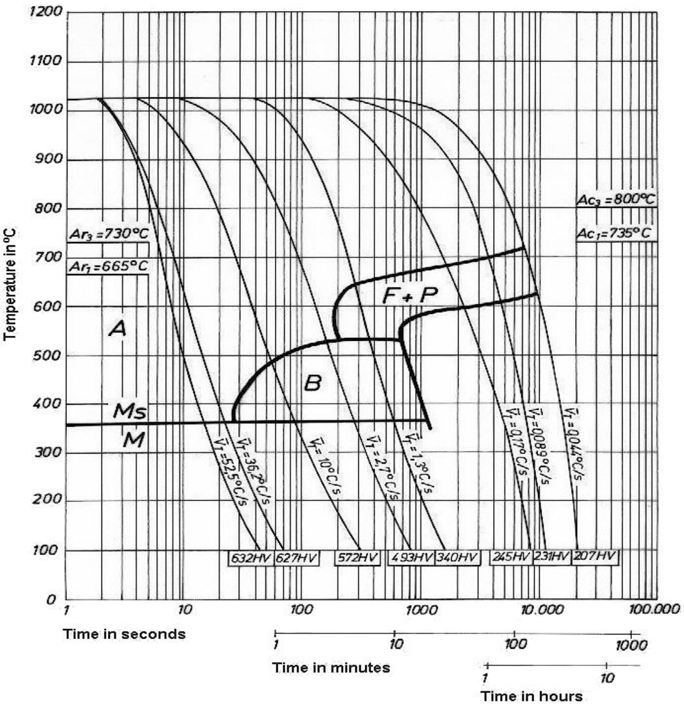

Slika 3: CCT diagram za jeklo 42CrMo4 [3]

Po enačbi 1 se izračuna ogljikov ekvivalent C_{eq}, ki glede na vsebnost ogljika in ostale kemijske v elemente v jeklu poda informacijo o tem, ali je obravnavano jeklo potrebno predgrevati.

$$\text{Ceq=C+}\frac{Mn}{6}+\frac{(Cr+Mo+V)}{5}+\frac{(Ni+Cu)}{15} \tag{1}$$

Pri izračunani vrednosti C_{eq} < 0,45, pomeni da je jeklo dobro varivo in predgrevanje ni potrebno. Kadar vrednost znaša C_{eq} med 0,46 in 0,6, je potrebno zvarjenec segrevati na temperaturo med 100 in 200 °C. Pri vrednosti C_{eq} nad 0,60 se obdelovanec predgreva na temperaturo med 200 in 350 °C. Izračunana vrednost C_{eq} za jeklo 42CrMo4 znaša 0,77, kar pomeni, da je predgrevanje pri varjenju zobnika s prirobnico nujno. S predgrevanjem se doseže naslednje:

- upočasnjevanje hitrosti ohlajevanja, kar omogoča difuzijo vodika, ki povzroča razpoke na zvarnem spoju;
- zmanjševanje trdote v TVP;
- zmanjševanje zaostalih napetosti kot posledica manjših temperaturnih razlik na zvarnem mestu;
- izravnavanje neenakomerne mikrostrukturne porazdelitve;
- preprečevanje razpok v hladnem in zniževanje toplotnih deformacij [1].

2.2 Varjenje zvarjencev

Za potrebe merjenja mehanskih lastnosti se je zvarilo dva enaka vzorčna zvarjenca, ki sta bila spojena z različnim tehnološkim postopkom. Osrednji del zvarjenca je predstavljal valj iz jekla 42CrMo4, ki je imel premer 160mm. Nanj se je privarilo prirobnico iz konstrukcijskega jekla S355, debeline 50 mm in dimenzije 390 mm. Ta dimenzija je bila potrebna zato, da smo lahko iz zvarjencev izrezali preizkuševalne vzorce ustreznih dimenzij, ki so bili uporabljeni pri merjenju natezne trdnosti in žilavosti. Na notranjem delu prirobnice je bil postružen zvarni žleb. Pri obeh zvarjencih se je postopek pričel s segrevanjem prirobnice z namenom povečanja tolerančne mere za krčni nased. S tem korakom sta bila surovca pripravljena na varjenje.

Prvi zvarjenec, ki smo ga poimenovali zvarjenec 1, je bil s plamenskim gorilnikom predgret na temperaturo 220°C. Preverjanje temperature, ki je prikazano pod točko a) na sliki 4 je potekalo s talilno kredo, ki se pri omenjeni temperaturi začne taliti in uparjati. Predgrevanje je potekalo izmenično po vsej površini surovca. Zvarni spoj je bil zavarjen v petih posameznih varkih. Zvarjenec 1 je bil po opravljenem varjenju položen v posodo z izolacijsko volno, kjer se je ohlajal za čas 24 ur. Točka b) na sliki 4 prikazuje ohlajanje zvarjenca 1.

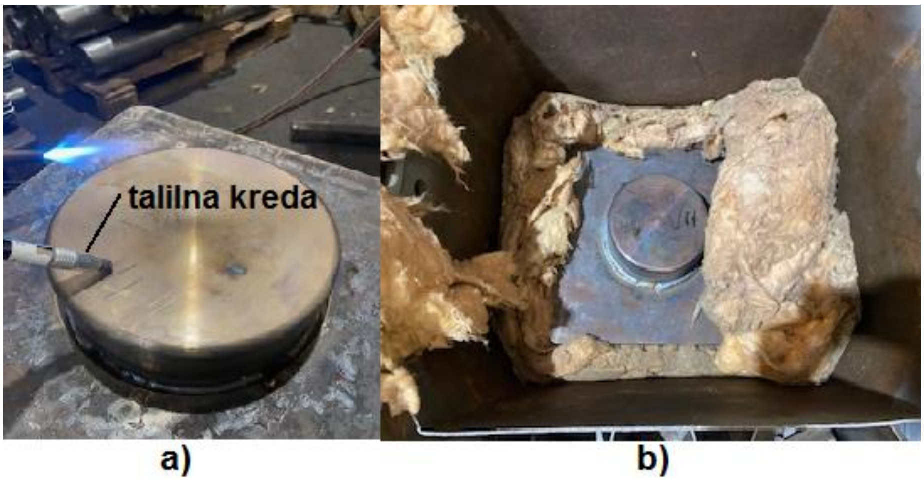

Slika 4: Zvarjenec 1

Varjenje zvarjenca 2 se je izvedlo brez predhodnega predgrevanja. Zvarni spoj je bil tako kot pri prejšnem zvarjencu izdelan v petih varkih. Zvarjenec 2 se je po varjenju ohlajal na zraku pri sobni temperaturi. Pri obeh zvarjencih so bili uporabljeni enaki varilni parametri in dodajni material. Zvarjenca sta bila nato poslana na inštitut TKC d. o. o. , ki je opravilo makroskopijo zvarnega spoja ter meritve trdote, natezne trdnosti in žilavosti. Poudarek je bil na samem zvaru in TVP jekla 42 CrMo4.

2.3 Merjenje trdote

Trdota pomeni odpornost materiala proti vdiranju tršega materiala. Material, ki ima enako sestavo in mikrostrukturo po vsem prerezu, ima enako trdoto tako na površini, kot tudi v notranjosti. Glede na vrsto merjenja trdote, se jo lahko razdeli na različne načine. Pri merjenju trdote jekel je najbolj pogosta *trdota vtiska*, kjer je opisana kot odpornost materiala na vtisk pod statično ali dinamično obremenitvijo. V našem primeru je bil izveden preizkus po Vickers metodi. [4]

Merjenje trdote po Vickersu je zaradi enostavnosti primeren za materiale različnih trdot. Vtiskovalni element predstavlja diamanta piramida s kotom 136°. Vtiskovana kalota ima obliko kvadratne osnovne ploskve. S pomočjo mikroskopa se izmeri njuni diagonali d_1 in d_2, ki služita za izračun srednje vrednosti diagonale d. Slednja vrednost predstavlja merilo, ki se ga uporabi za primerjavo podatkov na posebnih tabelah in preko njih določi trdote na posameznih vtiskih. [5]

Za merjenje trdote na zvarjencih 1 in 2, je bilo potrebno te najprej razrezati. Sledilo je poliranje merilne površine. Merjenje je potekalo na več različnih mestih, in sicer na OM verižnika 42CrMo4 in njegovem TVP, v korenu in temenu zvara ter v TVP in osnovnem materialu prirobnice z materialom S355. Meritev je potekala po standardu SIST EN ISO 9015-1:2012. Slika 5 prikazuje merilni stroj Zwick Roell, ki je povezan z računalnikom. Na ekranu, kjer se vidi vtisek z obliko piramide, se odčita velikost diagonal.

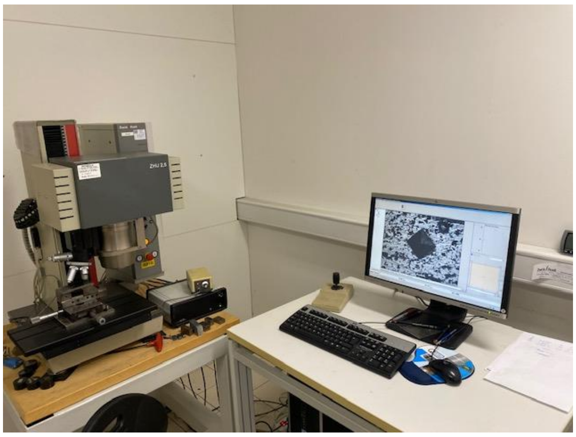

Slika 5: Naprava za merjenje trdote

Slika 6 prikazuje področja, kjer so bile izvedene meritve trdote. V našem primeru smo se osredotočili na odtiska 5 in 9, ki predstavlja TVP jekla 42CrMo4 in odtisek 1, ki predstavlja trdoto na OM.

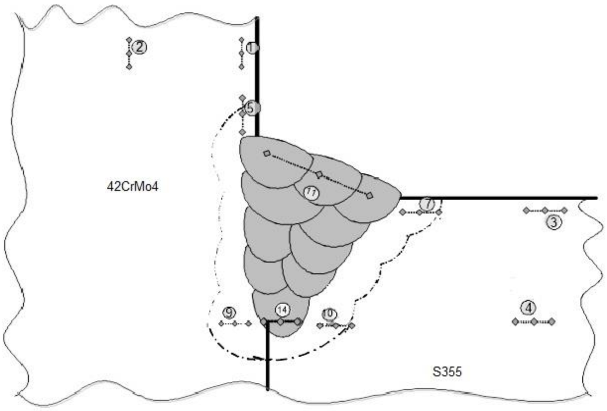

Slika 6: Prikaz področij za merjenje trdote

Slika 7 prikazuje prerezano in spolirano površino vzorca, ki je bil odvzet na zvarjencu 1. Na njem se vidijo vtiski, ki so nastali pri merjenju trdote. Poleg tega se na sliki vidijo posamezni varki, globina in širina celotnega zvara ter TVP, ki je še posebej izrazito na materialu 42CrMo4.

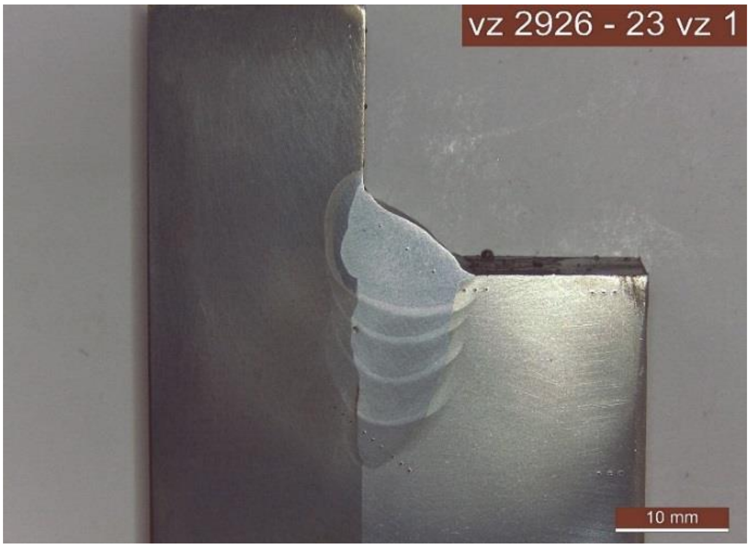

Slika 7: Merjenje trdote na vzorcu 1

2.4 Merjenje natezne trdnosti

Natezna trdnost se označuje s simbolom R_m. Definirana je kot največja sila, ki deluje na površino vzorca in predstavlja največjo napetost, ki jo material še prenese pod enoosno obremenitvijo. Enota za natezno trdnost je podana v njutnih na kvadratni milimeter (N/mm^2). Preizkus je semistatičen, kar pomeni da se izvaja z mirujočo oziroma statično silo, ki narašča z majhno hitrostjo, ki nima pomembnejšega vpliva na rezultate preizkušanja. Preizkus je standardiziran kar pomeni, da so naprave, oblike in velikosti vzorca ter pogoji preizkušanja natančno določeni. Z njim se določenemu materialu določa različne lastnosti, med katerimi so najbolj pogoste:

- natezna trdnost $R_{m,}$,
- napetost tečenja $R_{p0.2}$,
- modul elastičnosti E,
- raztezek e,
- kontrakcija q [5].

Mere vzorcev za natezni preizkus so standardizirane. Njihov prerez je lahko okrogel, kvadraten ali pravokoten. Glava vzorca ima večji prerez kot sredinski del. Namen tega je zagotavljanje trdnosti in eliminacija preloma na vpenjalnem delu ali blizu njega. Manjši premer v sredinskem delu zagotavlja konstantno porazdelitev napetosti po celem prerezu. Preizkus se izvaja na univerzalnih nateznih strojih. Vzorec se vpne v zgornjo in spodnjo vpenjalno čeljust. Spodnja čeljust je običajno toga, zgornja čeljust, ki je vpeta na hidravlični cilinder, pa se pomika v nasprotno stran od toge čeljusti. Slika 8 prikazuje univerzalni hidravlični stroj, ki se ga poleg merjenja natezne trdnosti uporablja tudi za druge mehanske preizkuse kot npr. za upogibni, tlačni ali strižni preizkus.

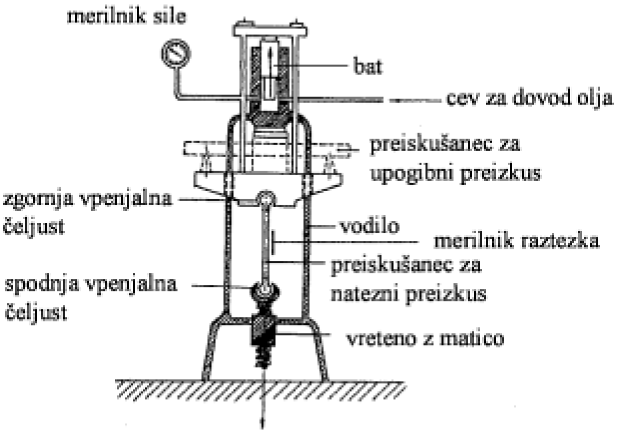

Slika 8: Univerzalni stroj za natezni in upogibni preizkus [4]

Za preizkus natezne trdnosti so bili iz obeh zvarjencev izrezani štiri vzorci. Pri obeh zvarjencih je eden vzorec na sredini vseboval zvarni spoj, drugi vzorec pa TVP jekla 42CrMo4. Nadaljnje so bili ustrezno obdelani na rezkalnem stroju. Njihov prerez je imel kvadratno obliko. Vzorci so bili označeni s sledečimi številkami:

- (vzorec iz predgrevanega zvarjenca 1, ki je v sredini vseboval zvarni spoj),
- 1-2 (vzorec iz predgrevanega zvarjenca 1, ki je v sredini vseboval TVP materiala 42CrMo4),
- 2-1 (vzorec iz nepredgretega zvarjenca 2, ki je v sredini vseboval zvarni spoj),
- 2-2 (vzorec iz nepredgretega zvarjenca 2, ki je v sredini vseboval TVP materiala 42CrMo4).

Slika 9: Vzorci za natezni preizkus

Na sliki 9, kjer so prikazani vzorci na natezni preizkus, lahko vidimo, da imajo njihove glave manjše zareze. Te zagotavljajo boljši oprijem v čeljustih trgalnega stroja in tako preprečujejo lezenje vzorcev med preizkušanjem.

2.5 Preizkus udarne žilavosti

Žilavost predstavlja mehansko lastnost, ki definira količino energije, ki jo material absorbira v plastičnem območju do porušitve materiala. Več energije kot jo material absorbira, večja je žilavost in boljša je odpornost proti porušitvi. Za prelom krhkih materialov je potrebno veliko manj energije, medtem ko je za žilave materiale značilno, da je za njihov prelom potrebna večja količina energije.

Z nižanjem zunanje temperature se spreminjajo tudi mehanske lastnosti materiala. Pri določeni temperaturi jeklo izgubi duktilno lastnost in postane krhko. Prehodna temperatura zavisi od velikosti kristalnih zrn jekla ter geometrijske oblike preizkušanca. Ugotavljanje prehodne temperature z nateznim preizkusom ni mogoče, saj ga odlikuje majhna hitrost deformacij. V ta namen je francoski metalurg Charpy leta 1901 razvil metodo za udarno merjenje žilavosti (ang. Charpy V notch impact energy) na preizkušancih z zarezo. Dimenzije preizkušanca so standardizirane, na sredini pa je prerez oslabljen, saj vsebuje zarezo v obliki črke V, ki določa mesto preloma med preizkusom. Prelom se izvede z udarnim kladivom, ki se ga spusti z višine h_1 ter zaniha in udari v sredino preizkušanca, ki je postavljen v razmaknjeni podpori in na koncu doseže višino h_2. Iz razlike višine kladiva pred in njegove mase se lahko izračuna uporabljeno energijo za prelom. Naprava za izvajanje preizkusa udarne žilavosti se definira po začetni energiji kladiva, in sicer 300, 150 ali 100 J. Oblika V zareze preizkušanca omogoča triosno napetostno stanje v njeni okolici. Posledično ima tak preizkušanec zadostno občutljivost za odkrivanje krhke pojavne oblike loma. S preizkusom udarne žilavosti se pri konstrukcijskih jeklih odkriva prehod v krhko stanje že pri sobni temperaturi. [6]

Preizkus se izvede tako, da se vzorec položi na dno naprave, kjer sta nameščeni dve podpori v razmaku 40 mm. Nato se iz višine h_1 spusti nihajno kladivo, ki pri spuščanju udari in prelomi vzorec, ter na drugem koncu doseže višino h_2. . Porabljeno delo za prelom preizkušanca se imenuje udarno delo, ki se ga izračuna z enačbo 2. V njej kot α predstavlja vpadni kot, β pa odbiti kot, r je dolžina droga, g pa predstavlja gravitacijski pospešek, ki znaša 9,81 m/s^2. Udarno delo se izraža v joulih. Slika 10 prikazuje princip merjenja udarne žilavosti po Charpyju. [6]

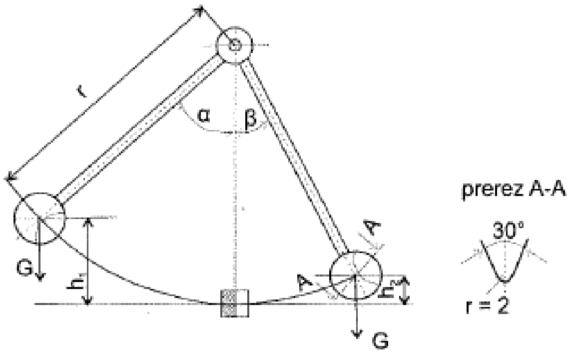

Slika 10: Merjenje žilavosti po Charpyju [2]

$$E = m \cdot g \cdot r(cos\beta - cos\alpha) \tag{2}$$

Vzorci za merjenje udarne žilavosti so bili prav tako izrezani iz obeh zvarjencev. Udarno žilavost je bila izmerjena na sredini zvarnega spoja in TVP jekla 42CrMo4. Preizkušanci so bili označeni z naslednjimi številkami:

- Z1-1, Z2-1, Z3-1 (preizkušanci, ki na mestu V zareze vsebujejo zvarni spoj zvarjenca 1),
- Z1-2, Z2-2, Z3-2 (preizkušanci, ki na mestu V zareze vsebujejo zvarni spoj zvarjenca 2),
- T1-1, T2-1, T3-1 (preizkušanci iz zvarjenca 1, ki na mestu V zareze vsebujejo TVP materiala 42CrMo4),
- T1-2, T2-2, T3-2 (preizkušanci iz zvarjenca 2, ki na mestu V zareze vsebujejo TVP materiala 42CrMo4).

Slika 11: Vzorci za merjenje udarne žilavosti

Vzorce, ki so prikazani na sliki 11, se je pred preizkusom ohladilo na temperaturo – 20 °C. Vzorci so se ohlajali v tekočem CO$_2$. Temperatura se je sproti preverjala s temperaturnim tipalom. V trenutku, ko je bila dosežena želena temperatura, so vzorci na tej temperaturi ostali še dve minuti, da so bili enakomerno ohlajeni po vsem prerezu. Ohlajeni vzorci so bili pripravljeni za preizkus udarne žilavosti.

3 REZULTATI MERITEV TRDOTE, NATEZNE TRDNOSTI IN ŽILAVOSTI

Meritve trdote so potrdile teoretične osnove. Vnos toplote med varjenjem in hitro ohlajanje sta povzročila kaljenje v TVP jekla 42CrMo4. Povečana trdota v TVP je bila prisotna pri obeh zvarjencih. V tabeli 1 so zbrane izmerjene trdote zvarjencev 1 in 2.

Tabela 1: Rezultati merjenja trdote v TVP 42CrMo4 in OM

	TVP na 42CrMo4 (teme vara - vtiski 5)	TVP na 42CrMo4 (koren vara - (vtiski 9)	OM na 42CrMo4 (vtiski 1)
Zvarjenec 1	251, 566, 556	258, 280, 398	269, 263, 265
Zvarjenec 2	250, 489, 644	219, 254, 400	261, 263, 261

Trdote v TVP jekla 42CrMo4 so se v primerjavi s trdotami v OM povečale pri obeh zvarjencih. V obeh primerih so bile izmerjene trdote višje v temenu kot v korenu zvara. Teme zvara se je ohlajalo hitreje kot koren zvara. Poleg tega pa je vnesena toplota pri naslednjih varkih ugodno vplivala na trdoto v korenu zvara, saj je prišlo do samopopuščanja. Najvišja trdota je bila izmerjena v temenu zvara na zvarjencu 2, ki pred varjenjem ni bil predgret.

Največja trdota, ki jo dovoljuje standard SIST EN ISO 15614-1:2017/A1:2020, znaša za jeklo 42CrMo4 450 HV. Ta vrednost je bila presežena pri obeh zvarjencih v TVP na vtiskih 5, ki so se nahajali v temenu zvara. Kot je že bilo omenjeno, se je teme zvara ohlajalo hitreje kot koren zvara, kar se kaže v kaljenju in povečanju trdote. Največja izmerjena trdota je bila izmerjena na zvarjencu 2 in je znašala 644 HV. Nekoliko manjša trdota je bila izmerjena na zvarjencu 1, vendar sta dve vrednosti trdote na vtisku 5 (566 HV, 556 HV) še vedno presegali maksimalno dovoljeno trdoto. Predgrevanje je torej ugodno vplivalo na trdoto v temenu zvara (vtiski 5), saj je bila izmerjena trdota na predgretem zvarjencu 1 manjša kot na zvarjencu 2, ki ni bil predgret. Preseganje maksimalno dovoljene trdote za jeklo 42CrMo4 pri predgretem zvarjencu 1, se je pripisalo nepopolnemu predgrevanju s plamenskim gorilnikom, s katerim ni bilo moč zagotoviti enakomerne temperature po vsem prerezu zvarjenca.

Rezultati nateznega preizkusa, ki so zbrani v tabeli 2, so v dveh primerih pokazali na nepravilnosti na lomni površini preizkušancev.

Tabela 2: Rezultati natezne trdnosti

Natezni preizkus: po SIST EN ISO 4136:2013						**Temp. preizkusa: 24°C**	
Pr. Št.	**Dimenzije b x t_s [mm]**	**Presek [mm^2]**	**Sila ob porušitvi [kN]**	**Natezna trdnost R_m [N/mm^2]**	**Raztezek A [%]**	**Nepravilnosti na prelomni površini**	**Mesto preloma**
1-1	15,01x15,09	226,50	108	476,82	/	zlep	zvar
1-2	14,98x15,07	225,74	109	482,85	/	zlep	zvar
2-1	14,99x15,08	226,04	125	552,99	/	/	OM-S355
2-2	14,98x15,05	225,44	125	554,47	/	/	OM-S355
Zahteve: S355 EN 10025-2 R_m : 470-630 N/mm^2, 42CrMo4+QT , EN 10083-3: R_m 750-900 N/mm^2							

Na vzorcih 1-1 in 1-2, ki sta bila odvzeta iz zvarjenca 1, je vizualni pregled pokazal na zlep zvara, kar se vidi na sliki 12. V tem primeru je prišlo do nepopolnega varjenja, saj je oblika zvarnega žleba omejevala optimalno pozicijo varilne pištole. Posledično energija varilnega obloka ni bila zadosti usmerjena v jeklo 42CrMo4, kar je vodilo v neraztaljevanje OM, to pa je rezultiralo v zlep zvara. Izmerjena natezna trdnost na omenjenih vzorcih je dosegla zgolj spodnjo zahtevo natezne trdnosti za jeklo S355, ki znaša 470 N/mm^2. Na vratu preizkušancev 1-1 in 1-2 je prišlo do krhkega loma, saj ni bilo mogoče zaznati predhodne plastične deformacije.

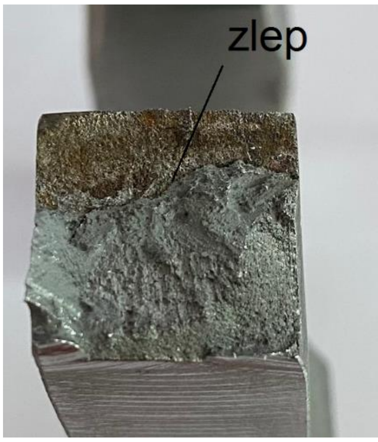

Slika 12: Zlep na vzorcu 1-1 za natezni preizkus

Nekoliko boljši rezultati so bili izmerjeni na vzorcih 2-1 in 2-2, ki sta bila odvzeta iz zvarjenca 2. Pri obeh vzorcih je zvar prenesel natezno obremenitev, saj je do preloma pričakovano prišlo na jeklu S355. Slednje jeklo ima manjšo nazivno natezno trdnost kot jeklo 42CrMo4. Na vzorcih je pred prelomom prišlo do plastične deformacije, kar se je pokazalo v zoženju vratu na preizkušancih. To je značilno za mehkejša jekla. Slika 13 prikazuje prelomljena vzorca 2-1 in 2-2, na katerih se vidi izrazito zoženje vratu.

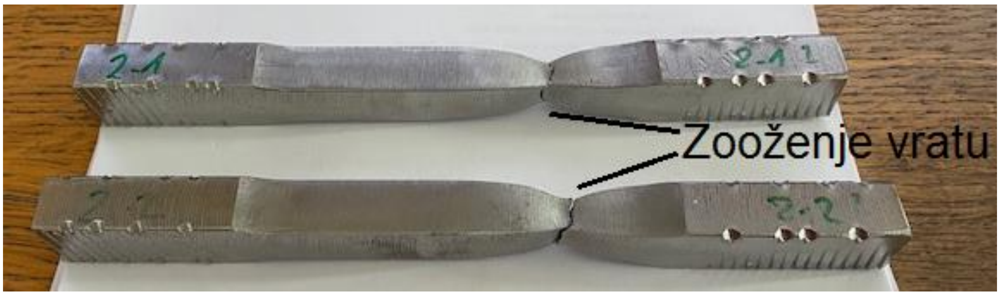

Slika 13: Zoženje vratu na vzorcih 2-1 in 2-2

Izmerjene natezne trdnosti so bile še vedno znatno večje od maksimalne izračunane površinske natezne trdnosti, ki se pojavijo pri obremenitvi verižnika. Največja površinska napetost, ki se pojavi pod obremenitvijo na tem delu verižnika znaša 90 N/mm^2. Kljub nepravilnostim na zvaru ta še vedno zagotavlja zadostno natezno trdnost.

Rezultati merjenja udarne žilavosti, ki so zbrani v tabeli 3, so pokazali bistveno poslabšanje žilavosti v TVP pri predgrevanem kot tudi nepredgrevanem zvarjencu.

Tabela 3: Izmerjene vrednosti udarne žilavosti

PREIZKUS UDARNE ŽILAVOSTI / Toughness tests po SIST EN ISO 148-1: 2017 in SIST EN ISO 9016:2013							**Temp. preizkusa: - 20ºC Test Temp**	
Vzorec /	**Debelina [mm]**	**Višina [mm]**	**Presek S_0 [mm^2]**	**Udarno delo / KV**	**Udarna žilavost Preračunana / 0,8cm^2**	**Udarna žilavost povprečna**	**Širjenje LE**	**Lega Zareze /**
				[J]	[J/0,8cm^2]	[J/0,8cm^2]	[mm]	
1Z1	10,00	8,00	80,00	46	/	48,66	/	VWT 0/0,5
1Z2	10,00	8,00	80,00	42	/		/	
1Z3	10,01	8,00	80,08	58	/		/	
1T1	10,00	8,00	80,00	31	/	27,66	/	VHT 1/0,5
1T2	10,00	8,00	80,00	22	/		/	
1T3	10,00	8,00	80,00	30	/		/	
2Z1	10,00	8,00	80,00	45	/	39,33	/	VWT 0/0,5
2Z2	10,00	8,00	80,00	35	/		/	
2Z3	10,00	8,00	80,00	38	/		/	
2T1	10,00	8,00	80,00	32	/	26,33	/	VHT 1/0,5
2T2	10,00	8,00	80,00	22	/		/	
2T3	10,00	8,00	80,00	25	/		/	
Zahteve: 35 J pri T= -20° C								

Pri obeh zvarjencih izmerjena žilavost v TVP jekla 42CrMo4 ni dosegla minimalne predpisane žilavosti, ki pri temperaturi – 20 °C znaša 35 J. Najmanjša žilavost je bila izmerjena na zvarjencu 2 v TVP in je znašala 26,33 J. Nekoliko boljša žilavost, vendar še vedno pod minimalno zahtevo, je bila izmerjena na zvarjencu 1 v TVP in je znašala 27,66 J. Boljši rezultati so bili izmerjeni na sredini zvara, saj so bile izmerjene žilavosti znotraj minimalne predpisane vrednosti. Največja žilavost je bila izmerjena pri zvarjencu 1 in je znašala 48,66 J. Nekoliko manjša žilavost je bila dobljena na zvarjencu 2 ter je znašala 39,33 J.

4 ZAKLJUČEK

Mehanske lastnosti jekla 42CrMo4 so se v TVP spremenile zaradi vnosa toplote in hitrega ohlajanja. To so potrdile meritve trdote in udarne žilavosti. Merjenje natezne trdnosti pa je pokazalo na nepopolni zvarni spoj, ki je bil posledica neraztaljenega OM pri varjenju.

Predgrevanje je ugodno vplivalo na trdoto v TVP, saj je bila največja trdota izmerjena na nepredgretem zvarjencu 2. Kljub predgrevanju na zvarjencu 1, je bila tudi tu presežena maksimalna dovoljena vrednosti, ki znaša 450 HV. Vzrok za to, se je pripisal nepopolnem predgrevanju s plamenskim gorilnikom. Pri obeh zvarjencih je bila največja trdota izmerjena v temenu zvara, kar nakazuje na to, da se na tem mestu zvarjenec ohlaja najhitreje.

Udarna žilavost v TVP se je v primerjavi z žilavostjo OM zelo poslabšala. Nazivna vrednost žilavosti za jeklo 42CrMo4 pri temperaturi – 20 °C znaša 60 J, medtem ko je minimalna zahteva pri preizkusu znašala – 35 J. Tudi tukaj je predgrevanje ugodno vplivalo na žilavost, saj je bila ta najslabša na nepredgretem zvarjencu 2, in sicer v njegovem TVP. Nekoliko višja žilavost v TVP je bila izmerjena na predgretem zvarjencu 1, vendar je bila v obeh primerih še vedno pod minimalno zahtevo. Tudi tukaj se je vzrok pripisal nepopolnemu predgrevanju ali prehitremu ohlajanju. Meritve žilavosti v sredini zvara so bile nad minimalno zahtevano vrednostjo.

Merjenje natezne trdnosti je bilo uspešno na nepredgrevanem zvarjencu, saj je zvarni spoj prenesel obremenitev in je do preloma preizkušanca prišlo na predelu, ki je vseboval šibkejše jeklo S355. Pri vzorcih, ki so bili vzeti iz predgrevanega zvarjenca, je do preloma prišlo v TVP na jeklu 42CrMo4. Prelomna površina preizkušancev je pokazala, da je bil na zvarnem spoju prisoten zlep, ki ni zagotovil zadostne trdnosti. Posledično je bila izmerjena natezna trdnost manjša na vzorcih iz predgrevanega zvarjenca. Preizkus natezne trdnosti je prav tako pokazal na neustrezen tehnološki postopek varjenja. Zlep, ki predstavlja nepopoln zvarni spoj, ne nudi zadostne trdnosti. Nenadna preobremenitev stebra dvigala lahko ob prisotnosti zlepa in nizki zunanji temperaturi privede do zloma verižnika.

LITERATURA

[1] Rak, *Tehnologija varjenja*. Ljubljana: Modrijan, 2008.
[2] V. Grdun in B. Godec. (2023). ''Neugodne mikrostrukturne sestavine v zvarnih spojih konstrukcijskih jekel.'' *Materiali in tehnologije* [splet]. Dosegljivo: http://mit.imt.si/izvodi/mit025/ grdun.pdf. [16.1.2023].
[3] SIJ elektrode. "Filtub 16b." *Dodajni materiali za varjenje* [spet]. Dosegljivo: https://elektrode.si/assets/magazine-files/Elektrode-dodajni-materiali-za-varjenje.pdf. [27 . 3. 2023].
[4] A. Bhaduri, *Mechanical properties and working of metals and alloys.* Singapure : Springer 2018.
[5] J. Grum*, Tehnologija in obdelava materialov.* Ljubljana : samozal., 2017.
[6] J. Vojvodič-Tuma, *Mehanske lastnosti kovin*. Ljubljana: Fakulteta za gradbeništvo in geodezijo, 2002.